# Tuning the spin-triplet superconducting state by a magnetic field in UTe2 and UCoGe.

Adrien Rosuel

THÈSE

Pour obtenir le grade de

**DOCTEUR DE L'UNIVERSITÉ GRENOBLE ALPES**

École doctorale : PHYS - Physique
Spécialité : Physique de la Matière Condensée et du Rayonnement
Unité de recherche : PHotonique, ELectronique et Ingéniérie QuantiqueS

# Contrôle de la supraconductivité spin-triplet par un champ magnétique dans UTe2 et UCoGe

# Tuning the spin-triplet superconducting state by a magnetic field in UTe2 and UCoGe.


Présentée par :

**Adrien ROSUEL**


Direction de thèse :

| | |
|---|---|
| **Jean-Pascal BRISON**<br>Directeur de recherche, CEA Centre de Grenoble | Directeur de thèse |

Rapporteurs :

**ANNE DE VISSER**
Associate professor, Universiteit van Amsterdam
**VALENTIN TAUFOUR**
Associate professor, University of California, Davis

Thèse soutenue publiquement le **15 mai 2023**, devant le jury composé de :

| | |
|---|---|
| **ANNE DE VISSER**<br>Associate professor, Universiteit van Amsterdam | Rapporteur |
| **VALENTIN TAUFOUR**<br>Associate professor, University of California, Davis | Rapporteur |
| **JULIA MEYER**<br>Professeur des Universités, UNIVERSITE GRENOBLE ALPES | Présidente |
| **KAMRAN BEHNIA**<br>Directeur de recherche, CNRS DELEGATION PARIS CENTRE | Examinateur |
| **ILYA SHEIKIN**<br>Directeur de recherche, CNRS DELEGATION ALPES | Examinateur |

# ABSTRACT

In 2018, superconductivity was discovered in the paramagnetic compound $UTe_2$ between 1.5 K and 2 K. The possibility of spin-triplet superconductivity, possibly induced by ferromagnetic fluctuations, and of topological superconductivity, has triggered a lot of study. Nevertheless, the pairing symmetry and mechanism remain unknown.

A striking property of $UTe_2$ at ambient pressure is its resilience to magnetic field. For a certain range of angles in the crystal, superconductivity is detected up to 60 T. Also, for a field along the b-axis of hard magnetisation, superconductivity is enhanced above 15 T up to a metamagnetic transition occurring at $H_m = 34.5$ T.

A major result of this work is the discovery of a thermodynamic transition line between two superconducting phases in the H-T phase diagram along the b axis. These measurements reveal the emergence of a second superconducting phase above 15 T when a field is applied along the b-axis. Moreover, they show that the two phases are of a different nature, not corresponding to a simple change of symmetry of the superconducting order parameter as proposed in previous theoretical studies. They confirm, as suggested by the pressure studies, that there are two competing pairing mechanisms in $UTe_2$. A likely scenario would be a low-field spin-triplet superconducting phase, possibly driven by ferromagnetic fluctuations, and a high-field spin-singlet phase, possibly driven by anti-ferromagnetic fluctuations as the metamagnetic transition approaches.

Specific heat measurements were also performed on the ferromagnetic superconductor UCoGe. It is a strong candidate for spin-triplet superconductivity. Despite its discovery sixteen years ago (in 2007), few thermodynamic measurements have been made. Our specific heat measurements have allowed us to establish a first complete thermodynamic phase diagram. A more detailed analysis of the results allows to demonstrate in a "direct" way the suppression of the pairing mechanism for magnetic fields applied along the easy magnetisation axis, and also shows a very unusual behaviour of the order parameter at low fields in the directions of hard magnetisation.

# ACKNOWLEDGEMENTS

First of all I would like to thank Anne de Visser and Valentin Taufour for accepting to be referees and their careful reading of my manuscript. I would also like to thank Julia Meyer, Kamran Behnia and Ilya Sheikin for having been part of my jury, alongside Anne and Valentin.

Je commence ces remerciements par le plus important, Jean-Pascal le manager de l'équipe IMAPEC, accessoirement mon directeur de thèse. Toujours disponible, malgré un agenda chargé, pour répondre à des questions, débloquer la manip, relire toutes les conneries que j'ai pu écrire... J'ai beaucoup appris pendant cette thèse, mais si il fallait retenir une chose, ce serait la grande rigueur scientifique dont il fait preuve et que j'espère honorer dans le futur. On en ne peut espérer mieux comme directeur de thèse.

Je continue avec Christophe, grand expert de la chaleur spécifique et grand fan du Japon. Ce fut un plaisir de faire ces campagnes de mesures au LNCMI. J'en profite donc pour remercier tous les membres du LNCMI rencontrés et de l'institut Néel, Thierry, Gabriel, Albin... Notamment Marie-Aude, avec qui j'ai fait mon stage de M1, que j'ai croisé dans le tram juste après le séminaire de Jean-Pascal et qui n'a eu que des choses positives à dire à son sujet et m'a vivement conseillé d'aller au CEA pour mon stage de M2, ce qui s'est avéré être un excellent conseil.

Un grand merci à tous les membres d'IMAPEC l'école des tailleurs de pierre, à commencer par Georg un pilier incontournable d'IMAPEC. Amoureux des codes couleurs et des traces en $T^2$, il a beau repeter tous les jours que ce qu'il fait est nul et pas interessant, et bah en realite c'est pas si nul que ça. (j'ai enleve les accents, ces choses compliquees et inutiles, pour lui faire plaisir)

En continuant avec les membres d'IMAPEC, Alexandre toujours prêt à initier des conversations, notamment politiques pour bien chauffer l'ambiance. Pierre expert du magnétisme et du magnétisme nucléaire, mais aussi un très bon pédagogue. C'est en partie de sa "faute" si le magnétisme nucléaire m'a intéressé au point de faire un postdoc en RMN. Daniel le roi de la pression. Iulian l'expert de la cryo et peut être bientôt des recondenseurs. Les membres du D5 et en particulier Gérard qui nous fournit en masses les meilleurs cristaux.

Mais il y a aussi des jeunes à IMAPEC, Simon le dernier terroriste cryogénique restant de l'équipe, Timothée futur star de twitch, ou encore Nils qui bat des

records de non-arrivé le matin. Ainsi que tous les thésards, stagiaires et postdocs passés par IMAPEC, Julia, Michal, Qun...

Puis il ne faut pas oublier les théoriciens et nos voisins de LATEX, sans oublier Marielle la meilleure des secrétaires. Enfin, tous ceux que je n'ai pas cité mais que j'ai eu l'occasion de croiser, de travailler ou de discuter avec eux, Tristan le Toulousain qui met plus de vin sur son pantalon que dans sa bouche, David un Rennais en Chine, Stéphane monsieur neutron, William le statisticien du covid et plein d'autres...

Et pour finir ma famille qui m'a toujours soutenu même s'ils ne comprennent rien à ce que je fais !

# CONTENTS

# 1

# INTRODUCTION AND PHYSICAL BACKGROUND

The major breakthrough in superconductivity over the last 40 years has been the discovery of several families of unconventional superconductors: heavy fermions, organic compounds, high $T_{sc}$ cuprates, pnictides and hydrides. All except hydrides are controlled by pairing mechanisms dominated by purely electronic interactions instead of the classical electron-phonon interaction (BCS [19]). These new pairing mechanisms also lead to new superconducting states, with different possible spin states (spin-singlet or spin-triplet). The nature of these pairing mechanisms is a crucial issue for a more global understanding of superconductivity.

In 2018 superconductivity was first detected in $UTe_2$ [113]. This compound quickly drew a lot of attention because of its unique properties and the possibility to host spin-triplet superconductivity, a rare state but highly sought after. The most remarkable is by far its strong resilience to magnetic field. Superconductivity is detected up to 60 T for a critical temperature $T_{sc}$ of $1.4 - 2$ K for certain crystal directions. However, before the measurements presented in this manuscript, few thermodynamic measurements had been performed on $UTe_2$, and no evidence of bulk superconductivity at high field had been provided.

This is the first reason that motivated these specific heat measurements. An other motivation was to provide new data to try to elucidate the origin of the pairing mechanism and the symmetry of the superconducting order parameter under field, since they are still both under debate, with many different measurements claiming support for opposite scenarios.

This thesis is mainly focused on $UTe_2$ and its critical field, but to introduce this compound and its unique properties, the best entry point are the ferromagnetic superconductors and more specifically UCoGe. Both compounds share similarities especially regarding their critical fields.

This manuscript is divided in five main chapters. First, some basic physical background on superconductivity will be given, then UCoGe and $UTe_2$ will be introduced. After, a chapter focused on specific heat will present some physical background and the techniques used to measure $UTe_2$ and UCoGe. Then the results on $UTe_2$ will be presented, showing a tuning of the pairing mechanism by magnetic field. The analysis of the critical fields based on strong-coupling theory will be presented, and the possibility of a change of superconducting symmetry (from spin-triplet to spin-singlet) induced by field is discussed.

At the end of the manuscript, some results obtained on UCoGe will also be presented together with a first analysis pointing a possible change of the **d**-vector orientation induced by field.

## 1.1 INTRODUCTION TO BASICS ON SUPERCONDUCTIVITY

### 1.1.1 *Introduction*

Before introducing UCoGe and $UTe_2$, let us briefly introduce ferromagnetic superconductors and some physical background.

Ferromagnetism and superconductivity are usually seen as two antagonist phenomena, but back in 1957 (year of the BCS theory) Ginzburg already proposed the coexistence of this two phenomena. Its conclusion was as long as the thermodynamic critical field $H_c(0)$ exceeds the internal field $B_0 = \mu_0 M_0$, both phase can coexist. This prediction was limited to the case of type I superconductors, and left little hope of finding such a system since the great majority of ferromagnets have internal fields which greatly exceed the usual value for thermodynamic critical fields in metals.

Later, Abrikosov and Gor'kov established a theory of the Cooper pair breaking by magnetic impurities. The conclusion is that when the magnetic impurities concentration increases, the critical temperature $T_{sc}$ decreases, and superconductivity is suppressed even for small amount of impurities (a few percent).

The first examples of superconductors with a lattice of magnetic ions were found in the mid seventies, with the discovery of the Chevrel phases ((Rare Earth)+$Mo_6S_8$) [34] and the ternary alloys with rhodium-boron ((RE)+$Rh_4B_4$).

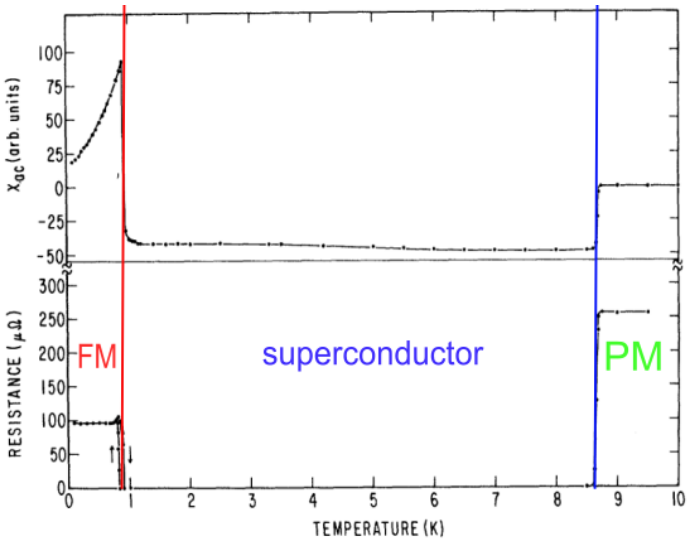


**Fig. 1.1:** *Measurements performed on $ErRh_4B_4$. Top: ac-susceptibility. Bottom: resistivity. Vertical lines has been added to separate the three different phases which are paramagnetic (PM), superconducting and ferromagnetic (FM). From ref [33].*

Figure 1.1 shows the measurements done on $ErRh_4B_4$ [33] which is the first example of ferromagnetism and superconductivity coexistence. Strictly speaking, it coexists in a very narrow range around the Curie temperature $T_C$. In this region, randomly oriented magnetic domains average out the dipolar and exchange fields on the scale $\xi_0$ (the superconducting coherence length). However, at $T_C$ the ferromagnetic order is favoured and superconductivity can survive in the domains walls [130], so microscopically there is no true bulk coexistence of ferromagnetism and superconductivity.

Another case of coexistence of the two orders are the Eu based pnictide systems where both orders correspond to different part of the sample [110].

The only cases of "real" coexistence of the two orders known today are the Uranium based superconductor $UGe_2$ [122], URhGe [10] and UCoGe [49]; where $T_C$ is well above $T_{sc}$ (see Figure 1.2 for UCoGe and URhGe). Diverse microscopic probes have shown the homogenous coexistence in the bulk of the two orders in these compounds. Another system, UIr [3] is also claimed to show coexistence of both orders. Like $UGe_2$, it exhibits superconductivity under pressure. However, UIr is non-centrosymmetric at ambient pressure unlike the three other that have orthorhombic symmetry. Moreover, few studies has been done on UIr, and the coexistence of ferromagnetism and superconductivity is not a settled question.

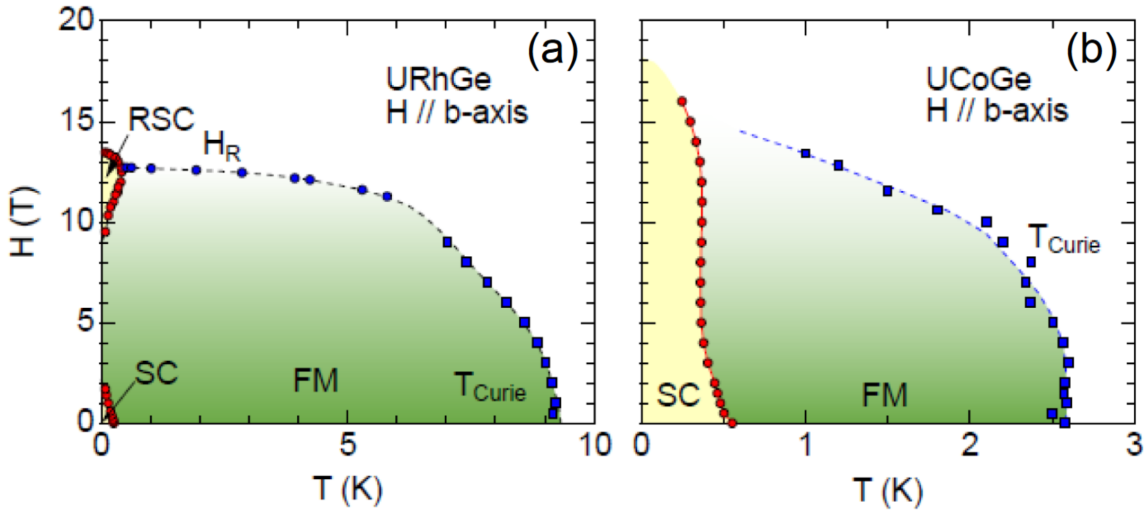


**Fig. 1.2:** *Phase diagrams of UCoGe and URhGe for field along their hard magnetisation axis at ambient pressure. The ferromagnetism (FM) overlaps with the superconductivity (SC and RSC). From ref [8].*

In what follows, some basic knowledge on paring symmetry in superconductors and on the critical field will be introduced. Then UCoGe and $UTe_2$ will be presented and compared.

### 1.1.2 *Pairing triplet/singlet*

#### *Spin-singlet pairing*

Superconductivity relies on the pairing of electrons into pairs (Cooper pairs [19, 26]) that condense into a coherent state. Because electrons are fermions, the pair wave function $\Psi_s^L(\mathbf{k})$ has to be antisymmetric, meaning $\Psi_s^L(\mathbf{k}) = -\Psi_s^L(-\mathbf{k})$. So either the spin part or the orbital part is antisymmetric.

The first case is when the orbital part is even. It is the most common pairing in superconductors (*s*-wave, cuprates, pnictides, Cerium based compounds...). Ignoring first the presence of the lattice, the cooper pairs have a definite orbital momentum L equals to $0, 2...$ (named *s*,*d*,... -wave in analogy to atomic physics). Thus the spin state is $S = 0$:

$$|S = 0\rangle = |\uparrow\downarrow\rangle - |\downarrow\uparrow\rangle \tag{1.1}$$

This state for the two spins can be expressed in the matrix form as $i\sigma_y$, where $\sigma_y$ is the Pauli matrix. The wave function of a pair can be defined like:

$$\Psi_s^L(\mathbf{k}) = \phi^L \chi^S \tag{1.2}$$

It is the product of the orbital part $\phi^L = g^L(\mathbf{k})$ (L the angular momentum) with the spin part $\chi^S = \chi^S(s_1, s_2)$ (S the spin of the pair and $s_1, s_2$ the spin of the electrons). Thus it can be rewritten as:

$$\Psi_0^L(\mathbf{k}) = g^L(\mathbf{k}) i\sigma_y \tag{1.3}$$

This wave function can be decomposed with spherical harmonics as:

$$\Psi_0^L(\mathbf{k}) = g^L(\mathbf{k}) i\sigma_y = \sum_{m=-L}^{L} a_{Lm} Y_{Lm}(\mathbf{k}) i\sigma_y \tag{1.4}$$

#### *Spin-triplet pairing*

Now let us focus on the case where the orbital part is odd ($L = 1, 3, ...$) and the spin is $S = 1$. Moreover we will restrict ourself to $L = 1$, the *p*-wave pairing. The possible spin states are:

$$|S = 1\rangle \begin{cases} S_z = 1 & |\uparrow\uparrow\rangle \\ S_z = 0 & |\downarrow\uparrow\rangle + |\uparrow\downarrow\rangle \\ S_z = -1 & |\downarrow\downarrow\rangle \end{cases} \tag{1.5}$$

The wave function can be rewritten like:

$$\Psi_1^1(\mathbf{k}) = g_\uparrow(\mathbf{k})|\uparrow\uparrow\rangle + g_0(\mathbf{k})(|\downarrow\uparrow\rangle + |\uparrow\downarrow\rangle) + g_\downarrow(\mathbf{k})|\downarrow\downarrow\rangle \tag{1.6}$$

It would be convenient to rewrite this wave function with vector. And the first vector we could think of is:

$$\mathbf{V} = g_{\uparrow}(\mathbf{k})\mathbf{e}_x + g_0(\mathbf{k})\mathbf{e}_y + g_{\downarrow}(\mathbf{k})\mathbf{e}_z \tag{1.7}$$

The norm of this vector is proportional to the superconducting density, however it does not transform properly under rotation of the quantisation axis. In a simpler way: the states $|\uparrow\uparrow\rangle$ and $|\downarrow\downarrow\rangle$ are perpendicular for the same quantisation axis. This behaviour under rotation is the result of trying to link a 3D vector with the spin state $SU(2)$.

This problem can be solved by introducing a complex vector called **d**-vector, which stems from Cayley-Klein Relation. With this **d**-vector, $(g)$ is rewritten like:

$$(g) = i(\mathbf{d}(\mathbf{k}).\boldsymbol{\sigma})\sigma_y \tag{1.8}$$

Where $\boldsymbol{\sigma}$ the Pauli matrices ($\boldsymbol{\sigma} = (\sigma_x, \sigma_y, \sigma_y)$). The components of the **d**-vector are:

$$\mathbf{d}(\mathbf{k}) \begin{cases} d_x(\mathbf{k}) = \frac{1}{2}(-g_{\uparrow}(\mathbf{k}) + g_{\downarrow}(\mathbf{k})) \\ d_y(\mathbf{k}) = -\frac{i}{2}(g_{\uparrow}(\mathbf{k}) + g_{\downarrow}(\mathbf{k})) \\ d_z(\mathbf{k}) = g_0(\mathbf{k}) \end{cases} \tag{1.9}$$

With this **d**-vector the pair wave function is redefined like:

$$\Psi_1^1(\mathbf{k}) = i\Psi \sum_{\alpha\beta} \langle\beta|((\mathbf{d}(\mathbf{k}).\boldsymbol{\sigma})\sigma_y)|\alpha\rangle|\alpha\beta\rangle \tag{1.10}$$

Where $\alpha$ and $\beta$ equal $\uparrow, \downarrow, 0$; and $\Psi$ is a proportionality factor independent of $\mathbf{k}$.

This **d**-vector seems difficult to handle at first sight but is very useful, because it gives all the informations on the orbital and spin state of the superconducting state. One of the most important properties for what is coming next is:

$$\mathbf{d}(\mathbf{k}).\mathbf{S} = 0 \tag{1.11}$$

It means if the **d**-vector is real, it is perpendicular to the spin direction, and the Equal Spin Pairing (ESP) states ($|\uparrow\uparrow\rangle$ and $|\downarrow\downarrow\rangle$) are perpendicular to the **d**-vector.

The average spin at given $\mathbf{k}$ is defined as:

$$< \mathbf{S}(\mathbf{k}) >= \frac{\langle\Psi|\mathbf{S}(\mathbf{k})|\Psi\rangle}{\langle\Psi||\Psi\rangle} = i\hbar(\mathbf{d}(\mathbf{k}) \times \mathbf{d}^*(\mathbf{k})) \tag{1.12}$$

A state is called non-unitary when:

$$\mathbf{d}(\mathbf{k}) \times \mathbf{d}^*(\mathbf{k}) \neq 0 \tag{1.13}$$

Consequently, a non-unitary state has a net average spin at given $\mathbf{k}$. For example, a ferromagnetic superconductor with a fully polarised Fermi sea (half metal) would be non-unitary, because $g_0(\mathbf{k})$ and $g_{\downarrow}(\mathbf{k})$ are equal to zero, thus:

$$< \mathbf{S}(\mathbf{k}) >= \frac{\langle\uparrow\uparrow|\mathbf{S}(\mathbf{k})|\uparrow\uparrow\rangle}{\langle\uparrow\uparrow||\uparrow\uparrow\rangle} = \hbar\mathbf{e}_z \tag{1.14}$$

The excitation spectrum is defined as:

$$\epsilon(\mathbf{k}) = \sqrt{\zeta(\mathbf{k})^2 + \Delta^2(|\mathbf{d}(\mathbf{k})|^2 \pm |\mathbf{d}(\mathbf{k}) \times \mathbf{d}^*(\mathbf{k})|^2)} \tag{1.15}$$

where $\zeta(\mathbf{k})$ is the dispersion relation without the superconducting gap. It implies a non-unitary superconductor is multi-gaped.

The last properties that can be calculated is the average orbital momentum of Cooper pairs, $< \mathbf{L}(\mathbf{k}) >$, and is defined as:

$$< \mathbf{L}(\mathbf{k}) >= \frac{\hbar}{i} \oint \frac{d\Omega}{4\pi} \sum_i d_i^*(\mathbf{k} \times \nabla_{\mathbf{k}}) d_i(\mathbf{k}) \tag{1.16}$$

It can be seen that if the **d**-vector is real, $< \mathbf{L}(\mathbf{k}) >= 0$. It would be purely imaginary otherwise. Superconductors for which $< \mathbf{L}(\mathbf{k}) >$ is non-zero are called "chiral superconductors" and quite looked-after for their potential topological properties.

However, if only triplet superconductors can be non-unitary, this is not the case for chirality: both spin-singlet and spin-triplet superconductors can be chiral. In case of spin-singlet, the superconductor needs to be unconventional (not *s*-wave), and intrinsically complex for $< \mathbf{L}(\mathbf{k}) >$ to be non zero. This is the case for *d*-wave superconductors of type "$d + id$".

### *Spin-Orbit coupling*

The definitions above are correct when spin-orbit coupling at atomic scale is neglected. If there is such a coupling, the spin can no longer be considered as a good quantum number. However, if time reversal symmetry is conserved, the electron are still degenerate, and a pseudo-spin can be used to recover the same definition of the pair wave function. If time reversal symmetry is broken, like in the case of ferromagnetic superconductors, but the crystal symmetry has an inversion centre, odd-parity and even-parity states can still be distinguished.

At the opposite, if there is no inversion centre in the crystal, and time reversal symmetry is present, the superconducting state should be a mixture of spin-singlet and spin-triplet pairing.

In the case of spin-triplet superconductors another spin-orbit interaction should be considered, the interaction between the Cooper pair spin and its orbital angular momentum. Its strength, weaker than the one at atomic scale, is more difficult to evaluate. We can differentiate two cases. First, if the spin-orbit coupling is weak, the relative orientation of the spin and the orbital angular momentum are decoupled. The **d**-vector is reoriented when field is applied to minimise the Zeeman energy. The paradigm of such a state is superfluid $^3$He [81]. The second case is if the spin-orbit coupling is strong, the orbital state expected to be pinned to the lattice will prevent a reorientation of the spin when field is applied. Crudely speaking, the **d**-vector is pinned to the lattice. Most of the theories on heavy-fermion superconductivity are developed in this limit.

This spin-orbit coupling can be indirectly probed, by NMR measurements of Knight shift for example. The first thing to know, when magnetic field is applied,

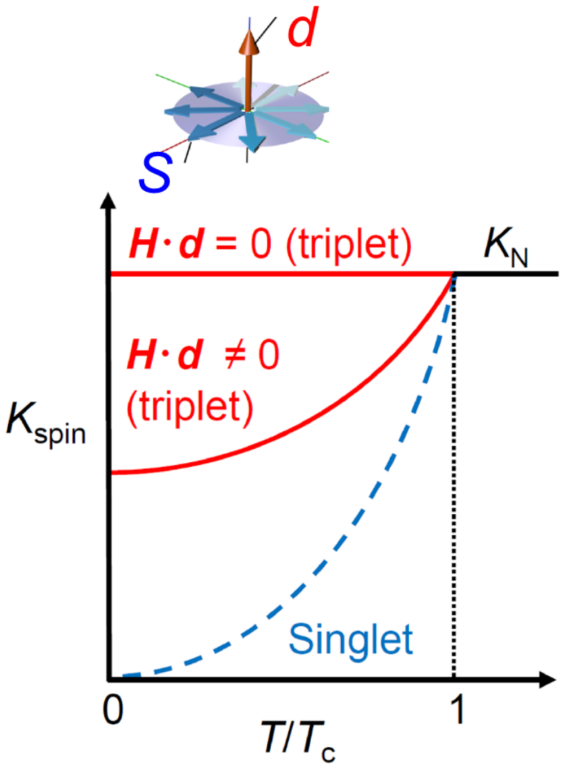


**Fig. 1.3:** *Schematic temperature dependence of the Knight-shift depending of the field orientations with respect to the **d**-vector. From ref [35].*

the spin up and spin down Fermi surfaces are split. In a spin-singlet superconductor, a part of the electrons wont be paired, so the condensation energy is reduced. However, at low fields it is energetically advantageous to decrease the polarisation than to reduce the condensation energy. Thus, the spin susceptibility of the electrons in the superconducting phase $\chi_s$ decreases below $T_{sc}$. The Knight shift being proportional to the spin susceptibility of the conduction electrons, in a spin-singlet superconductor it decreases below $T_{sc}$, because $\chi_s < \chi_n$ ($\chi_n$ the spin susceptibility in the normal state).

However, in a spin-triplet superconductors, shifting the Fermi surface does not affect the possibility of $|\uparrow\uparrow\rangle$ and $|\downarrow\downarrow\rangle$ condensation. Therefore, when field is applied along the ESP axis, so when $\mathbf{H} \perp \mathbf{d}$: $\chi_s = \chi_n$. And when the field is applied perpendicular to the ESP axis ($\mathbf{H}\|\mathbf{d}$), $\chi_s$ is decreased below $T_{sc}$.

Figure 1.3 shows a scheme summarising the temperature dependence of the Knight-shift, depending of the field orientation with respect to the **d**-vector (from ref [35]).

### *Crystal lattice symmetry*

As already evoked, lattice has an impact on the pair wave function. In a crystal, the symmetry is lowered from a continuous rotation group with an infinite number of Irreducible Representations (IR) to a discrete point group with only a few IR. Each IR have a set of basis functions, and the pair wave function is defined as a

linear combination of these basis functions. The IR that gives the highest $T_{sc}$ will determine the wave function (a linear combination of basis functions) describing the superconducting state just below $T_{sc}$. Hence, these IR allow to classify the possible symmetries in the superconducting phase.

### *Tuning of the superconducting symmetry*

Even if one IR has the highest $T_{sc}$, magnetic field or pressure can tune superconductivity and change the symmetry, promoting a different IR to have the highest $T_{sc}$. This happens with spin-triplet superconductors. The most famous example is $^3$He, which is a superfluid but the first example of *p*-wave pairing [81]. Figure 1.4 shows its phase diagram H-T-P, where we see three different superfluid phases with different symmetries for each of them.

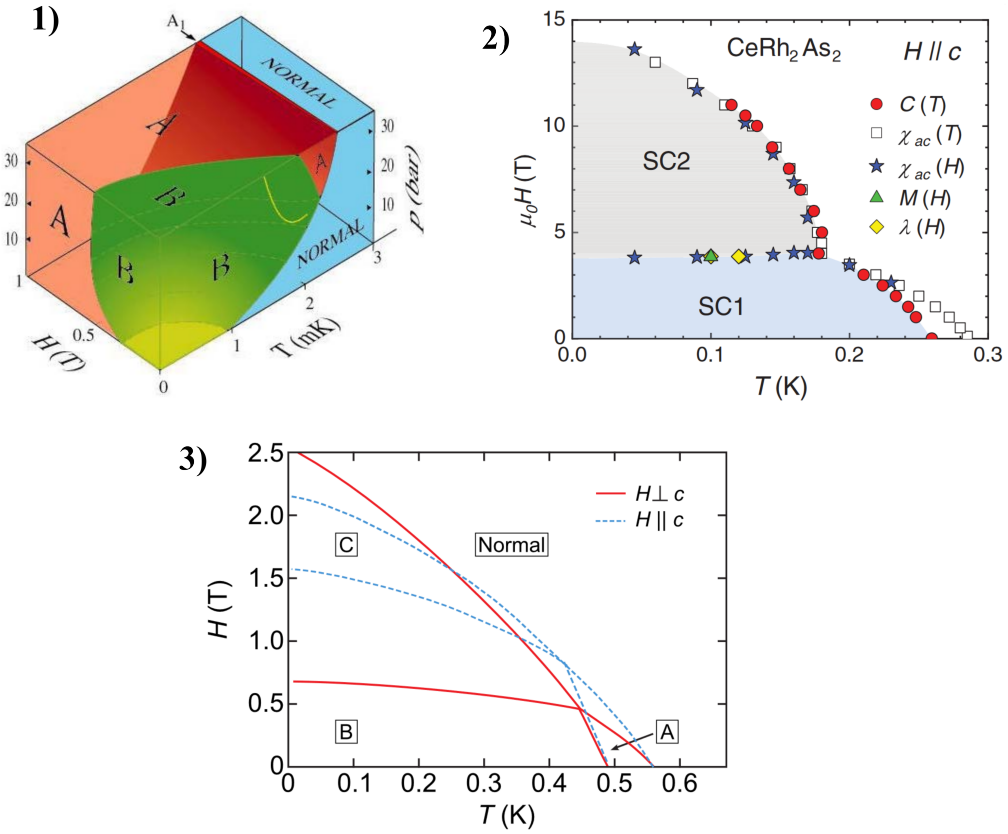


**Fig. 1.4:** *1) Phase diagram H-T-P of $^3$He. The different superfluid states are labelled A,B and A1.*
*2) Phase diagram H-T of $CeRh_2As_2$ from ref [67]. The spin-singlet phase is labelled SC1, and the spin-triplet phase SC2.*
*3) Schematic phase diagram H-T of $UPt_3$ for field parallel and perpendicular to basal plane. The three superconducting phases are labelled A,B and C. From [39].*

A second example is $UPt_3$ [2]. Figure 1.4 shows its schematic H-T phase diagram, where three different superconducting phases are present. Each of them correspond to a different symmetries of the order parameter (different IR).

A third example is the recently discovered $CeRh_2As_2$ which might exhibit a transition from a spin-triplet state to a spin-singlet state [67], as shown in Figure 1.4. Here, it goes beyond a change of IR, it is a change of spin state.

It is important to note, in all the superconductors that exhibit a change of symmetry by applying pressure or magnetic field, the pairing mechanism remains the same.

### 1.1.3 *Critical field*

One well known property of superconductors is the suppression of superconductivity when magnetic field is applied. In type II superconductors, this suppression originates from two phenomenons: the orbital and paramagnetic limitations.

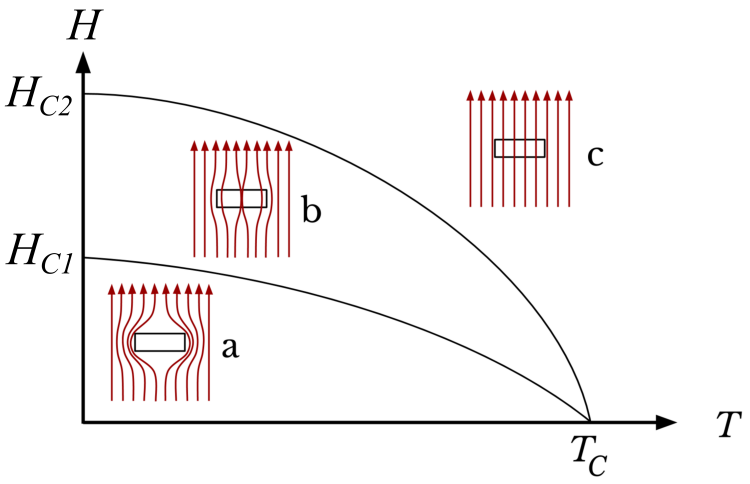


**Fig. 1.5:** *Schematic phase diagram of type II superconductors. Below $H_{c1}$, it is the Meissner phase where magnetic field is expelled from bulk (a). Between $H_{c1}$ and $H_{c2}$ is the vortex phase where magnetic lines penetrate the bulk through the vortices (b). And above $H_{c2}$ is the normal phase (c).*

#### *Orbital limitation* $H_{c2}^{orb}$

The first phenomenon is the orbital limitation giving rise to a critical field $H_{c2}^{orb}$. From a classical point of view, when a magnetic field is applied, a Lorentz force is exerted on the Cooper pairs. Once the Larmor radius of electrons is larger than the coherence length $\xi$, the pairs break:

$$r_L = \frac{m v_F}{e \mu_0 H} > \xi \tag{1.17}$$

Where $r_L$ is the Larmor radius and $v_F$ the electron velocity. Thus, we understand that the orbital limitation depends on the Fermi velocity.

The other way to understand this mechanism is to consider the vortices. Above $H_{c1}$, the magnetic field induces the nucleation of vortices (Figure 1.5). Their cores which are non-superconducting, have a diameter of the order of $\xi(T)$. Each vortex bears one quantum flux. So, with increasing field, the number of vortices in-

creases. The orbital limitation corresponds to the field where vortex cores occupy the whole sample. Thus we can define $H_{c2}^{orb}$ as:

$$H_{c2}^{orb} 2\pi\xi(T)^2 = \phi_0 \tag{1.18}$$

where $\phi_0$ is the quantum flux. This equation is also derived from the Ginzburg-Landau theory, so it is exact near $T_{sc}$. The temperature dependence near $T_{sc}$ of $\xi(T)$ can also be extracted from Ginzburg-Landau theory and BCS theory:

$$\xi(T) = 0.74\xi_0 \left(1 - \frac{T}{T_{sc}}\right)^{-0.5} \tag{1.19}$$

Where $\xi_0$ the coherence length at 0 K is given by:

$$\xi_0 = 0.18 \frac{\hbar v_F}{k_B T_{sc}} \tag{1.20}$$

By combining the three equations 1.18, 1.19 and 1.20 we determine that close to $T_{sc}$:

$$H_{c2}^{orb} = \alpha_0 \frac{T_{sc}(T_{sc} - T)}{\langle v_F \rangle^2} \tag{1.21}$$

Where $\alpha_0$ is a numerical factor equal to 3.2 $10^8$ $TK^{-2}m^2s^{-2}$. We see that the orbital limit is inversely proportional to the square of the average Fermi velocity in the plane perpendicular to the magnetic field. Also, near $T_{sc}$ the $H_{c2}^{orb}$ is linear and its slope is determined by:

$$\left.\frac{dH_{c2}^{orb}}{dT}\right|_{T_{sc}} = -\alpha_0 \frac{T_{sc}}{\langle v_F \rangle^2} \propto T_{sc} m^{*2} \tag{1.22}$$

The anisotropy of $dH_{c2}^{orb}/dT_{sc}$ in a crystal is linked to the anisotropy of the Fermi velocity. It is also important to note that the orbital limitation is proportional to the square of the effective mass $m^*$. This is the reason why critical fields in heavy-fermion superconductors are much higher than in other compounds for the same $T_{sc}$.

### *Strong coupling effect on $H_{c2}^{orb}$*

Increasing the superconducting pairing strength will impact $H_{c2}^{orb}$. The coupling strength is parametrised by the strong-coupling constant $\lambda$, first introduced by Midgall to characterise the electron-phonon coupling [92]. Later Eliashberg used this constant in its superconducting theory to generalise the BCS theory to the case of strong coupling ($\lambda > 0.8$) [31]. $\lambda$ is defined as:

$$\lambda = 2 \int_0^\infty \frac{\alpha^2(\omega) N_{ph}(\omega)}{\omega} d\omega \tag{1.23}$$

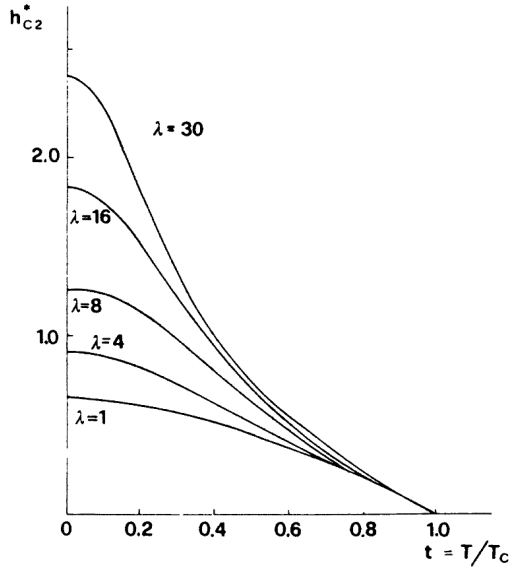


**Fig. 1.6:** $H_{c2}^{orb}$ *renormalised by the slope at* $T_{sc}$*, calculated for different values of* $\lambda$ *with a strong-coupling model in the dirty limit with an Einstein spectrum [22].*

where $N_{ph}(\omega)$ is the phonon density of state and $\alpha(\omega)$ the frequency dependent electron-phonon interaction. Eliashberg's theory was established for superconductivity induced by electron-phonon interaction. However, it is expected that the main physical trends implied by a stronger pairing strength remain valid for other type of pairing mechanism like magnetic fluctuations. Eliashberg's theory requires that the characteristic energy of the fluctuation $\Omega$ is lower than the Fermi energy.

A first effect of the strong-coupling regime is to renormalise the effective mass $m^*$ of the electrons:

$$1+\lambda = \frac{m^*}{m_b} \tag{1.24}$$

where $m_b$ is the electron mass renormalised by all interactions except the one inducing superconductivity. So $H_{c2}^{orb}$ is increased as coupling is strengthened. The $T_{sc}$ is also increased as shown by the empirical MacMillan's law [88]:

$$T_{SC} = \frac{\hbar\Omega}{1.2}\exp\left(-\frac{1.04(1+\lambda)}{\lambda-\mu^*(1+0.62\lambda)}\right) \tag{1.25}$$

where $\mu^*$ is the repulsive Coulomb potential. Note that this law implies an increase of $T_{sc}$ with $\lambda$ becoming weaker for larger $\lambda$ values.

But, $T_{sc}$ being higher, superconductivity is also suppressed by thermal fluctuations (thermal phonons) which are pair breaking. As temperature is lowered this suppression is decreased, the fluctuations are "frozen". Hence, superconducting properties are reinforced at low temperatures compared to the BCS weak-coupling predictions. This is also true for the upper critical field, and for strong enough $\lambda$ value, it may lead to an upward curvature of $H_{c2}^{orb}$ as seen in Figure 1.6 showing several $H_{c2}^{orb}$ calculated for different $\lambda$.

To conclude, in Figure 1.6 the orbital critical fields drawn is renormalised by the slope at $T_{sc}$. So the slope is equal to $-1$. However, one should not be mistaken, the slope is influenced by $\lambda$. When the coupling strength is reduced the slope at $T_{sc}$ decreases.

### *Paramagnetic limitation $H_p$*

The second limitation in field is the Pauli or paramagnetic limit. In the case of a spin-singlet superconductor, the spins of the paired electrons are anti-parallel. When $H$ is applied and the Zeeman energy exceeds the superconducting gap, electrons can no more be bound into Cooper pair. To have an order of magnitude we can follow the demonstration of Clogston for a weak-coupling regime [25]. The difference of free energy in the normal phase ($F_N$) and in the superconducting phase ($F_S$) is established by the BCS theory at $T = 0$ as:

$$F_N - F_S = \frac{1}{2}N(0)\Delta(0) \tag{1.26}$$

where $\Delta(0)$ is the superconducting gap at $T = 0$, and $N(0)$ the density of states. And we can say the difference of free energy is also equal at $T = 0$ to:

$$F_N - F_S = \frac{1}{2}(\chi_N - \chi_S)H_p^2 \tag{1.27}$$

where $\chi_N$ and $\chi_S$ are the paramagnetic susceptibilities in the normal and superconducting states. BCS also told us at $T = 0$ due to the condensation of the electrons, $\chi_S = 0$. Taking $\chi_N = \frac{1}{2}(g\mu_b)^2N(0)$, the paramagnetic limitation $H_p$ is:

$$H_p = \frac{\sqrt{2}\Delta(0)}{g\mu_b} \tag{1.28}$$

To have an order of magnitude, if we take the free electron value $g = 2$:

$$H_p = 1.85T_{sc} \tag{1.29}$$

Thus, in the case of strong-coupling regime, the superconducting gap is enhanced (with respect to $T_{sc}$) with increased coupling ($\lambda$ getting large). As a consequence the paramagnetic limit will be higher than in the weak-coupling regime.

In most superconductors, the paramagnetic limit plays little role because it is much higher than orbital limitation. But for the heavy-fermions compounds, the orbital limitation is high because of the large effective masses. Since the paramagnetic limit is not controlled by the density of states or the Fermi velocity and the $T_{sc}$ are in the Kelvin range, it will play an important role on $H_{c2}$. Figure 1.7 shows calculations of typical critical fields for classical and heavy-fermion superconductors. The pure paramagnetic limit (dash-dotted red line) is much higher than the $H_{c2}$ of classical superconductors. Their $H_{c2}$ are entirely driven by the orbital limitation. In the case of heavy-fermion superconductors, the orbital limitation (dash-dotted blue line) can largely exceed the paramagnetic limit. As a

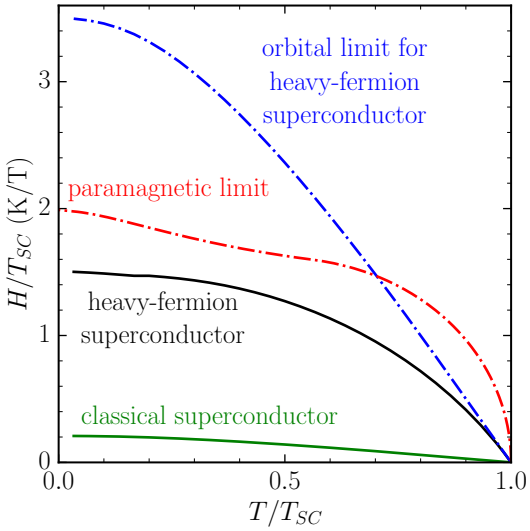


**Fig. 1.7:** *Typical critical fields calculated for classical and heavy-fermion superconductors for a paramagnetic limit with* $g = 2$ *(dash-dotted red line).*

consequence, $H_{c2}$ is strongly suppressed at low temperatures. So if this paramagnetic limitation is removed, $H_{c2}$ can reach extremely high values in heavy-fermion superconductors. It is notably the case for UCoGe and $UTe_2$ as we will see later.

In the case of spin-triplet superconductivity, if pairing is established with parallel spins in ESP states, there is no paramagnetic limit for fields along these spins directions. More generally, if field is applied along a direction with no components of the **d**-vector, no paramagnetic limit is expected. By contrast, along a direction with finite components of the **d**-vector, a paramagnetic limit is expected. Of course it is true if the spin-orbit coupling is strong enough to prevent a reorientation of the **d**-vector with field.

A last remark that will be of use for the analysis coming later on $UTe_2$ and UCoGe: near $T_{sc}$ $H_p$ is almost vertical ($H_p \propto (1 - T/T_{sc})^{1/2}$) so $H_{c2}$ is always governed by $H_{c2}^{orb}$ near $T_{sc}$. Hence, the slope of $H_{c2}$ at $T_{sc}$ is only controlled by $H_{c2}^{orb}$.

### *Jaccarino-Peter effect*

The study of conventional superconductors with a coexistence of magnetism and superconductivity had revealed a mechanism that allows to exceed the paramagnetic limitation without implying spin-triplet pairing: the Jaccarino-Peter effect [61]. It relies on the compensation of an external applied field by the exchange field acting on the conduction electrons, and originating from the magnetic ions. It is observed in organic superconductors [18]. But the most famous examples are in the $Eu_xSn_{1-x}Mo_6S_8$ systems. Figure 1.8 shows the critical field measured in $Eu_{0.75}Sn_{0.25}Mo_6S_{7.2}Se_{.8}$ ref [90]. In the this compound the orbital limitation is high, 25 T at $T = 0$. But $H_{c2}$ is rapidly suppressed below 1 T because of the paramagnetic limitation induced by exchange field associated to the Eu ions. When

increasing the applied field above a certain value, it will start to compensate the exchange field and superconductivity re-appears.

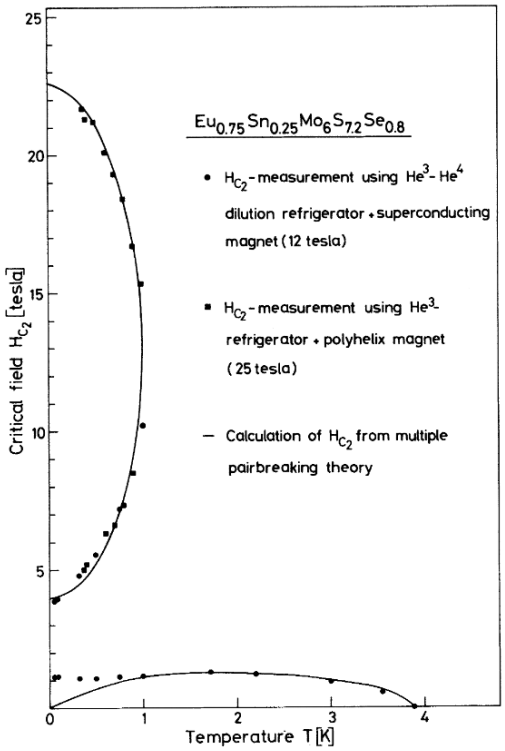


**Fig. 1.8:** *Critical field of $Eu_{0.75}Sn_{0.25}Mo_6S_{7.2}Se_{.8}$ from ref [90], showing re-entrant superconductivity generated by Jaccarino-Peter effect.*

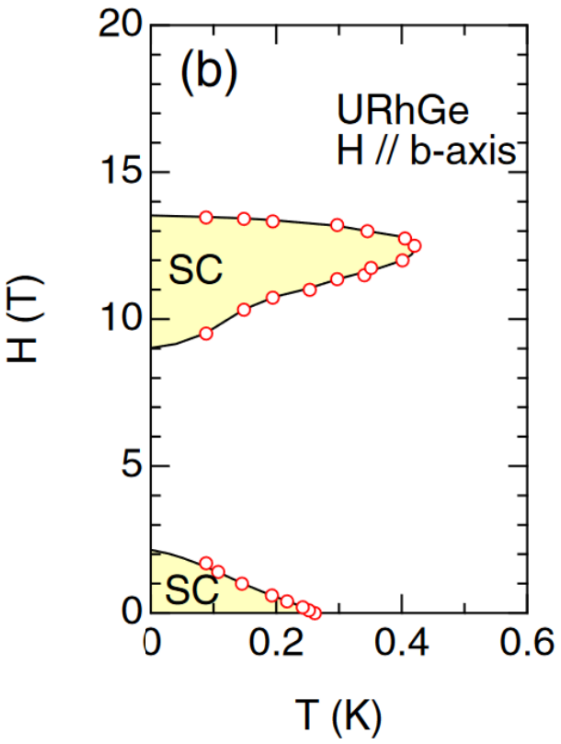


**Fig. 1.9:** *Critical field of URhGe from ref [8], for field along its hard magnetisation axis.*

Even without experimental sign, this mechanism has been discussed for UCoGe and URhGe, especially to explain the re-entrance of superconductivity in URhGe along its **b** axis [45]. However, the main counter arguments are: the low field phase already exceeds the paramagnetic limit [43] but looks purely orbitally limited, and the re-entrant phase largely exceeds the orbital limit. So, a mechanisms with an increase of the coupling strength is needed in order to raise the orbital limit.

### *FFLO*

The second mechanism allowing to exceed the paramagnetic limit is the Fulde-Ferrell, Larkin-Ovchinnikov (FFLO) phase [38], which is less straightforward to understand as the Jaccarino-Peter effect. Due to Zeeman effect, when a field H is applied, electrons in a Cooper pair (spin-singlet pairing) will see their energy shifted by an amount $g\mu_B H$. Generally the pair will break at the paramagnetic limit. However, the difference of Zeeman energy can be compensated by the difference of kinetic energy when a fraction of the electrons are paired in a state $[(-\mathbf{k}_F + \mathbf{q})_\downarrow(\mathbf{k}_F)_\uparrow]$. Here $\mathbf{q} = \frac{2\mu_b \mathbf{H}}{\hbar \mathbf{v}_F}$ the centre-of-mass momenta of the pairs. Since this centre-of-mass momentum is no more equal to 0, the order parameter $\Delta(\mathbf{r})$

is multiplied by a factor $e^{iq.r}$ [38]. This induces a spatial modulation of the order parameter, either of the amplitude or of the phase. In the real space it induces a breaking of the translational spatial symmetry. The FFLO phase should appear in clean systems, because impurities can break the modulation responsible of the phase.

For an amplitude modulation, it generates nodal planes (where the gap is zero) perpendicular to the applied field. This may lead to a new pining mechanism of the vortices (see Figure 1.10).

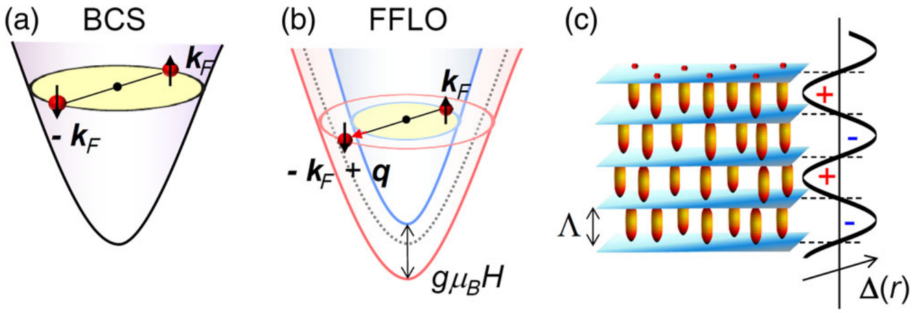


**Fig. 1.10:** *(a) Schematic illustration of Cooper pairing* $[(-\boldsymbol{k}_F)_\downarrow(\boldsymbol{k}_F)_\uparrow]$ *in the superconducting state and (b)* $[(-\boldsymbol{k}_F + \boldsymbol{q})_\downarrow(\boldsymbol{k}_F)_\uparrow]$ *in the FFLO state. (c) Schematic illustration of the superconducting order parameter* $\Delta(r)$ *in real space and the segmentation of magnetic flux lines by the nodal planes. From ref [64].*

In order for the FFLO phase to appear, the orbital pair breaking effect must be weak compared to the paramagnetic effect. This condition is characterised by the Maki parameter which is defined as:

$$\alpha_{Maki} = \sqrt{2}\frac{H_{C2}^{orb}}{H_p} \tag{1.30}$$

$\alpha_{Maki}$ is of the order of $\Delta/E_F$, it is usually much less than 1, indicating that the influence of the paramagnetic effect is negligibly small in most superconductors. For FFLO phase to occur, a large value of $\alpha_{Maki}$ is needed, typically value above 1.8 [41]. Heavy-fermion systems seemed very good candidates for its appearance, but confirmed observation where finally done in organics superconductors [54, 82] or in iron pnictides [64]. This is certainly related to the fact that the reinforcement of $H_{c2}$ triggered by the FFLO phase grows when dimensionality is reduced.

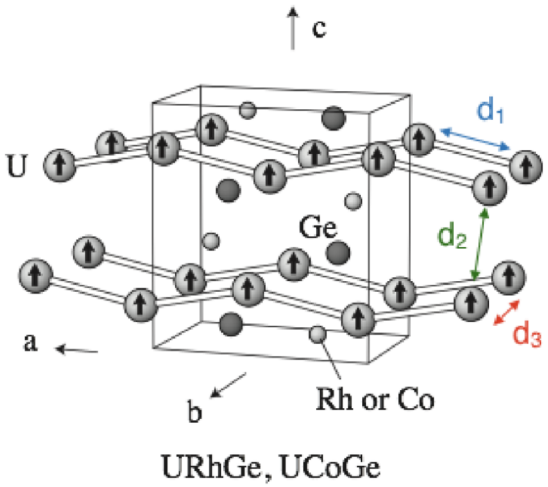


**Fig. 1.11:** *Crystal structure of UCoGe which shares the same with URhGe.*

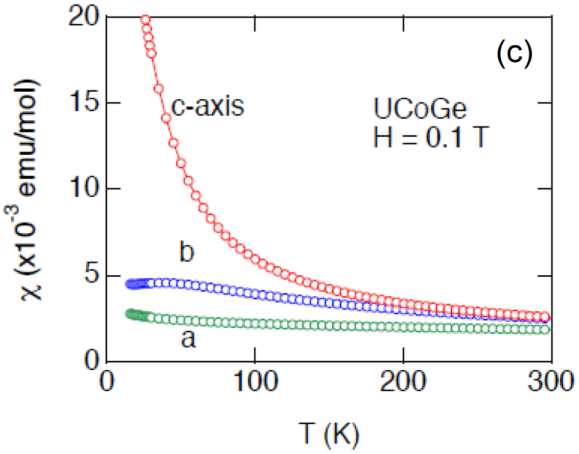


**Fig. 1.12:** *Magnetic susceptibility as a function of temperature for the three axes in UCoGe. [8]*

## 1.2 UCoGe

UCoGe discovered in 2007 [49], is one of the two known ferromagnetic superconductors at ambient pressure with URhGe. Its Curie temperature $T_C$ is between 2 K and 3 K (depending on samples), and superconductivity emerges at around 550 mK, which is also sample dependant. UCoGe is orthorhombic with the space group Pnma ($D_{2h}^{16}$), the crystal structure is shown in Figure 1.11. An ubiquitous feature for ferromagnetic superconductors is the zigzag chain of U atoms along the hard magnetisation **a** axis, with an inversion centre lying between two Uranium atoms.

Figure 1.12 shows the magnetic susceptibility along the three axes, we see that the hard magnetisation axis is **a**, and the easy one is **c**. The ferromagnetism is claimed to be itinerant because of the small magnetic moment and photoelectron spectroscopy pointing to itinerant 5 *f* electrons [36]. Nonetheless, the itinerancy is not firmly established yet.

However, NMR [46, 50] and neutron inelastic measurements [127] have revealed the presence of Ising type longitudinal magnetic fluctuations along the **c** axis.

When it comes to superconductivity, the phase diagram shown in Figure 1.13, obtained by resistivity measurements highlights a strong anisotropy of $H_{c2}$ and a field reinforcement of $H_{c2}^{\mathbf{b}}$ [11]. This exact S-shape for $H_{c2}^{\mathbf{b}}$ is sample and measurement dependant, but the reinforcement is intrinsic. Furthermore, despite a large effective mass compared to classical superconductors, due to Kondo interaction, $H_{c2}$ largely exceeds the orbital limitation deduced from the initial slopes at $T_{sc}$ in UCoGe.

It is worth to note that the renormalisation of the Sommerfeld coefficient is modest in UCoGe, ($\gamma \sim 0.055$ $JK^{-2}mol^{-1}$) in comparison to other heavy-fermion compounds ( $UBe_{13}$ has $\gamma \sim 1$ $JK^{-2}mol^{-1}$). This does not indicate a small renormalisation of the effective mass in UCoGe, but rather a small density of carriers.

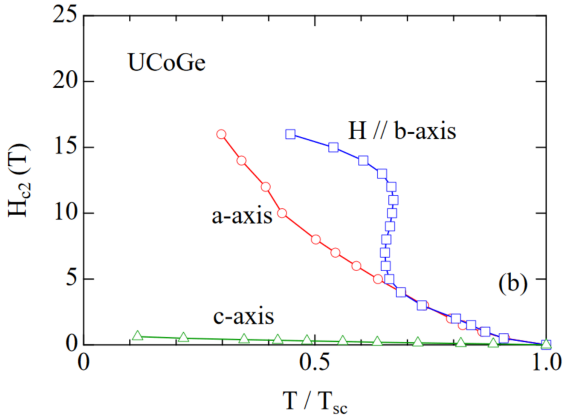


**Fig. 1.13:** *Phase diagram of the superconducting phase along the three axes in UCoGe, established with resistivity measurements. [11]*

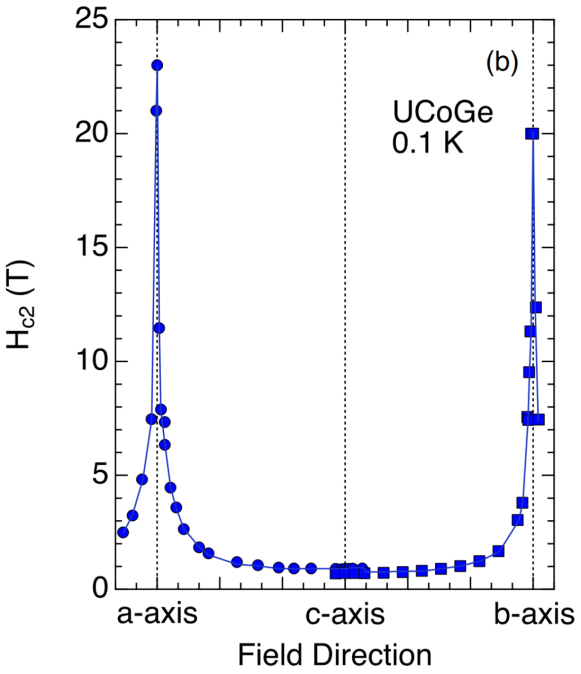


**Fig. 1.14:** *Angle dependence of $H_{c2}$ at 100 mK in UCoGe. [7]*

The anisotropy of $H_{c2}$ is similar to 2D materials, however, UCoGe is 3D as emphasised by the anisotropy of the resistivity in the normal phase [46].

This strong anisotropy has been explained by a field dependence of the superconducting mechanism itself, as it will be explained below. Figure 1.14 shows the angle dependence of $H_{c2}$ at 100 mK, highlighting the strong an unusually sharp anisotropy [7]. Recent specific heat measurements have also shown a strong angle dependence of $H^{b}_{c2}$ [102]. A small misalignment from **b** or **a** axis toward **c** axis immediately suppresses the superconductivity.

### 1.2.1 *Pairing mediated by ferromagnetic fluctuations*

For a ferromagnetic orthorhombic superconductor, only two possible spin-triplet states exist because of symmetry consideration [94, 96]. In the case of strong spin-orbit coupling, the A phase is:

$$\begin{cases} g^{A}_{\uparrow}(\mathbf{k}) = \gamma^{\uparrow}_{x}\hat{k}_{x} + i\gamma^{\uparrow}_{y}\hat{k}_{y} \\ g^{A}_{\downarrow}(\mathbf{k}) = \gamma^{\downarrow}_{x}\hat{k}_{x} + i\gamma^{\downarrow}_{y}\hat{k}_{y} \\ g^{A}_{0}(\mathbf{k}) = \gamma^{0}_{z}\hat{k}_{z} \end{cases} \tag{1.31}$$

And the B phase is:

$$\begin{cases} g^{B}_{\uparrow}(\mathbf{k}) = \eta^{\uparrow}_{z}\hat{k}_{z} \\ g^{B}_{\downarrow}(\mathbf{k}) = \eta^{\downarrow}_{z}\hat{k}_{z} \\ g^{B}_{0}(\mathbf{k}) = \eta^{0}_{x}\hat{k}_{x} + i\eta^{0}_{y}\hat{k}_{y} \end{cases} \tag{1.32}$$

Note that in this case, the representation of the order parameter as $\Psi = g_{\uparrow}(\mathbf{k})|\uparrow\uparrow\rangle + g_{\downarrow}(\mathbf{k})|\downarrow\downarrow\rangle + g_0(\mathbf{k})(|\uparrow\downarrow\rangle + |\downarrow\uparrow\rangle)$, is more convenient than the **d**-vector representation.

Both, $\gamma$ and $\eta$ are complex coefficients and they can be **k** independent as long as they are invariant for all symmetry operations of the point group. The superconducting state in ferromagnetic superconductors is non-unitary because $|g_{\uparrow}| > |g_{\downarrow}|$ and the amplitude of $g_0$ is zero or negligible, because most of the electrons are polarised ($T_{sc} < T_C$).

Taking that into account, point nodes along the z axis are expected for the A state, and line nodes in the (x,y) plane for the B state. The gap structure has been investigated with different probes. Thermal conductivity measurements did not find any sign of nodal structures of the gap [132], and NMR measurements exhibit a $T^3$ behaviour of the $1/T_1T$ below $T_{sc}$, suggesting the presence of lines node [105]. However, owing to the presence of large residual terms at $T = 0$, we cannot conclude on the nodes locations in UCoGe.

However, knowing the symmetry of the superconducting state would not reveal the nature of the pairing interactions nor explain the field reinforcement of $H_{c2}^{\mathbf{b}}$ as well as the strong $H_{c2}$ anisotropy.

Heavy-fermion superconductors are model systems for strong correlated electrons systems, and were the firsts for which magnetism was shown to drive the pairing mechanism [87].

De Gennes gave a simple approach to understand how an attractive interaction can appear in a magnetic medium [40]. Considering the interaction between an electron (spin $S_i$) and the local magnetisation $M(r)$ as:

$$H_i = -T\mathbf{S}_i.\mathbf{M}(\mathbf{r}) \tag{1.33}$$

where T is the strength of the coupling. By assuming low frequencies limit, after Fourier transform, the potential of two electrons interacting has the form:

$$V(\mathbf{q}) = -T^2 \sum_{\alpha\beta} S_{i\alpha}\chi_{\alpha\beta}(\mathbf{q})S_{j\beta} \tag{1.34}$$

where $\chi_{\alpha\beta}(\mathbf{q})$ is the static susceptibility tensor of the medium, which can be diagonalised. The principal values $\chi_{\alpha\alpha}(\mathbf{q})$ should be positive, otherwise the magnetic medium would be unstable. We can conclude that for parallel spins (spin-triplet), the potential is negative so attractive. While in the case of antiparallel spins (spin-singlet) the potential is positive. However, it is still possible to have an attractive potential if the superconducting wave function changes of sign on the Fermi surface (line or point nodes) at **q** vectors with maximum $\chi_{\alpha\alpha}(\mathbf{q})$. This is the case of cuprates (*d*-wave) and Ce based superconductors.

To come back to UCoGe, since it is most likely a spin-triplet, a pairing through magnetic fluctuations is possible. It is now largely accepted that ferromagnetic fluctuations induce superconductivity in UCoGe (and also in URhGe).

NMR measurements revealed longitudinal fluctuations ,most likely ferromagnetic, of Ising type along the **c** axis [46, 50]. Furthermore, they revealed a strong

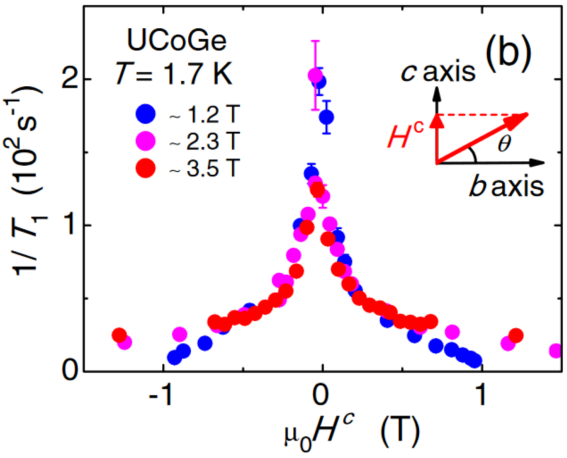


**Fig. 1.15:** $1/T_1$ *against* $H_c$ *the field component on* **c** *axis (in the* **b**,**c** *plane), measured in three different magnetic fields at* 1.7 *K. Ref [46]*

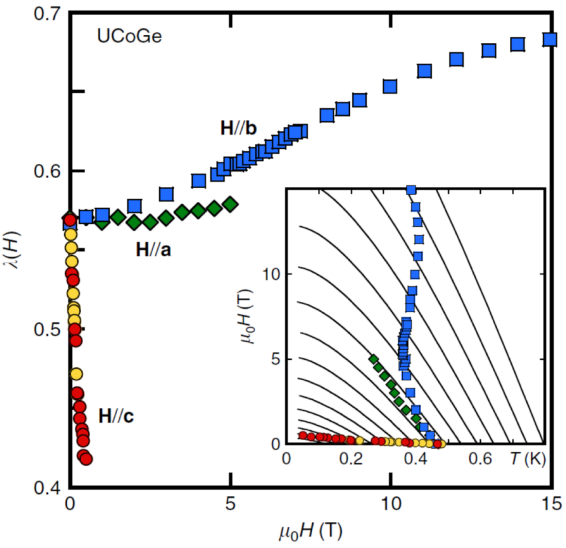


**Fig. 1.16:** *Field dependence of the strong-coupling constant* $\lambda$ *for the three axes extracted from the* $H_{c2}$*. Inset:* $H_{c2}$ *used. The black lines correspond to* $H_{c2}$ *calculated for different* $\lambda$*. Ref [140].*

anisotropy of the fluctuations. Figure 1.15 shows $1/T_1$ as a function of the field component along **c** axis. It demonstrates that ferromagnetic fluctuations are immediately suppressed when a small component of the field is applied along the **c** axis.

The superconductivity induced by ferromagnetic fluctuations is suppressed when field is applied along the **c** axis, reducing the pairing strength so $H_{c2}^{c}$.

This has been shown to explain the $H_{c2}$ anisotropy by extracting the strong-coupling constant dependence in field $\lambda(H)$ from $H_{c2}$ [140], with a model that will be presented much later in section 4.2.1. Figure 1.16 shows $\lambda(H)$ extracted for the three axes, and the behaviour expected for a coupling induced by ferromagnetic fluctuations is recovered. Furthermore, the A coefficients from resistivity measurements, which are proportional to $(m^*)^2$, also exhibit an increase for $H\|\mathbf{b}$ and $H\|\mathbf{a}$, and a fast decrease for $H\|\mathbf{c}$ [7]. This might be due to the field dependence of magnetic fluctuation , so to the pairing strength.

The decrease of $\lambda(H\|\mathbf{c})$ is also supported by specific heat measurements exhibiting a fast decrease of $\gamma$ at low fields (remember: $\gamma(H) \propto (1+\lambda(H))$[1]) [140].

More recently, field-angle-resolved specific heat measurements recovered the same anisotropy as NMR measurements: C/T at 0.8 K, which can be considered as $\gamma$, is sharply decreased when the field is misaligned from the **a** and **b** axis toward the **c** axis [102].

1 The Sommerfeld coefficient $\gamma$ is proportional to $m^*$. In the strong-coupling regime, as explained before, the electronic effective mass is renormalised by $1+\lambda$, thus $\gamma \propto m_b(1+\lambda)$, where $m_b$ is the electronic mass renormalised by all interactions except the one inducing superconductivity.

However, realistic microscopic theories to describe superconductivity induced by ferromagnetic fluctuations in ferromagnetic superconductors do not existed yet, due to the complex magnetic background and a non-fully determined pairing mechanism.

Nevertheless, there are studies based on Landau formalism for magnetism, that capture the physics of this superconducting mechanism in a weak coupling regime, and allow comparison to experimental results [95]. In these studies the pairing interaction is assumed to be mediated by the magnetic polarisation, and the pairing Hamiltonian $\mathcal{H}_{pairing}$ defined as:

$$\mathcal{H}_{pairing} = -\frac{\mu_B^2 I^2}{2} \int S_i(\mathbf{r}) \chi_{ij}(\mathbf{r}-\mathbf{r'}) S_j(\mathbf{r'}) d\mathbf{r}^3 d\mathbf{r'}^3 \tag{1.35}$$

where I is the exchange constant, $S_i(\mathbf{r})$ the spin density operator and $\chi_{ij}$ the system susceptibility. $\mathcal{H}_{pairing}$ after some algebra can be rewritten like a BCS Hamiltonian with the pairing amplitude $V$ described by the odd part of the medium static susceptibility [121]. Then the order parameter components are calculated by linear combination as:

$$\Delta^{\uparrow}(\mathbf{k},\mathbf{q}) = -T \sum_{n} \sum_{\mathbf{k'}} \left( V^{\uparrow\uparrow}(\mathbf{k},\mathbf{k'}) G^{\uparrow} G^{\uparrow} \Delta^{\uparrow}(\mathbf{k'},\mathbf{q}) + V^{\uparrow\downarrow}(\mathbf{k},\mathbf{k'}) G^{\downarrow} G^{\downarrow} \Delta^{\downarrow}(\mathbf{k'},\mathbf{q}) \right) \tag{1.36}$$

$$\Delta^{\downarrow}(\mathbf{k},\mathbf{q}) = -T \sum_{n} \sum_{\mathbf{k'}} \left( V^{\downarrow\downarrow}(\mathbf{k},\mathbf{k'}) G^{\downarrow} G^{\downarrow} \Delta^{\downarrow}(\mathbf{k'},\mathbf{q}) + V^{\downarrow\uparrow}(\mathbf{k},\mathbf{k'}) G^{\uparrow} G^{\uparrow} \Delta^{\uparrow}(\mathbf{k'},\mathbf{q}) \right) \tag{1.37}$$

where $G^{\uparrow,\downarrow}$ are the diagonal parts of the matrix of the normal-metal Green's function. Here the $S_z = 0$ component of the order parameter is neglected for this overview. The pairing amplitudes are equal to:

$$\begin{cases} V^{\uparrow\uparrow}(\mathbf{k},\mathbf{k'}) = -\mu_B^2 I^2 \chi^u_{zz} \\ V^{\downarrow\downarrow}(\mathbf{k},\mathbf{k'}) = -\mu_B^2 I^2 \chi^u_{zz} \\ V^{\uparrow\downarrow}(\mathbf{k},\mathbf{k'}) = -\mu_B^2 I^2 (\chi^u_{xx} - \chi^u_{yy} - 2i\chi^u_{xy}) \\ V^{\downarrow\uparrow}(\mathbf{k},\mathbf{k'}) = -\mu_B^2 I^2 (\chi^u_{xx} - \chi^u_{yy} + 2i\chi^u_{xy}) \end{cases} \tag{1.38}$$

And the odd part of the susceptibility $\chi^u_{ij}$ is defined as:

$$\chi^u_{ij}(\mathbf{k},\mathbf{k'}) = \frac{1}{2} \left( \chi_{ij}(\mathbf{k}-\mathbf{k'}) - \chi_{ij}(\mathbf{k}+\mathbf{k'}) \right) \tag{1.39}$$

In all these equations $z$ axis is considered as the easy magnetisation axis, so **c** axis in UCoGe.

It is important to note here: no assumption on magnetic order have been made, so it is still applicable to ferromagnet as well as paramagnet (which will be the case of $UTe_2$).

In UCoGe the susceptibility along **c** axis is much higher than along the other axes. Thus, the pairing and its field dependence will be determined by $V^{\uparrow\uparrow}(\mathbf{k},\mathbf{k'})$ and $V^{\downarrow\downarrow}(\mathbf{k},\mathbf{k'})$, so by the field dependence of $\chi^{u}_{zz}$, which is in agreement with NMR measurements claiming a pairing controlled by longitudinal fluctuations along **c** axis.

The susceptibility $\chi_{zz}$ is defined by deriving the magnetisation determined from the Landau free energy formalism ($\chi_{ij} = \partial M_i/\partial H_j$) supposed to be valid also at finite **k** [95]. For field $H\|\mathbf{c}$ ($\mathbf{H}\|z$) it is equal to:

$$\chi_{zz}(\mathbf{k}) = \frac{1}{2(\alpha_z + 6\beta_z M_z^2 + \gamma_{ij}k_i k_j)} \tag{1.40}$$

Where the coefficients $\alpha_z$, $\beta_z$ and $\gamma_{ij}$ come from the Landau formalism. They are not important for the physics we are looking at, but ref [95] gives their complete definitions. The same calculus can be performed for a field perpendicular to $z$, so for $\mathbf{H} \perp \mathbf{c}$, and lead to another definition of $\chi_{zz}(\mathbf{k})$.

From this susceptibility and expressions for $T_{sc}$ in the weak-coupling limit given in [95], one can extrapolate a field dependence of the pairing strength (the strong-coupling constant $\lambda$) as:

$$\lambda(H) = \lambda(0)\frac{(1+A^2)^2}{(\Theta + A^2)^2} \tag{1.41}$$

Where $A = \xi k_F$, $k_F$ the Fermi wave vector and $\xi$ a parameter defined as:

$$\xi = \sqrt{\frac{2\gamma}{4\beta_z M_0^2}} \tag{1.42}$$

Where $M_0$ is the spontaneous magnetisation, and $\gamma$,$\beta$ coefficients from Landau free energy. $\xi$ typically corresponds to the coherence length of the ferromagnetic order. In equation 1.41, the factor $\Theta$ is given depending on the applied field orientation by:

$$\Theta(\mathbf{H}\|\mathbf{c}) = \frac{1}{2}\left(3\frac{M_z^2}{M_0^2} - 1\right) \tag{1.43}$$

$$\Theta(\mathbf{H} \perp \mathbf{c}) = \frac{T_C(H) - T_{sc}}{T_C(0) - T_{sc}} \tag{1.44}$$

So the pairing strength is inversely proportional to the magnetic moment ($M_z$) along the **c** axis when $H\|\mathbf{c}$. Furthermore for this field direction, we can say that $\frac{d\lambda}{dH}$ is proportional to $\frac{\partial\Theta}{\partial H}$, hence to $M_z\frac{\partial M_z}{\partial H}$, so it is expected that $\frac{d\lambda}{dH}$ is finite at zero field because $M_z$ is finite at $H = 0$ in a ferromagnetic compound: $\frac{d\lambda}{dH}\big|_{H=0} < 0$. This was experimentally verified through specific heat measurements.

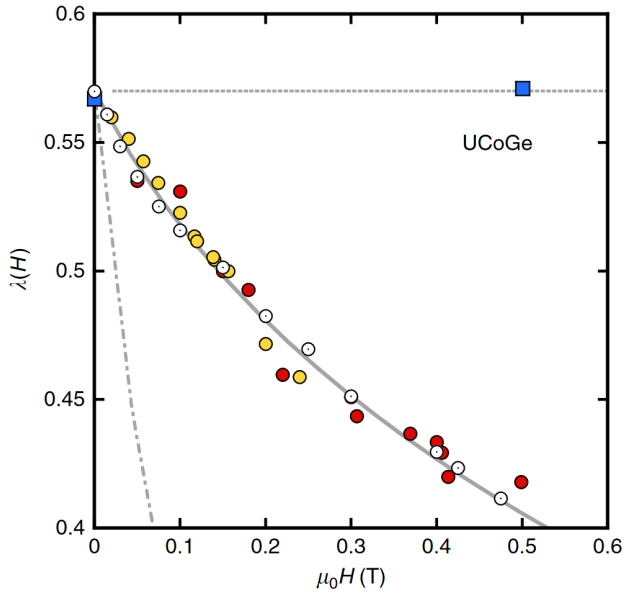


**Fig. 1.17:** $\lambda(H)$ *for* $H \| \mathbf{c}$ *determined from different measurements: filled circles are from the experimental* $H_{c2}^{c}$*, open circles are from specific heat measurements. Lines are prediction from equation 1.41: solid line for* $A = 3.2$ *(itinerant magnetism) and dash-dotted line for* $A = 1$ *(localized magnetism). Blue squares:* $\lambda(H)$ *from* $H_{c2}^{b}$*. Doted line: prediction from equation 1.41. From ref [140].*

Figure 1.17 shows a comparison $\lambda(H)$ determined from $H_{c2}$ and the electronic specific heat with $\lambda(H)$ determined from the calculations explained above.

We see the model and the measurements are in very good agreement for the case of an itinerant systems, which is believed to be the case for UCoGe.

For the other two axes ($H \perp \mathbf{c}$), the theory indicates a dependence to the Curie temperature $T_C$: $\lambda$ is enhanced when $T_C$ decreases. This decrease is seen for $H \| \mathbf{b}$ (see Figure 1.18), but not for $H \| \mathbf{a}$. It might be a limit of the Landau formalism probably not adequate to describe the evolution of the magnetisation in UCoGe for $H \| \mathbf{b}$ or $H \| \mathbf{a}$. At low field ($H < 1$), however, $T_C$ does not change so $\lambda$ should not, which is in agreement with $\lambda(H)$ extracted from $H_{c2}$.

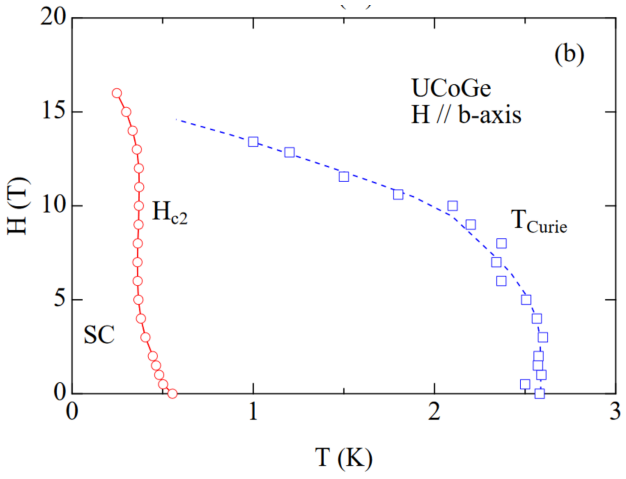


**Fig. 1.18:** *Phase diagram for* $H \| \mathbf{b}$ *showing* $H_{c2}$ *and* $T_C$ *determined with resistivity measurements. From ref [11].*

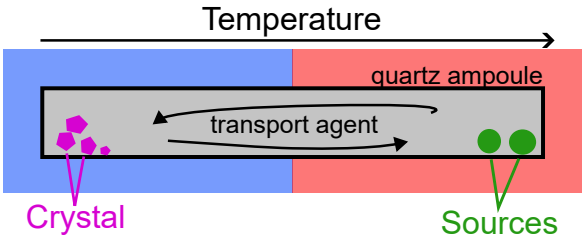


**Fig. 1.19:** *Schematic view of the CVT technique.*

## 1.3 $UTe_2$

The first growth of $UTe_2$ intended for a study of its low-temperature properties was done back in 2006 [51]. At this time no superconductivity was detected. The method used was chemical vapour transport (CVT) with iodine as transport agent. It is more recently in 2018 that superconductivity was detected in $UTe_2$ below 1.5 K [16, 113], with the same growth technique.

CVT is performed by placing Uranium and Tellurium sources at one side of a quartz ampoule filled by a gas, which is the transport agent, Iodine for $UTe_2$. By applying a thermal gradient on the ampoule (hotter part on the sources side), the volatile derivatives from the sources migrate through the ampoule and crystallise on the colder part of the ampoule. Figure 1.19 shows a schematic view of the technique.

The first crystal grown after 2018 exhibited superconductivity, however with a residual term in the specific heat (of the order of 50% of $\gamma$) and relatively "low" $T_{sc}$ (around 1.5 K). They were produced starting with stoichiometric amounts of U and Te. The next generation of samples were produced starting with off stoichiometric amounts, and by lowering the temperature of synthesis [23, 115]. They exhibit higher $T_{sc}$ (around 1.8 K) and smaller residual term in the specific heat ($\sim$ 20% of $\gamma$). This highlights that the discrepancies between samples arises from defects (different chemical phases of departures from exact stoichiometry) and not from impurities since with the same starting materials, the results can be very different.

Very recently, a new generation of samples with a $T_{sc}$ around 2 K and RRR ranging from 200 up to 1000 (instead of a maximum $\sim$ 55 previously) was produced by molten salt flux (MSF) method [120]. This technique consists to placed the sources of Tellurium and Uranium in a crucible with a mixture of sodium chloride and potassium chloride (salt). Then the crucible is heated so the sources dissolve in the salt, and a saturated solution is obtained. Finally the crucible is cooled in order to allow the desired material to precipitate. Salt is removed by dissolving it in water, and $UTe_2$ samples are extracted.

The improved RRR of this new samples generation allowed to detect quantum oscillations [14, 30]. Moreover, the residual term in the specific heat is even lower in these crystals (less than 20% of $\gamma$).

### 1.3.1 *Normal phase properties*

$UTe_2$ is an astonishing system for almost all its properties, starting with the fact that it is metallic only thanks to strong electronic correlations. Band calculations predicted an insulator state, but when introducing the Coulomb repulsion $U$ term and turning it on, the metallic state is recovered for a large $U$ [60, 125, 141]. Figure 1.20 shows an example of how the band gap at the Fermi level is expected to close as a function of $U$. In this calculation, when $U$ is close to 1 the gap is closed and metallic state recovered.

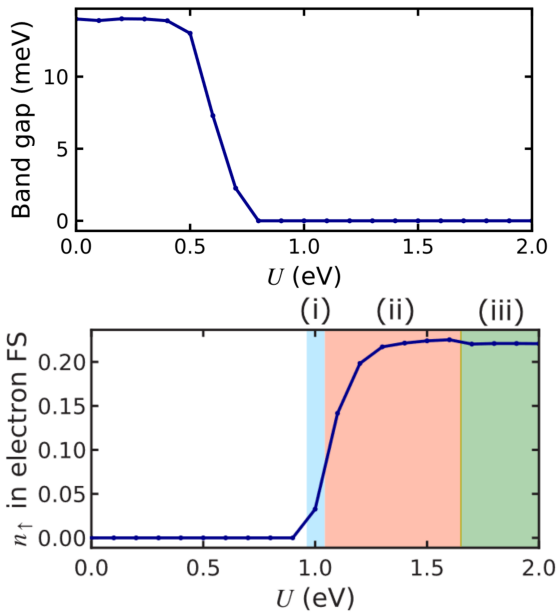


**Fig. 1.20:** *Top: Coulomb interaction U dependence of the band gap at the Fermi level. Bottom: the electron number n per spin in electron Fermi Sea. Insulator-metal transition occurs at U = 1.0 eV. Metallic states with different topology of Fermi surface are labelled by (i)-(iii). Ref [60].*

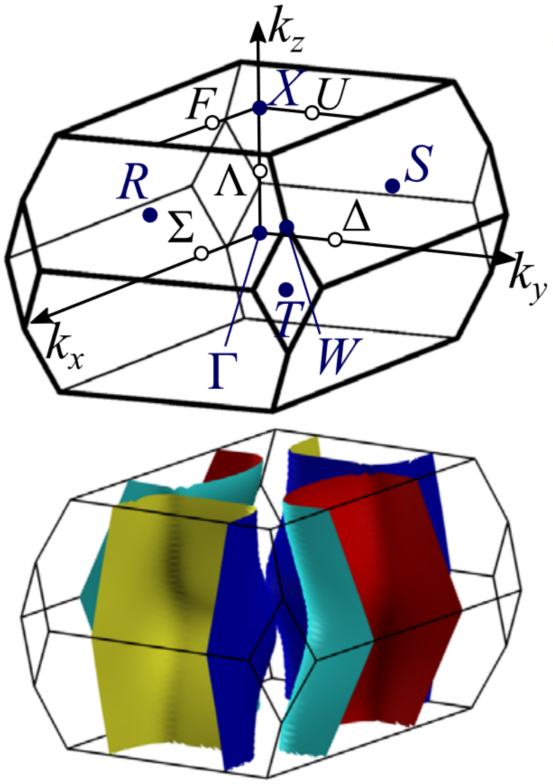


**Fig. 1.21:** *Top: First Brillouin Zone and symmetry points. Bottom: Fermi surfaces of $UTe_2$ by GGA+U for U = 2.0 eV (region (iii)), corresponding to dHvA measurements. The electron sheet are cyan and red, and the hole sheet are blue and yellow. Ref [60].*

The electronic structure of $UTe_2$ won't be discussed in detail, but it is worth to note that the recent dHvA quantum oscillations measurements confirmed the GGA+$U$ band calculations (the possible Fermi surface is shown in Figure 1.21) [14]. These measurements revealed cylindrical quasi 2D Fermi surface. The total value of the electronic specific heat determined from these dHvA measurements is 100 $mJK^{-2}mol^{-1}$, which roughly agrees with the value of ~ 130 $mJK^{-2}mol^{-1}$ in the specific heat measurements, indicating that the dHvA experiment detected the main Fermi surfaces of $UTe_2$. However, a possible 3D pocket is still being sought.

The valence is still under debate with two ARPES studies claiming different results [37, 91]. One study claims that the dominant contribution to the Fermi surfaces is the itinerant U$-5f^3$ state [37], while the other study claims that it is from U$-5f^2$ state [91].

$UTe_2$ is orthorhombic with the space group *Immm* ($D_{2h}^{25}$). The crystal structure is shown in Figure 1.22. Uranium atoms form a two-leg ladder along the **b** axis. The shortest distant between U, which is along the rung (**a** axis), is of 3.78Å. It is larger than the Hill limit of 3.5Å which gives a rational criterion for the overlap of the 5*f* wave functions. So the U moments are expected to be localised and a magnetic ordering to appear at low temperatures.

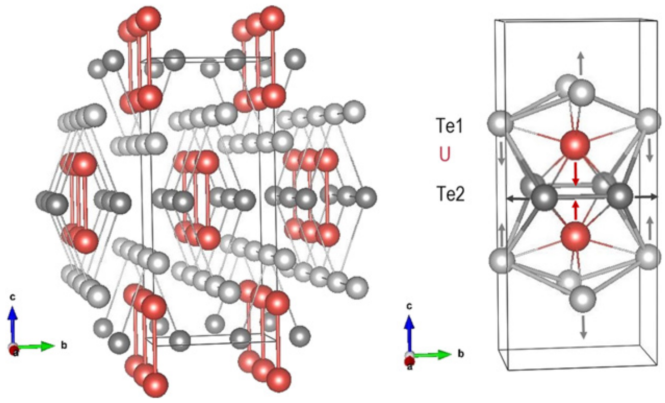


**Fig. 1.22:** *Crystal view of $UTe_2$. From ref [6].*

But no magnetic ordering is found down to 25 mK. $UTe_2$ is a paramagnet with the easy axis **a** and hard axis **b** at low temperatures, as shown by M/H measurements presented in Figure 1.23 [113]. It was initially believed that $UTe_2$ is nearly ferromagnetic [113, 128, 136], but this has not been confirmed by any measurement up to now.

One of the most salient features in magnetisation measurements is the metamagnetic transition occurring at 35 T when field is applied H$\|$**b**: it is characterised by a large jump of magnetisation (see Figure 1.24) [100].

Its link with a putative ferromagnetic instability is not straightforward and it remains an intriguing phenomena. Usually, it is expected that metamagnetism in a nearly ferromagnetic systems occurs along the easy magnetisation axis, as observed in UCoAl [12], or in the paramagnetic state above the critical pressure in $UGe_2$ [108, 131].

This metamagnetic transition is also seen in resistivity measurements [74], exhibiting a jump and an hysteresis due to the first order character of the transition [76]. The hysteresis is also seen in magnetisation measurements [100].

The metamagnetic transition was also studied by specific heat in pulsed fields [55] and magnetocaloric effect [123]. All measurements (thermodynamic and transport) suggest an increase of the effective mass on approaching $H_m$ (Figure 1.25).

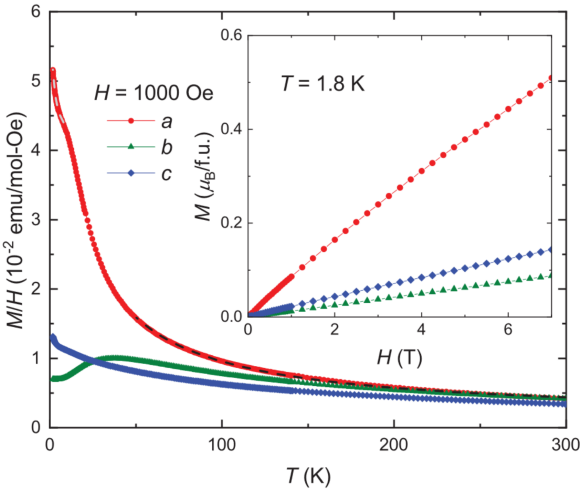


**Fig. 1.23:** M *as a function of temperature for the three axes at* 0.1 *T. Inset:* M *as function of field at* 1.8 *K. Ref [113]*

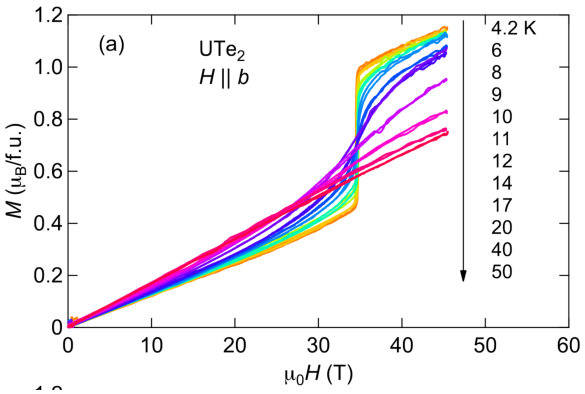


**Fig. 1.24:** M *as a function of field for* H||***b*** *at different temperatures above* $T_{sc}$*. The metamagnetic transition happens near* 35 *T. Ref [100]*

This could be related to magnetic fluctuations being enhanced when approaching $H_m$. However, the nature of these magnetic fluctuations is not known.

One last feature of the metamagnetic transition: it seems connected to a broad maximum of the magnetic susceptibility for H||**b** at a temperature label $T_{\chi,max}$. Figure 1.26 shows the H-T phase diagram following $T_{\chi,max}$: it extrapolates to the metamagnetic at a critical point (misnamed CEP [2] in ref [74, 100] and figure 1.26). At the CP the hysteresis seen in magnetisation and resistivity measurements is closing, marking the end of the first order transition line (hence the name CP). Therefore, both $T_{\chi,max}$ and $H_m$ should be dominated by the same energy scale.

2 A critical end point (CEP) is defined as a point where a line of second-order transitions terminates at a line of first-order transitions, with the first-order line continuing into an ordered region, which is not the case here in $UTe_2$. [21] A Critical Point (CP) corresponds to the end of a line of first-order transitions, like in the phase diagram of water.

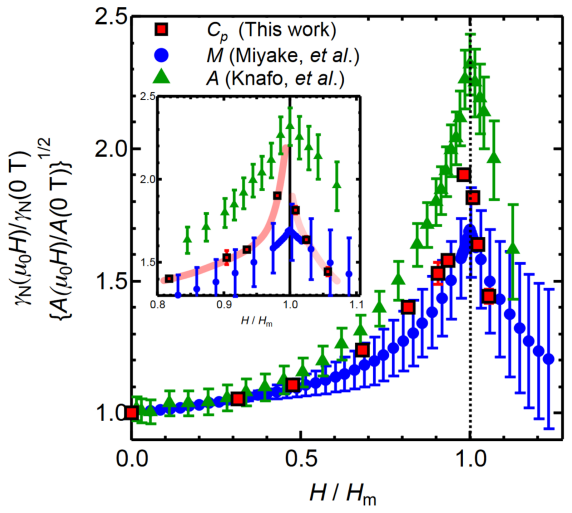


**Fig. 1.25:** *Sommerfeld coefficient $\gamma$ normalised at zero field from specific heat [55] and magnetisation measurements [100] and $A^{1/2}$ coefficient normalised at zero field from resistivity measurements [74] are plotted against $H/H_m$. Ref [55].*

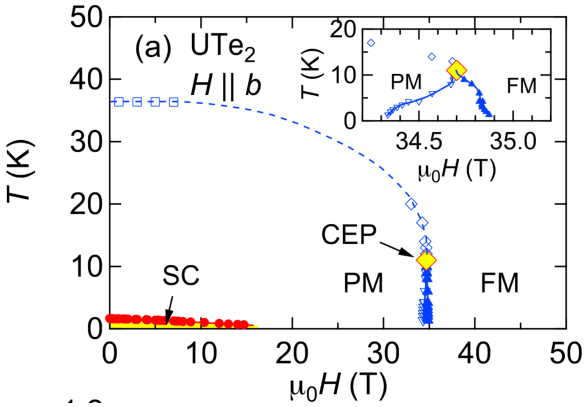


**Fig. 1.26:** *Magnetic phase diagram for $H \| \boldsymbol{b}$ showing $T_{\chi,max}$ (squares and diamonds) joining the metamagnetic transition at the CEP. Inset: enlargement near the CEP. The upward (downward) triangles correspond to the $H_m$ for up-sweep (down-sweep). The dotted lines are guide to the eyes. Ref [100]*

### 1.3.2 *Critical fields and superconducting phase*

Figure 1.27 shows $H_{c2}$ for the three directions established with resistivity measurements [76]. The paramagnetic limit of $\simeq 3$ T (free electron case) is largely exceeded for the three directions, suggesting a spin-triplet pairing. The anisotropy of $H_{c2}$ is far less pronounced than in UCoGe: the lowest $H_{c2}$ along the easy magnetisation **a** axis, and highest along the hard magnetisation **b** axis (intermediate axis in UCoGe). This rough similarity with UCoGe led to propose that ferromagnetic fluctuations could drive superconductivity in $UTe_2$ [113]. However, no ferromagnetic fluctuations have been detected yet, only antiferromagnetic ones [28, 73].

The most striking feature is along **b** axis, superconductivity is reinforced above 15 T up to the metamagnetic transition at 35 T, where superconductivity is abruptly suppressed. This high-field superconductivity is very sensitive to field alignment, while the low-field superconductivity is more robust, as shown in Figure 1.28 [76]. The positive curvature of $H_{c2}$ above 15 T is pointing to a reinforcement of the coupling strength with field, like in ferromagnetic superconductors.

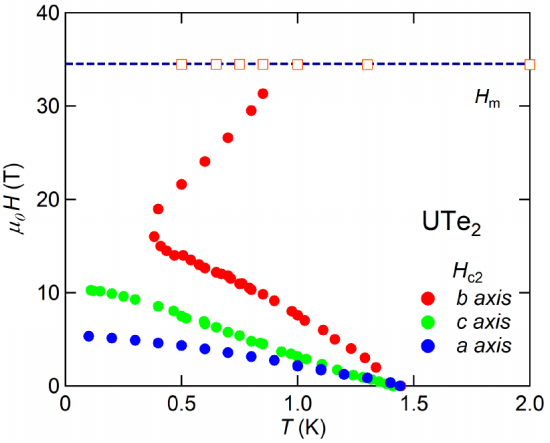


**Fig. 1.27:** $H_{c2}$ *for three axes determined by resistivity measurements. Ref [76]*

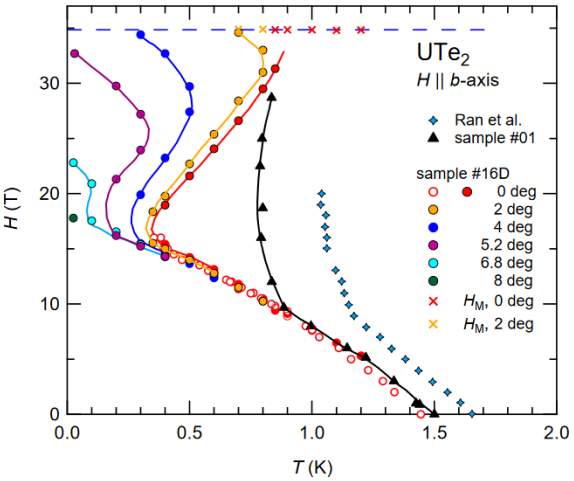


**Fig. 1.28:** *Phase diagram up to 36 T for different angle in the (b,a) plane from resistivity measurements, ref [76]. The triangles correspond to another sample, and blue diamonds to the sample from ref [113]* $H \| \boldsymbol{b}$.

Another mechanism called Lebed mechanism was also proposed to explain this reinforcement of $H^{\mathbf{b}}_{c2}$ [79, 93]. This mechanism could lead to a complete suppression of the orbital limitation in quasi 1D [78] or quasi 2D superconductors. Thus, in quasi 1D or quasi 2D spin-triplet superconductors with no paramagnetic limitation, $T_{sc}$ in high fields could be the same as in zero field. This mechanism of suppression of the orbital limitation can be understood in the quasiclassical picture. Electron trajectories oscillate in the directions perpendicular to the applied field, with an amplitude inversely proportional to the field. In a quasi-2D superconductor with field in the conducting plane, at high fields, electrons become confined in the plane, consequently the orbital effect is suppressed. This picture shows that this mechanism can work if well defined conducting planes are separated by insulating regions, like in the cuprates. This is required for the confinement of the charge carriers within these planes at high fields. However, for its normal state transport properties, or the anisotropy of $H_{c2}$ $UTe_2$ is a 3D system.

Nevertheless, an estimation of the characteristic field $B^*$ where field-induced reinforcement of $H_{c2}$ from the Lebed mechanism should appear can be done. Assuming the field is applied along the **b** axis, with the smallest coupling along the **c** axis, if d is the distance between (**a**,**b**) planes, $\xi_0$ the coherence length controlling $H^{\mathbf{b}}_{c2}$, and $\frac{dH^b_{c2}}{dT_{sc}}$ the slope of $H^{\mathbf{b}}_{c2}$ at $T_{sc}$, $B^*$ should be of the order:

$$B^* = \frac{\hbar v^c_F}{v^a_F e d^2} \tag{1.45}$$

$$= 2H^b_{c2}\left(\frac{\xi^b_0}{d}\right)\left(\frac{dH^c_{c2}/dT_{sc}}{dH^a_{c2}/dT_{sc}}\right) \tag{1.46}$$

Where $v^c_F$ and $v^a_F$ are the Fermi velocity. With the largest distance between U ions along **c** axis of order 0.38 nm, $B^*$ is above 1000 T. Thus, $UTe_2$ is not enough 2D for

this mechanism to help understanding the reinforcement of $H_{c2}^{\mathbf{b}}$. With theoretical support, we have performed numerical calculations to confirm the behaviour of the critical field in the Lebed mechanism framework. The results confirmed the conclusion expressed just before.

Thus, the most likely scenario for $H_{c2}^{\mathbf{b}}$ is an enhancement of the coupling strength with field.

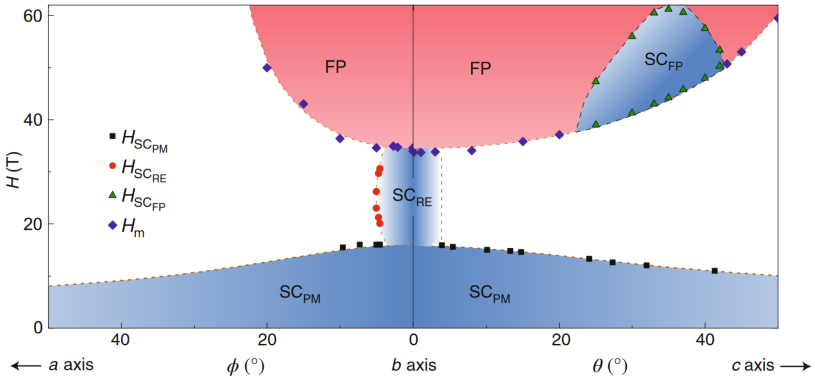


**Fig. 1.29:** *Field angle dependence of* $H_{c2}$ *established by resistivity measurements in pulse field. Blue regions represent superconductivity, and red one the polarised phase above* $H_m$ *(purple diamonds). Ref [112]*

Most surprisingly, superconductivity is also detected at higher fields, above the metamagnetic transition [71, 112]. For an angle between 25° and 40° in the (**b**,**c**) plane, a pocket of superconductivity is detected above $H_m$ up to 60 T. This pocket is a conundrum for theorist. While $H\|\mathbf{b}$ the superconductivity is suppressed at $H_m$, in this range of angle superconductivity appears above $H_m$. The Lebed mechanism has been proposed for the pocket, however, it is ruled out by the same argument than $H\|\mathbf{b}$.

A Jaccarino-Peters mechanism was also proposed but refuted in ref [112] because $UTe_2$ would lack the requested localised moments and the pocket is present over a wider field-angle range than is typical of the Jaccarino-Peters effect.

However, further investigations on this scenario might be required, because the U-U distance is larger than the Hill limit, hence a local picture for the magnetism could be adequate. Moreover, the angular dependence will depend on the precise mechanism.

### *Symmetry of the superconducting phase*

Let us come back to superconductivity below $H_m$. The symmetry of the superconducting state is a highly debated subject in $UTe_2$, but all proposals have a common assumption: superconductivity is spin-triplet, at least below 15 T. NMR measurements of the Knight-shift K have shown an anisotropic temperature dependence [35]. Figure 1.30 shows the temperature dependence of K for the three axes. For

H||**a** no decrease is seen contrasting with H||**c** and H||**b**. This would indicate a **d**-vector perpendicular to the **a** axis (no component along **a** axis).

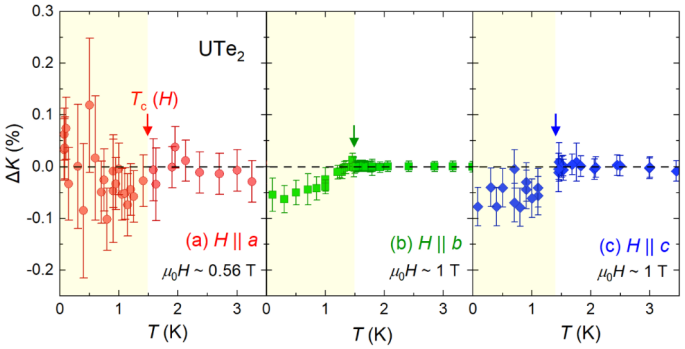


**Fig. 1.30:** *Temperature dependence of the Knight-shift along the three axes with the normal phase background removed. From ref [35].*

It is important to note that recent NMR measurements not yet published were performed on the new generation of samples with a $T_{sc} \simeq 2$ K. These measurements reveal a strong decrease of K below $T_{sc}$ for H||**a**, which contradicts completely the previous measurements. This strong discrepancy between the two studies from the same team should caution us, and will be hopefully clarified in the near future. However, if those last measurements are confirmed, they would require a large component of **d**-vector along the **a** axis, refuting the $B_{3u}$ IR at low fields.

The first study showing no change of K below $T_{sc}$ for H||**a**, is in agreement with what is expected if longitudinal ferromagnetic fluctuations along **a** axis induce superconductivity. If true, we can expect a similar orientation of the **d**-vector as in UCoGe, perpendicular to the easy magnetisation axis, the **a** axis.

| IR | Basis Functions | Gap symmetry |
|---|---|---|
| $A_u$ | $k_a\hat{a}, k_b\hat{b}, k_c\hat{c}$ | full gap |
| $B_{1u}$ | $k_b\hat{a}, k_a\hat{b}$ | point node (**c** axis) |
| $B_{2u}$ | $k_a\hat{c}, k_c\hat{a}$ | point node (**b** axis) |
| $B_{3u}$ | $k_c\hat{b}, k_b\hat{c}$ | point node (**a** axis) |

**Fig. 1.31:** *Table summarising the 4 possible IR in $UTe_2$ for spin-triplet, their basis functions and their gap symmetry.*

The point group symmetry of $UTe_2$ is $D_{2h}$, so there are four irreducible representations (IR) possible for spin-triplet superconductivity in the strong spin-orbit limit. Table 1.31 summarises the four IR, the corresponding basis functions of the **d**-vector and the symmetry of the gap. The $f$-wave components have been neglected. The **d**-vector is a linear combination of the basis function.

So, considering the NMR measurement presented above, the **d**-vector should have no component along the **a** axis. This corresponds only to a $B_{3u}$ state, with a **d**-vector defined as:

$$\mathbf{d}(\mathbf{k}) = \beta k_c \hat{b} + \gamma k_b \hat{c} \tag{1.47}$$

This $B_{3u}$ is presently the basis of all theoretical proposals for the low-field state [59, 60, 126]. The two microscopic calculations done to explore the superconducting ground state, found that the $B_{3u}$ and $A_u$ are favoured at ambient pressure [59, 143].

Experimentally, the gap symmetry can be probed in order to locate the point nodes, however, experimental results are contradicting. Most of them agree on the presence of point nodes, but not on their location. Three different penetration length studies have been carried on, the three with different conclusions. One claim point node in the (**a**,**b**) plane, with support of thermal conduction measurements [89]. Another claims point nodes close to the (**a**,**b**) plane with a chiral order parameter [17]. While the last study claims point nodes close to **b** and **c** axis, with an order parameter $B_{3u} + iA_u$ [58]. It might seem odd to invoke a chiral state, but polar Kerr effect measurements have shown a breaking of time reversal symmetry [48], so the necessity of such a chiral state. This point will be rediscussed during the presentation of the results on $UTe_2$ in section 3.2.

An angle resolved specific heat study found a behaviour in temperature inside the superconducting phase $H\|\mathbf{a}$ indicating point nodes along **a** axis [70]. The corresponding order parameter could be either chiral as $k_b + ik_c$ or $B_{3u}$.

Recent thermal conduction measurements unpublished yet, claim a fully gap state, thus an $A_u$ state. Such a symmetry is also supported by the latest NMR studies. Therefore, explanations for the violation of the paramagnetic limit for $H\|\mathbf{a}$ would then have to be reconsidered.

To conclude, experimental studies are numerous and not convergent, and relatively few predictive theoretical studies have been done. Therefore the pairing symmetry remains an active issue.

### 1.3.3 *Superconducting phases under pressure*

The behaviour of $UTe_2$ under pressure is complex and the physics rich. Here, only the main results will be presented, as a complement discussion on the possible superconducting order parameter in $UTe_2$.

When pressure is applied, a new superconducting phase emerges at zero field 1.32. Figure 1.32 shows the P-T phase diagram established at zero field from specific heat measurements. The SC1 phase found at ambient pressure is suppressed and a second phase SC2 emerges. Then at a critical pressure of $\sim$ 1.7 GPa, superconductivity is suppressed and an antiferromagnetic phase emerges. This phase diagram has been confirmed by all groups working on $UTe_2$ under pressure [135].

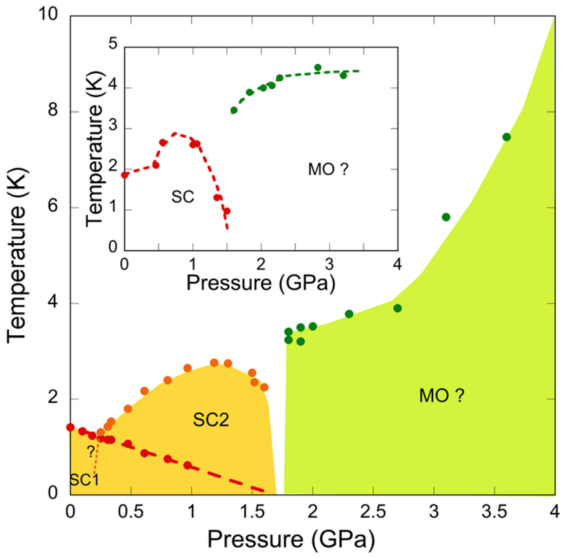


**Fig. 1.32:** *Phase diagram P-T at zero field established from specific heat measurements. Ref [20]*

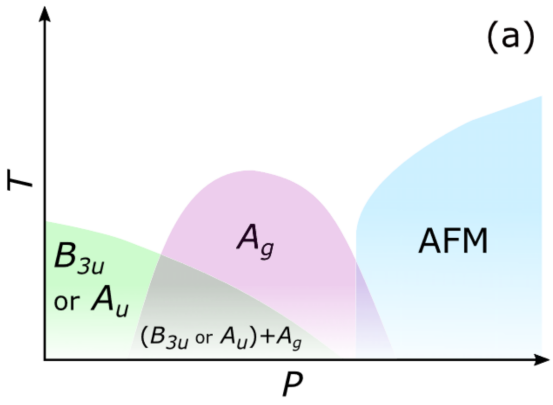


**Fig. 1.33:** *Schematic phase diagram under pressure expected from the 24 band periodic Anderson model. Ref [59]*

To clarify the superconducting phase of $UTe_2$ under pressure, a microscopic theoretical study has been conducted based on the 24band periodic Anderson model [59]. In this study the magnetic-fluctuation-mediated superconductivity has been studied, and the pressure dependence of the superconducting instability has been predicted. At ambient pressure, the ferromagnetic fluctuations are predicted to stabilise odd-parity spin-triplet superconductivity, and the moderately Ising-type magnetic anisotropy favours a **d**-vector perpendicular to the **a** axis, similarly to what is expected for UCoGe. In the high pressure region, antiferromagnetic fluctuations dominate and stabilise an even-parity spin-singlet superconducting state ($A_g$ phase in Figure 1.33).

Figure 1.34 shows the pressure dependence of the maximum eigenvalues for several IR, revealing stable odd-parity superconductivity at low pressures $p < 2$ as well as stable even-parity superconductivity at high pressures $p > 2$ (The pressure scale on Figure 1.33 is in arbitrary units). For the odd-parity superconductivity, the $B_{3u}$ and $A_u$ states are almost degenerate. This is probably a consequence of the Ising-type ferromagnetic fluctuations with $\chi_a > \chi_b \sim \chi_c$.

The even-parity superconducting state favoured in the high pressure region is the $A_g$ state. This symmetry is equivalent to the conventional *s*-wave superconductors, but the order parameter changes sign in the Brillouin zone like in the $s\pm$-wave superconducting state of pnictides. Thus, the $A_g$ state is nodeless.

The P-T phase diagram expected for this scenario is shown in Figure 1.33. However, this scenario relies on the competition of ferromagnetic and antiferromagnetic fluctuations.

Despite the claim of nearly ferromagnetic magnetic correlations in the first paper [113], it is now expected that the magnetic correlations in $UTe_2$ are not limited to a single type of spin fluctuations. Inelastic neutron scattering measurements

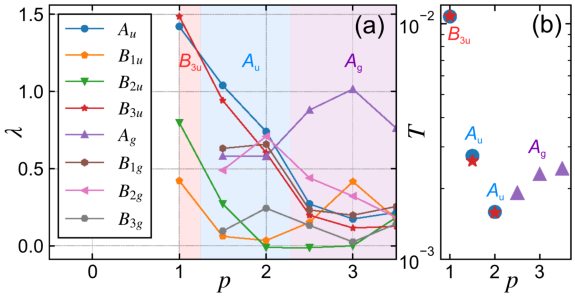


**Fig. 1.34:** *(a) Eigenvalues λ of the Eliashberg equation for various IR of $UTe_2$. The parameter p > 1 indicates applied pressure. (b) Transition temperatures of the $A_u$, $B_{3u}$ and $A_g$ superconducting states. Ref [59]*

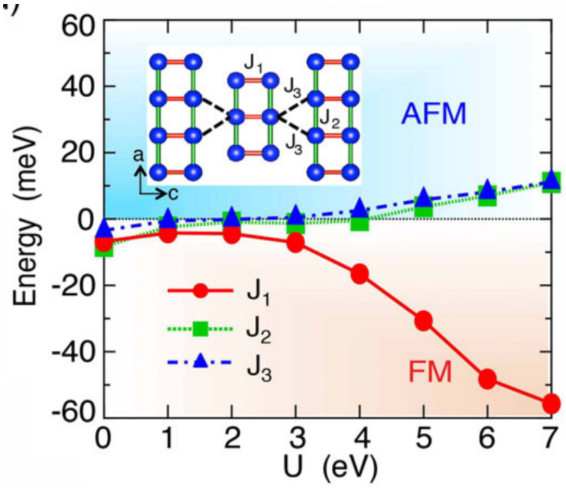


**Fig. 1.35:** *The ground state energy of $J_i$ with varying U, showing a dominant ferromagnetic (FM) rung coupling $J_1$ and much smaller antiferromagnetic (AFM) couplings $J_2$ on the leg and $J_3$ between ladders at large U. Inset: illustration of how magnetic frustrations are induced between ladders. Ref [141]*

have detected antiferromagnetic fluctuations [28, 29, 73, 114]. NMR detected low frequency fluctuations which could be ferromagnetic [136]. Therefore, it could be that a competition between antiferromagnetic and ferromagnetic fluctuations takes place in $UTe_2$.

The same theoretical study claims that an instability between ferromagnetic and antiferromagnetic order happens on increasing the hybridisation. So the dominant fluctuations might change when applying a magnetic field or pressure.

Another study based on first-principle calculations has also claimed an instability between ferromagnetic and antiferromagnetic order happens on increasing the Hubbard on site Coulomb repulsion $U$ [141]. Figure 1.35 shows the different coupling J between various Uranium site as a function of $U$. It shows a dominant ferromagnetic rung coupling $J_1$ and much smaller antiferromagnetic couplings $J_2$ on the leg and $J_3$ between ladders at large $U$, also required in this model to explain the metallic ground state.

Another theoretical proposal claims that the SC2 phase is a $B_{2u}$ state, having no component of the **d**-vector along the **b** axis, with a pairing mechanism controlled by local ferromagnetic correlations [126]. This will be rediscussed in section 3.2, together with the claims supporting a chiral superconducting state.

## 1.4 OBJECTIVES ON $UTe_2$

The specifics heat measurements performed in this work were mostly motivated by three main objectives. First, to establish the first complete thermodynamics phase diagram. Second, to probe the superconducting phase for $H \| \mathbf{b}$ by thermodynamics measurements, to detect possible changes of the symmetry of the superconducting order parameter. And last, to determine the field dependence of the electronic specific heat $\gamma(H)$ in order to compare it to a possible variation of the strong-coupling constant $\lambda$ both can be connected from the relation: $\gamma(H) \propto 1 + \lambda(H)$.

# 2

# SPECIFIC HEAT

## 2.1 INTRODUCTION TO SPECIFIC HEAT

Specific heat is a thermodynamics variable. It is proportional to the amount of heat $\delta Q$ needed to raise the temperature of an infinitesimal amount $dT$, and is defined as:

$$C = \frac{\delta Q}{dT}$$

The second principle of thermodynamics allows to link the specific heat to the entropy as:

$$\delta Q = T dS = C dT \tag{2.1}$$

$$C = T\frac{\partial S}{\partial T} \tag{2.2}$$

It is important to remember that this holds if other variables like magnetic field, volume or pressure are fixed. If these parameters vary, like magnetic field, other effects have to be taken into account, like magnetocaloric effects.

Specific heat can also be directly derived from the free energy $F$ as:

$$C = -T\frac{\partial^2 F}{\partial T^2} \tag{2.3}$$

This equation will be very useful to determine the theoretical specific heat contribution of certain mechanisms (like nuclear contribution as explained later).

Before explaining how to measure specific heat, basic contributions to specific heat found in superconductors will be presented.

### 2.1.1 $C/T$ *in the normal phase*

In a crystal there are several possible contributions to specific heat. But all crystal have a contribution from phonons $C^{phonon}$. At high temperature the volume specific heat $C_v^{phonon}$ is constant and equals to $3Nk_b$. This is the Dulong and Petit's law which states that the molar specific heat $c_v^{phonon}$ has a universal value for solids equal to $3R$ ($R$ the perfect gas constant).

When temperature is lowered the phonon specific heat is going to vary and to decrease. This behaviour is captured by the Debye model. At low temperatures only the acoustic modes, which are not gapped, can be thermally excited. The

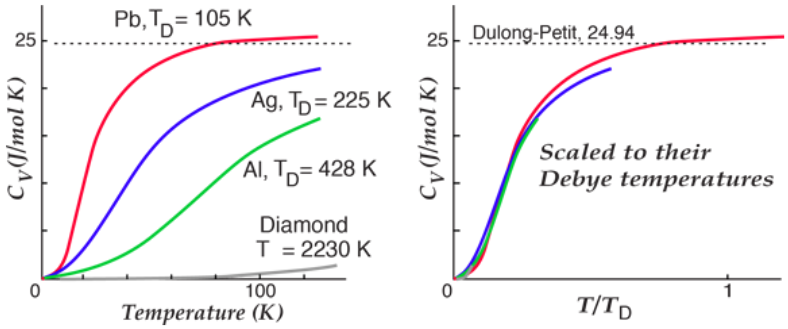


**Fig. 2.1:** *On left: phonon specific heat for several materials. On right the phonon specific heat rescaled by their Debye temperature, showing an universal behaviour. From ref [109]*

frequency can be approximated by $\omega(k) = ck$ (c the sound velocity). The molar specific heat is calculated as:

$$c_v^{phonon} = 9R\left(\frac{T}{T_D}\right)^3 \int_0^{T_D/T} \frac{x^4 e^x}{(e^x-1)^2} dx \tag{2.4}$$

where x is a dimensionless variable and $T_D$ the Debye temperature defined as:

$$x = \frac{\hbar ck}{k_B T} \tag{2.5}$$

$$T_D = \frac{\hbar c k_D}{k_B} \tag{2.6}$$

$T_D$ quantifies the rigidity of the lattice and corresponds to the temperature above which all modes start to be excited. At very low temperatures, below $T_D/12$, the molar specific heat can be approximated to a power law as:

$$c^{phonon} = R\frac{12\pi^4}{5}\left(\frac{T}{T_D}\right)^3 = \beta T^3 \tag{2.7}$$

In a metal, in addition to the phonon contribution, the conduction electrons give rise to an additional contribution to specific heat. At low temperatures, in the limit where the density of states $N(E)$ has no singularity or divergence at $E_F \pm k_B T$, the Sommerfeld expansion leads to a specific heat:

$$C^{elec} = N(E_F)\frac{\pi^2}{3}k_B^2 T = \gamma T \tag{2.8}$$

This relation is valid for a fermion gas as well as a Fermi liquid, in which the electron mass is renormalised due to interactions. $\gamma$ is called the Sommerfeld coefficient.

### 2.1.2 *C/T in the superconducting phase*

Superconductivity has a strong impact on the specific heat. At the transition a jump in the specific heat occurs with a magnitude $\Delta C$. It arises from the difference

of free energy $\Delta F$ between the superconducting and normal states at $T_{sc}$. Thus, from equation 2.3:

$$\Delta C|_{T_{SC}} = -T_{SC} \left.\frac{\partial^2 \Delta F}{\partial T^2}\right|_{T_{SC}} \tag{2.9}$$

The specific heat in the superconducting phase is given by the statistical entropy taking into account the Fermi-Dirac distribution as well as the dispersion relation of the quasi-particles. The latest is defined as:

$$\epsilon(\mathbf{k}) = \sqrt{\zeta(\mathbf{k})^2 + |\Delta(\mathbf{k})|^2} \tag{2.10}$$

where $\zeta(\mathbf{k})$ is the dispersion relation without the superconducting gap, and $\Delta(\mathbf{k})$ the superconducting gap. In the BCS theory, the gap is isotropic and specific heat in the superconducting phase $C_s$, at temperatures below $T_{sc}/3$ where the gap at $T = 0$ K $\Delta_0$ is constant, is expressed as:

$$C_s(T) = 2N(E_F)\sqrt{\frac{2\pi\Delta_0^5}{T^3}} e^{-\Delta_0/k_B T} \tag{2.11}$$

Where $\Delta_0$ is the gap at $T = 0$ K. At $T_{sc}$ the ratio of the jump with $\gamma$ has a fixed known value:

$$\frac{\Delta C}{\gamma T_{sc}} = 1.43 \tag{2.12}$$

Equation 2.11 works only for *s*-wave superconductors with one gap. However, many superconductors exhibit power laws instead of a thermal activation law below $T_{sc}$ because of the anisotropy of the gap. The jump will also be modified and decreased to conserve the entropy balance. Figure 2.2 shows examples of calculated specific heat below $T_{sc}$ for three different cases [98].

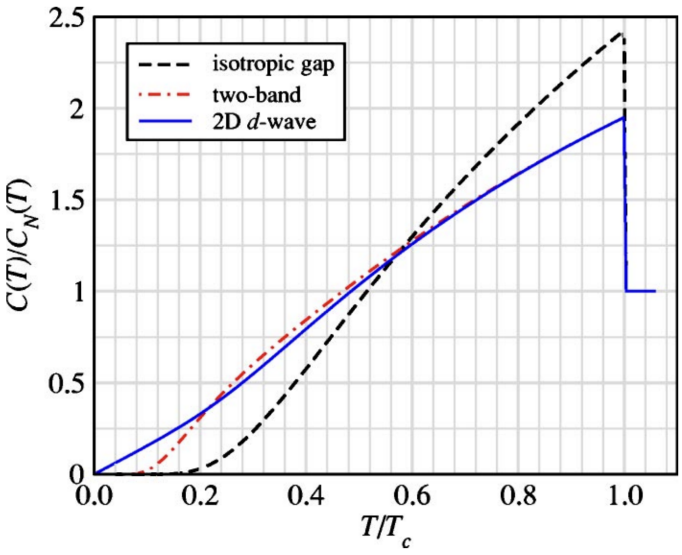


**Fig. 2.2:** *Calculated specific heats in the superconducting phase normalised by the normal state, for a s-wave superconductor with isotropic gap, with two bands ($MgB_2$) and for a* 2D *d-wave superconductor (cuprates). From ref [98].*

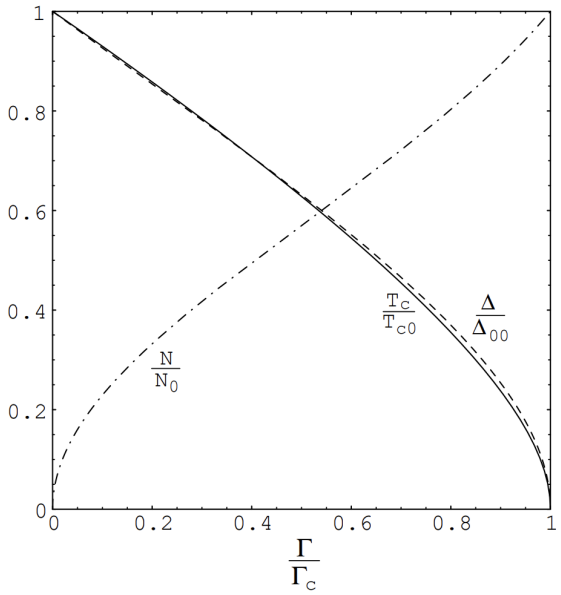


**Fig. 2.3:** *Calculation of the order parameter $\Delta$ (dashed line), the $T_{sc}$ (plain line) and the residual density of states $N$ (dash-dotted line) all normalised by their value at $\Gamma = 0$. Calculations were performed for a p-wave superconductor with a gap $\Delta(k) = \Delta\hat{d}(\hat{k}_1 \pm i\hat{k}_2)$, from ref [67].*

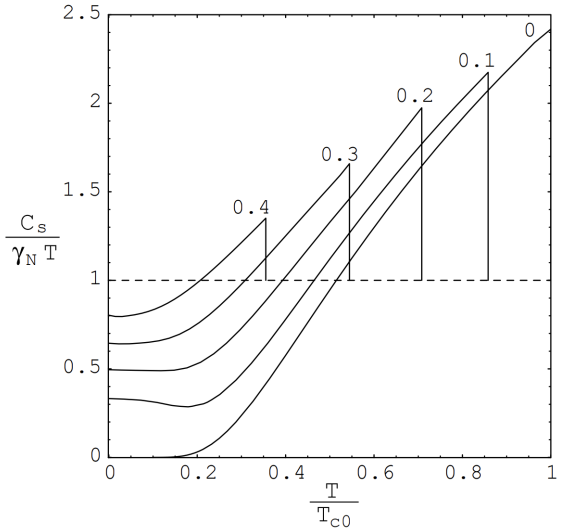


**Fig. 2.4:** *Specific heat in the superconducting state calculated for several values of $\Gamma/\Gamma_c$, in the case of a p-wave superconductor with a gap $\Delta(k) = \Delta\hat{d}(\hat{k}_1 \pm i\hat{k}_2)$, from ref [67].*

### *Impurities effects*

Impurities have different effects depending on pairing symmetry and on their magnetism. *S*-wave superconductors are known to be strongly resilient to non-magnetic impurities, as stated by the Anderson theorem: the critical temperature barely depends on material purity, or more generally on defects [5]. By contrast unconventional superconductors are sensitive even to non-magnetic impurities. This can be understood simply from the order parameter broken symmetry: if an electron with an initial wave vector $k_i$ is scattered to $k_f$ and the phase of the order parameter is different between $k_i$ and $k_f$, the phase coherence of the pair is lost and the pair is broken. Hence, normal impurities become pair-breaking.

This results in a residual specific heat term at $T = 0$ K, denoted $\gamma_r$. Of course, when the concentration of impurities $\Gamma$ is increased, the pair-breaking effect becomes more dominant, so $\gamma_r$ increases and, as a consequence, the transition jump decreases (entropy balance). Additionally, $T_{SC}$ is suppressed. When $\Gamma$ reaches a critical value $\Gamma_c$, superconductivity is completely suppressed. All of these statements are summarised in Figures 2.3 and 2.4 that show calculations done for a p-wave superconductor with a gap $\Delta(k) = \Delta\hat{d}(\hat{k}_1 \pm i\hat{k}_2)$ (long time the most popular superconducting order parameter for $Sr_2RuO_4$) [84].

*Magnetic field effects*

We saw earlier that magnetic field suppresses superconductivity. Moreover, in type II superconductors, a magnetic field above $H_{c1}$ induces the nucleation of vortices. The cores of these vortices contribute to the specific heat. One vortex core has a typical size of $2\pi\xi^2$ ($\xi$ the coherence length), so the total vortex density is $H/\Phi_0$. Since the vortex core is not superconducting, this adds a contribution $\gamma$ to the specific heat. Therefore, for a superconductor with an isotropic gap, the vortices contribution $C_{vor}$ varies roughly linearly with field:

$$C_{vor}(H) = \gamma \frac{H 2\pi\xi^2}{\Phi_0} T = \gamma \frac{H}{H_{c2}} T \tag{2.13}$$

This results in a residual contribution to $C/T$, like for the impurities, proportional to the field.

For an anisotropic gap, a second contribution must be taken into account. It arises from the Doppler shift of the energy by the superfluid currents around vortices in the vicinity of point or line nodes [137]. In fact, the main specific heat contribution in field for an anisotropic gap comes from this contribution. The resulting field dependence of the residual term is not simple and depends on the nodal structure of the gap and on the field orientation.

Therefore, the field dependence of the residual term can be measured and give an indication of the gap structure of a superconductor, if theoretical calculations are made to compare with experimental results. It is often necessary to perform microscopic calculations to interpret experimental results, which limits the interest of this approach [4].

The other consequence of field on the superconducting transition is a direct consequence of the residual term emerging from the contribution of the vortices. By entropy balance, the jump of the transition decreases.

### 2.1.3 *Effect of strong coupling*

The strong-coupling regime has also an influence on the specific heat and especially on the Sommerfeld coefficient as already evoked earlier. The entropy is renormalised by the electron-phonon interaction (electron-electron for a pairing through magnetic fluctuations) like $S = 2\pi^2 k_B^2 N(E_F)(1+\lambda)T/3$. The Sommerfeld coefficient is:

$$\gamma T = T \frac{\partial S}{\partial T} = \frac{2\pi}{3} N(E_F)(1+\lambda) k_B T \tag{2.14}$$

If the value and the variation of $\lambda$ with field are large enough to be detected, the behaviour of $\gamma(H)$ will be proportional to $\lambda(H)$, and:

$$\frac{\gamma(H)}{\gamma(0)} = \frac{1+\lambda(H)}{1+\lambda(0)} \tag{2.15}$$

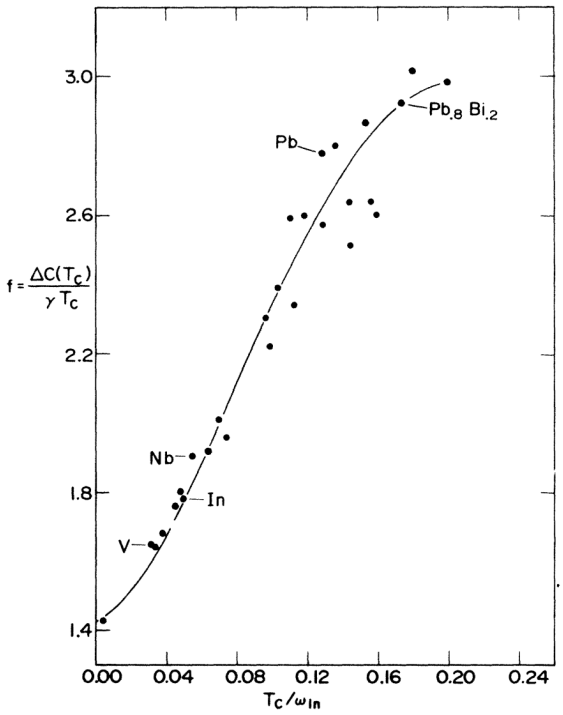


**Fig. 2.5:** *Specific-heat jump ratio* $\Delta C(T_c)/\gamma T_c$ *vs* $T_c/\omega_{ln}$ *for several compounds. The dots represent the accurate results from the full numerical solutions of the Eliashberg equations. The line correspond to* $\Delta C(T_{sc})/\gamma T_{sc} = 1.43[1 + 53(T_c/\omega_{ln})^2 \ln(\omega_{ln}/3T_c)]$. *Ref [86]*

Another effect of the strong coupling is the enhancement of the relative specific heat jump at the superconducting transition [86]. The ratio $\frac{\Delta C}{\gamma T_{sc}}$ will have a higher value than in the BCS regime. The specific heat jump at $T_{sc}$ is then a good indication of the pairing strength.

Calculations based on Eliashberg's theory in ref [86] have predicted a dependence of the relative specific heat jump at $T_{sc}$, like:

$$\frac{\Delta C(T_{sc})}{\gamma T_{sc}} = 1.43\left(1 + 53\left(\frac{T_{sc}}{\omega_{ln}}\right)^2 \ln\left(\frac{\omega_{ln}}{3T_{sc}}\right)\right) \tag{2.16}$$

$\omega_{ln}$ is called Allen-Dynes frequency and corresponds to an average phonon frequency. The ratio $T_{sc}/\omega_{ln}$ is linked to $\lambda$ through the equation:

$$\frac{T_{sc}}{\omega_{ln}} = \frac{k_B}{1.13} e^{-\frac{1+\lambda}{\lambda-\mu^*}} \tag{2.17}$$

Where $\mu^*$ is the Coulomb parameter (usually of order $0.1 - 0.15$).

Figure 2.5 from ref [86], shows the specific heat jump ratio at $T_{sc}$, $\Delta C(T_{sc})/\gamma T_{sc}$ as a function of $T_{sc}/\omega_{ln}$ calculated accurately for several compounds. It clearly demonstrates that the specific heat jump ratio increases with $\lambda$.

### 2.1.4 *Model for the superconducting transition*

We have used a numerical analysis of the specific heat measurements to extract the critical temperature, as well as the amplitude of the jump and of the width of the

transition. The analysis relies on the simple hypothesis that transition broadening is controlled by a Gaussian distribution of $T_{sc}$ of the form:

$$p(T_{sc}) = \frac{1}{\sigma\sqrt{2\pi}} \exp\left(-\frac{1}{2}\left(\frac{T_c - T_{c0}}{\sigma}\right)^2\right) \tag{2.18}$$

For the specific heat, we can write:

$$\frac{C}{T} = \int_{-\infty}^{\infty} dT_{sc}\, p(T_{sc})\, \frac{C}{T}(T, T_{sc}) \tag{2.19}$$

Where we used a simple expression for $\frac{C}{T}(T, T_{sc})$: a constant $\gamma$ term above $T_{sc}$, a jump $\frac{\Delta C}{T}$ at $T_{sc}$ followed by a constant negative slope below $T_{sc}$. If both the slope and the jump are independent of $T_{sc}$, then:

$$\frac{C}{T}(T, T_{sc}) = \gamma + \theta(T_{sc} - T)\left(\frac{\Delta C}{T} + \alpha\,(T - T_{sc})\right) \tag{2.20}$$

Before calculating the total specific heat, let us recall the definition of the repartition and **erf** functions:

$$\begin{aligned} \Phi(x) &= \int_{-\infty}^{x} \frac{du}{\sqrt{2\pi}} \exp\left(-\frac{u^2}{2}\right) \\ \Phi(x) &= \frac{1}{2} + \frac{1}{2}\,\mathrm{erf}\left(\frac{x}{\sqrt{2}}\right) \end{aligned} \tag{2.21}$$

The total specific heat can be expressed as:

$$\begin{aligned} \frac{C}{T}(T) &= \gamma + \int_{T}^{\infty} dT_{sc}\, p(T_{sc})\, \left(\frac{\Delta C}{T} + \alpha\,(T - T_{sc})\right) \\ \frac{C}{T}(T) &= \gamma + (\frac{\Delta C}{T} + \alpha(T - T_{c0}))\left[1 - \Phi\left(\frac{T - T_{c0}}{\sigma}\right)\right] - \alpha \int_{(T-T_{c0})/\sigma}^{\infty} \frac{du}{\sqrt{2\pi}}\, \sigma u \exp\left(-\frac{u^2}{2}\right) \\ \frac{C}{T}(T) &= \gamma + (\frac{\Delta C}{T} + \alpha(T - T_{c0}))\left[\frac{1}{2} - \frac{1}{2}\,\mathrm{erf}\left(\frac{T - T_{c0}}{\sigma}\right)\right] - \alpha\frac{\sigma}{\sqrt{2\pi}} \exp\left(-\frac{1}{2}\left(\frac{T - T_{c0}}{\sigma}\right)^2\right) \end{aligned} \tag{2.22}$$

This expression for $\frac{C}{T}(T)$ works perfectly for the zero field transition, where $\frac{C}{T}$ is independent of $T_{sc}$. However, under field the broadening of the transition may originate from a change of slope of $H_{c2}$ (proportional to $T_{sc}$ for clean type II superconductors). We can expect $\frac{\Delta C}{T}$ to be suppressed by field, with a decrease controlled by $H/H_{c2}(T = 0)$. So $\frac{\Delta C}{T}$ will not be constant within the broadened transition. More simply, we can assume that the jump will be suppressed like $T_{sc}(H)/T_{sc}(0)$. The point is to link $T_{sc}(H)$ and $T_{sc}(0)$, or more precisely, to get the $T_{sc}(0)$ corresponding to a given $T_{sc}(H)$. Then we could take for a model of

the transition where $\frac{\Delta C}{T}$ is proportional, within the transition, to $T_{sc}(H)/T_{sc}(0)$. A simple way to find this relation is to assume a proportionality to the broadening so that :

$$\begin{aligned} T_{sc}(H) - T_{c0}(H) &= \frac{\sigma}{\sigma_0}\left(T_{sc}(0) - T_{c0}(0)\right) \\ T_{sc}(0) &= T_{c0}(0) + \frac{\sigma_0}{\sigma}\left(T_{sc}(H) - T_{c0}(H)\right) \\ \frac{\Delta C}{T}(T_{sc}) &= \frac{\Delta C}{T}(T_{c0})\frac{T_{sc}/T_{c0}}{1+\frac{\sigma_0}{\sigma}\frac{T_{sc}-T_{c0}}{T_{c0}(0)}} \end{aligned} \tag{2.23}$$

In the last expression, we wrote $T_{sc} = T_{sc}(H)$ and $T_{c0} = T_{c0}(H)$.

The slope after the transition should similarly depend on $T_{sc}$. In high field for example, where the temperature dependence of $\frac{C}{T}$ is close to linear down to $T = 0$, the slope should depend both on $T_{sc}$ and $\frac{\Delta C}{T}$. One way to keep some consistency within the transition is to assume that we have the same entropy balance for all the curves at different $T_{sc}$ at a given field. At low field, where $\frac{C}{T}(T)$ has no reason to remain close to linear at low $T/T_{sc}$, there is no peculiar constraint on this entropy balance (the linear behaviour of $\frac{C}{T}$ at temperatures below $T_{sc}$ is valid only close enough to $T_{sc}$). However, for fields closer to $H_{c2}(0)$, we can expect that this entropy balance should be more or less close to zero. And we can enforce that :

$$\begin{aligned} \int_0^{T_{sc}} \left[\frac{\Delta C}{T}(T_{sc}) + \alpha(T_{sc})\,(T - T_{sc})\right] dT &= \beta\, T_{sc} \quad \text{, with } \beta \text{ independent of } T_{sc} \\ \frac{\Delta C}{T}(T_{sc})\, T_{sc} - \alpha(T_{sc})\frac{T_{sc}^2}{2} &= \beta\, T_{sc} \\ \alpha(T_{sc}) &= \frac{2}{T_{sc}}\left[\frac{\Delta C}{T}(T_{sc}) - \beta\right] \end{aligned} \tag{2.24}$$

For a perfect entropy balance, $\beta = 0$.

Inserting equations (2.23) and (2.24) in the first line of equation (2.22), we obtain a final expression for $\frac{C}{T}(T)$. It depends linearly on the parameters $\gamma$, $\frac{\Delta C}{T}(T_{c0})$ and $\beta$ (with a value close to zero in high fields), and non linearly on $\sigma$ and $T_{c0}$. It has two additional inputs, determined from the zero field transition: $\sigma_0$ and $T_{c0}(0)$.

$$\begin{aligned} \frac{C}{T}(T) &= \gamma + \int_T^\infty dT_{SC}\, p(T_{sc}) \left(\frac{\Delta C}{T}(T_{sc}) + \alpha(T_{sc})\,(T - T_{sc})\right) \\ \frac{C}{T}(T) &= \gamma + \int_T^\infty dT_{SC}\, p(T_{sc}) \left(\frac{\Delta C}{T}(T_{sc})\left(\frac{2T}{T_{sc}} - 1\right) + 2\beta\left(1 - \frac{T}{T_{sc}}\right)\right) \\ \frac{C}{T}(T) &= \gamma + \frac{\Delta C}{T}(T_{c0}) \int_T^\infty dT_{sc}\, p(T_{sc}) \frac{T_{sc}/T_{c0}}{1+\frac{\sigma_0}{\sigma}\frac{T_{sc}-T_{c0}}{T_{c0}(0)}} \left(\frac{2T}{T_{sc}} - 1\right) \\ &\quad + 2\beta \int_T^\infty dT_{sc}\, p(T_{sc}) \left(1 - \frac{T}{T_{sc}}\right) \end{aligned} \tag{2.25}$$

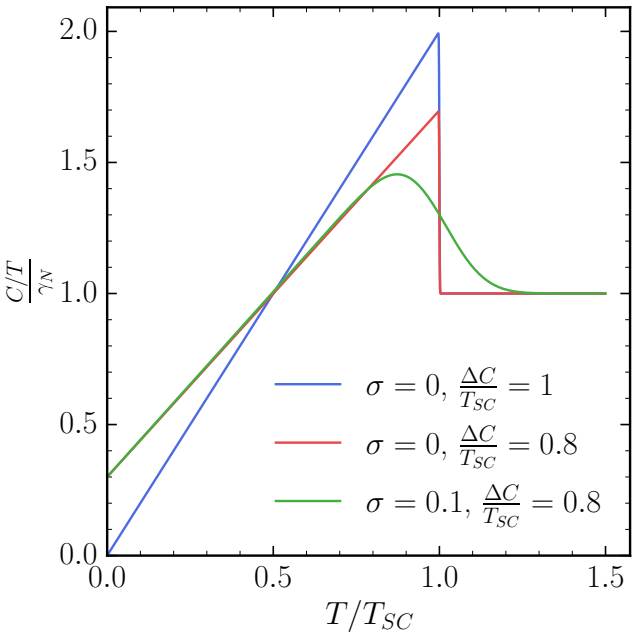


**Fig. 2.6:** *Specific heat* C/T *calculated with the Gaussian model and* $\beta = 0$, $\sigma_0 = \sigma$, *for three different sets of parameters.*

This last equation is easily numerically resolved in its integral form. To help the calculation the integrals are cut at $5\sigma$ instead of $\infty$. This gives very good results.

Figure 2.6 shows three different transitions calculated with the model presented and $\beta = 0$ and $\sigma_0 = \sigma$. We can see that when the jump is decreased the residual term increases, a consequence of entropy balance.

Note that we use formula 2.25 only in a limited range of T around $T_{sc}$ to analyse the measurements. The curves are reported on Figure 2.6 down to $T = 0$ to visualise the relations between the different parameters when entropy balance is enforced ($\beta = 0$).

### 2.1.5 *Nuclear specific heat*

At very low temperatures the nuclear spin contribution to specific heat $C_N$ can be detected and in some case becomes non negligible, or even the main contribution. We will see later, that for UCoGe the contribution from Co is extremely important.

If only the Zeeman contribution is involved, the nuclear contribution can be evaluated quite easily. Let us suppose a nuclear spin I with $2I + 1$ level. At zero field these levels are degenerate. When applying a field, the levels are shifted from each other by an energy gap $\Delta$ which is proportional to the Zeeman energy so proportional to H. The corresponding free energy is:

$$F = \sum_{n=0}^{2I+1} e^{-\beta \Delta n} \tag{2.26}$$

Where $\beta = 1/k_B T$. Knowing:

$$C = -T\frac{\partial^2 F}{\partial T^2} \tag{2.27}$$

We determine $C_N$ as:

$$C_N = cR\left(\frac{\Delta}{T}\right)^2\left(\frac{e^{-\Delta/T}}{(1-e^{-\Delta/T})^2} - \frac{n^2 e^{-\Delta n/T}}{(1-e^{-\Delta n/T})^2}\right) \tag{2.28}$$

Where c is the concentration of ions with the nuclear spin I and R the ideal gas constant. And also the gap $\Delta$ is expressed in Kelvin. For the high-temperature regime, a second order development gives:

$$C_N = \left(\frac{\Delta}{T}\right)^2 \tag{2.29}$$

The gap being proportional to the magnetic field applied H, then $\Delta = \Delta_0 H$. We can then write:

$$C_N(H) = \left(\frac{\Delta_0}{T}\right)^2 H^2 \tag{2.30}$$

Figure 2.7 shows the molar nuclear specific heat of Ge. The nuclear spin comes from $^{73}$Ge with $I = 9/2$ and a natural abundance of 7.76%. From ref [24] the gap is of 1.48 MHz/T, which is equivalent to 7.1 $10^{-5}$ K/T. When field is applied the anomaly is shifted toward higher temperatures as expected, and $1/T^2$ behaviour is found in the high-temperature region of the anomaly. In practice for our measurements we are always in this "high-temperature" regime even at 15 T at 20 mK.

Figure 2.8 shows the nuclear specific heat of Ge for different temperatures as a function of $H^2$. We see a $H^2$ dependence of $C_N(H)$ in the "high-temperature" regime (curves at 5 mK and 10 mK).

So in our specific heat measurements, the hyperfine contribution should lead to an upturn of C/T proportional to $1/T^3$ and proportional to $H^2$ when field is applied.

In metals the Knight-Shift K has to be taken into account, which is done by multiplying the field by $1 + K$ (K is in percent).

More generally, at zero applied field the nuclear spin levels can be non-degenerate because of the chemical shift or the interaction of the quadrupolar electric moment with the local electric gradient arising from the nucleus environment in the lattice. Then an upturn can be seen at zero field in C/T which will also be proportional to $1/T^3$ in our temperature range. The chemical shift, crudely speaking, is an effective hyperfine field seen by the nucleus, which can be treated like an applied field. The quadrupolar moment requires more elaborate treatment.

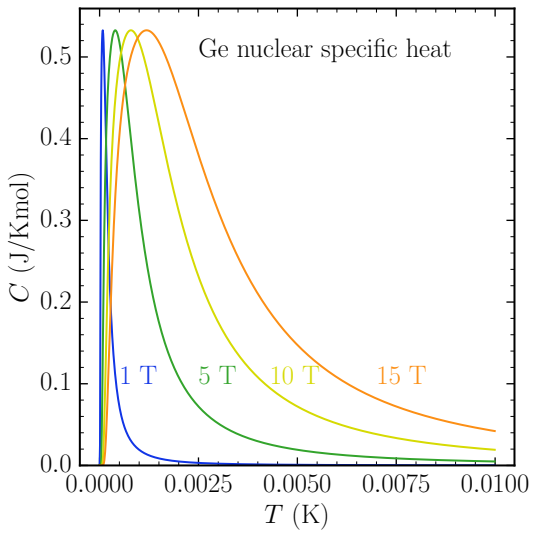


**Fig. 2.7:** *Ge nuclear specific heat calculated as a function of temperature for different magnetic fields.*

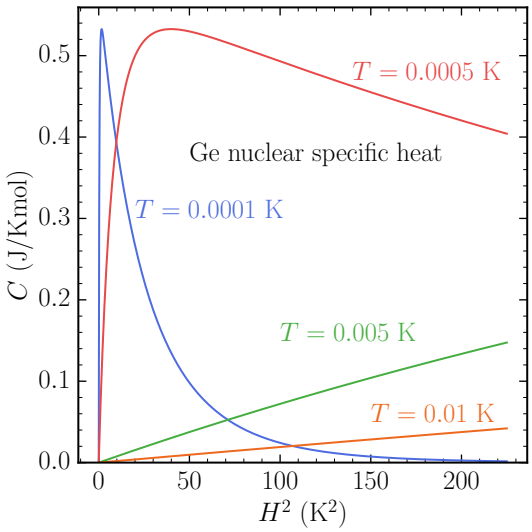


**Fig. 2.8:** *Ge nuclear specific heat calculated as a function of* $H^2$ *at different temperatures.*

If the correct and precise nuclear contribution is needed, a complete hyperfine Hamiltonian has to be used. This hamiltonian is the addition of the Zeeman hamiltonian $\mathcal{H}_Z$ and the quadrupolar hamiltonian $\mathcal{H}_Q$, and is defined as:

$$\begin{aligned}\mathcal{H} =& \mathcal{H}_Z + \mathcal{H}_Q && (2.31)\\ =& -\gamma_N \hbar(1+\mathbf{K})\mathbf{I}.\mathbf{H} && (2.32)\\ &+ \frac{\hbar\omega_q}{6}\left((3I_z^2 - I(I+1)) + \frac{1}{2}\eta(I_+^2 + I_-^2)\right) && (2.33)\end{aligned}$$

Where $\gamma_N$ is the gyromagnetic ratio of the nucleus, $\mathbf{K}$ the Knight-shift tensor, $\omega_q$ the quadrupole frequency, and $\eta$ the asymmetric parameter of the Electrical Field Gradient (EFG). Value of $\eta = 0$ is between 0 and 1, the case $\eta = 0$ corresponds to an axial symmetry of the nuclear surroundings. This Hamiltonian $\mathcal{H}$ is expressed in a particular coordinate system, namely, the principal axis of the EFG. The z axis is the direction where the EFG is maximum, and the y axis is the second maximum direction. The prefactor $\hbar\omega_q/6$ is equal to:

$$\frac{\hbar\omega_q}{6} = \frac{e^2qQ}{4I(2I-1)} \qquad (2.34)$$

Where q is the EFG at the nucleus and Q the nuclear quadrupole moment.

This Hamiltonian $\mathcal{H}$ can be numerically diagonalised to determine the different energy levels $E_i$.

The average energy $< E >$ of the nuclear system is defined as:

$$< E >= -\frac{d\ln Z}{d(1/k_B T)} \qquad (2.35)$$

Where Z is the partition function.

Thus, $C_N$ is calculated by:

$$C_N = N\frac{d < E >}{dT} \tag{2.36}$$

$$= \frac{R}{k_B T^2}\frac{\sum_{i=-I}^{I}\sum_{i=-I}^{I}(E_i^2 - E_i E_j)e^{-(E_i+E_j)/k_B T}}{\sum_{i=-I}^{I}\sum_{i=-I}^{I}e^{-(E_i+E_j)/k_B T}} \tag{2.37}$$

Where N the number of nuclei and R the ideal gas constant [1]. The parameters of the hamiltonian $\mathcal{H}$, especially $\omega_q$ and $\eta$, can be taken from NQR/NMR measurements.

However, in our case, we checked that as soon as the nuclear contributions had a significant impact on the measurements, only the Zeeman contribution renormalised by the chemical shift and the Knight shift mattered.

## 2.2 EXPERIMENTAL METHODS

There are many different methods for measuring specific heat, but the principle remains the same: applying a certain amount of heat and determining the corresponding response of the sample temperature.

In our case there are two main difficulties. First, for low temperature measurements, the choice of the thermometer and materials used for the set-up are crucial to reduce the addenda and to have an homogenous thermalisation. The second difficulty is the torque induced by the magnetic field on the magnetic moment of the sample. This torque can induce a misalignment in field, or even worse, it can tear off the sample. Therefore, a rigid set-up is preferred when it is possible.

Two different techniques have been used in these studies. The first method is a "quasi-adiabatic" technique or relaxation method. And the second is ac calorimetry or ac specific heat.

### 2.2.1 *Quasi-adiabatic technique*

The thermal model of the set-up is displayed in Figure 2.9. A heater and thermometer are connected to the sample. The sample is connected to the fridge through a thermal link with a thermal resistance R (in practice a fine gold wire). The resistance between the thermometer and the sample $R_{th}$ is neglected for the moment. The equation describing the set-up is simply:

$$C\frac{dT}{dt} = P(t) - \frac{(T - T_0)}{R} \tag{2.38}$$

Where $P(t)$ is the time-dependent heat power applied to the sample, $T$ the time-dependent temperature of the sample and $T_0$ the temperature of the fridge. We consider that there is no thermal gradient in the sample, so its temperature is homogenous. The best way to avoid these diffusion effects is to have a small sample with a geometry as close as possible of a thin layer.

We will also assume that the temperature of the fridge is stable, so $T_0$ is constant.

The method is to apply a small heat pulse and to extract the specific heat from the temperature response of the sample through the equation 2.38.

First, we let the temperature stable during a time $t_0$, so $T = T_0$. Then we apply a pulse during a time $t_d$. During this time, $T$ evolves as:

$$T(t) = T_0 + A\left(1 - e^{\frac{-(t-t_0)}{\tau}}\right) \tag{2.39}$$

This equation is obtained from equation 2.38 with $P(t) = P$, $\tau = RC$ and $A = PR$. $P$ is equal to $i^2 R_c$ where $i$ is the current sent into the heater resistance $R_c$. After the pulse at $t = t_0 + t_d$ we let the temperature relaxes. With equation 2.38 and setting $P(t) = 0$, we determine $T(t)$ after the pulse:

$$T(t) = T_0 + A\left(1 - e^{-\frac{(t_d)}{\tau}}\right) e^{-\frac{t-(t_0+t_d)}{\tau}} \tag{2.40}$$

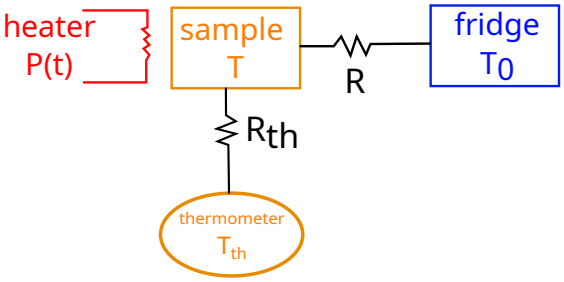


**Fig. 2.9:** *Thermal model of the quasi-adiabatic set-up.*

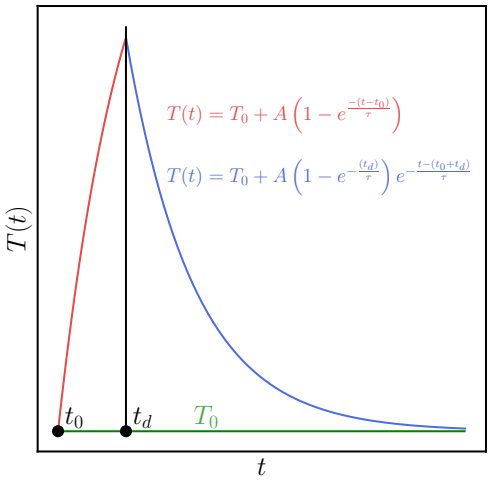


**Fig. 2.10:** *Theoretical heat pulse sequence.*

With the two equations 2.39 and 2.40 the whole pulse sequence can be fitted; A and $\tau$ determined.

To determine C we first need to redefine $\Delta Q$ and $\Delta T$ with our parameters:

$$C = \frac{\Delta Q}{\Delta T} = \frac{P t_d}{\Delta T} = \frac{\tau}{R} \Rightarrow \Delta T = \frac{P R t_d}{\tau} = \frac{A t_d}{\tau} \tag{2.41}$$

Then C is simply determined as:

$$C = \frac{\Delta Q}{\Delta T} = \frac{P\tau}{A} = \frac{R_c i^2 \tau}{A} \tag{2.42}$$

These formula are valid for any ratio $\frac{t_d}{\tau}$. However, C will be best determined if $t_d << \tau$, as in this case $\Delta T$ is close to $T(t_d)$ and C depends little on $\tau$ (adiabatic limit).

Typically, for the measurements on $UTe_2$ we used $t_d = 0.4$ s for $\tau$ varying from 2 to 10 s. This duration can be adapted, for example the measurements on UCoGe exhibited a sensitivity to heat diffusion in the sample and the exponential relaxation was distorted. By increasing $t_d$ to 3 s for the same amount of heat applied allowed the sample to thermalise more homogeneously allowing to neglect the diffusion effects and to recover the single exponential relaxation. The thermal link to the fridge R has also to be adjusted, so that $\tau$ is still measurable even at very low temperatures where C becomes very small.

Something that should not be neglected in practice is the thermal link between the thermometer and the sample characterised by a thermal resistance $R_{th}$. It means a second time constant $\tau_{th} = R_{th} C_{th}$ has to be introduced in the model. $C_{th}$ is the thermometer specific heat. The second equation to solve is then:

$$C_{th} \frac{dT_{th}}{dt} = P(t) - \frac{(T_{th} - T)}{R_{th}} \tag{2.43}$$

Solving equation 2.43 with T determined by equation 2.38 we can redefine the two equations 2.39 and 2.40 as:

$$T_{th}(t) = T_0 + A\left[1 + \left((\alpha-1)e^{\frac{-(t-t_0)}{\tau_{th}}}\right) - \left(\alpha e^{\frac{-(t-t_0)}{\tau}}\right)\right] \tag{2.44}$$

and,

$$T_{th}(t) = T_0 + A\left[\alpha e^{-\left(\frac{t-t_0-t_d}{\tau}\right)}\left(1-e^{-\left(\frac{t_d}{\tau}\right)}\right) - (\alpha-1)e^{-\left(\frac{t-t_0-t_d}{\tau_{th}}\right)}\left(1-e^{-\left(\frac{t_d}{\tau_{th}}\right)}\right)\right] \tag{2.45}$$

With $\alpha = \tau/(\tau-\tau_{th})$ in both equations. With these two equations we can fit the pulse sequence and, as in the ideal case, determine A and $\tau$ to obtain C.

The most suitable experimental condition is when we can neglect $R_{th}$ to recover the ideal case. This can be done by making the best thermal link possible between the sample and the thermometer. This point will be discussed later during the presentation of the experimental set-up.

A final important case is when an additional specific heat contribution exists, not well coupled to the dominant heat carriers of the sample. This happens typically with nuclear contribution. The nuclear spin is not coupled directly to the electrons in the metal, so the heat is not homogeneously distributed between the two systems. This nuclear specific heat contribution will respond to the heat pulse with a latency, so a second characteristic time has to be introduced in the model.

We can model this situation as an additional specific heat $C_n$ coupled through a thermal link with a resistance $R_n$. It requires to introduce a second characteristic time $\tau_n$. First, equation 2.38 has to be rewritten as:

$$C\frac{dT}{dt} = P(t) - \frac{T-T_0}{R} - \frac{T-T_n}{R_n} \tag{2.46}$$

And $C_n$ is determined by:

$$C_n\frac{dT_n}{dt} = -\frac{T_n-T}{R_n} \tag{2.47}$$

We obtain after some algebra, the equivalent of equations 2.44 and 2.45. They are:

$$\begin{aligned} T_{th}(t) = T_0 + A_1\left[1 + \left((\alpha_1-1)e^{\frac{-(t-t_0)}{\tau_{th}}}\right) - \left(\alpha_1 e^{\frac{-(t-t_0)}{\tau_1}}\right)\right] \\ + A_2\left[1 + \left((\alpha_2-1)e^{\frac{-(t-t_0)}{\tau_{th}}}\right) - \left(\alpha_2 e^{\frac{-(t-t_0)}{\tau_2}}\right)\right] \end{aligned} \tag{2.48}$$

and,

$$\begin{aligned} T_{th}(t) = T_0 + A_1\left[\alpha_1 e^{-\left(\frac{t-t_0-t_d}{\tau_1}\right)}\left(1-e^{-\left(\frac{t_d}{\tau_1}\right)}\right) - (\alpha_1-1)e^{-\left(\frac{t-t_0-t_d}{\tau_{th}}\right)}\left(1-e^{-\left(\frac{t_d}{\tau_{th}}\right)}\right)\right] \\ + A_2\left[\alpha_2 e^{-\left(\frac{t-t_0-t_d}{\tau_2}\right)}\left(1-e^{-\left(\frac{t_d}{\tau_2}\right)}\right) - (\alpha_2-1)e^{-\left(\frac{t-t_0-t_d}{\tau_{th}}\right)}\left(1-e^{-\left(\frac{t_d}{\tau_{th}}\right)}\right)\right] \end{aligned} \tag{2.49}$$

In both of them, $\alpha_1 = \frac{\tau_1}{\tau_1 - \tau_{th}}$ and $\alpha_2 = \frac{\tau_2}{\tau_2 - \tau_{th}}$. Also, $\tau_n = \frac{A_1\tau_2 + A_2\tau_1}{A_1 + A_2}$ and $\tau = \frac{A_1 + A_2}{(A_1/\tau_1) + (A_2/\tau_2)}$. Figure 2.12 shows several theoretical pulse sequences calculated with $\tau_1 = 1$. We can see how the second relaxation time deforms the temperature response of the thermometer.

To calculate the specific heat C (electronic part), $\Delta T$ is redefined as:

$$\Delta T = t_d \left( \frac{A_1}{\tau_1} + \frac{A_2}{\tau_2} \right) \tag{2.50}$$

Then, C is determined by:

$$C = \frac{\Delta Q}{\Delta T} = R_c i^2 \left( \frac{A_1}{\tau_1} + \frac{A_2}{\tau_2} \right)^{-1} \tag{2.51}$$

The total specific heat $C_{tot}$ is equal to $C + C_N$, where $C_N$ is determined by:

$$C_N = C \left( \frac{A_1 A_2}{(A_1 + A_2)^2} \right) \left( \frac{1}{\tau_1} - \frac{1}{\tau_2} \right)^2 \tau_1 \tau_2 \tag{2.52}$$

This double exponential contribution to the pulses will be evoked again in the presentation of UCoGe measurements where the large contribution of Co is inducing a double exponentials in the pulse. For $UTe_2$ the pulses exhibited clean single exponential.

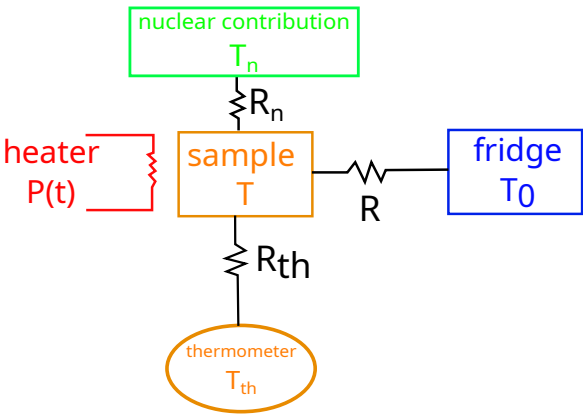


**Fig. 2.11:** *Thermal model of the set-up with a nuclear contribution to specific heat.*

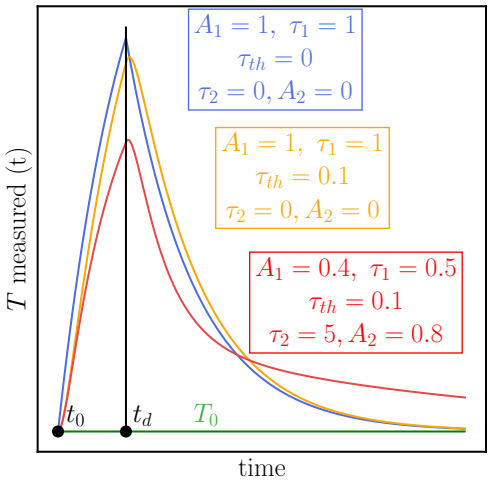


**Fig. 2.12:** *Theoretical heat pulse sequences with double exponentials for different parameters. Also,* $T_{measured} = T_{th}$.

In practice how a specific heat measurements is performed? First, we set the temperature of the fridge to a given value $T_0$. Once the temperatures of the fridge and the sample are stabilised, the pulse sequence starts. Then, we obtain a value of C for the temperature $\frac{T_0 + \Delta T}{2}$. Then, it is possible to either sweep in temperature by changing the set point of the fridge, or sweep in field by changing it.

The last parameter to discuss is the amount of heat applied. The resulting $\Delta T$ should not be greater than the temperature step during a sweep. Moreover, the evolution of specific heat has be taken into account. For example, if C has an anomaly with a strong variation of specific heat (sharp superconducting transition, first order divergence etc.), $\Delta T$ should not be greater than the width of the anomaly, otherwise the specific heat obtained is a value averaged over the whole anomaly.

Typically, the $\Delta T$ realised are of the order 1.5% of T. But at low temperatures, when the noise increases, $\Delta T$ can be increased up to 4% so the pulse is relatively larger than the noise. By contrast, in a sharp superconducting transition $\Delta T$ is decreased down to 0.5% of the temperature.

### 2.2.2 *The set-up*

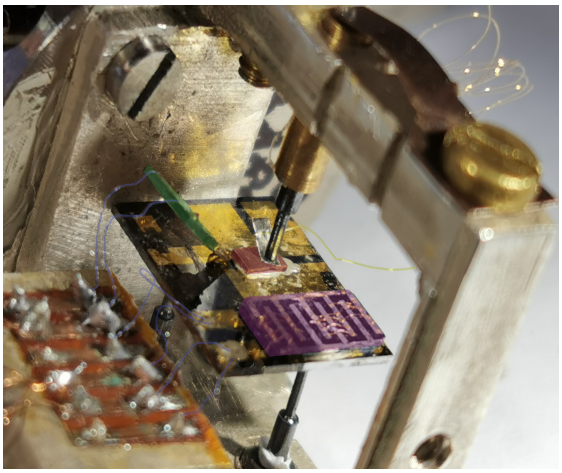

**Fig. 2.13:** *Close picture of the set-up. Colours of the shades correspond to those in Fig.2.14.*

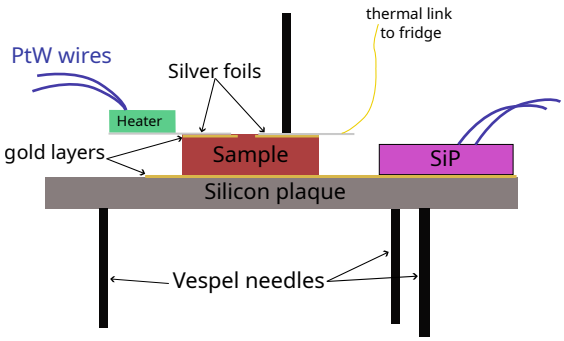


**Fig. 2.14:** *Schematic view from side of the set-up in Fig.2.13.*

Figure 2.13 shows the set-up, and Figure 2.14 a schematic view of it. The sample is placed on a silicon plate, same for thermometer (SiP). Silicon appeared as the best choice at low temperatures. We tried with amorphous $SiO_2$ plate instead, but the heat was not homogeneously distributed below 1 K, so the thermometer was overheated during the pulses. Furthermore, the specific heat of silicon is rather small at low temperatures because it is mainly due to phonons with negligible hyperfine contribution, minimising the addenda of the set-up. The problem of inhomogeneous heat conduction by ballistic phonons was bypassed by evaporating a gold layer on the silicon plate. It also improves the thermal link with the sample.

This plate is placed on three vespel needles to minimise thermal links unwanted with the fridge. The rigidity of the set-up is coming from the four vespel needles supporting and fastening the plate. Despite their bad thermal conductance, they may be the main heat leak between 1 K and 7 K.

The thermometer is a layer of silicon doped with phosphorus (SiP). Since it is mainly Si, its specific heat contribution to the addenda is small. This thermometer suffers from a small lack of reproducibility between different cooling of the experiment, so the calibration has to be done after each cooling. It is time consuming, but the calibration has to be established very carefully. Specific heat is the first derivative of temperature, therefore the calibration of the thermometer must be very accurate and the second derivative as smooth as possible to avoid anomalies in C/T due to wrong calibration.

Our reference thermometers are Ge thermometers placed on the fridge in the compensated field region. These thermometers are very reliable and reproducible. The use of these reference thermometers lead to a small relative error, of few per thousand of the temperature. The absolute error is of order of one percent.

This SiP thermometer is sensitive over a large range of temperatures from 7 K down to 20 mK, and has a short response time (0.1 s at 10 mK). Furthermore, the SiP has a large magnetoresistance which requires accurate recalibration under fields but yields high sensitivity with field and decreasing temperature.

In order to cool down the sample to the lowest temperatures, it is necessary to have a negligible thermal contact resistance between the sample and the heat link (R) with the fridge. For insulators or easily oxidised metals like UCoGe, a thin gold layer ($\sim$ 1000Å) can be evaporated on the surfaces of the sample.

The thermal link to the fridge (R) is a gold wire welded by ball bonding on a silver foil. This wire is adapted (length and radius) to have a reasonable $\tau$, meaning small enough so the measurements are fast, and long enough so the exponential relaxation is measurable. Typically, we seek a $\tau$ around 5 s, or at least 1 s when we cannot do better. The difficulty is to keep a reasonable $\tau$ in the whole temperature range. In the case where the thermal resistance $R_{th}$ is negligible, R goes like 1/T. Depending of the temperature dependence of the specific heat of the sample, it can be necessary to use two different heat leaks to cover the whole temperature range required for the measurements. It means two different experiments have to be run.

The silver foil is glued on the sample with a very small amount of silver paste and pressed by a vespel needle on the sample. This needle is maintained by a CuBe spring.

The heater is a chrome meander evaporated on a plate of silicon. It is glued on a silver foil that is itself glued on the sample with GE varnish. Chrome meanders are sensitive to electrostatic discharge, but they are very convenient: $R_c$ remains constant below 7 K, of the order of 10 k$\Omega$, which is 100 times larger than the resistance of the wires connected to the heater, so we are sure the power is mainly dissipated by $R_c$.

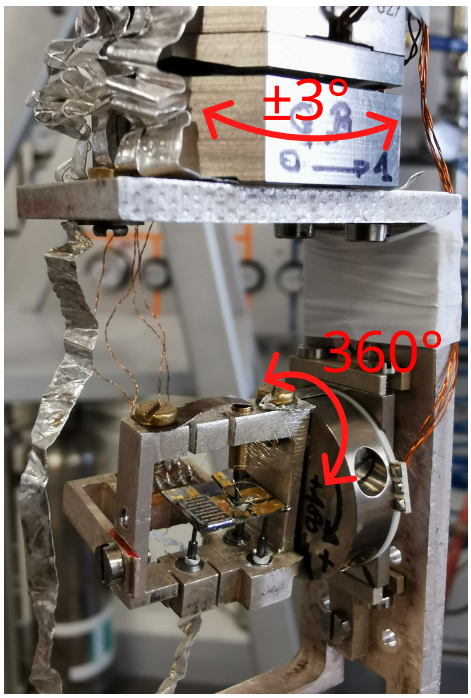


**Fig. 2.15:** *Pictures of the set-up showing the piezoelectric rotator and goniometer.*

The SiP and heater are connected with PtW wires. The resistivity of these wires is large enough so that heat is not transported by these wires (or a negligible part of it in comparison with the thermal link R). The parallel resistance of all wires is larger than 10 Ω.

The silver framework supporting the set-up is fixed on a piezoelectric rotator, allowing a 360° rotation (see Figure 2.15). In practice, we cannot do more than a 110° rotation due to the finite length of the wires, and the silver foil thermalising the set-up on the fridge. This is enough to align the sample in field, and to change the axis on the crystal by doing a 90° rotation. This rotator is fixed to a silver piece, itself screwed on a goniometer allowing a rotation of ±3° in the plane perpendicular to the rotator. This goniometer is used to fine-tune the alignment in field.

### 2.2.3 *ac calorimetry*

The ac calorimetry is based on the same schematic set-up as the quasi-adiabatic method, a sample connected to a thermometer and a heater, and the whole connected to the fridge by a thermal link R (Figure 2.9). But in this ac calorimetry case, $P(t)$ is modulated in time. So, the sample temperature $T(t)$ will oscillate in response to $P(t)$. The specific heat of the sample dampens the oscillation of $T(t)$ and shifts the phase compared to the oscillation of $P(t)$. Mathematically, we start with the same equation:

$$C\frac{dT}{dt} = P(t) - \frac{(T - T_0)}{R} \tag{2.53}$$

If we impose a current $I(t) = I_{AC}\cos(\omega t)$ the corresponding power is equal to:

$$P(t) = R_c(I_{AC}\cos(\omega t))^2 = P_{AC}(1+\cos(2\omega t)) \tag{2.54}$$

Equation 2.53 can now be solved, and the alternative part of the sample temperature is:

$$T_{AC} = \frac{P_{AC}}{\kappa + 2i\omega C} \tag{2.55}$$

where $\kappa = 1/R$ the thermal conductivity of the thermal link. With the alternative part of T, C can be determined without knowing $\kappa$. First, the amplitude $|T_{AC}|$ and the phase $\phi$ of $T_{AC}$ have to be determined:

$$\begin{aligned} |T_{AC}| &= \frac{P_{AC}}{\sqrt{\kappa^2 + 4\omega^2 C^2}} \\ \phi &= -\arctan\left(\frac{2\omega C}{\kappa}\right) \end{aligned} \tag{2.56}$$

From these two equations we see that the specific heat of the sample, as indicated above, leads to a damping of the oscillation and a shift of the phase. Finally, C is determined by equation:

$$C = \frac{P_{AC}|\sin(\phi)|}{|T_{AC}|2\omega} \tag{2.57}$$

ac specific heat measurements have many advantages, especially the good signal-to-noise ratio due to the use of lock-in amplifier. A major advantage for high-field measurements is the speed. Specific heat is measured almost continuously, so the field or temperature can be swept continuously without steps like for the "quasi-adiabatic" method. The ac calorimetry also makes it possible to scan the specific heat in frequency, which is impossible with all other techniques.

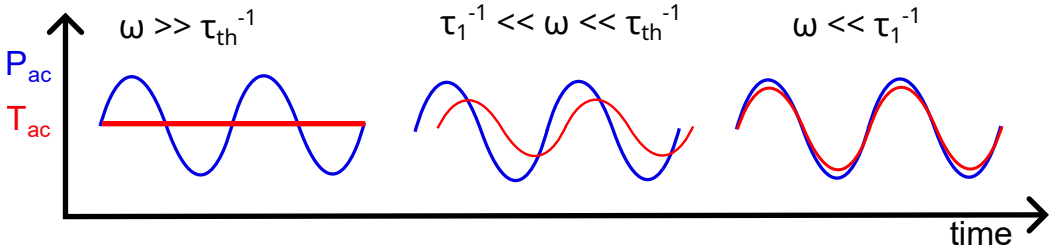


**Fig. 2.16:** *Schema of the imposed oscillation ($P_{ac}$) and the temperature response of the sample ($T_{ac}$) for three different frequency regimes.*

The equations determined above apply to the ideal case. Like the "quasi-adiabatic" method, a decoupling with the thermometer can be introduced. The effects will be seen in the amplitude and on the phase of the oscillation.

The effects on the oscillations can be understood without calculations. Let us first neglect a possible second contribution that is not well coupled. If the oscillation frequency is $\omega >> 1/\tau_{th}$, the oscillation is too fast and will not be measured.

If $\omega << 1/\tau$ the oscillation is too slow and all the heat is directly sent to the fridge. In this case, the specific heat is not measured:

$$|T_{AC}| = \frac{P_{AC}}{\kappa} \tag{2.58}$$

$$\phi = 0 \tag{2.59}$$

For a good measurement $1/\tau >> \omega >> 1/\tau_{th}$. Figure 2.16 shows a scheme that summarises this three regimes.

These ac specific heat measurements have been performed in collaboration with Christophe Marcenat (CEA) and Thierry Klein (CNRS, Néel Institut), with their set-up.

In practice, a small resistive chip (Cernox thermometer) is cut in half, one side used as the heater and the other as the thermometer. Everything is attached to a copper ring (of ~ 1 cm of diameter) with PtW wires that are used to measure the resistance and apply current to the heater. Due to the size of the set-up, only very small samples can be measured (in the µg range).

There is one disadvantage with this set-up: it is not completely rigid. Therefore, the torque under magnetic field, especially at high fields (30 T), can be a problem for alignment. Nevertheless, we did not observe any movement of the sample in our high-field measurements on $UTe_2$.

**Fig. 2.17:** *Close picture of the set-up for ac specific heat.*

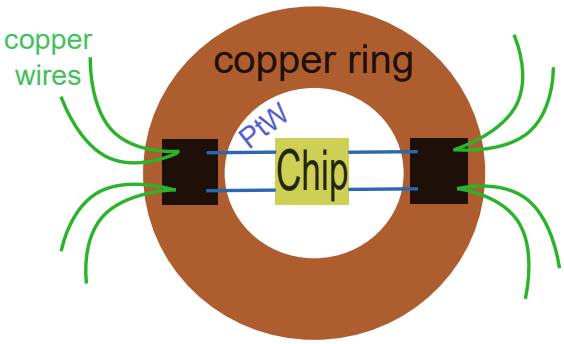


**Fig. 2.18:** *Schematic view from the top of the set-up in Fig.2.17.*

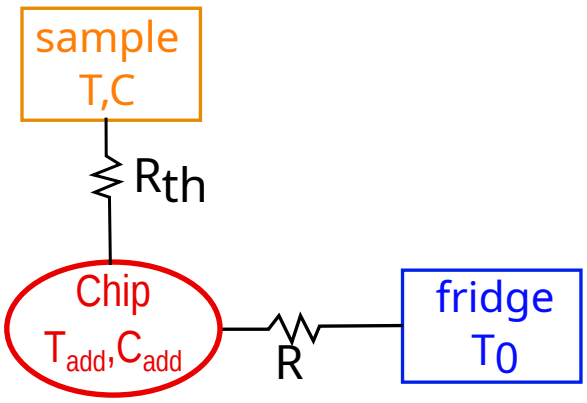


**Fig. 2.19:** *Thermal model of the ac specific heat set-up with a decoupling of the sample.*

One issue that needs to be carefully addressed is the possible decoupling of the sample, which is what happened during the first high-field measurements campaign. To understand the effect on the measurements, let us determine $T_{ac}$ for the experimental set-up. The schematic thermal model of the set-up is shown in Figure 2.19, where $C_{add}$ corresponds to the specific heat of the chip (the addenda). The equations describing the temperature response of the set-up are:

$$C\frac{dT}{dt} = k_{th}(T_{add} - T) \tag{2.60}$$

$$C_{add}\frac{dT_{add}}{dt} = P(t) + k_{th}(T - T_{add}) + k(T_0 - T_{add}) \tag{2.61}$$

Here $k_{th} = \frac{1}{R_{th}}$ and $k = \frac{1}{R}$. In this model the possible internal decoupling of the heater and thermometer in the chip is neglected. In practice, frequency tests have been done to verify that the internal coupling was good.

After some algebra, the oscillating part of the chip temperature $T_{AC}$ can be written as follows:

$$T_{AC} = \frac{P_{AC}}{i\omega(C_{add} + \alpha C) + k + k_{th}(1-\alpha)} \tag{2.62}$$

And from this equation are derived:

$$|T_{AC}| = \frac{P_{AC}}{\sqrt{(k + k_{th}(1-\alpha))^2 + \omega^2(C_{add} + \alpha C)^2}} \tag{2.63}$$

$$\phi = -\arctan\left(\frac{\omega(C_{add} + \alpha C)}{k + k_{th}(1-\alpha)}\right) \tag{2.64}$$

In all these equations, $\alpha = \frac{1}{1+(\omega/\omega_{th})}$, where $\omega_{th} = \frac{k_{th}}{C}$ (equivalent to $1/\tau_{th}$). This $\alpha$ parametrises the decoupling of the sample. If $\alpha = 1$, the sample is perfectly coupled and the ideal case is recovered.

In practice, this $\alpha$ can depend on the temperature, and the sample can be decoupled when temperature decreases. As a consequence, only a fraction of the sample specific heat is measured, thus the total specific heat measured is drastically decreasing.

To detect possible decoupling, frequency tests must be performed. Indeed, when $\omega$ becomes much smaller than $\omega_{th}$ the ideal case is recovered and the whole specific heat $(C + C_{add})$ is measured.

If the sample is decoupled, the frequency can be decreased to recover a correct measurement of the total specific heat. However, the frequency cannot be reduced too much because of the $1/f$ noise. In our specific heat measurement on $UTe_2$, the frequency has been reduced to 4 Hz. Figure 2.20 shows three ac specific heat measurements done on $UTe_2$ that illustrate the loss of signal with increasing frequency when the sample is decoupled. At 32 Hz, the superconducting transition at 600 mK is no longer detected .

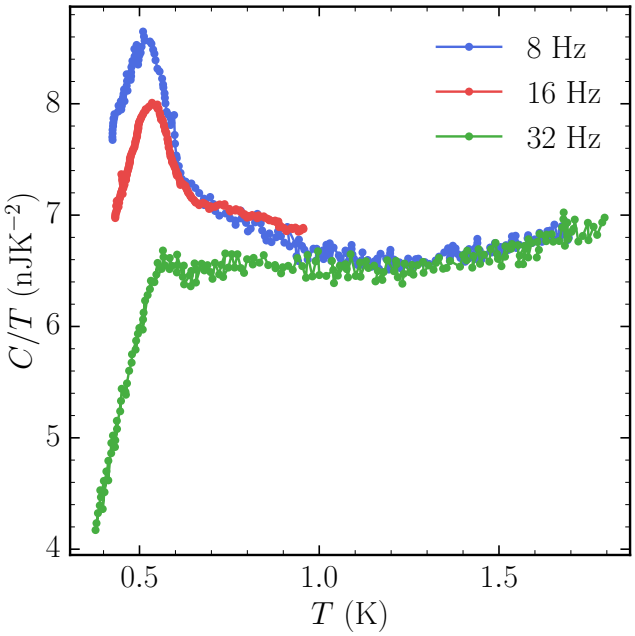


**Fig. 2.20:** *Specific heat measurements done on $UTe_2$ with three different frequencies. The sample is decoupled when temperature decreases below 1 K. With increasing frequency a part of the signal is lost.*

# 3

# SPECIFIC HEAT MEASUREMENTS ON $UTe_2$

| | $T_{sc}$ (K) | $\Delta T_{SC}$ (mK) | $\Delta C/C$ | mass (mg) |
|---|---|---|---|---|
| #1 | 1.469 | 22 | 1.2 | 12.3 |
| #2 | 1.849 | 20 | 1.88 | 5.6 |
| #3 | 1.847 | 33 | 1.51 | 12.7 $10^{-3}$ |
| LAP97 | 1.975 | 97 | 2.1 | 6.8 |

**Table 3.1:** *The table summarises the main properties of the three samples, their $T_{sc}$, widths of the transition $\Delta T_{SC}$, relative jumps at $T_{sc}$ $\Delta C/C$ and masses.*

Two samples from different growths were mainly measured, one with a $T_{SC} = 1.43$ K at zero field (sample #1), and one with $T_{SC} = 1.849$ K at zero field (sample #2). All sample studied were grown in the laboratory with the same source of depleted Uranium. They were measured by quasi adiabatic technique in a home made dilution fridge down to 50 mK when possible, and in a superconducting magnet up to 15 T. A third sample (#3) of 12.7 µg from the same growth as sample #2 with a $T_{SC} = 1.847$ K was used for the high fields measurements with the ac calorimetry technique. Table 3.1 shows the properties of the different samples. The high fields measurements were done at LNCMI in Grenoble in resistive coils up to 36 T (permanent field). Below 18.5 T, the ac specific heat measurements on sample #3 were done in superconducting coils with a larger radius than the resistive coils. It allowed to add a piezoelectric rotator to align the sample in the field, but also to measure with different angles in the (**b**,**c**) plane.

## 3.1 NORMAL PHASE

Before discussing the superconducting phase, let us focus on the normal phase. As explained previously, one purpose of the measurements was to determine precisely $\gamma$ to link its variation with field to the variation of the superconducting strong-coupling constant $\lambda$. In general, heavy fermions compounds, far away from quantum criticality, behave like classical Fermi liquids at low temperatures. So one could expect $C/T$ to behave like $\gamma + \beta T^2$ in $UTe_2$. However, $C/T$ does not exhibit a linear behaviour when plotted as a function of $T^2$ as shown in Figure 3.1(a). We could imagine this coming from non analytic corrections to the electronic specific heat, but when H is applied along the **b** axis, the slope slightly increases, and

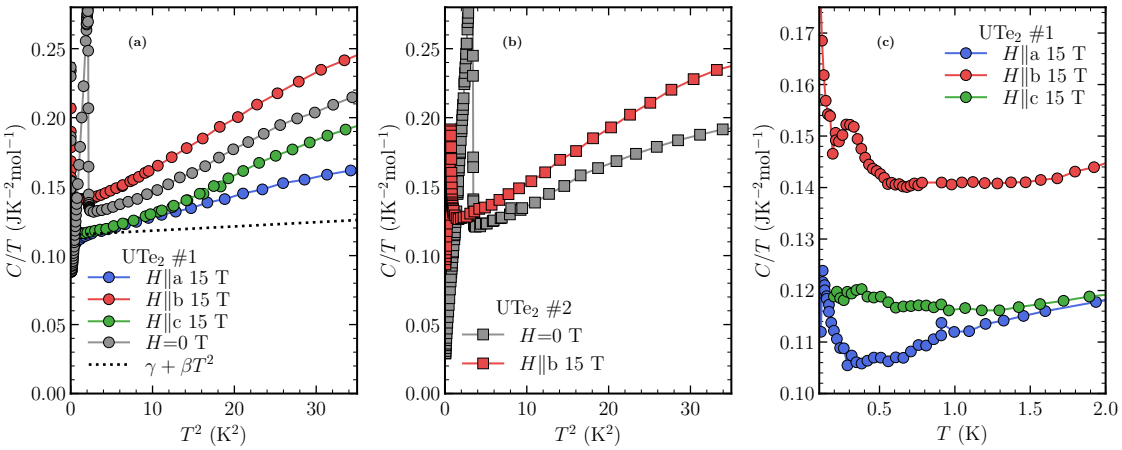


**Fig. 3.1:** *Temperature dependence of* C/T *(sample* #1*) for fields applied along the three crystallographic directions. (a)* C/T *as a function of* $T^2$*, measured on sample* #1*: no linear behaviour is seen. At* 15 *T for* H||***a****, the temperature dependence is drastically suppressed compared to measurements at* 0 *T. whereas it is slightly larger for* H||***b****, The doted line is the sum of a constant Sommerfeld term and a phonon contribution estimated from a Debye temperature deduced from high-temperature measurements Ref. (b) Same data for* H||***b*** *on sample* #2*: the anomalous magnetic contribution seems more pronounced than for sample* #1*. (c)* C/T *at low temperatures at* 15 *T along the three axis measured on sample* #1*. The superconducting transition at* 0.5 *K remains visible for* H||***b****.*

when applied along the **a** axis the slope drastically decreases. This is shown in Figure 3.1(a) and (b). This would mean that β term is field dependant. However, the phonon are not so easily influenced by magnetic fields. Thus, there is an additional contribution to the specific heat which is influenced by field.

This additional contribution can be attributed to an anomaly seen around $T^*$ ~12 K in high-temperature specific heat measurements [138]. C/T Measurements were done in the laboratory on a different sample from 1 K up to 300 K using a commercial instrument (Physical Properties Measurement System). By fitting above 30 K with a simple Debye law (the integral form seen in section 2.1.1 , see Figure 3.2), one can extract a Debye temperature of $T_\theta = 185$ K and subtract the corresponding phonon contribution to the specific heat. The remaining specific heat exhibits a significant anomaly around $T^* \simeq 12$ K, which moves toward high temperatures when a field is applied along the **a** axis (Figure 3.3). This explains the drastic decrease of the slope for H||**a** seen in Figure 3.1(a). We can also calculate from $T_\theta$ the corresponding β and then determine γ by setting its value as the value of C/T just above the superconducting transition. It is shown by the dotted black line in Figure 3.1(a) with $\gamma = 0.133$ JK$^{-2}$mol$^{-1}$ and $\beta = 0.3$ mJK$^{-4}$mol$^{-1}$. It clearly shows that the phonon contribution is small between $T_{sc}$ and 6 K, supporting the existence of a large additional contribution to C/T arising from the anomaly at $T^*$.

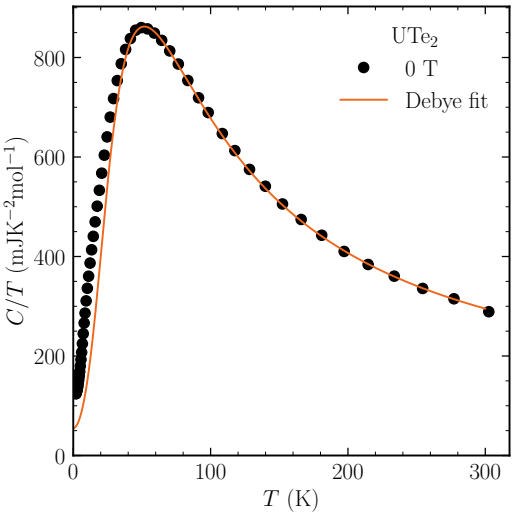


**Fig. 3.2:** C/T *at zero field and the Debye fit (orange line) done above* 30 *K giving* $T_D = 185$ *K.*

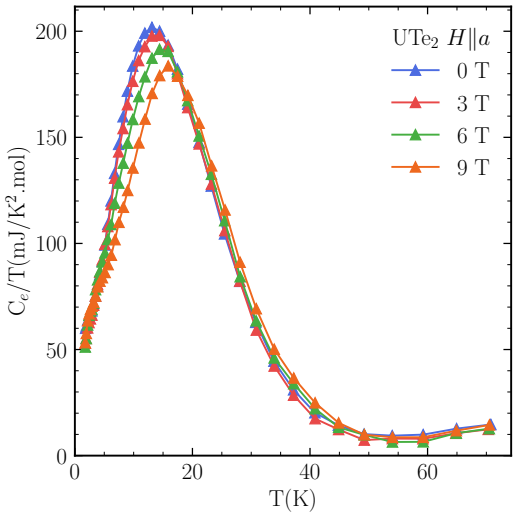


**Fig. 3.3:** C/T *obtained by removing the phonon specific heat determined by the Debye fit in Figure 3.2.*

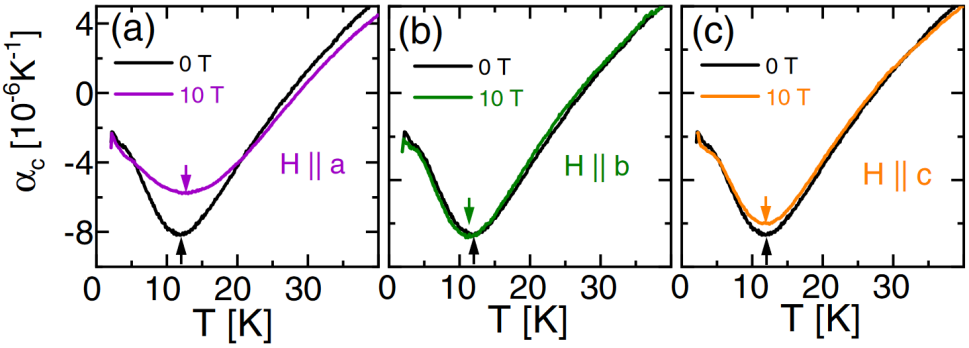


**Fig. 3.4:** *Temperature dependence of* $\alpha_c$ *in* 0 *and* 10 *T applied fields along the three directions. From ref [138].*

This anomaly has been seen with thermal expansion as a minimum of $\alpha$ as shown in Figure 3.4 [138]. Similarly, it shifts towards high temperatures when H is applied along the **a** axis. In addition, when H is applied along **b** axis, the minimum shifts towards low temperatures. This shift is less pronounced than the one for H||**a**, explaining why it is unseen at 9 T in the high-temperature specific heat measurements, and we only see a slight increase of the slope at 15 T in Figure 3.1(a) and (b). Regarding this anomaly, a maximum of $1/T_2$ in NMR measurements occurs in the same temperature range as $T^*$ [136]. It is evidenced in Figure 3.5. And a change in the magnetic fluctuations is also detected in the neutron scattering measurements [73] as shown in Figure 3.5. It suggests a magnetic origin for the anomaly at $T^*$.

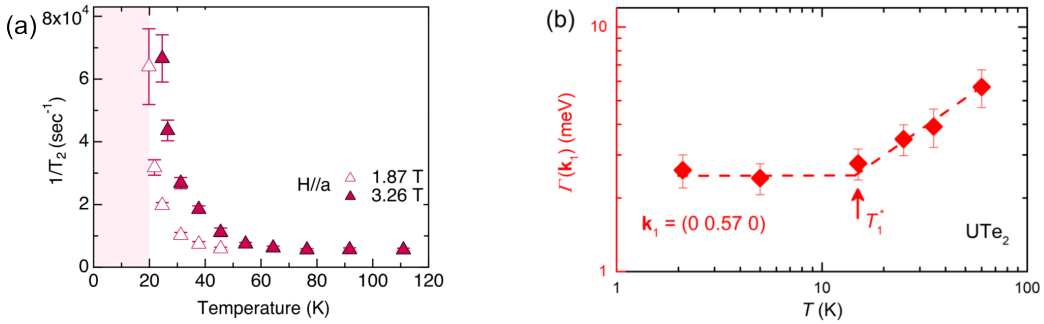


**Fig. 3.5:** *(a) Temperature dependence of* $1/T_2T$ *in small fields from ref [136]. (b) Temperature dependence of the relaxation rate* $\Gamma(k_1)$ *extracted from the neutron diffraction spectra from NMR measurements in ref [73]. The change of behaviour is denoted by* $T_1^*$.

However, a study based on DMFT calculation claims that crystal-field splitting of the $5f^2$ configuration yields to a Schottky-like anomaly in agreement with diverse measurements [68]. But it is not clear how field could influence such a mechanism and lead to the behaviour found in the specific heat and thermal expansion measurements under field.

### 3.1.1 *C/T field dependence in the normal phase*

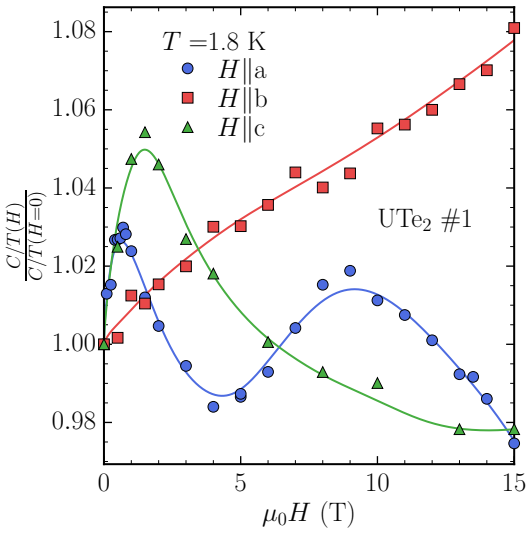


**Fig. 3.6:** C/T *normalized at* $H = 0$ *T as function of* H *at 1.8 K on sample #2. Lines are guide to the eyes.*

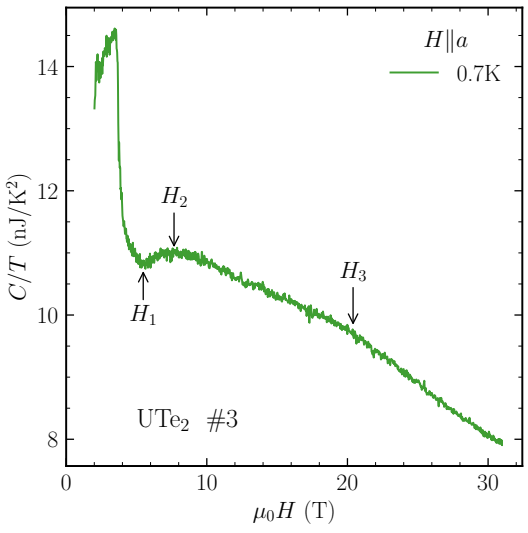


**Fig. 3.7:** *Field sweep* $H\|\boldsymbol{a}$ *at 700 mK on sample #3 with the three anomalies in the normal phase indicated.*

Since there is no simple behaviour of the temperature dependence of C/T, $\gamma$ can not be extracted unambiguously. Nevertheless, below 2 K, C/T seems to remain roughly constant for fields along **c** and **b** axis (see Figure 3.1(c)), at least down to 0.5 K far from the upturn at low temperatures. So the values at 1.8 K can be

considered as a reasonable estimation of the electronic specific heat. For H||**a**, the behaviour at low temperatures is unusual, but this might come from the proximity to Lifshitz transitions that will be discussed below. Figure 3.6 shows C/T at 1.8 K as a function of field for the three directions.

For field applied along the **b** axis, C/T(1.8 K) increases monotonically from 0 T to 15 T, which might be the sign of an increase of the coupling constant. This increase is in agreement with the magnetisation measurements that show an increase of $\gamma$ determined through the Maxwell relations, up to the metamagnetic transition[99, 100]. The resistivity measurements also show an increase of the A coefficient of the inelastic contribution, expected to be proportional to $(m^*)^2$ [71, 74].

For field applied along the two other directions, the behaviour of C/T is rather puzzling. For H||**a**, C/T exhibits a peak below 1 T followed by a minimum at 4.5 T and another maximum at 9 T. Actually, the origin of the peak at low field (< 1 T) is unknown.

The two anomalies occurring at 4.5 T and 9 T coincide with anomalies seen in thermoelectric power and Hall effect measurements attributed to Lifshitz transitions [104].

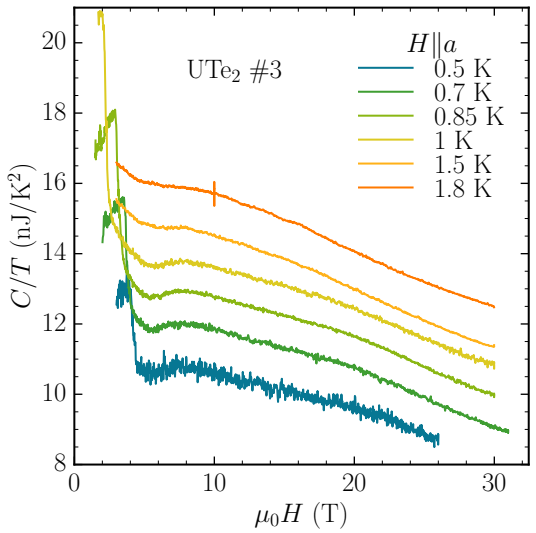


**Fig. 3.8:** *Field sweeps H||**a** done on sample #3. Curves have been shift of 1 nJ/K² from each other for clarity.*

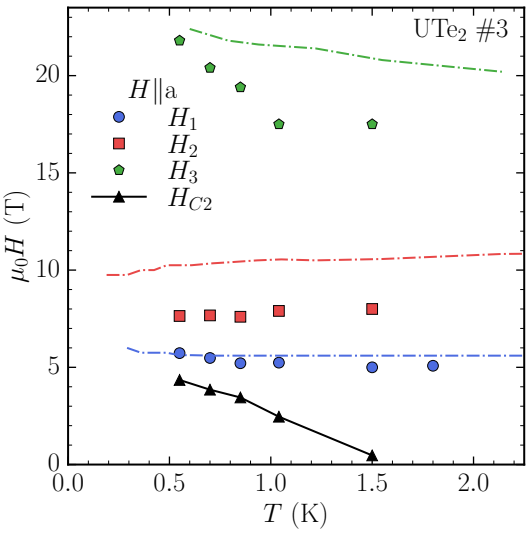


**Fig. 3.9:** *Phase diagram obtained with the field sweeps H||**a**. The dash-dotted lines correspond to the phase diagram from [104].*

This minimum followed by a maximum is also seen in the field sweeps performed on sample #3 with ac calorimetry up to 31 T. A change of slope is also visible at field around 24 T. Figure 3.7 shows the field sweep performed at 700 mK and the three anomalies denoted $H_1$, $H_2$ and $H_3$; the minimum, the maximum and the change of slope respectively. Figure 3.8 shows all the field sweeps performed. If we plot the temperature dependence of the three anomalies we obtain the phase diagram shown in Figure 3.9, where the dash-dotted lines correspond

to the phase diagram obtained by the thermoelectric power measurements in ref [104]. The two phase diagrams are similar and the quantitative differences for $H_2$ and $H_3$ might come from a misalignment of the sample in our C/T measurements. This strong similarity leads to conclude that the anomalies seen in C/T H||**a** are Lifshitz transitions, the same seen in the thermoelectric power measurements.

To conclude, C/T(H) H||**a** is unreliable to discuss the field dependence of the coupling strength on this axis due to all these anomalies parasitising C/T(H).

For field along **c** axis, a strong peak at 1.5 T is visible. Its origin is unknown like for H||**a**, but it makes C/T(H) for H||**c** also unreliable to discuss the coupling strength field dependence.

All these results lead to the conclusion that C/T(H) is unreliable to discuss the coupling strength dependence with field. Only C/T(H) for H||**b** seems to be not too much influenced by parasitic contributions, and might be related to $m^*$.

### 3.1.2 *Low temperatures upturn*

As seen in Figure 3.10 all samples exhibit an upturn at low temperatures of C/T, below 100 mK, and the residual term of C/T. These are sample dependent and are seen at 0 T and reported in many different studies [16, 70, 89]. Their origins are still unclear and under debate. However, we can estimate the nuclear contribution for the upturn.

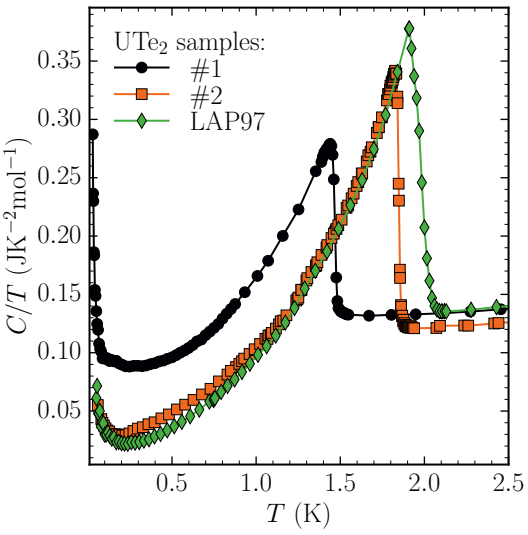


**Fig. 3.10:** C/T *at zero field for samples* #1 *and* #2. *LAP97 is a sample made by molten salt flux technique with* $T_{SC} \simeq 2$ *K.*

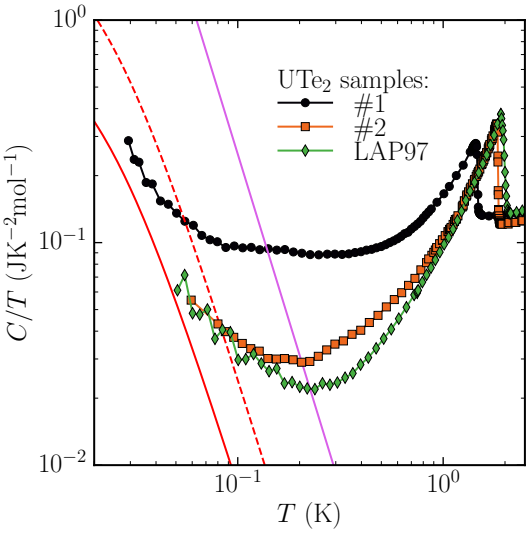


**Fig. 3.11:** C/T *with a logarithmic scale of same samples as in Figure 3.10. The red lines correspond to the hyperfine contribution due to* $^{235}U$ *chemical shift for a concentration of* 0.1%*(plain line) and* 0.3% *(dashed line). The plain magenta line correspond to* $^{235}U$ *quadrupolar moment contribution with the same parameters as in* $USb_2$ *[65].*

Figure 3.11 shows C/T for different samples with a log-log scale. The first important remark, the upturn in C/T does not follow a $1/T^3$ dependence as expected for a nuclear Schottky anomaly in this temperature range. Most of studies claiming a nuclear origin for this upturn are restricted to temperatures above 100 mK, so only a small part of the upturn is visible. However, for studies that go below 100 mK the upturn does not have a $1/T^3$ behaviour. One study claims a divergent behaviour as $1/T^{1/3}$ [89]. Our specific heat measurements are close to a divergence with a 1/T behaviour, but it has no direct physical meaning.

Regarding the possible nuclear contribution, the upturn seen at 0 T invalidates a contribution of Te since it has no quadrupolar moment. A possibility is the quadrupolar contribution from $U^{235}$ [52, 65]. The asymmetric factor of electric field gradient (EFG) tensor and its maximal component are needed to have an exact calculation of this contribution (see section 2.1.5). Those are unknown for $UTe_2$, and would require theoretical calculations. Neglecting $\eta$ value like in $USb_2$ [65], as done in ref [120], we can roughly determine the quadrupolar contribution to specific heat. The contribution is depicted as the purple line in Figure 3.11, and it corresponds to a concentration of 0.1% of $U^{235}$, which is the smallest possible in depleted Uranium (our samples are all made from depleted Uranium). It is clearly too large compared to the measured C/T. This means the maximum component of the EFG is much lower in $UTe_2$ than in $USb_2$.

A second contribution from $U^{235}$ is expected and was never discussed in other studies on $UTe_2$. A chemical shift is induced by the 5*f* shell of $U^{235}$, leading to a hyperfine field on the nucleus. This phenomena has been studied on other Uranium compounds by EPR [83], NMR [52, 53], Mössbauer spectroscopy [117] or specific heat measurements [118]. Typically the hyperfine field due to the chemical shift has a value around 300 T on the nucleus. The gap between levels of the nuclear spin determined by EPR measurements has a value of 14 mK, and the resonance frequency in NMR measurements of 0.76 MHz/T. These correspond to a hyperfine field of 396 T. The corresponding specific heat contribution is depicted in Figure 3.11 as a red line for 0.1% of $U^{235}$ and by a dashed red line for 0.3%. For the smallest concentration of $U^{235}$ it could match to the upturn at zero field.

To conclude on the nuclear contributions, $U^{235}$ could lead to an upturn below 100 mK. What is surprising is to have such a small upturn considering the expected quadrupolar and the chemical shift contributions. The most plausible origin is an addition of contributions from nuclear quadrupole moment and chemical shift of $U^{235}$, and from defects in samples.

Samples with higher $T_{sc}$ have less upturn and also a lower residual term [23, 115]. Theoretical calculations support the fact that defects could induce a residual term at low temperatures [97]. The amount of residual term would be correlated to $T_{sc}$, which is also an experimental fact, as seen in Figure 3.10.

A study claimed that the residual term comes from the freezing of magnetic clusters [129]. It relied on muon spectroscopy showing the presence of fast and slow relaxation rates pointing an homogenous spin freezing in a fraction of the sample, in magnetic clusters. The fraction of the magnetic clusters in different

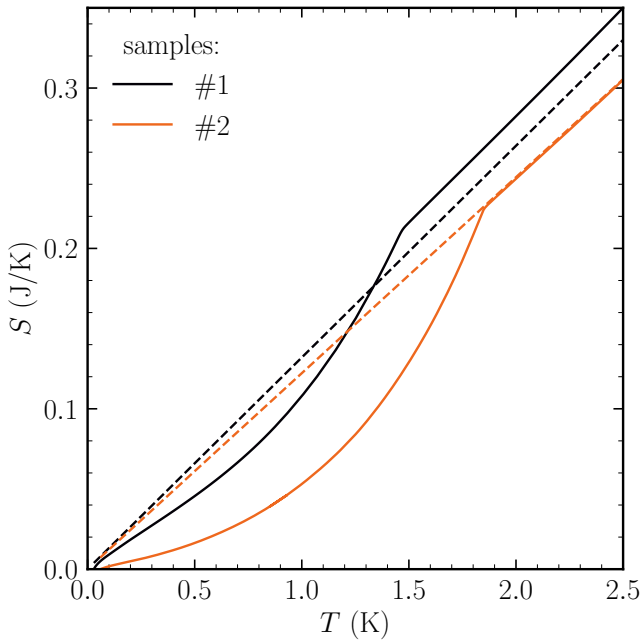


**Fig. 3.12:** *The entropy* S(T) *at zero field of samples* #2 *and* #3 *determined by integration of* C/T. *Dashed lines correspond to the electronic entropy* ($\gamma$T).

samples have been shown to be proportional to their residual term in specific heat. Thus, it supports the idea that defects in $UTe_2$, which are most likely different crystal phases, generate the residual term.

It is also worth to note that most of our measurements were done on samples #2 and #3 from the same batch and that the entropy balance is perfectly satisfied at $T_{sc}$ on sample #2, as shown in Figure 3.12. Which mean impurities that might be present have a negligible contribution to specific heat.

## 3.2 THE SUPERCONDUCTING TRANSITION

One striking property of $UTe_2$ is the sharpness of the superconducting transitions, the width being as small as 20 mK for the best sample we measured (sample #2, see table 3.1).

However, it was claimed for a time that there were two transitions at zero field, as shown in Figure 3.13, and for samples exhibiting only one transition, these two transitions were degenerate [48]. This claim was first published with Polar Kerr effect measurements detecting a Time Reversal Symmetry Breaking (TRSB). Figure 3.13 shows the Kerr angle for two different runs in which the sample is warmed up past $T_{sc}$ after being cooled in an applied field. The finite value of the Kerr angle indicates a TRSB.

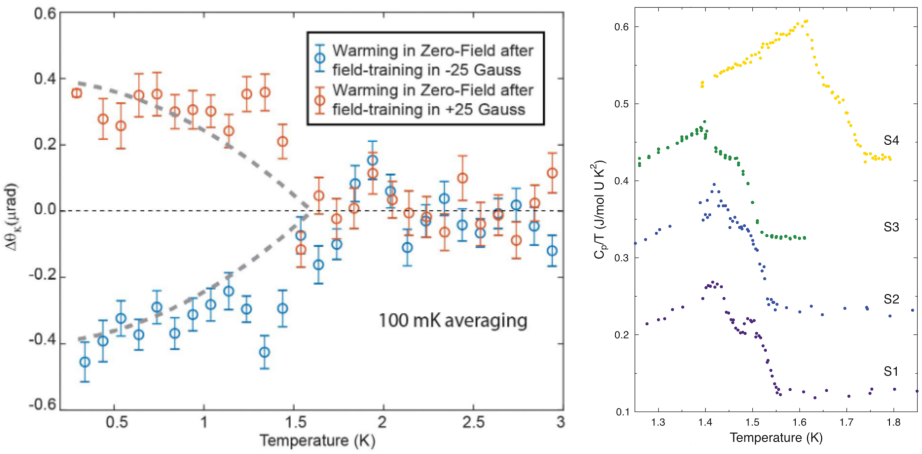


**Fig. 3.13:** *Left panel: Kerr angle for two different sweeps in which the sample is warmed up past Tc after being cooled in an applied field. For a positive (negative) applied field of +25 G (−25 G), a positive (negative) Kerr signal emerges at $T_{sc}$ and saturates around 400 nrad.*
*Right panel: Specific heat superconducting double transitions at zero field measured on different samples.*
*All from ref [48]*

For a TRSB to occur, the superconducting order parameter needs to have two components $(p + ip)$. $UTe_2$ has the point group $(D_{2h})$ which has only single component representations. Because of the strong spin-orbit coupling in $UTe_2$, the only way to obtain a two components order parameter is to add two single component representations. According to the trainability of the TRSB seen along the **c** axis, there are two possibilities: $B_{3u} + iB_{2u}$ or $A_u + iB_{1u}$. Just after this study, a theoretical one supported by DFT calculations claimed that the only possibility is $B_{3u} + iB_{2u}$ [126].

Such a multicomponent order parameter as $B_{3u} + iB_{2u}$ state imposes double superconducting transitions at zero field. The first one to transition from the normal to the superconducting $B_{3u}$ state, and the second one which breaks time reversal symmetry to transition into the $B_{3u} + iB_{2u}$ state. The corresponding schematic H-T phase diagram for $H\|\mathbf{b}$ is presented in Figure 3.14. This scenario could also

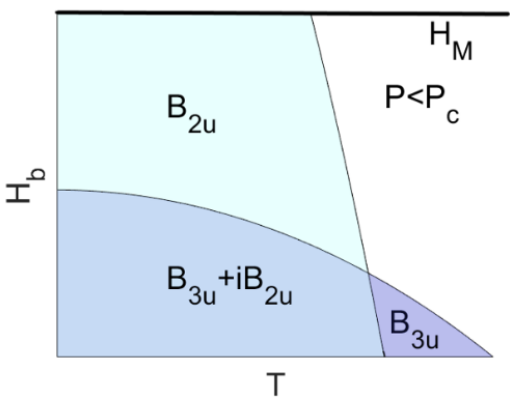


**Fig. 3.14:** *Schematic phase diagram* $H\|\boldsymbol{b}$ *for the* $B_{3u}+iB_{2u}$ *state scenario at ambient pressure. From ref [126]*

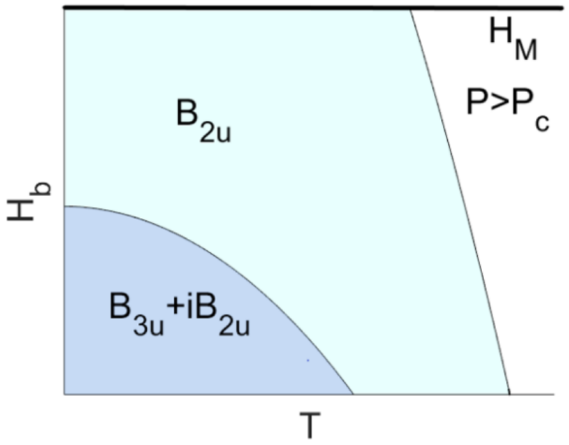


**Fig. 3.15:** *Schematic phase diagram* $H\|\boldsymbol{b}$ *at pressure above* $p_c$ *(*$p_c$*: pressure at which SC2 emerges), for the* $B_{3u}+iB_{2u}$ *state scenario. From ref [126]*

explain the behaviour of the superconducting phase under pressure. As explained in the introduction (see section 1.3.3) a second superconducting phase (SC2) appears when pressure is applied (see Figure 3.16). In the scenario claimed in ref [126], pressure favours $B_{2u}$ state which would correspond to the SC2 phase seen under pressure. Figures 3.15 shows H-T phase diagram for $H\|\mathbf{b}$ at pressure below the one at which the SC2 phase emerges [126].

The $B_{3u}+iB_{2u}$ state is chiral (see section 1.1.2) with the chiral axis parallel to **c** axis. However, STM measurements claimed detection of chiral state, with the chiral axis parallel to **a** axis [62]. This discrepancy is a problem. These STM measurements and the conclusion drawn from Polar Kerr effect measurements were highly discussed for a time, especially for existence of the double transitions in specific heat.

But, today it is clear that the double transitions are just due to the inhomogeneity of the samples and are not intrinsic to $UTe_2$. It was nicely demonstrated by specific heat measurements under pressure [135]. According to the scenario of the $B_{3u}+iB_{2u}$ explained before, a transition line should be visible in the P-T phase diagram when the pure $B_{2u}$ state is favoured. This hypothetical transition line is denoted by a "?" and depicted by a dashed line in Figure 3.16. The study in ref [135] showed that this line does not exist in high quality samples.

Another simple experiment to do is to cut a sample showing a double transition at zero field into pieces, and to measure the pieces individually. The result is shown in Figure 3.17 from [6], the double transitions disappear on the small pieces, exhibiting a sharp single transition proving the extrinsic origin of the double transitions.

However, it leaves open the question on the origin of the breaking of time reversal symmetry seen in the polar Kerr effect signal and also on the possibility of a chiral superconducting state. Diverse measurements have been performed to

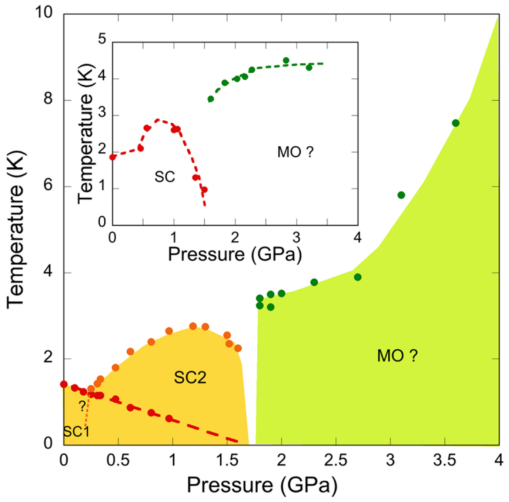


**Fig. 3.16:** *P-T phase diagram established with specific heat measurements. From ref [20]*

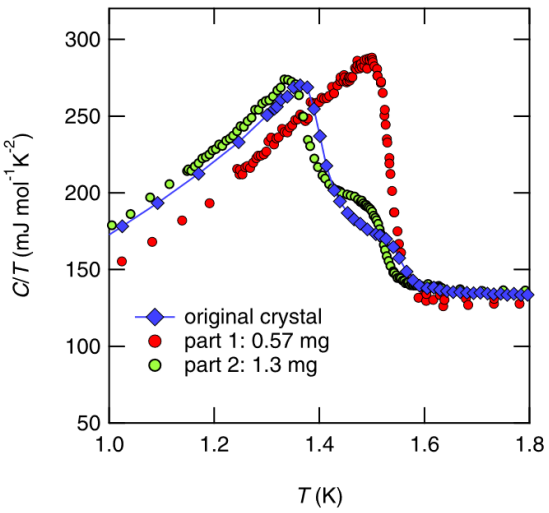


**Fig. 3.17:** *Superconducting transitions measured by specific heat on cut samples. From ref [6]*

explore the gap symmetry, and some of them claim chiral superconducting state (see section 1.3.2). But actually there is no consensus. It is worth remembering the muon spectroscopy measurements showing a freezing of magnetic clusters. It might be an explanation of the TRSB signal seen in the polar Kerr effect, knowing these measurements have been performed on the first generation of samples with a relativity bad homogeneity.

All the sample we measured exhibit a sharp and single transition at zero field, indicating the high quality and homogeneity of the samples, see table 3.1 for their respective widths. The ratio of the jump $\Delta C$ over $\gamma T_{SC}$ are above the BCS value of 1.43 for the sample #2 and #3, indicating a strong-coupling superconducting regime ($\gamma$ is approximated by the value of C/T just above the superconducting transition). For the sample #1 the ratio is equal to 1.2, however, there is a large residual term ($\gamma_0 = 0.087$ $JK^{-2}mol^{-1}$) at low temperatures so the jump is artificially smaller than what it could be with less residual term as in samples #2 and #3. The superconducting transition remains sharp enough when field is applied along the three axes so it can be easily followed, and fitted by the Gaussian model presented in chapter 2.1.4, to determine the phase diagram.

## 3.3 THE CRITICAL FIELD $H_{c2}$ IN THE LOW FIELDS REGION ($H < 15$ T)

The sharp transition seen at zero field can be followed when field is applied: its width remains small and its jump large enough to detect it easily up to 15 T for H‖**b**, and lower fields for H‖**a** and H‖**c**. With such a sharp transition the alignment H‖**b** was easy to realise, then a rotation of 90° was enough to rotate toward **c** or **a** axis depending how the sample is mounted on the setup. And the alignment was perfected for both axes.

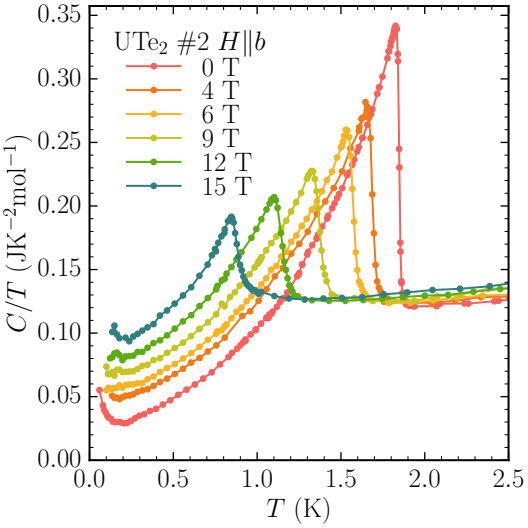


**Fig. 3.18:** *Specific heat superconducting transitions for different values of the field applied along the **b** axis on sample #2.*

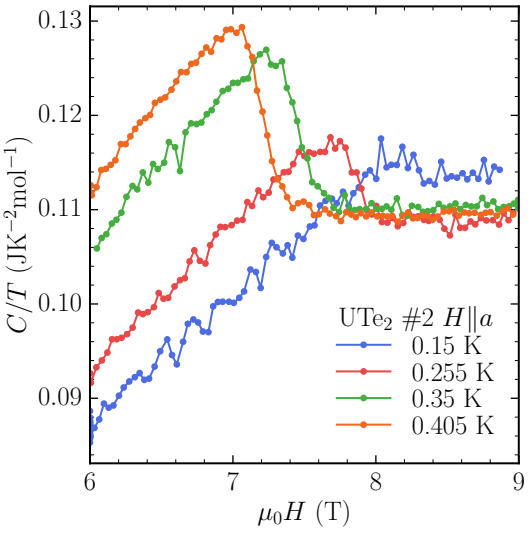


**Fig. 3.19:** *Field sweeps perform below 400 mK along the **a** axis on sample #2, in a field range to detect the superconducting transition.*

Figure 3.18 shows several specific heat transitions for different fields H‖**b** on sample #2. It demonstrates how sharp the transition remains under field, even at 15 T. For the whole data on sample #2 including directions H‖**a** and H‖**c** see Appendix A.1. At low temperatures we also performed field sweeps for H‖**a** to complete the phase diagram down to 100 mK. The field sweeps are shown in Figure 3.19. With the model of a Gaussian distribution of $T_{sc}$ (or a distribution of fields for the field sweeps) presented in chapter 2.1.4, we can extract the $T_{sc}$ and determine the $H_{c2}$ along the three axes. The phase diagram obtained is shown in Figure 3.20.

All the previous determinations of $H_{c2}$ had been obtained from transport measurements. They presented an anisotropy: $H^{b}_{C2} > H^{c}_{C2} > H^{a}_{C2}$. Thermodynamics measurements reveal a different anisotropy near $T_{sc}$. From our measurements we derive a slope of $H_{c2}$ near $T_{sc}$ of the same order of magnitude for H‖**a** and H‖**b**: −20 T/K and −34 T/K respectively. The slope of $H^{a}_{c2}$ at $T_{sc}$ is displayed by the dotted black line in Figure 3.20. The slope at $T_{sc}$ of $H^{a}_{c2}$ is much larger than the one

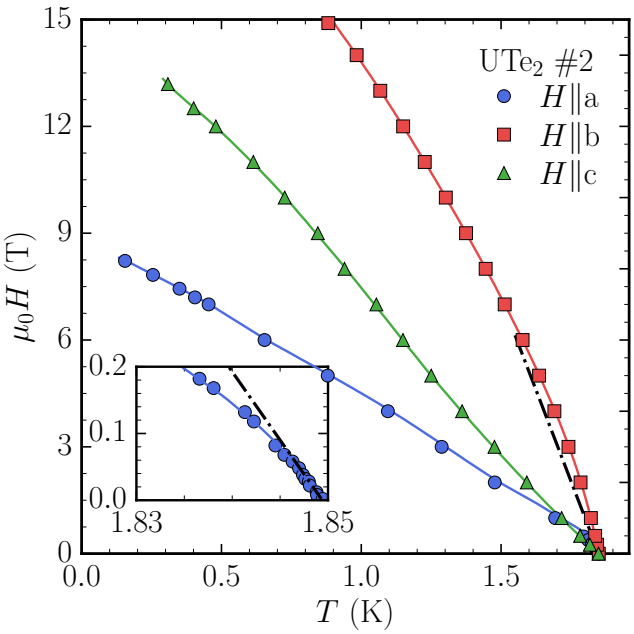


**Fig. 3.20:** $H_{c2}$ *along the three directions determined on sample #2. Plain lines correspond to calculated* $H_{c2}$ *with* $\lambda$ *varying. The dotted black line is the slope at* $T_{sc}$ *of* $H^{a}_{c2}$*. Inset: a zoom at low fields on* $H^{a}_{c2}$*.*

obtained in several resistivity measurements around −5 or −6 T/K [16, 113]. For $H^{b}_{c2}$, the slope at $T_{sc}$ determined by specific heat is also stronger but of the same order than the one determined with resistivity measurements (−25 T/K). The slopes of $H^{a}_{c2}$ and $H^{b}_{c2}$ are well above that of $H^{c}_{c2}$ of −7.5 T/K. Thus the anisotropy of $H_{c2}$ determined from our specific heat measurements is different from the one determined by transport measurements, and is, near $T_{sc}$:$H^{b}_{C2} > H^{a}_{C2} > H^{c}_{C2}$.

Away from the region near $T_{sc}$ we recover the same anisotropy as found with resistivity measurements. This is possible thanks to a strong negative curvature of $H^{a}_{c2}$ at very low fields below 200 mT, $H^{a}_{c2}$ and $H^{c}_{c2}$ end up crossing each other around 1 T. In the inset of Figure 3.20, the slope at $T_{sc}$ is drawn for H‖**a** contrasting with the much smaller slope observed for temperatures a few percent below $T_{sc}$ (for field above 100 mT).

Figure 3.21 present very low-field measurements of $H^{a}_{c2}$ on different samples. To deal with the remanent field of the superconducting coil and measure precisely at low fields we performed measurements with negative fields to determine at what field $T_{sc}$ is maximum. It corresponds to the zero field seen by the sample, so to the inverse of the remanent field. Then $H_{c2}$ just need to be shifted by this remanent field. All the $H^{a}_{c2}$ of the different samples exhibit a strong curvature at low fields. Moreover previous specific heat measurements done by Kittaka et al. [70] showed also a strong curvature. The $H_{c2}$ are shown in Figure 3.22. But this feature is not discussed in this study, and it lacks points at low fields to determine correctly the slope at $T_{sc}$.

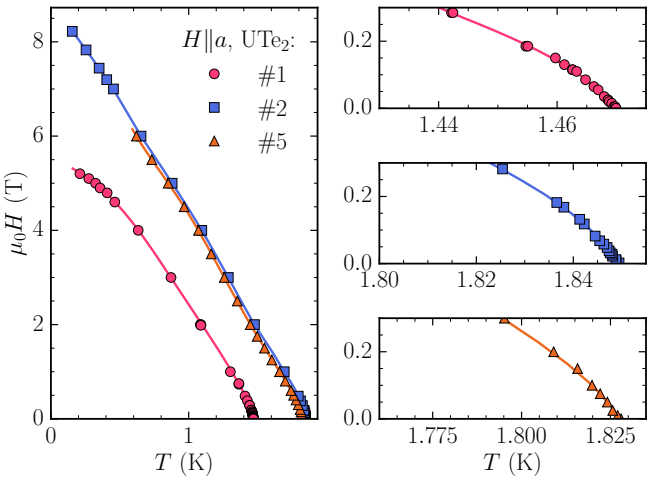


**Fig. 3.21:** *On the left, $H^{a}_{c2}$ for different sample (sample #5 comes from a batch with a $T_{sc}$ of 1.83 K). On the right, zooms on the low fields part for each sample.*

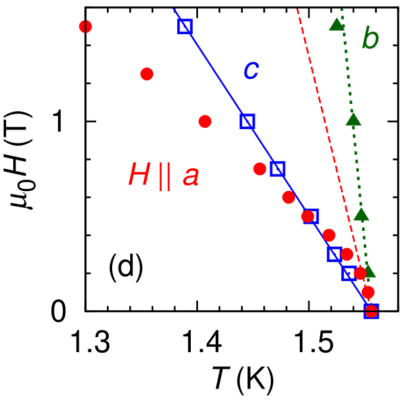


**Fig. 3.22:** *The enlarged view near $T_{sc}$ of $H_{c2}$ along the three directions determined by specific heat measurements in ref [70]. The dashed lines correspond to the slopes at $T_{sc}$.*

More recently, measurements on samples grown with the molten salt technique with a $T_{sc}$ around 2 K also show the same strong curvature of $H^{a}_{c2}$ [57]. So we can safely conclude that all these results confirm that the strong curvature of $H^{a}_{c2}$ is intrinsic to $UTe_2$ and not sample dependent.

The large slope at $T_{sc}$ along the **a** axis compares very well with the lower critical field $H_{c1}$: this will be discuss later in chapter 4.1. At first sight, the strong curvature evokes a strong paramagnetic limitation along the **a** axis. This would contradict the common belief that $UTe_2$ is a p-wave superconductor with a **d**-vector perpendicular to **a** axis. This would also contradicts the NMR measurements showing no Knight-shift along the **a** axis [35]. Furthermore, the paramagnetic limit needed to reproduce the curvature is unreasonable. A gyromagnetic factor g equals to 6.5 is needed in the strong-coupling regime, which is well above the free electrons value of 2.

Another possibility is a decrease of the superconducting coupling constant $\lambda$ when H is applied along the **a** axis. This would lead to a decrease of $H_{c2}$ and be coherent with the scenario where ferromagnetic fluctuations give rise to superconductivity. The precise analysis of $H^{a}_{c2}$ will be presented in the next chapter 4.3.

To conclude on the low fields part of the phase diagram, at first sight $H_{c2}$ along the **b** axis and **c** axis seems to have an usual behaviour. But a more detailed analysis (chapter 4.3) will show, even on these axes, the temperature dependence of $H_{c2}$ is also anomalous, pointing to a superconducting coupling varying with field.

## 3.4 HIGH-FIELD MEASUREMENTS (H > 15 T), H||**b**

All the specific heat measurements above 15 T were performed on the sample #3 of 12.7 µg by ac calorimetry. From 15 T up to 18.5 T the measurements were done in a superconducting magnet with a rotator allowing to align accurately H||**b** and to rotate in the (**b**,**c**) plane. Above 18.5 T up to 36 T, the measurements were done in a resistive magnet allowing to measure in a continuous field.

### 3.4.1 *A second superconducting phase*

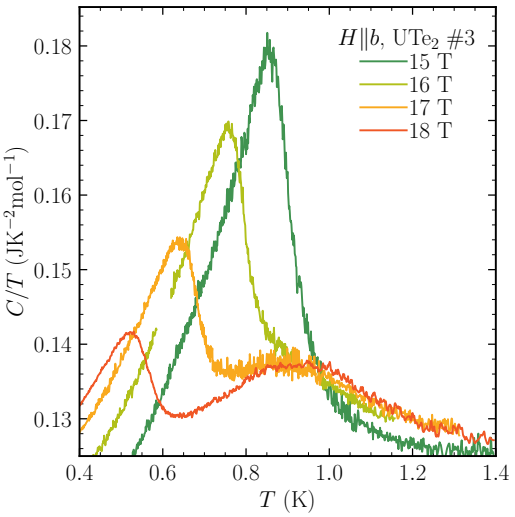


**Fig. 3.23:** C/T *for fields* H||***b*** *where the HF transition emerges (broad anomaly between* 0.8 *K and* 1 *K). Measured on sample* #3.

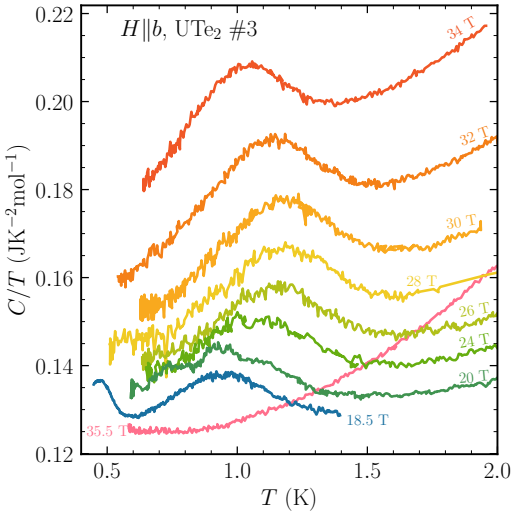


**Fig. 3.24:** *Temperature sweeps for* H||***b*** *up to* 35.5 *T above the metamagnetic transition, to follow the HF transition. Measured on sample* #3.

The surprise of these measurements has been the emergence of a second very broad anomaly above 15 T (350 mK width at 18 T). This specific heat anomaly is shown in Figure 3.23, and corresponds to superconductivity in the high-field region. This has been proved by resistivity and thermal expansion measurements, on the same crystal where sample #3 is cut from [116]. We were expecting a superconducting transition at these fields according to resistivity measurements. However, we did not anticipate such a drastic change of shape of the superconducting transition. And the existence of a transition line separating the low-field phase from the high field-reinforced phase was an open question.

Above 17 T, this second transition is well detached from the sharp superconducting transition, and can be followed up to the metamagnetic transition at $H_m = 34.75$ T (see section 3.5). This broad transition abruptly disappears above $H_m$ as shown in Figure 3.24 showing C/T(T) at different fields. Above $H_m$ in addition to the disappearance of the anomaly, C/T strongly drop (see curve at 35.5 T

in Fig. 3.24). $H_m$ is seen in field sweeps measurements and will be presented after in section 3.5. The critical temperature of this broad anomaly is increasing with field, except very close to $H_m$ (H>30 T) where the transition shifts slightly to lower temperatures. This may be due to a slight misalignment of the sample in the high-field experiments or to the torque at the highest fields inducing a misalignment, but it could also be intrinsic.

The complete phase diagrams for $H\|\mathbf{b}$ is shown in Figure 3.25. Since sample #2 has roughly the same $T_{sc}$ as #3 at zero field, we can use its $H_{c2}$ below 15 T rescaled by the $T_{sc}$ at zero field to complete the phase diagram. The phase diagram shows clearly two superconducting phases, one at Low Field (LF) determined by the sharp transition followed from 0 T, and a second one at High Field (HF) determined by the broad transition emerging at 15 T up to $H_m$ where superconductivity is abruptly suppressed. The $H_{c2}$ points between 15 T and 17 T, where the two transitions merge, are hard to determine for the HF phase. To do so, the jump of the HF transition is fixed since it is roughly constant in field (see after Figure 3.26) below 20 T, to guide the fit and extract a $T_{sc}$ and width for the HF transitions with the same criteria than at higher fields. These points are indicated by empty crosses in Figure 3.25.

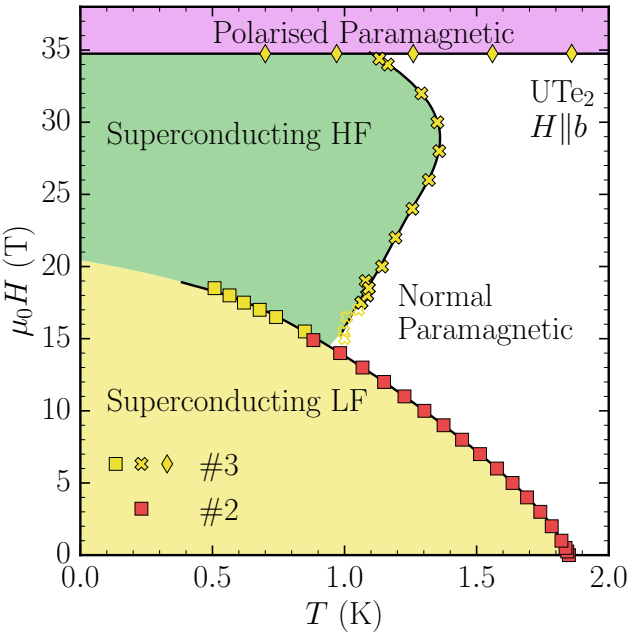


**Fig. 3.25:** *Phase diagram $H\|\boldsymbol{b}$. The squares correspond to the sharp LF transitions. The crosses correspond to the broad HF transitions. The empty crosses are the points determined by fixing the width of the HF transition. The diamonds correspond to $H_m$. The different colours of the points distinguish the two samples used to establish the phase diagram.*

$H_{c2}$ for fields around 15 T raises a first question concerning thermodynamics. The two $H_{c2}$ of the LF and HF phase join at 15 T. However, thermodynamics imposes conditions on the slope of transition lines at a multicritical point. Theoretical

studies have discussed these conditions for $^3$He [80] and $UPt_3$ [142]. Generally, a second order transition line cannot end on another one, the two lines have to cross each other. For $UTe_2$, in our experiment despite intense measurements we do not see a fourth line prolonging the $H_{c2}$ of the HF phase into the LF phase. This might be due to a lack of resolution, the transition becoming too broad and small to be detected below the LF transition. Or the $H_{c2}$ of the HF phase could be tangentially touching the $H_{c2}$ of the LF phase and the lack of resolution near 15 T with the HF transition merging with the LF one, makes it impossible to see it.

A last possibility could be the transition from LF to HF phase is first order, as suspected also for a similar case in $CeRh_2As_2$ [67]. So other thermodynamic probes with better resolution in the 15 T region are needed to settle this problem. The new generation of samples with a $T_{sc}$ of 2 K could be a solution if the HF transition is sharper.

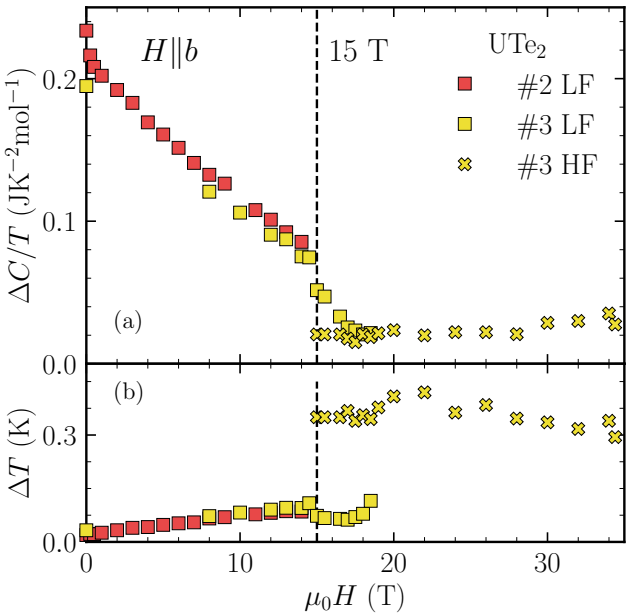


**Fig. 3.26:** *(a) The jump (ΔC/T) at $T_{sc}$ of the LF (squares) and HF (crosses) transitions as a function of field.*
*(b) The widths (ΔT) of the LF (squares) and HF (crosses) transitions as a function of field.*

The Gaussian analysis of the temperature dependence of C/T allows also to deconvolute broadening effects and to determine the jump ΔC/T at $T_{sc}$ and the width of the transition as a function of magnetic field (see chapter 2.1.4 for the model). They are shown in Fig 3.26. The specific heat jump of the LF transition decreases monotonously with field up to 15 T, as expected for a superconducting transition. When the HF transition appears above 15 T, the jump of the LF superconducting transition displays a marked drop seen also in the raw data presented in Appendix A.2. Essentially, it goes down to the same level as the HF transition, which remains roughly constant up to $H_m$ with maybe a very slight increase. As

expected, the emergence of the HF transition goes along with a redistribution of entropy between the two phases, explaining the sudden drop of $\Delta C/T$ of the LF transition around 15 T.

The behaviour of the width $\Delta T$ of the transitions is even more odd. For the LF transition, $\Delta T$ increases monotonously up to 15 T where it suddenly stops with a slight decrease above 15 T. It is not expected that a superconducting transition becomes suddenly sharper when applying field. For the HF transition, $\Delta T$ remains constant with field which is also not expected.

In conclusion, above 15 T the widths and jump of the LF and HF transitions have unusual behaviours, especially the width of the LF transition above 15 T. Also the strong difference of width between the LF and HF transitions is the most important point discussed just below.

### 3.4.2 *Conclusion on the phase diagram $H \| \boldsymbol{b}$*

The main discovery of these measurements is the existence of two different superconducting phases for $H \| \mathbf{b}$. However, it was expected by phenomenological theoretical studies [60, 126], evoking a rotation of the **d**-vector between the two phases in order to overcome the paramagnetic limit due to a finite component of the **d**-vector along **b** axis. Such a change of symmetry induced by the magnetic field at ambient pressure is not unique. Beside superfluid $^3$He, the two other known compounds with different superconducting phases at ambient pressure are $UPt_3$ and $CeRh_2As_2$. In the case of $UPt_3$, which is a spin-triplet superconductor, the symmetry of the order parameter changes between the three superconducting phases at ambient pressure [44, 63]. Figure 3.27 shows the phase diagram determined by ultrasound for field applied perpendicular to the basal plane [2]. The same phases are also found for fields in the basal plane.

For $CeRh_2As_2$, when field is applied perpendicular to the basal plane, the present hypothesis is that it induces a transition between a spin-singlet phase at low field (SC1) and a spin-triplet phase at higher field (SC2) [67]. The phase diagram is shown in Figure 3.28.

For these two examples the superconducting pairing mechanism remains the same between the different phases, and the shape of the specific heat anomaly at the superconducting transitions are similar for the different phases. $CeRh_2As_2$ exhibits an anomalous behaviour of the superconducting transition jump along $H_{c2}$ near the junction of the two phases [124], the jumps suddenly increases as shown in Figure 3.28. But nothing as drastic as $UTe_2$ between the two phases (LF and HF).

This is the real difference between $CeRh_2As_2$, $UPt_3$ and $UTe_2$. For $UTe_2$, there is a drastic change of the specific heat anomaly in the two superconducting transitions (LF sharp and HF broad).Together with the sudden re-enforcement of $H_{c2}$ in the HF phase, this is the sign of a change of coupling mechanism between the LF and HF phases induced by the field. On this aspect $UTe_2$ is unique.

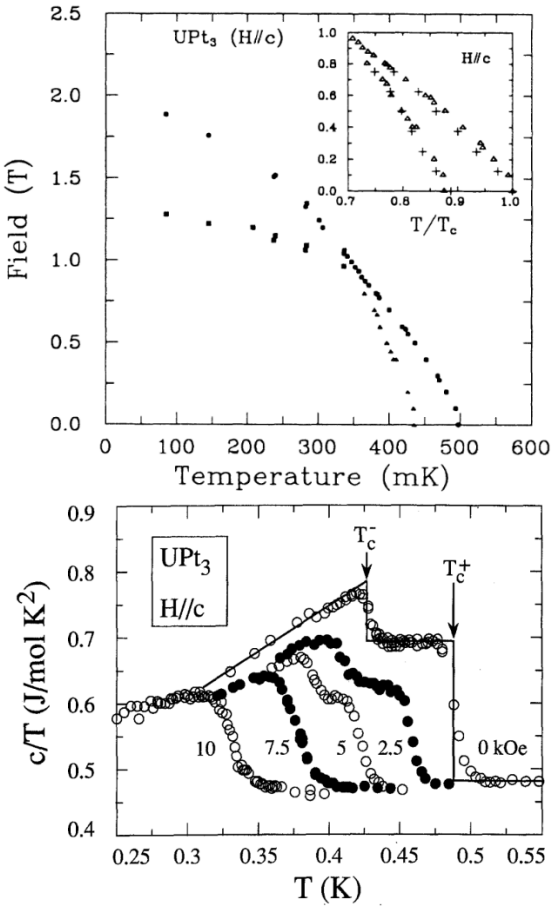


**Fig. 3.27:** *Top panel: Phase diagram of $UPt_3$ for* H‖c *determined by ultrasound measurements in ref [2].*
*Bottom panel: specific heat superconducting transition for* H‖c *from ref [44].*

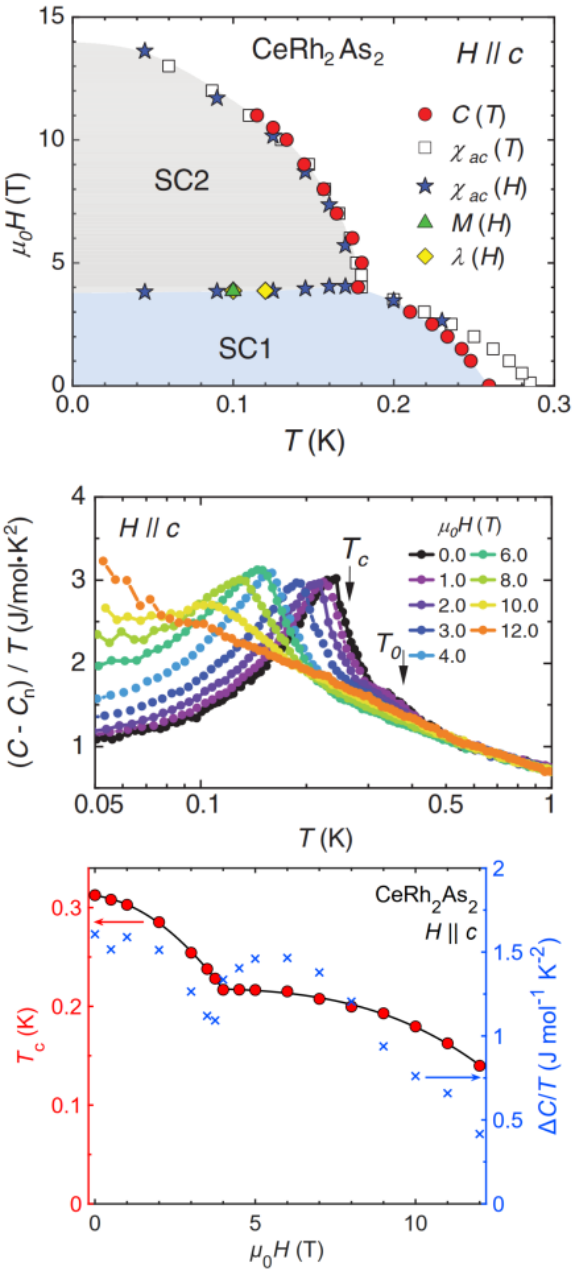


**Fig. 3.28:** *Top panel: Phase diagram of $CeRh_2As_2$ for* H‖c. SC1 *is the spin-singlet phase and* SC2 *the spin-triplet. Ref [67]*
*Middle panel:* C/T *for* H‖c *measured on the sample used to establish the phase diagram above. Ref [67]*
*Bottom panel: Left axis is $H_{c2}$ for* H‖c *established by specific heat measurements. Right axis is the ideal specific heat jump at $T_{sc}$ of the superconducting transition. Ref [124]*

## 3.5 THE METAMAGNETIC TRANSITION

As evoked earlier, there is a metamagnetic transition around 35 T for H||**b** [76, 99, 111]. This has been seen with diverse probes, and specific heat measurements had only been done in pulsed fields until the present work [55].

### 3.5.1 *Specific heat measurements at the metamagnetic transition*

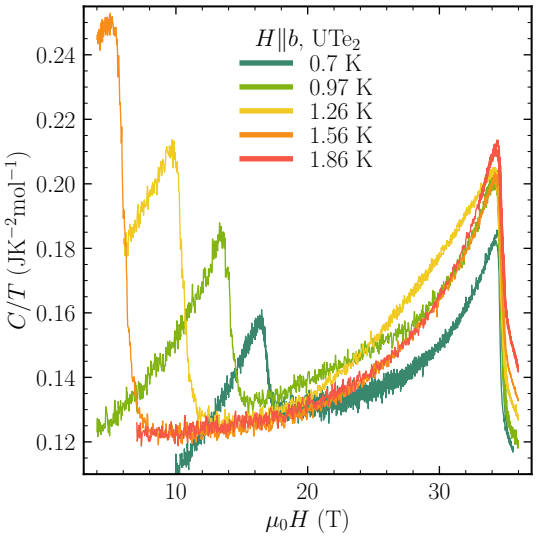


**Fig. 3.29:** *Field sweeps performed at different temperatures* H||***b*** *on sample #3. The sharp anomalies below* 18 *T correspond to the LF transitions. The sharp drops at* 34.7 *T correspond to the metamagnetic transition.*

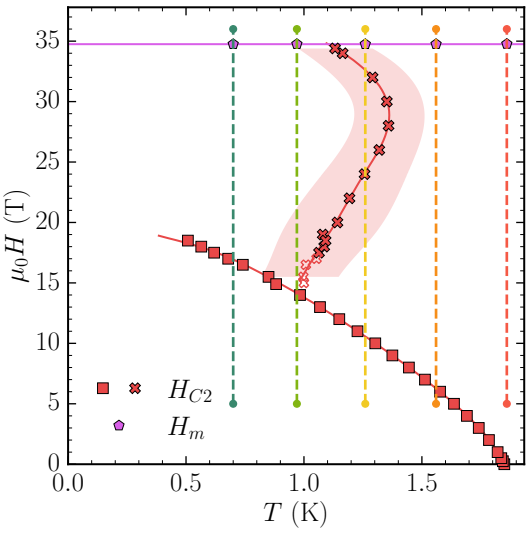


**Fig. 3.30:** $H_{c2}$ *for* H||***b****, with the HF transition width depicted as the shaded area. Dashed lines correspond to all field sweeps performed. Their colours correspond to Figure 3.29.*

To study the metamagnetic transition occurring around 34.75 T, field sweeps were performed up to 36 T. Figure 3.29 shows all the field sweeps we have done. The LF superconducting transitions are sharp with a large jump, making them easy to detect. For the HF transitions, very broad and small anomalies are visible. They are noticeable only by comparing curves at different temperatures. This is due to the broad widths in temperature of the HF transitions in combination with an almost vertical $H_{c2}$. It is shown in Figure 3.30 of the phase diagram for H||**b** with the width of the HF transition depicted by the shaded red area and the fields sweeps performed represented by vertical dashed lines.

Apart from the superconducting transitions, C/T increases up to the metamagnetic transition at $H_m = 34.75$ T where C/T suddenly drops. The drop was also seen in the temperature sweeps measurements (Figure 3.24). This drop is large of the order of 25% of C/T. The transition at $H_m$ is marked both by a clear hysteresis and by a slight broadening of the drop of C/T that can be attributed to a distri-

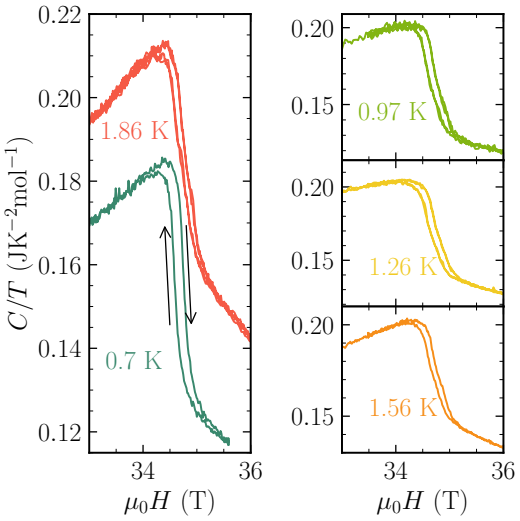


**Fig. 3.31:** *Enlargement on the metamagnetic transition of each field sweeps* H‖***b*** *on sample #3.*

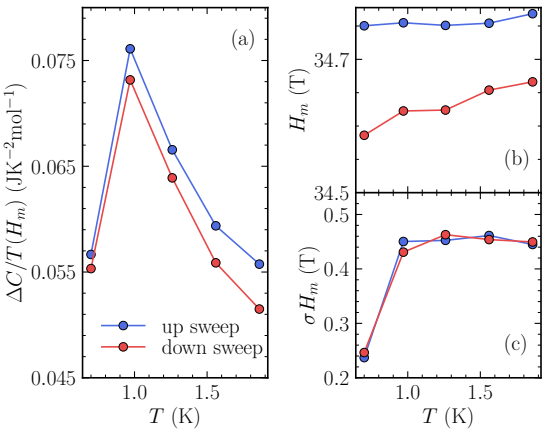


**Fig. 3.32:** *(a) Jump (drop) of* C/T *at* $H_m$*, (b)* $H_m$ *and (c) width at half-height (2.35*σ*) of the transitions as a function of the temperature, for the up and down sweeps.*

bution of $H_m$ of 1.4%. This distribution of $H_m$ possibly comes from the strong sensitivity of $H_m$ to pressure or most likely to stress.

The hysteresis had also been seen in resistivity measurements [76]. We could checked that the hysteresis did not depend on the field sweep rate by varying it between ±350 and ±50 Gauss/sec. Figure 3.31 shows an enlargement on each hysteresis. The sweeps at 1.86 K and 0.97 K have been done with two sweep rates, and we clearly see no difference for the hysteresis and drop of C/T.

At these sweep rate, we also did not detect any magnetocaloric effect. By contrast, a study in pulsed field of the magnetocaloric effect does show a clear signature at $H_m$ [123]. The reason we did not detect anything is maybe the difference of sweep rate, and a much better thermalisation of our very small sample.

A model similar to the one used for the superconducting transition, with a Gaussian distribution of $H_m$, is used to extract the width, the drop, and $H_m$ from the hysteresis. The parameters obtained are displayed in Figure 3.32. $H_m$ for the up sweeps is essentially constant between 700 mK and 2 K, while for the down sweeps, $H_m$ slightly increases with the temperature (of ~ 0.2%).

The $H_m$ value determined by specific heat is slightly above the one obtained by resistivity measurements. This is probably due to a small misalignment of the sample in the specific heat measurements, which could explain also the downward curvature of $H_{c2}$ above 25 T (Figure 3.25). This angle dependence of $H_m$ and $H_{c2}$ is known from the resistivity measurements done at high fields [76, 112], as said in the introduction section 1.3.2 the HF phase is sensitive to misalignment for H‖**b** ($H_{c2}$ is suppressed), and $H_m$ increases.

The width of the transition at $H_m$ increases abruptly from 0.24 T to 0.45 T (~ 1.7%) between 0.7 K and 0.97 K, and then stays constant with temperature.

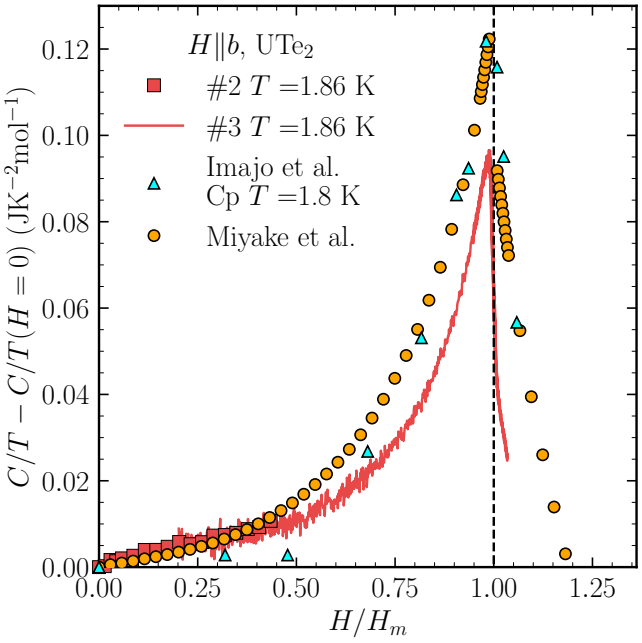


**Fig. 3.33:** *Cyan triangles: specific heat measurements done in pulsed fields in ref [55]. Orange circles:* $\gamma(H) - \gamma(H = 0)$ *determined from the magnetisation measurements through thermodynamic relations in ref [99]. Red squares and line: our* C/T *measurements.*

The drop of the specific heat at $H_m$ is sharpest at the lowest temperature (700 mK) with a width of 0.25 T, then increases abruptly at 0.97 K and decreases above this temperature. However, a possible interplay between the superconducting and metamagnetic transitions at 0.7 K may influence the shape of the anomaly.

We can push further the comparison with different measurements. Figure 3.33 shows the comparison of $C/T - C/T(H = 0)$ near $T = 1.8$ K, in the normal phase, for field along the **b** axis determined from our experiment performed on samples #3 and #2, and experiments performed in pulsed fields. First, ref [55] reports specific heat experiments in highly stabilised fields, using the long pulsed fields facility at ISSP. Second, [99] reports magnetisation measurements. In this study, the Sommerfeld coefficient $\gamma$ has been determined from $M(T)$ using Maxwell's relation for $H \neq H_m$ as $\frac{\partial \gamma}{\partial H}\Big|_T = \frac{\partial^2 M}{\partial T^2}\Big|_H$, and using the Clausius-Clapeyron relation for the first order transition: $\frac{\mu_0 dH_m}{dT} = \frac{-\Delta S}{\Delta M}$ to get the jump $\Delta\gamma = \Delta S/T$ at $H_m$. This analysis indicates a discontinuous jump of $\Delta\gamma = -30 mJK^{-2}mol^{-1}$ at $H_m$, which is lower than the one measured in the specific heat experiment. However, across $H_m$ $\Delta\gamma$ is equal to $\Delta\frac{\partial S}{\partial T}$, which mathematically can be quite different from $\frac{\Delta S}{T}$. Despite some quantitative differences (e.g. the absolute variation of $C/T(H) - C/T(H = 0)$ is larger in both pulsed fields experiments) the general behaviour is similar: an increase with H when approaching $H_m$ and a drop at $H_m$ followed by a strong decrease. A similar field dependence has been observed for the A coefficient of the electrical resistivity, except that the jump at $H_m$ depends on the injection current direction, which is something not yet understood [133].

### 3.5.2 *Discussion about* $H_m$

An important issue regarding this metamagnetic transition, especially for the discussion of the pairing mechanism in the HF phase, is the nature of the magnetic correlations associated with $H_m$. The question is still open today since inelastic neutron experiments at such high fields are still unavailable. If the metamagnetic transition would occur along the easy magnetisation axis like in UCoAl [12], the fluctuations would most likely be ferromagnetic, but it appears along the hard magnetisation axis in $UTe_2$.

Other criteria like the value of the Wilson ratio claims to support ferromagnetic fluctuations at low fields due to its large value [138]. Nevertheless, it is of no help close to $H_m$: calculating this ratio when approaching $H_m$ from raw data is questionable in such a complex multi-band system with local moment contributions. Moreover, this calculation would lead to much smaller values along the **b** axis than along the **a** axis at low fields: the susceptibility $\partial M/\partial H$, is at least six times smaller for $H\|\mathbf{b}$ than for $H\|\mathbf{a}$, and the specific heat increases almost by a factor 2 between zero field and $H_m$, suppressing the Wilson ratio deduced for $H\|\mathbf{a}$ by at least a factor 10.

Arguments for antiferromagnetic fluctuations exist but are not solid: inelastic neutron measurements at low fields have found predominant antiferromagnetic fluctuations [28][73]. But it tells nothing on the fluctuations which might emerge on approaching $H_m$. It is worth noting that the scaling relation found in many antiferromagnetic systems between the temperature of the maximum of the susceptibility $T_{\chi,max}$ (35 K) and the value of $H_m$ ($33-35$ T) is well obeyed in $UTe_2$ (see ref [9]for the scaling relation).

## 3.6 FIELD ANGLE MEASUREMENTS

On sample #3, ac specific heat measurements were done in a superconducting coil below 18.5 T with a larger radius than the resistive coils. It allows to add a piezoelectric rotator to align the sample in the field, but also to measure with different angles in the (**b**,**c**) plane to determine the angle dependence of the superconducting transitions (HF and LF).

The field was fixed at several values and C/T was measured for different angles. Figure 3.34 show C/T at 18.5 T for different angles in the (**b**,**c**) plane. When the field is tilted away from the **b** axis, the LF transition is shifted toward low temperature like the HF transition. However, the HF transition seems to be more sensitive to the angle, and its jump decreases with the field being tilted.

The other possible measurement is to fix the angle and to do temperature sweeps for different fields. An example at 10° is shown in Figure 3.35. With these measurements we can established a part of the phase diagram for a certain angle in the (**b**,**c**) plane. Figure 3.36 shows $H_{c2}$ for $H\|\mathbf{b}$ and for an angle of 10° and 15° in the (**b**,**c**) plane. Clearly the HF phase is more sensitive to the field direction than

the LF phase. This is in agreement with the resistive measurements showing a fast suppression of the HF phase when the field is tilted away from the **b** axis [76].

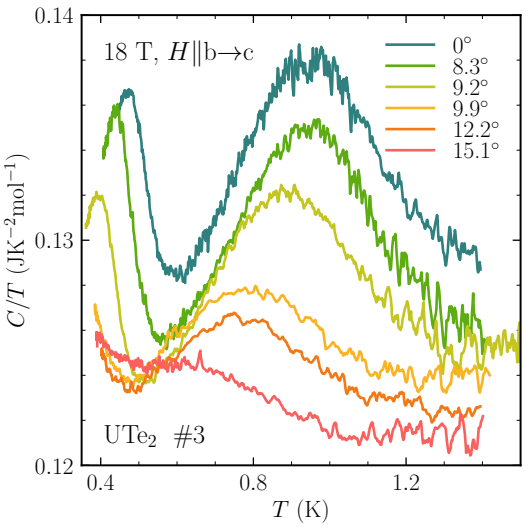


**Fig. 3.34:** C/T *measurements done at* 18.5 *T for different angles in the (**b**,**c**) plane.*

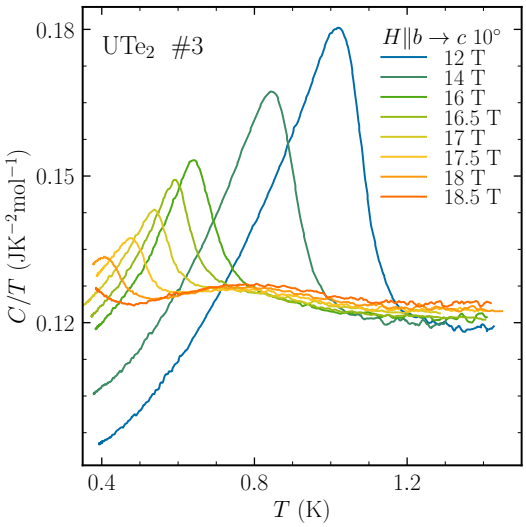


**Fig. 3.35:** C/T *measurements done at* 10° *in the (**b**,**c**) plane for different fields.*

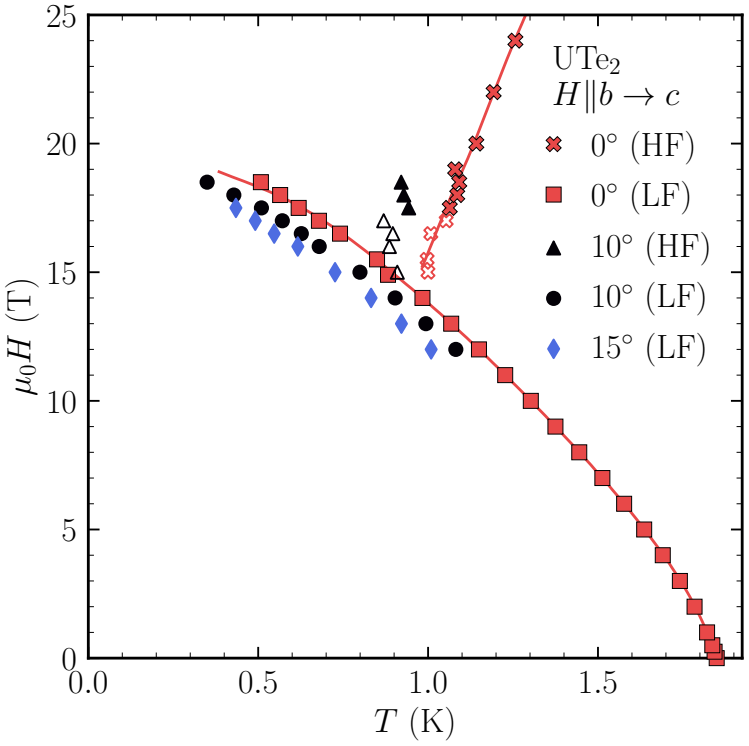


**Fig. 3.36:** *Phase diagram* H||***b*** *and for field tilted* 10° *and* 15° *toward* ***c*** *axis deduced from ac and quasi adiabatic measurements. The empty symbols correspond to* $T_{sc}$ *determined by fixing the HF transition width.*

# 4

# ANALYSIS OF THE RESULTS ON $UTe_2$

In this chapter, the analysis performed on $H_{c2}$ are presented.

$H_{c2}$ is analysed in order to explain the reinforcement seen in the HF phase. We will discuss a field dependent pairing strength as encountered in the ferromagnetic superconductors [8].

However, to put constraints on this model, we will examine first the very low-field behaviour and compare $H_{c2}$ and $H_{c1}$ [106].

## 4.1 COMPARISON OF $H_{c2}$ WITH $H_{c1}$ NEAR $T_{sc}$.

As said earlier (chapter 3.3) near $T_{sc}$ the anisotropy of $H_{c2}$ found with the specific heat measurements is different from the one found by resistivity. The latter was in disagreement with the measurements of $H_{c1}$ [106]. With the anisotropy revised a re-analysis of $H_{c1}$ is needed. In the Ginzburg Landau regime, meaning near $T_{sc}$, the anisotropy of $H_{c1}$ is inverse to the one of $H_{c2}$. In this regime, $H_{c1}$ and $H_{c2}$ are related to each other through the equations:

$$H_{c1} = \frac{H_c}{\sqrt{2}}(\ln(\kappa) + 0.49) \tag{4.1}$$

and

$$H_{c2} = \sqrt{2}\kappa H_c \tag{4.2}$$

In these equations, $H_c$ is the thermodynamic critical field and $\kappa$ the Ginzburg Landau parameter equals to the penetration length divided by the coherence length.

$UTe_2$ is a multi-band superconductor, so even $H_{c1}$ does not necessarily satisfy equation 4.1 at low temperatures. But, close to $T_{sc}$ the Ginzburg Landau equations should still be valid. Thus, the slopes of $H_{c1}$, $H_{c2}$ and $H_c$ should satisfy equations 4.1 and 4.2.

The slope of the thermodynamic field $\frac{dH_c}{dT_{sc}}$ can be determined by a double integration of the superconducting transition at 0 T. Indeed, by definition $H_C^2(T) = 2\mu_0 \int_T^{T_{sc}} (S_n - S_{sc})dT$ where $S_n$ and $S_{sc}$ correspond to the entropy of the normal phase and the superconducting phase respectively. For sample #2, $\frac{dH_c}{dT_{sc}} = 0.059$ T/K.

Then with equation 4.1 and $\frac{dH_{c1}}{dT_{sc}}$ extracted from measurements in ref [106] (Figure 4.1) we determine $\kappa$. Finally, with equation 4.2 we calculate the corresponding

| | $\frac{dH_{c1}}{dT_{sc}}$ (T/K) | κ | $\frac{dH_{c2}}{dT_{sc}}$ (T/K) | $\frac{dH_{c2}}{dT_{sc}}$ (T/K) rescaled | $\frac{dH_{c2}}{dT_{sc}}$ (T/K) #2 |
|---|---|---|---|---|---|
| H‖**a** | −0.00113 | 202.683 | −16.052 | −20.480 | −20 |
| H‖**b** | −0.00227 | 86.482 | −6.849 | −8.738 | −34.5 |
| H‖**c** | −0.00252 | 75.838 | −6.006 | −7.663 | −7.5 |

**Table 4.1:** *Table summarising the different parameters of the comparison of $H_{c2}$ sample #2 and $H_{c1}$ from ref [106] for the three axes. $\frac{dH_{c1}}{dT_{sc}}$ is extracted from the measurements ref [106], κ and $\frac{dH_{c2}}{dT_{sc}}$ are determined from it. The fourth column is $\frac{dH_{c2}}{dT_{sc}}$ rescaled by the ratio of $T_{sc}$ of sample #2 and the sample of ref [106]. Last column is $\frac{dH_{c2}}{dT_{sc}}$ extracted from the specific heat measurements on sample #2.*

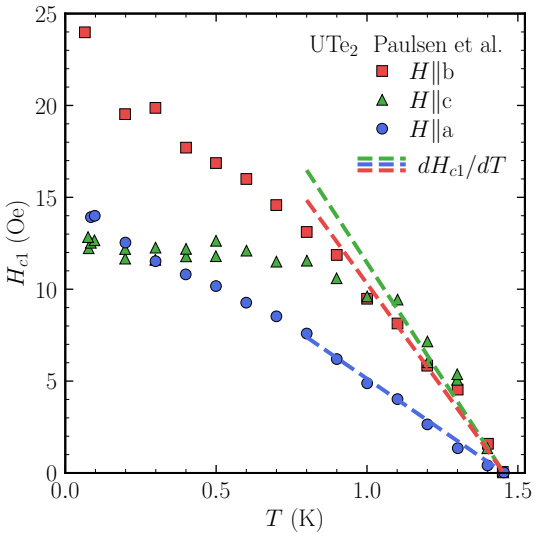


**Fig. 4.1:** $H_{c1}$ *from ref [106]. The dashed lines correspond to* $\frac{dH_{c1}}{dT_{sc}}$ *near* $T_{sc}$.

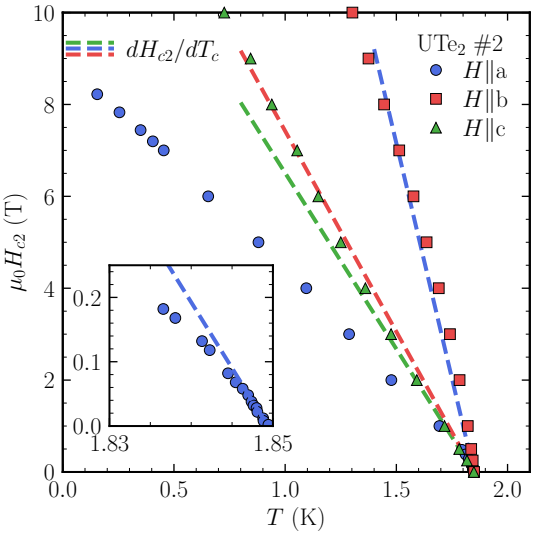


**Fig. 4.2:** $H_{c2}$ *measured on sample #2. The dashed lines correspond to* $\frac{dH_{c2}}{dT_{sc}}$ *determined from* $\frac{dH_{c1}}{dT_{sc}}$ *Fig 4.1. The inset shows a enlargement at low fields for* H‖***a***.

$\frac{dH_{c2}}{dT_{sc}}$. These $\frac{dH_{c1}}{dT_{sc}}$ are from measurements on a crystal with a $T_{sc}$ of 1.5 K at 0 T, so we rescaled the obtained $\frac{dH_{c2}}{dT_{sc}}$ by the ratio of the $T_{sc}$ for samples #2. All the parameter are displayed in table 4.1.

Figure 4.2 shows $H_{c2}$ of sample #2 with the $\frac{dH_{c2}}{dT_{sc}}$ calculated from $H_{c1}$. The slopes calculated at $T_{sc}$ along the **a** and **c** axes do correspond to those measured. However, along the **b** axis, the slope measured is much stronger than the one calculated.

This confirms that the large slope of $H_{c2}^{\mathbf{a}}$ measured with our specific heat measurements very close to $T_{sc}$ is not an artefact. Accordingly, the strong curvature below 0.2 T is also confirmed.

However, this discrepancy of $H_{c2}^{\mathbf{b}}$ and $\frac{dH_{c2}^{b}}{dT_{sc}}$ shows that $H_{c2}^{\mathbf{b}}$ is enhanced already at very low fields, so that the slope measured is larger than $\frac{dH_{c2}^{b}}{dT_{sc}}$ determined from $H_{c1}$. Such a change of slope of $H_{c2}$ requires that $d\lambda^{b}(H)/dH > 0$ at $T_{sc}$. So for the

oncoming calculation of $H_{c2}$ we will use the $\frac{dH^b_{c2}}{dT_{sc}}$ determined from $H_{c1}$ since these measurements were done at very low fields ($H < 20$ Oe) where the effect of the coupling varying with field is negligible.

All these analysis are also applicable to sample #1 and lead to the same conclusion than for sample #2. However, sample #1 exhibits an upturn of $C/T$ at low temperature due to extrinsic contributions, so we cannot determines $\frac{dH_c}{dT_{sc}}$. The solution is simply to rescale $\frac{dH_c}{dT_{sc}}$ obtained on sample #2 by the ratio of their $T_{sc}$.

Recently, a similar study with a comparison of $H_{c1}$ and $H_{c2}$ has been done on the generation of sample with a $T_{sc}$ around 2 K [57]. The conclusion is the same.

## 4.2 CALCULATION OF $H_{c2}$

In this section the model and the procedure used to reproduce the $H_{c2}$ and to extract $\lambda(H)$ is presented.

### 4.2.1 *Model used to determine $\lambda(H)$.*

To reproduce $H_{c2}$, a model for strong coupling superconductors is used. This model is fully described in ref [22]. The inclusion of the paramagnetic limit to this model is detailed in ref [134]. In the following, only the basic equations will be presented. This model is derived from the Eliashberg theory for electron-phonon interaction in s-wave superconductors. We believe that it remains relevant for the estimation of strong-coupling effects on $H_{c2}$ in unconventional superconductors. Today, no model for the critical field of unconventional superconductors has been yet established in the strong-coupling regime. A simplified form of the Eliashberg interaction is used. However, it captures the most important properties of the strong coupling regime: the renormalisation of the Fermi velocity and the pair-breaking effects due to the presence of thermal phonons (thermal magnetic fluctuations in our case) close to $T_{sc}$ when the strong coupling constant $\lambda$ gets large. The spectral density of interactions is taken as a delta function, as for an Einstein spectrum:

$$\alpha^2 F(\omega) = \left(\frac{\lambda\Omega}{2}\right)\delta(\omega - \Omega) \tag{4.3}$$

Where $\omega$ is the frequency, $\Omega$ is the characteristic energy of the interaction and $\lambda$ the strong coupling constant. $H_{c2}$ is then determined by solving the system of self-consistent equations:

$$\Delta(i\tilde{\omega}_n) = \left(\frac{\pi T}{\Omega}\right)\sum_{|\omega_m|<\omega_c}(\lambda(\omega_n - \omega_m) - \mu^*)\chi(\tilde{\omega}_m)\Delta(i\tilde{\omega}_m) \tag{4.4}$$

Where $\omega_n = \pi T(2n+1)$ are the Matsubara frequencies, $\mu^*$ is the screened Coulomb pseudo potential and $\omega_c$ is a frequency cut-off (8 to 10 times $\Omega$). $\tilde{\omega}_m$ is defined as:

$$\tilde{\omega}_n = \omega_n + \pi T \sum_m \lambda(\omega_n - \omega_m) sgn(\omega_n)$$
$$\lambda(\omega_n - \omega_m) = \frac{\lambda\Omega^2}{\Omega^2 + (\omega_n - \omega_m)^2} \tag{4.5}$$

The function $\chi(\tilde{\omega}_n)$ in eq.4.4 contains the effects of the magnetic field B on the gap equations due to the orbital and paramagnetic effects:

$$\chi(\tilde{\omega}_n) = \int_0^\infty dx \frac{\beta exp(-\beta x)}{\sqrt{\tilde{Q}^2 + x}} tan^{-1}\left(\frac{\sqrt{\tilde{Q}^2 + x}}{\frac{|\tilde{\omega}_n| + ig\mu_B B/2 sgn(\tilde{\omega}_n)}{\Omega}}\right) \tag{4.6}$$

Here $\beta = \frac{2\Omega^2}{\hbar e B (\bar{v}_F^{bare})^2}$ parametrises the orbital effect: $\bar{v}_F^{bare}$ is a bare average Fermi velocity, meaning a Fermi velocity without renormalisation by the pairing interaction, perpendicular to the applied magnetic field. The paramagnetic limit is parametrised by the gyromagnetic factor g in the direction of the applied field. $\tilde{Q} = \frac{\hbar \bar{v}_F^{bare} Q}{2\Omega}$ is the dimensionless amplitude of the (potential) FFLO wave vector, which has to be taken into account for a dominant paramagnetic limit. Hence for non zero g, the system of equations 4.4 has to be solved (with the usual techniques of linear algebra) optimising the solution with respect to Q for maximum $H_{c2}$. In the case of a dominant paramagnetic limitation, a finite Q marking the entrance in the FFLO state can be found for temperatures below $0.55T_{sc}$. If g is fixed at zero, we are in the case where the Zeeman splitting is inexistent. It corresponds to case where the field is along the quantisation axis of an ESP state of a spin-triplet superconductor.

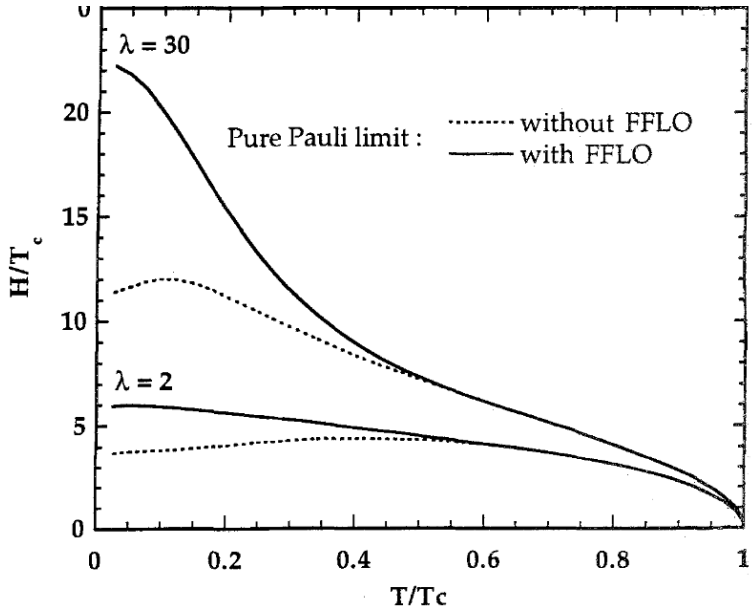


**Fig. 4.3:** *Critical field calculations with the same strong-coupling model used for the analysis of $UTe_2$. Ref [134].*

One last remark about this FFLO wave vector. Strictly speaking there is not necessarily a FFLO phase. At low temperatures when paramagnetic limit is dominant the transition also becomes first order, which is more complex to calculate than a second order transition. It would result in a decreasing $H_{c2}$, as shown in Figure 4.3 from ref [134], which is unphysical. When adding the FFLO modulation, the correct form of $H_{c2}$ is recovered and the difference between the second order transition of FFLO and the first order transition is in any case very small.

Even though this model for the critical field is meant for electron-phonon interaction, the main features should remain correct for other types of interactions as long as $\Omega$ is lower than $E_F$.

The last parameters of the model is $\mu^*$. In general, the value is found between 0.1 and 0.15. But a precise calculation of $\mu^*$ is a real challenge even for conventional superconductors. The precise value of $\mu^*$ has little influence on the physics and in the following analysis we will keep arbitrary the value at 0.1.

### 4.2.2 *Procedure to model $H_{c2}$ and to determine $\lambda(H)$*

In our model, $T_{sc}/\Omega$ is a function of $\lambda(H=0)$ and $\mu^*$. With $\mu^* = 0.1$, we have two parameters $\Omega$ and $\lambda(H=0)$ to adjust $T_{sc}$. In the case of weak coupling ($\lambda < 0.8$), $T_{sc}$ is proportional to $\Omega$ as:

$$T_{sc} \sim \Omega \exp\left(-\frac{1}{\lambda(H=0) - \mu^*}\right) \tag{4.7}$$

For the strong coupling case there is no analytic formula, the relation is more complex, but the ratio of $T_{sc}$ with $\Omega$ is still proportional to a function of $\lambda(H=0)$ and $\mu^*$. For $UTe_2$, which is in the strong-coupling regime ($\Delta C/C$ large at $T_{sc}$), we choose to fix $\lambda(H=0) = 1$.

Once $\Omega$ is determined, the second step is to adjust $v_F$ to match the experimental slope of $H_{c2}$ at $T_{sc}$.

At last, the gyromagnetic factor $g$ controls the paramagnetic limitation. With $g = 0$, there is no paramagnetic limitation and it mimics the case of an ESP. If $g = 2$ (free electron value) there is a full paramagnetic limitation as for a spin-singlet superconductors with no spin-orbit coupling.

A calculation done properly for a spin-triplet superconductor would mainly introduce two effects: a different relation between the slope at $T_{sc}$ and $v_F$, with an additional anisotropy arising from an angular average of the superconducting order parameter; and an anisotropic paramagnetic limitation depending on the **d**-vector orientation.

To go a step further and determine $\lambda(H)$, we used the parameters determined previously ($\Omega$ and $v_F$) and we map the phase diagram of $H_{c2}$ with different $\lambda$ values. Then at fixed field we extract the $\lambda$ corresponding to the experimental $H_{c2}$.

As shown by equation 4.7, a variation of $\lambda$ has a dominant effect on the change of $T_{sc}$, and this remains true in the strong-coupling regime. $\mu^*$ could also have

an influence, but it is controlled by "high energy physics", thus not expected to change with field even at 35 T.

Figure 4.4 shows an example of such a mapping for $H_{c2}^{\mathbf{b}}$ on $UTe_2$, with $g = 2$ and $g = 0$. It also highlights the effect of saturation of $H_{c2}$ due to the paramagnetic limit. In the case of $\lambda = 1.3$ and $g = 2$ (paramagnetic limitation) the value of $H_{c2}$ when $T \to 0$ K is more than 3 times inferior to the one for $g = 0$ (no paramagnetic limitation).

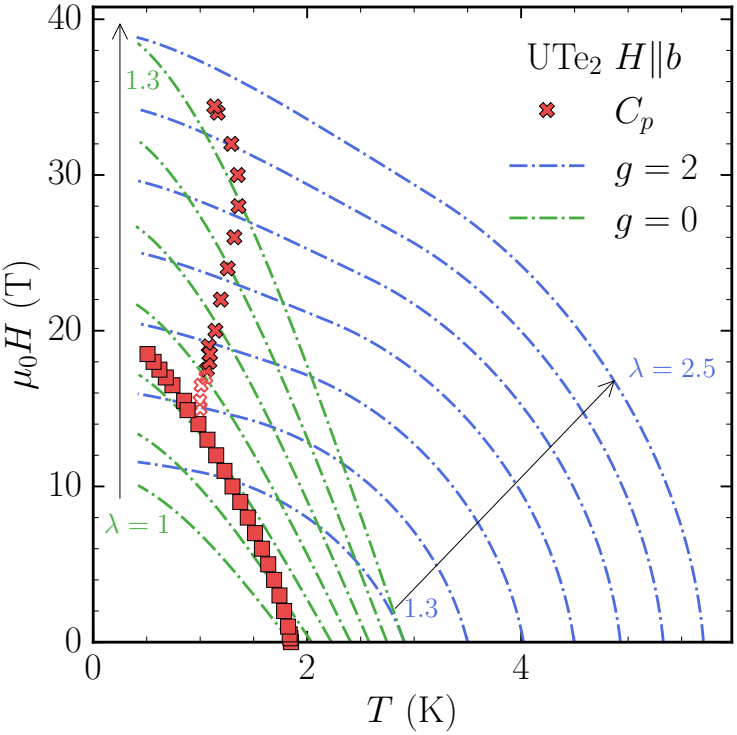


**Fig. 4.4:** *Phase diagram of $UTe_2$ $H \| \boldsymbol{b}$ (red crosses). The dash-dotted lines corresponds to the $H_{c2}$ calculated for several $\lambda$. The colours of the lines differentiate the calculation with $g = 0$ and $g = 1$.*

## 4.3 ANALYSIS OF $H_{c2}$ IN THE LF PHASE.

In this section we are going to analyse $H_{c2}$ with the strong coupling model presented earlier, so as to explore whether or not the superconducting coupling is field dependant.

### 4.3.1 *Fit with a constant $\lambda$.*

Before invoking a coupling constant varying with field, let us try to reproduce $H_{c2}$ for the three axes with a conventional temperature dependence at constant $\lambda$. The value of $\Omega$ is 28.4 K for $T_{sc} = 1.86$ K and $\lambda = 1$. The best fits are shown in Figure 4.5. To reproduce the strong curvature of $H_{c2}^{\mathbf{a}}$, a $g$ factor of 6.5 is needed, which is

unrealistic. Furthermore, it only reproduces correctly the strong curvature at low fields and fails for fields above 1.5 T.

If we want to stick to this common belief that $UTe_2$ is p-wave with the **d**-vector perpendicular to **a** axis, g should be taken to zero along this axis in our calculation. In Figure 4.5 the blue dash-dotted line corresponds to the calculation with $g = 0$, and it is clear that it does not fit except at very low fields (0.2 T), which are not visible in the figure.

For the **b** axis, there is also some curvature at low fields, and the best fits require a value of $g = 0.8$. But the calculated $H_{c2}$ is then saturating too fast above 7 T, its curvature is too strong. For the **c** axis, above 4 T the calculation even with $g = 0$ does not match the experimental $H_{c2}$: it is pointing to an unusual positive curvature of $H_{c2}$.

So, a model where the coupling is constant with the field fails to explain $H_{c2}$ along the three directions, specifically along the **a** axis where the strong curvature at very low fields ($H < 0.2$ T) is hard to reproduce, and of course along the **b** axis.

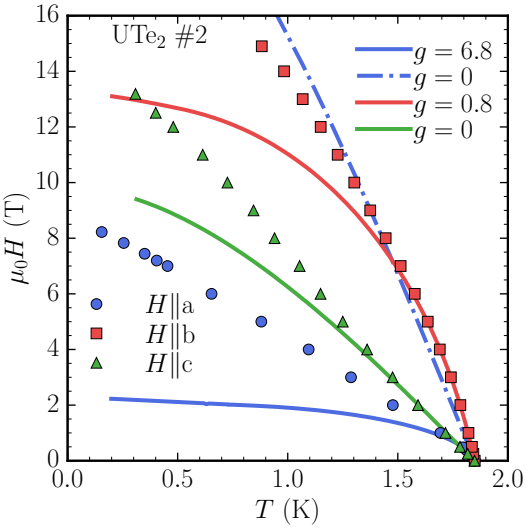


**Fig. 4.5:** $H_{c2}$ *of* $UTe_2$ *of the LF phase. The lines correspond to calculated* $H_{c2}$ *with* $\lambda = 1$ *and different* g *depending on the axis.*

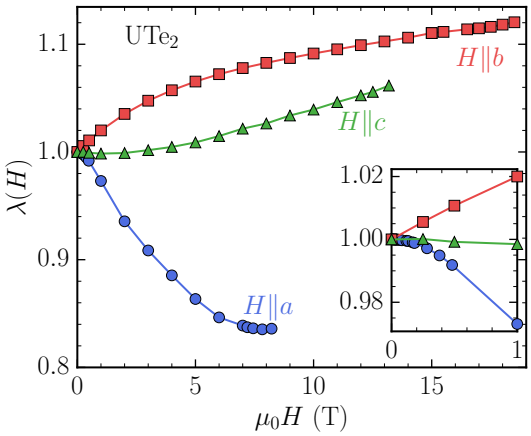


**Fig. 4.6:** $\lambda$ *as a function of* H *for the LF phase. Inset: enlargement of fields below* 1 *T.*

### 4.3.2 *Fit with a variable* $\lambda$.

A solution to reproduce the experimental behaviour of $H_{c2}$ is to let $\lambda$ vary with field.

Taking into account the NMR results [101], we assumed a negligible paramagnetic limit in the three directions by fixing $g = 0$. Another assumption is that $v_F$ is not modified by field, or at least not enough to influence $H_{c2}$ more than the variation of $\lambda$. The last assumption is that the $\Omega$ is independent of the field, as its potential variations would have much less effects than the variation of $\lambda$.

For the Fermi velocities, we took those that would give a $\frac{dH_{c2}}{dT_{sc}}$ as deduced from the comparison with $H_{c1}$. Thus, we took a $v_F$ for $H\|\mathbf{b}$ close to the value for $H\|\mathbf{c}$, imposing that the difference with the measured value arises from the field dependence of $\lambda$.

The $\lambda(H)$ obtained are displayed in Figure 4.6. As expected, $\lambda$ increases since zero field $H\|\mathbf{b}$ and keep increasing monotonously up to 15 T. For $H\|\mathbf{c}$, $\lambda$ is constant up to 2 T and then slightly increases. For $H\|\mathbf{a}$, $\lambda$ is strongly suppressed between $T_{sc}$ and $T \to 0$ K, by 20%. However, very close to $T_{sc}$ it is constant, which is a direct consequence from our choice of matching $\frac{dH_{c2}}{dT_{sc}}$ at constant $\lambda$ with the values deduced from $H_{c1}$.

This anisotropy of the superconducting coupling, ie a decreases for the field applied along the easy magnetisation axis and an increase along the perpendicular axes, corresponds to the one expected for a coupling driven by ferromagnetic fluctuations as presented for UCoGe in section 1.2.1. Especially for field along the easy magnetisation axis ($H\|\mathbf{a}$) it is expected that $\frac{d\lambda}{dH} \propto M_z \frac{\partial M_z}{\partial H}$ near $T_{sc}$, where $M_z$ is the magnetisation along the easy axis. So for a paramagnetic superconductor like $UTe_2$, at $H = 0$: $\frac{d\lambda}{dH} = 0$.

Thus, this LF phase might arise from ferromagnetic fluctuation as proposed in the very early studies.

Before discussing the HF phase, it is worth to precise what is the $v_F$ used in the model to calculate the $H_{c2}$. The $v_F$ we are adjusting to match the measured initial slopes of $H_{c2}$ are a bare average Fermi velocity for field along an axis i: $\bar{v}_F^{bare,i}$. These are the average Fermi velocity renormalised by all the interaction except the interaction driving superconductivity. The effective Fermi velocity controlling the orbital limit and so $\frac{dH_{c2}}{dT_{sc}}$ (at fixed $\lambda$) is renormalised by the superconducting interaction as $\bar{v}_F^i = \frac{\bar{v}_F^{bare,i}}{1+\lambda}$. If $\lambda$ is field dependent, this effective Fermi velocity $\bar{v}_F^i$ is also field dependent. Knowing the different $\bar{v}_F^i$, we can calculate the Fermi velocity along each i-axis: $v_F^i$, through $v_F^i = \frac{\bar{v}_F^j \bar{v}_F^k}{\bar{v}_F^i}$, where j and k are the axes perpendicular to i axis. The $v_F^i$ for $UTe_2$ are displayed in Table 4.2. The anisotropy of the $v_F^i$ (a larger velocity along the **a** axis than along the other axes) is in rough agreement with the transport measurements [32].

However, the $v_F^i$ controlling $H_{c2}$ are an average over the Fermi sheets weighted by the interaction strength and the superconducting order parameter. A comparison with the normal state transport, or determinations from quantum oscillations measurements is not straightforward.

| | $\overline{v}_F^i(H=0)$ (m/s) | $\overline{\xi}_0^i$ (Å) | | $v_F^i(H=0)$ (m/s) | $\xi_0^i$ (Å) |
|---|---|---|---|---|---|
| H‖**a** | 5400 | 40 | **a** axis | 14400 | 106 |
| H‖**b** | 8600 | 64 | **b** axis | 5680 | 42 |
| H‖**c** | 9044 | 62 | **c** axis | 5130 | 38 |

**Table 4.2:** *Table summarising: the values* $\overline{v}_F^i(H=0)$ *used in the fit for field along each axes and then the corresponding coherence lengths* $\overline{\xi}_0^i = 0.18\frac{\hbar\overline{v}_F^i(H=0)}{k_B T_{sc}}$. *Then it summarises the* $v_F^i(H=0)$ *for each axes and the corresponding* $\xi_0^i$.

## 4.4 ANALYSIS OF $H_{c2}$ IN THE HF PHASE.

Theoretical models for the HF phase have proposed a field-induced symmetry change of the order parameter [59, 60, 126]. The main idea is that for a spin-triplet superconducting state arising from ferromagnetic fluctuations along the easy magnetisation axis, at low fields, the **d**-vector should be perpendicular to the **a** axis (similar to the ferromagnetic superconductors). Thus, a $B_{3u}$ (or more generally $B_{3u} + iB_{1u}$ state under field) should be favoured at low fields. By contrast, for high fields along the **b** axis, a rotation of the **d**-vector is expected toward a $B_{2u}$ state (or $B_{2u} + iA_u$), to minimise the component of the **d**-vector along the **b** axis. Such a symmetry change would imply a phase transition between the LF and HF states, which had not been detected until our specific heat measurements. Nevertheless, the rotation of the **d**-vector cannot explain the positive curvature of $H_{c2}$ observed in the HF phase between 15 T and the metamagnetic transition at 34.8 T. Moreover, the drastic change of shape of the superconducting transitions between the LF and HF phases indicates a change of the pairing mechanism between the two phases as discussed in chapter 3.4.2. These observations show that there is more than a "simple" rotation of the **d**-vector between the LF and HF phases. It is most likely that the superconducting coupling is reinforced in HF due to the emergence of a new pairing mechanism.

Diverse physical parameters in the HF phase seem to peak at the metamagnetic transition (A coefficient from ρ measurements, γ extracted from M measurements). It is most likely that superconductivity in the HF phase arises from the magnetic fluctuations driving the metamagnetic transition. Today the nature of these fluctuations is still unclear, only antiferomagnetic fluctuations at 0 T have been found by neutron scattering experiments [28, 73].

The phase diagram H‖**b** is also to be compared to the phase diagram under pressure (Figure 4.7 from ref [20]). Above 0.3 GPa, a second superconducting phase emerges (SC2). And the $H-T$ phase diagram under pressure shows that this second superconducting phase corresponds to the HF phase at ambient pressure [75]. There are two main theoretical proposals for this phase (SC2). The first one is a $B_{2u}$ phase having no component of the **d**-vector along the **b** axis, with a pairing mechanism controlled by local ferromagnetic correlations [126]. This is the most

natural proposal explaining the transition between the two different phases (LF and HF) by a rotation of the **d**-vector imposed by the Zeeman coupling. However, as explained before, there is more than a rotation of the **d**-vector between the LF and HF phases. In this scenario nothing should be changed to determine $\lambda(H)$ between the LF and HF phases. The resulting $\lambda(H)$ is reported in Figure 4.8 corresponding to the points for $g$ fixed at 0 in both phases. $\lambda(H)$ displays a weak increase of the pairing strength, approximately 30% between 0 T and $H_m$, which is far from the factor 2 observed on C/T at 1.8 K (Figure 3.6).

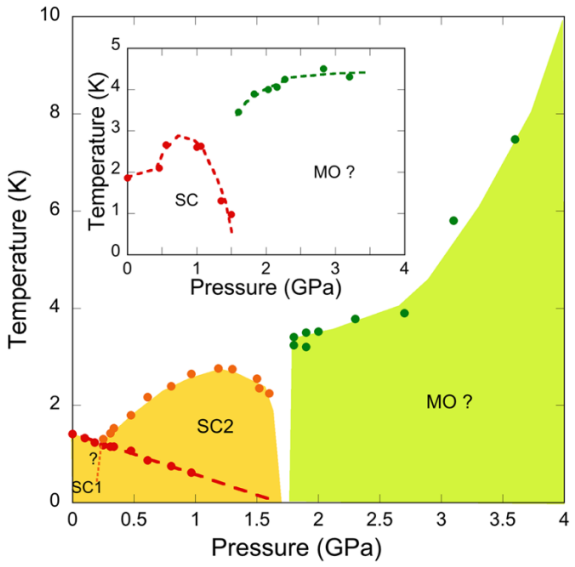


**Fig. 4.7:** *Phase diagram under pressure at zero field of $UTe_2$ obtained from specific heat measurements. From ref [20].*

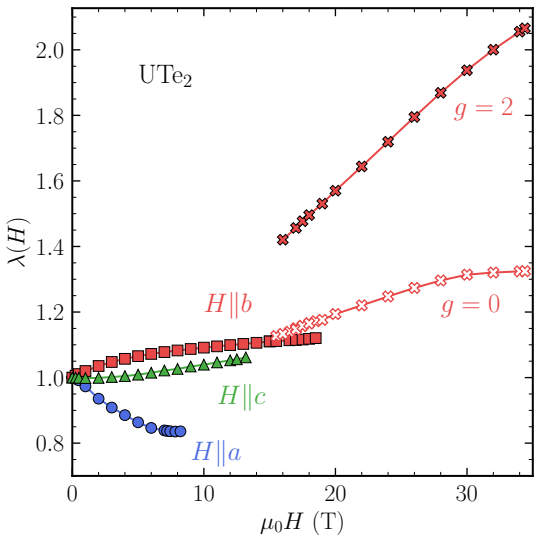


**Fig. 4.8:** $\lambda(H)$ *for the three axes. The red crosses correspond to* $\lambda(H)$ *in the HF phase in the two cases* $g = 0$ *and* $g = 2$.

### 4.4.1 *Spin-singlet state in the HF phase*

The second proposals for the HF phase is a spin-singlet state, induced by antiferromagnetic correlations. Some theoretical models have predicted that they would become dominant over ferromagnetic fluctuations under pressure [59, 60, 141]. Having a spin-singlet phase appearing at high fields seems unnatural due to the paramagnetic limitation. However with the strong coupling effect and the increase of the pairing strength with the field, the paramagnetic limit can be easily exceeded. This explains how the spin-singlet state can survive at 34 T with a paramagnetic limitation. In this scenario determination of $\lambda(H)$ depends on additional parameters: for a new mechanism we can expect a different $\Omega$, and the precise value of $g$ is unknown.

We have taken the same $\Omega$ as the one in the LF phase, considering that both pairing mechanisms should have similar characteristics in order to lead to similar critical temperatures. Using different values of $\Omega$ (but the same $g$) changes little to the following analysis, the physics remains the same. As for $g$, we have taken

the free electron value $g = 2$, the idea being to explore the consequences of a new mechanism with paramagnetic limitation.

The $\lambda(H)$ obtained is shown in Figure 4.8 (red plain crosses). The fields dependence is larger than in the case of the $B_{2u}$ phase, because of the requirement to overcome the saturation of $H_{c2}$ at fixed $\lambda$ induced by the paramagnetic limitation. This large increase is also in agreement with the strong increase of $C/T$ observed in this field range up to $H_m$. This shows that the spin-singlet scenario for the HF phase does not lead to unphysical results at this stage.

### 4.4.2 *Reproduction of the HF superconducting transition*

However, we can go a step further in the analysis by showing that the spin-singlet scenario explains the broad width of the HF superconducting transition.

We just saw that the superconducting constant $\lambda$ is field dependant, so the critical temperature at fixed field depends on the field, throught the orbital and paramagnetic effects, and on $\lambda(H)$: $T_{sc} = T_{sc}(H, \lambda(H))$. We also saw that the widths of HF superconducting transitions are much larger than the LF transitions. Thus, an additional broadening of the superconducting transition may come from a field-dependent dispersion of $\lambda$.

In the very likely hypothesis where the field increase of the pairing arises from the proximity to $H_m$, a simple hypothesis is that $\lambda$ is a function of $H/H_m$. Then, a dispersion of $H_m$ will translate into a distribution of $T_{sc}$ through a distribution of $\lambda$, and will lead to an additional mechanism for the broadening of the HF superconducting transitions. From the calculation of $H_{c2}$ at fixed $\lambda$ used to extract the field dependence of the pairing, we can determine a function $\phi$ as:

$$T_{sc} = \phi\left(H, \tilde{\lambda}\left(\frac{H}{H_m}\right)\right) \tag{4.8}$$

This allows to determine the effect of the distribution of $H_m$ on the specific heat anomalies of the HF phase. We can rewrite:

$$\tilde{\lambda}\left(\frac{H}{H_m}\right) = \lambda\left(H\frac{H_{m0}}{H_m}\right) \tag{4.9}$$

Where $H_{m0}$ is the centre of the distribution of $H_m$ at the metamagnetic transition determined from the specific heat measurements and $\lambda(H)$ is displayed in Figure 4.8. From the relation 4.8, we can calculate the effect of a Gaussian distribution of $H_m$ on the specific heat anomaly of the superconducting transition at constant field, using for $C/T$:

$$\frac{C}{T} = \int p(H_m)\frac{C}{T}(T, T_{sc}(H, H_m))dH_m \tag{4.10}$$

With this equation 4.10 we can calculate $C/T$ and reproduce the specific transitions measured for the different models (spin-singlet or spin-triplet). In Figure 4.9 are

shown the calculated transitions at several fields in both case, spin-singlet and spin-triplet, with a distribution of $H_m$ of 0.55% (0.19 T). For the spin-singlet pairing ($g = 2$), half of the width of the HF transitions can be explained. By contrast, the spin-triplet case totally fails to reproduce the transitions. This conclusion can be easily understood by a short calculation.

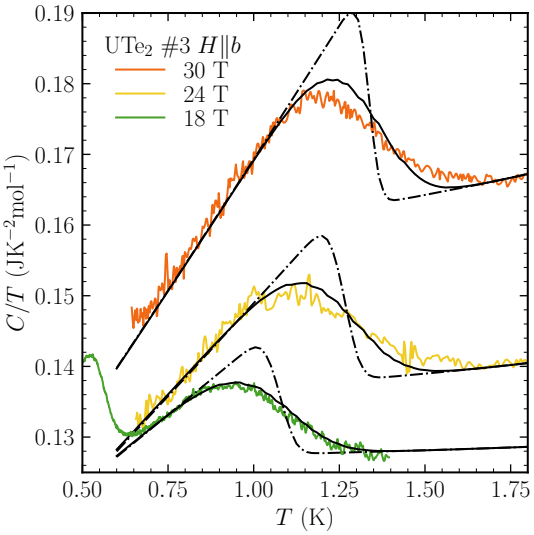


**Fig. 4.9:** *HF transitions measured on sample #3 at 18, 24 and 30 T H||**b**. The dash-dotted lines correspond to C/T calculated with a distribution of $H_m$ and the width multiplied by 2 in the case of spin-triplet pairing. The plain lines are for the spin-singlet case.*

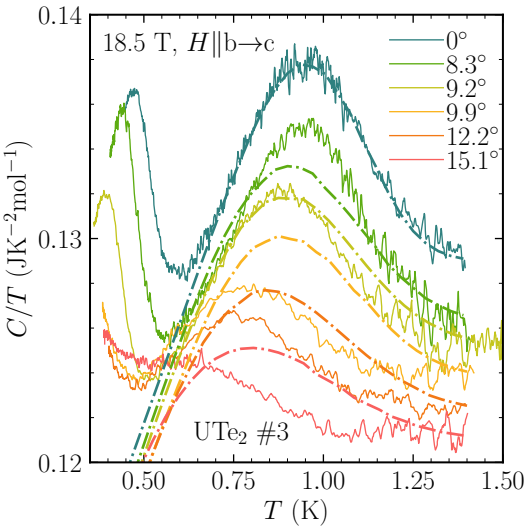


**Fig. 4.10:** *C/T at 18.5 T for several angles in the (**b**,**c**) plane. The dash-dotted lines correspond to the HF transitions calculated with a distribution of $H_m$ in the spin-singlet scenario.*

Even without a full determination of the shape of the anomaly, requiring the numerical integration of Eq.4.10, we can understand why the broadening is larger when there is a paramagnetic limitation of $H_{c2}$. From Eq.4.8, we can derive $T_{sc}$ with respect to $H_m$ at fixed H and for $H_m = H_{m0}$. This expresses the sensitivity of $T_{sc}$ to $H_m$, so the broadening of the C/T anomaly due to a distribution of $H_m$:

$$\left.\frac{\partial T_{sc}}{\partial H_m}\right|_H = \left.\frac{\partial T_{sc}}{\partial \lambda}\right|_H \left(-\frac{H}{H_{m0}}\right) \frac{d\lambda}{dH} \tag{4.11}$$

And finally we can compute the temperature derivative of $H_{c2}$ from Eq.4.8:

$$dT = \left.\frac{\partial T_{sc}}{\partial H}\right|_\lambda dH_{c2} + \left.\frac{\partial T_{sc}}{\partial \lambda}\right|_H \left(\frac{H_{m0}}{H_m}\right) \left(\frac{d\lambda}{dH}\right) dH_{c2} \tag{4.12}$$

Then by combining with Eq.4.11 we obtain:

$$\frac{dT}{dH_{c2}} - \left.\frac{\partial T_{sc}}{\partial H}\right|_\lambda = -\left.\frac{\partial T_{sc}}{\partial H_m}\right|_H \left(\frac{H_{m0}}{H}\right) \tag{4.13}$$

This equation (Eq.4.13) shows that the difference between models for $\left.\frac{\partial T_{sc}}{\partial H_m}\right|_H$ does not arise directly from $\left(\frac{d\lambda}{dH}\right)$, but rather from $\left.\frac{\partial T_{sc}}{\partial H}\right|_\lambda$. This term becomes larger

when $H_{c2}$ at constant $\lambda$ is flat due to the paramagnetic limitation in the case of spin-singlet pairing. In the case of spin-triplet pairing (ESP state) there is a pure orbital limitation and $\frac{\partial T_{sc}}{\partial H}\Big|_{\lambda}$ is smaller. So it explains why the spin-singlet pairing reproduces well the width of the specific heat transitions in the HF phase, while the spin-triplet pairing fails, because of the sensitivity to a distribution to $H_m$.

Within the same scheme, the dispersion of $H_m$ is found to have a negligible influence on the LF transition, so that it gives a first explanation for why the two superconducting phases could be marked by such different specific heat anomalies.

### 4.4.3 *Angle dependence of the HF phase*

We can also go a step further in the analysis with the field angle dependence of C/T to support the spin-singlet scenario. ac specific heat measurements have been performed on sample #3 up to 18.5 T for several angles in the (**b**,**c**) plane. At fixed field, when H is shifted toward **c**, the HF transitions are shifted to low temperatures and the jump decreases (Figure 4.10 for $H = 18.5$ T).

Taking only into account the angular dependence of $H_m$ [112] as $H_{m0}/\cos(\theta)$, thus $\lambda(H\cos(\theta))$, and a hypothetical mosaicity of 3° in our crystal, we can roughly reproduce the huge broadening of the anomaly at finite angles, with the same dependence of $T_{sc}$ on $H_m$. The dash-dotted lines in Figure 4.10 represent the HF transitions calculated for each angles.

The $H_{c2}$ can also be calculated for different angles of the field. In order to do that, we assumed that the bare average Fermi velocity (see section 4.3.2) for field with an angle $\theta$ in the (**b**,**c**) plane is:

$$\bar{v}_F(\theta) = \sqrt{(\bar{v}_F(b)\cos(\theta))^2 + (\bar{v}_F(c)\sin(\theta))^2} \tag{4.14}$$

Where $\bar{v}_F(b)$ and $\bar{v}_F(c)$ are the bare average Fermi velocities for $H\|\mathbf{b}$ and $H\|\mathbf{c}$ respectively.

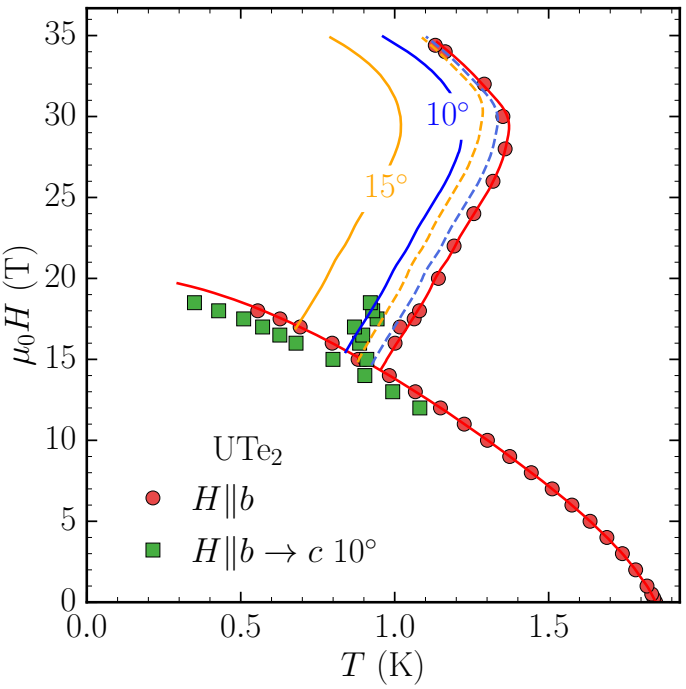


**Fig. 4.11:** $H_{c2}$ *determined by our specific heat measurements for* $H \| \boldsymbol{b}$ *(red circles) and for field* 10° *toward* **c** *axis (green squares). Plain lines are* $H_{c2}$ *calculated with the strong coupling model and* $g = 2$ *in the HF phase, for different angles of the field. Dashed lines are* $H_{c2}$ *calculated with* $g = 0$ *in the HF phase.*

Figure 4.11 shows the $H_{c2}$ in the HF phase calculated for an angle of the field of 10° and 15° in the (**b**,**c**) plane. It shows that we can recover the experimental $H_{c2}$ at 10° in the case of $g = 2$. If $g = 0$, the model fails to reproduce the $H_{c2}$ measured. This is one more argument in favour of the spin-singlet scenario in the HF phase.

The same analysis could be done for the LF phase, however the field dependence of $\lambda(H)$ for a given angle in the (**b**,**c**) plane have to be taken into account. This is something actually unknown, thus the model failed to reproduce the $H_{c2}$ in LF phase at 10° and 15°.

## 4.5 CONCLUSION

The main results from these measurements on $UTe_2$ are the requirement of a field-dependent pairing strength along all directions of the applied field, and the presence of two different superconducting phases for $H \| \mathbf{b}$ with different pairing mechanisms.

The strong decrease of the pairing strength along the **a** axis in the LF phase is reminiscent of the results on UCoGe along its easy magnetisation axis [140]. It seems best compatible with a pairing mechanism involving true ferromagnetic fluctuations. As said earlier: $\frac{d\lambda}{dH} = 0$ at $T_{sc}$ ($H = 0$) is what is expected for paramagnetic systems like $UTe_2$.

There are also several theoretical studies exploring other mechanisms leading also to spin triplet pairing in $UTe_2$, like finite momentum magnetic fluctuations [77], or only local ferromagnetic correlations within a unit cell [126]. The field dependence of such mechanisms has not been explored yet. However, the Fermi surface instability observed at 6 T along the easy magnetisation axis could play a key role if a **Q**-dependent pairing is important. Even though ferromagnetic fluctuations are the most plausible mechanism for the LF phase of $UTe_2$, we cannot exclude that future investigations of these alternative mechanisms could also lead to satisfying explanations of the C/T measurements presented.

### 4.5.1 H||*b*: *comparison with other studies*

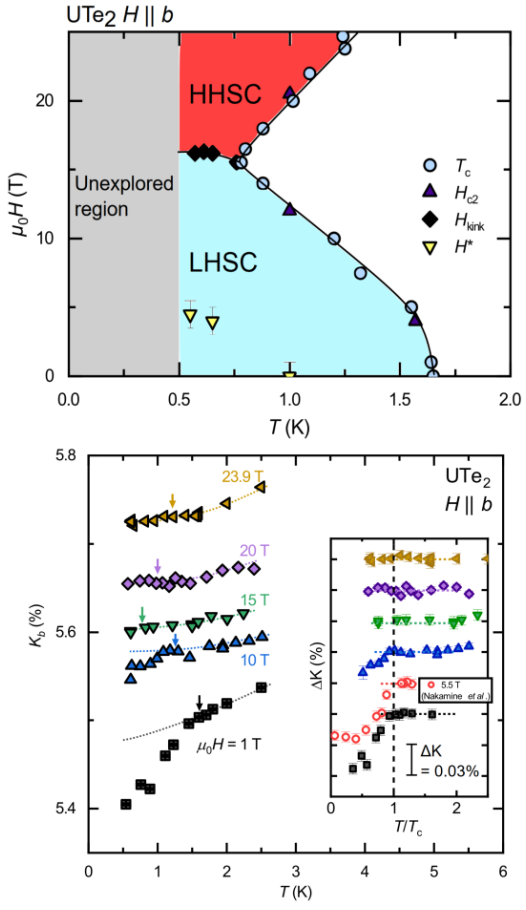


**Fig. 4.12:** *Top: the phase diagram of $UTe_2$ established with ac susceptibility measurements for H||**b**. Bottom: temperature dependence of the Knight-shift at different field H||**b**. All from ref [69].*

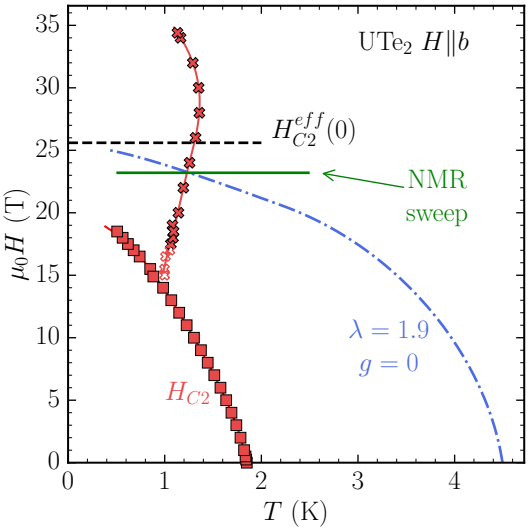


**Fig. 4.13:** $H_{c2}^{b}$ *from our specific heat measurements. Green line corresponds to a typical temperature sweep done in NMR measurements at fixed field of 23 T. Dot-dashed blue line corresponds to* $H_{c2}$ *calculated for* $\lambda(H = 23\ T)$. *Black dashed line corresponds to* $H_{c2}^{eff}(0)$ *at fixed field of 23 T.*

High-field NMR measurements coupled to ac susceptibility have been performed soon after our specific heat measurements, recovering a similar phase diagram as reported (see Figure 4.12), but identifying the HF phase as a spin-triplet $A_u + iB_{2u}$

state [69]. This comes from the temperature dependence of the Knight-shift in the HF phase, showing no detectable decrease across $T_{sc}$, which might imply no paramagnetic limitation (see Figure 4.12). However, according to our model, due to the field dependence of the pairing strength, these measurements in the HF phase are all performed at values of $\frac{H}{H_{c2}^{eff}(0)}$ close to 1, where $H_{c2}^{eff}(0)$ is the effective value of $H_{c2}(0)$ with the value of the pairing strength $\lambda(H)$ at the field $H$ (see Figure 4.13). At these large field values (with respect to $\frac{H}{H_{c2}^{eff}(0)}$ ), only little change is expected for the behaviour of the Knight-shift in temperature, whatever the spin-state. Thus, these NMR results are also in agreement with a spin-singlet pairing in the HF phase.

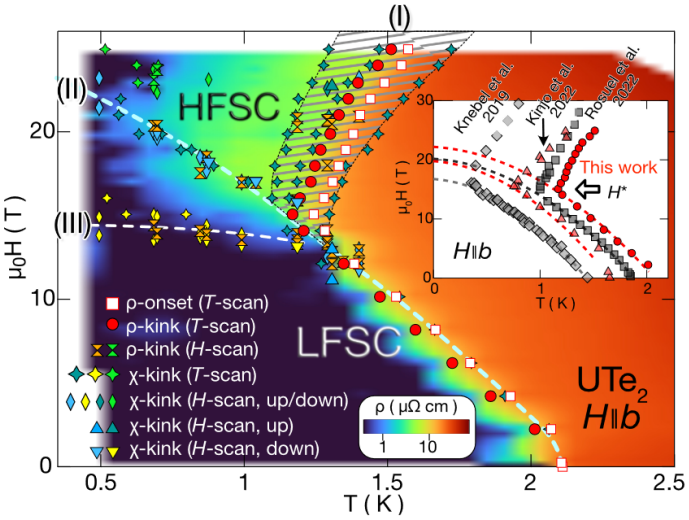


**Fig. 4.14:** *Phase diagram $H \| \boldsymbol{b}$ of $UTe_2$ determined by resistivity and AC susceptibility measurements in ref [119].*

More recently, a similar phase diagram was also reported from resistivity and ac susceptibility measurements on the new generation of sample with a $T_{sc}$ around 2 K [119] (Figure 4.14). As explained earlier, thermodynamics imposes that either there is a fourth transition line in the LF phase (denoted as (III) in Figure 4.15), or the transition between the LF and HF phase is first order (denoted as (II) in Figure 4.15). This study claims to see the fourth transition line expected in the LF phase, noted (III) in Figure 4.14. However, these are non-thermodynamic measurements, and the criterion used to establish the phase diagram can be criticised. Thus, there is actually no solid proof of the existence of a fourth transition line.

The anomalies observed at the transitions in both of these works revealed also a broadening of the transition in the HF phase like our specific heat measurements. This highlights the ubiquitous nature of the broadening, still present on the best samples available today. This change of the specific heat anomaly is a unique case showing that this new superconducting phase does not arise from a simple change of symmetry like in $UPt_3$ or $CeRh_2As_2$, or from a rotation of the **d**-vector: it has to arise from a new pairing mechanism strongly reinforced on approaching $H_m$. We have found support for a paramagnetic limitation of $H_{c2}$ in the HF phase, hence for

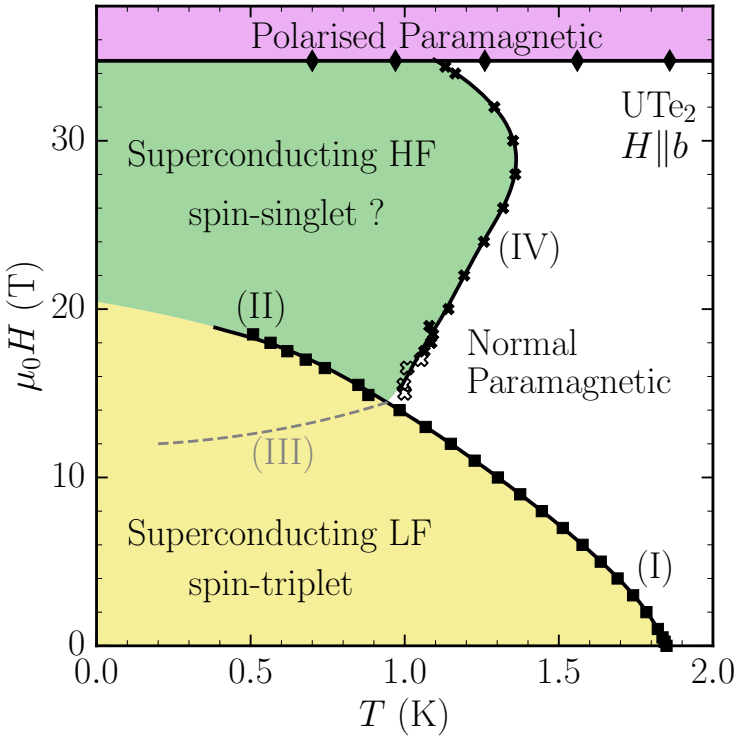


**Fig. 4.15:** *Phase diagram H||**b** of $UTe_2$ from our specific heat measurements. The dashed grey line annotated (III) corresponds to the hypothetical fourth transition line not detected in our specific heat measurements.*

a spin-singlet superconducting phase, as it can explain a large part of the strong broadening of the specific heat anomaly in the HF phase, and the behaviour of the transition when turning away from the **b** axis in the (**b**,**c**) plane.

It is worth to mention a theoretical work proposing an alternate explanation for the phase diagram of $UTe_2$, without field reinforced pairing [144]. By admitting the existence of a transition line between a LF and HF superconducting phases, the "deep" of $H_{c2}$ at 15 T would be caused by thermal superconducting fluctuations boosted by a spatial distribution of critical temperatures in the sample. This scenario should now be explored against the present precise determination of the transition lines, and the change of the specific heat anomaly between the LF and HF phases.

### 4.5.2 *Transition line between LF and HF phases*

An open question is the order of the different transition lines, and the precise slopes of the lines at the multicritical point at 15 T. As for $CeRh_2As_2$ [67], in the case of a direct spin-triplet to spin-singlet transition, a first order transition is expected. Figure 4.15 shows the final phase diagram of $UTe_2$ with H||**b**, with the different transition lines labelled. In our specific heat measurements, we did not

detect any hysteresis effects on the transition line (II). We could imagine that the temperature is too high to detect an hysteresis. So, ac specific heat measurements up to 36 T at LNCMI were performed with a dilution fridge on the sample #3. The measurements were successful and the field sweeps are display in Figure 4.16 only in the field range around the superconducting transition (LF one). A sweep was performed at 110 mK but as we can see in Figure 4.16, the transition is no more visible at 250 mK, so the field sweep at 110 mK is not shown in the Figure 4.16. If we plot the corresponding phase diagram (Figure 4.17), we see it could correspond to a misalignment of 10° toward the **c** axis of the sample, which is plausible since the alignment in this measurement was more tricky. In any case, we did not detect any hysteresis effect at the transition between the two phases. There are many cases in condensed matter physics, where first order transitions lead to negligible hysteresis: see ref [42], or the well known example of the $^3$He melting curve.

Apart from the hysteresis, a first order transition must have latent heat: on crossing the first order transition by continuous heating, due to latent heat, the temperature of the sample should remain constant for a short time. But in practice it is hard to detect such a behaviour, even when the transition appears as a very high and sharp peak, or a divergence, of the specific heat (See measurements done on the magnetic compound $GdLiF_4$ in Appendix A.3). In practice it is very difficult to distinguish a constant temperature due to latent heat or just due to the strong increase of C/T. In the case of $UTe_2$ this experiment was unsuccessful maybe because of a too small latent heat to be detected.

In $CeRh_2As_2$ the same question also remains open: there is no experimental proof of the first order character of the transition.

Finally the only salient feature is seen in Figure 3.26: there is a slight narrowing of the specific heat anomaly along the transition line between the LF and HF phase (line (II) in Figure 4.15) compared to the same anomaly along the $H_{c2}$ line of the LF phase (line (I)). This slight narrowing leaves open the possibility that the transition from LF to HF phases could be weakly first order. This point requires, however, further experimental investigations. If this transition is first order, of course, the question of the multicritical point is solved. If it is not, it remains an issue to determine if there is an additional transition line within the LF superconducting phase, as depicted by the dashed line (III) in Figure 4.15. And whether or not the three transition lines determined in this work join with different slopes, or if the $H_{c2}$ line has no change of slope (only a very strong positive curvature) at the multicritical point as explain in section 3.4.1. The entrance into the HF phase along $H_{c2}$ cannot be done in a mixed singlet-triplet superconducting phase: it would require, like for the chiral superconducting state [48], a double transition which is not observed.

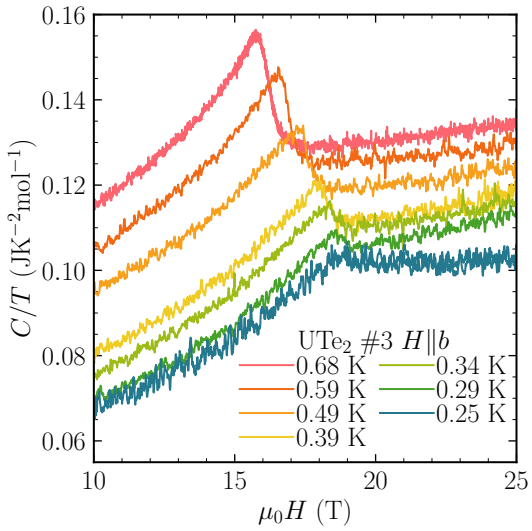


**Fig. 4.16:** C/T *field sweeps performed on sample #3 in dilution fridge at high fields, in the field range around the LF transition.*

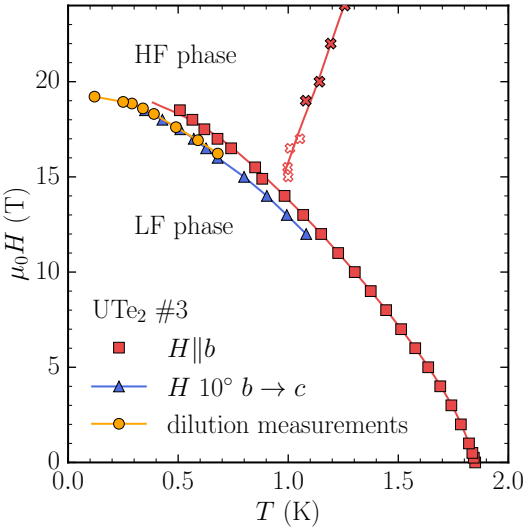


**Fig. 4.17:** *Phase diagram of sample #3. The red points correspond to* H$\|$***b*** *and blue triangles to a misalignment of* 10° *toward* ***c*** *axis. The orange points correspond to measurements done in dilution fridge at high fields.*

Theoretical works based on microscopic calculations have predicted that the interplay between ferromagnetic and antiferromagnetic fluctuations could lead to competing pairing interactions [59, 141]. This competition could be central both for the pressure and the field induced phases of $UTe_2$. At ambient pressure, at the opposite of $CeRh_2As_2$, it could lead to a paradoxical spin-singlet phase at high fields, possibly driven by strong antiferromagnetic correlations on approaching the metamagnetic transition. Under pressure, this HF phase would become the highest $T_{sc}$ phase with the lowering of the metamagnetic field along the **b** axis, whereas the pure spin-triplet phase would survive essentially for large enough fields along the easy **a** axis. $UTe_2$ is probably the first system where two competing pairing mechanism of similar strength exist that can be tuned by field or pressure. It is an ideal case to challenge theoretical models and understand which conditions allow for the emergence of spin-triplet superconductivity.

# 5

# MEASUREMENTS ON UCoGe

At days this chapter is written, the measurements and analysis are still in progress, but the main part of measurements is finished and presented. The dependence with field of C/T in the normal phase won't be discussed, and no analysis of $H_{c2}$ as detailed as for $UTe_2$ will be presented.

The problematic on UCoGe is the same as in $UTe_2$. Few thermodynamic studies have been done, except for a recent study of the angular dependence of C/T [102], and an older one on the thermal expansion for $H \| \mathbf{b}$ [103]. Thus, no complete phase diagram along the three axes of the same crystal has been established with thermodynamic probes. The first aim of this study was to determine the complete phase diagram, and to probe the superconducting phase to detect if different phases are present like in $UPt_3$ or $UTe_2$. The second aim was to determine the electronic specific heat field-dependence in the normal phase to connect it to the field-dependence of the strong-coupling constant.

There are, however, experimental differences with $UTe_2$. First $T_{sc}$ is at much lower temperature (between 500 and 600 mK).Second, there is a much more pronounced anisotropy with the **c** axis: a small component of field along the **c** axis is enough to strongly suppress superconductivity [15]. This was well demonstrated by NMR measurements [46, 47], and more recently by specific heat measurements [102]. Thus, the alignment is crucial for UCoGe. Third, the specific heat anomaly is smaller and much broader. The experimental conditions are therefore much less favourable overall.

## 5.1 ZERO FIELD SAMPLE PROPERTIES

The sample measured is a nice platelet of 7.63 mg, with a RRR of 162, a rather good sample for UCoGe.

Figure 5.1 shows the specific heat at 0 T. The superconducting transition as well as the ferromagnetic transition were fitted by a model with a Gaussian distribution of $T_{sc}$ and $T_C$ respectively (see chapter 2.1.4). As already known, the ferromagnetic transition at $T_C = 2.77$ K and the superconducting one at $T_{SC} = 0.538$ K are very wide, 850 mK and 200 mK of width respectively. It is a common feature of UCoGe samples. It would be a great step forward to be able to grow samples with sharper superconducting transitions and/or ferromagnetic transitions. The transition jump ratio $\frac{\Delta C}{T_{SC}\gamma}$ is equal to 0.78, if C/T above $T_{sc}$ is consider as $\gamma$. This low value compared to the BCS ratio, emphasises the weak-coupling regime in

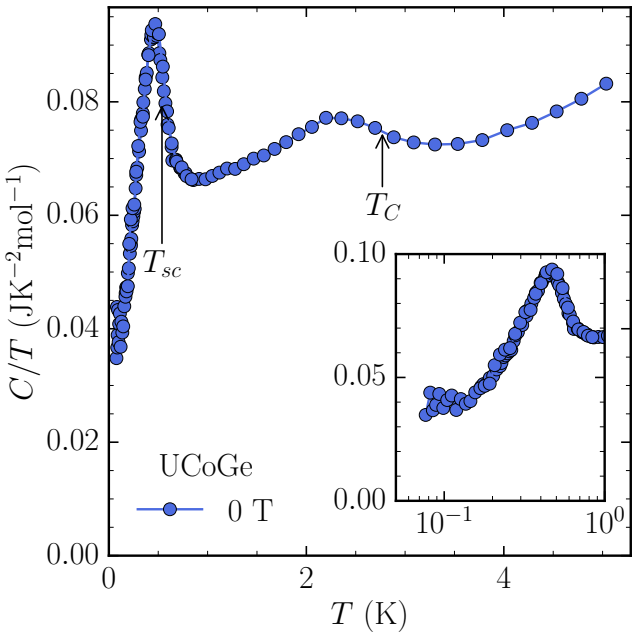


**Fig. 5.1:** *Specific heat of UCoGe at zero field. inset: enlargement on the superconducting transition (temperature log scale).*

UCoGe and the large residual term at low temperatures certainly originating from pair-breaking effects.

In the inset of Figure 5.1, we clearly see the residual term $\gamma_r$ at low temperatures. $\gamma_r \simeq 0.04$ JK$^2$mol$^{-1}$, approximately 60% of C/T just above the superconducting transition, twice larger than the extrapolation from temperatures above 150 mK. This large residual term is an usual feature on UCoGe. The first suggestion is this $\gamma_r$ comes from impurities. But, it is also believed it comes from self-induced vortex state. The internal field due to ferromagnetism being larger than $H_{c1}$, even at 0 T vortices are already present and the Meissner phase is absent [27]. Thus, the vortex cores contribution to specific heat induces a residual term. But, considering the large residual term that we measured, the self-induced vortex state scenario is less likely than impurities or pair-breaking defects contribution. It highlights again the necessity of better quality samples and a similar breakthrough as realised as the last $UTe_2$ 2 K samples.

The measurements on UCoGe are more noisy than the ones done on $UTe_2$. Indeed, the specific heat is smaller than $UTe_2$. Above the superconducting transition, C/T $\simeq 0.066$ JK$^{-2}$mol$^{-1}$ for UCoGe, and C/T $\simeq 0.133$ JK$^{-2}$mol$^{-1}$ for $UTe_2$. The UCoGe sample mass is of the same order as those of $UTe_2$ (sample #1 and #2). It means the total specific heat measured is much lower, so the thermal leak between the sample and the fridge needs to be weaker. As a consequence the measurements are more sensitive to parasitic powers. Furthermore, above 5 K the addenda is of same order as the specific heat of UCoGe. To have order magnitude,

the addenda represents 6% of the specific heat measured at 1 K, and 42% at 5 K. Thus, measurements above 5 K are unreliable, and won't be shown.

The large width of the superconducting transition in addition to more noisy measurements make it harder to accurately determine the $T_{sc}$, the jump and the width.

### 5.1.1 *Co nuclear contribution*

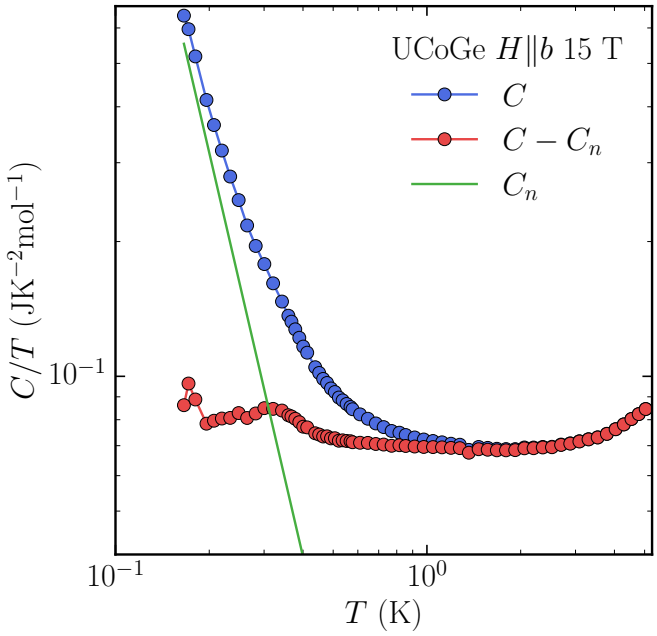


**Fig. 5.2:** *Specific heat of UCoGe (C), with subtraction of the Co nuclear contribution ($C_n$) at 15 T H$\|\boldsymbol{b}$.*

Co is known for having a huge nuclear contribution to specific heat. This is due to the large nuclear spin (7/2) of $Co^{59}$, its high sensitivity to field and its 100% abundance. In comparison, Ge has a spin 9/2, but its sensitivity is 200 times smaller than Co and its abundance is 7.6%. For NMR measurements it is a boon since it allows to have good signal. But for specific heat measurements it brings a huge hyperfine contribution at low temperatures. Thus, it is critical to estimate correctly the Co contribution in order to subtract it.

To do so, the hyperfine Hamiltonian is determined and the eigenvalues extracted to calculate the specific heat, see chapter 2.1.5 for more explanation. The parameters used in the Hamiltonian were taken from NMR measurements in ref [85]. And the NMR spectrum was calculated and compared to the measurements to verify the validity of our calculations. It results on a large specific heat contribution as expected, see Figure 5.2 which compares the specific heat measured at 15 T and the nuclear contribution of Co.

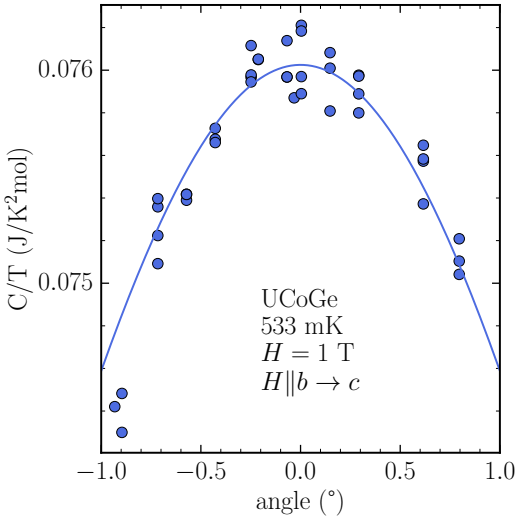


**Fig. 5.3:** *Specific heat of UCoGe at* 1 *T with different angle in the (**b**,**c**) plane, at* 553 *mK (in the superconducting transition).*

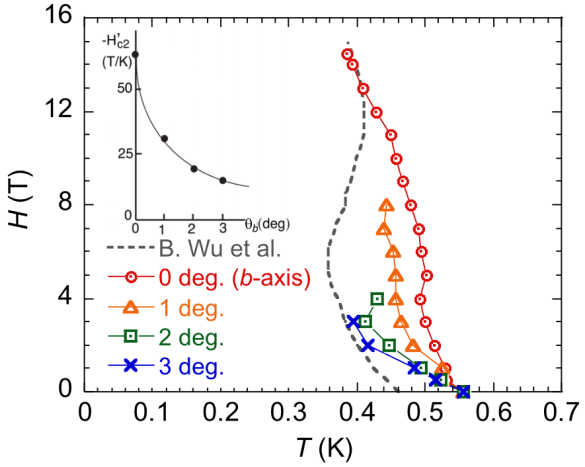


**Fig. 5.4:** $H_{c2}$ *established by specific heat measurement for* $H\|\mathbf{b}$ *and for different angle in the (**b**,**c**) plane. From ref [102]*

For $H\|\mathbf{c}$ at 15 T we had to take into account the precise temperature and field variation of the Knight shift, since the susceptibility is not linear for $H\|\mathbf{c}$ [72, 105]. Therefore, we calculated the Knight shift K for each field of our measurements using NMR and magnetisation data. From ref [85] NMR measurements indicate $K = 0.24$ at 3 T, and magnetisation measurements in ref [72] indicate $\frac{M}{H}|_{H=3} = 0.0462\ \mu_b T^{-1}/U$ at 3 T. Then for each field H we have K equals to 0.24 times $\left(\frac{M}{H}\right)$ determined from ref [72], divided by $\frac{M}{H}|_{H=3}$. Below 1 T, the susceptibility is almost linear so we can take a constant value of K. In ref [105], $K = 0.30$ at 1.5 T. We recovered this value with the procedure explained above which confirms that the $K(H)$ we determined is correct. With this $K(H)$, the nuclear specific heat was accurately removed for $H\|\mathbf{c}$, otherwise it would have been larger than C/T measured at 15 T.

For the other axes the susceptibility is roughly linear below 15 T, so the Knight-shift does not evolve with field (or at least its evolution is negligible). So we took the values at 3 T from ref [85].

Experimentally, the sample need to be aligned precisely in the field. To do so, we placed the sample on the set-up so as to rotate in the (**b**,**c**) or (**a**,**c**) plane. Due to the strong sensitivity to a **c**-component we could easily align the sample along the **b** or **a** axis. Figure 5.3 shows C/T at 1 T in the superconducting transition as a function of angle in the (**b**,**c**) plane. When the sample is perfectly aligned in the field, C/T is maximum. We see a strong angle dependence. For comparison, in $UTe_2$ in a range of 3° around the **b** axis C/T is constant at 12 T. The strong sensitivity to angle is a known effect in UCoGe, and recently well demonstrated by specific heat measurements in ref [102]. In this study at 3 T, $T_{sc}$ is decreased by 17% with an angle of 3° in the (**b**,**c**) plane, as shown in Figure 5.4 from ref [102].

## 5.2 THE CURIE ANOMALY

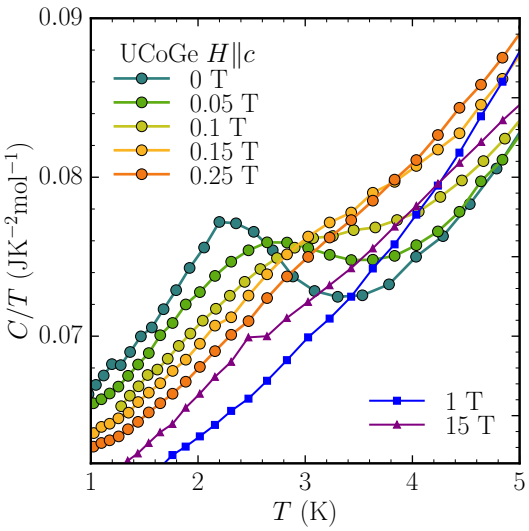


**Fig. 5.5:** *Specific heat at the Curie anomaly for several field* H‖***c****.*

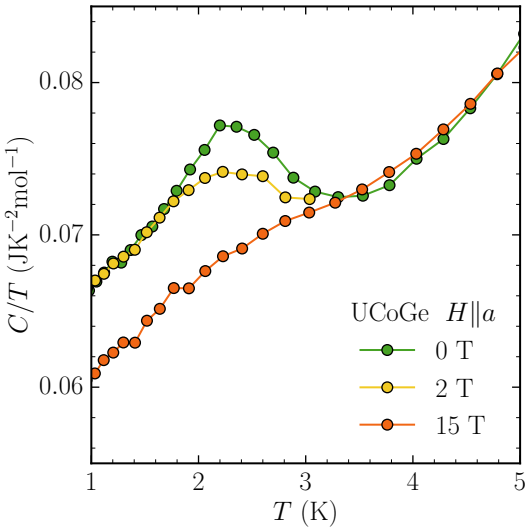


**Fig. 5.6:** *Specific heat at the Curie anomaly for* H‖***a****.*

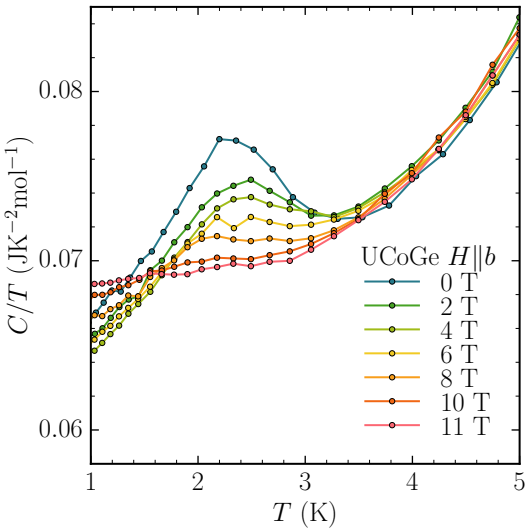


**Fig. 5.7:** *Specific heat at the Curie anomaly for* H‖***b****.*

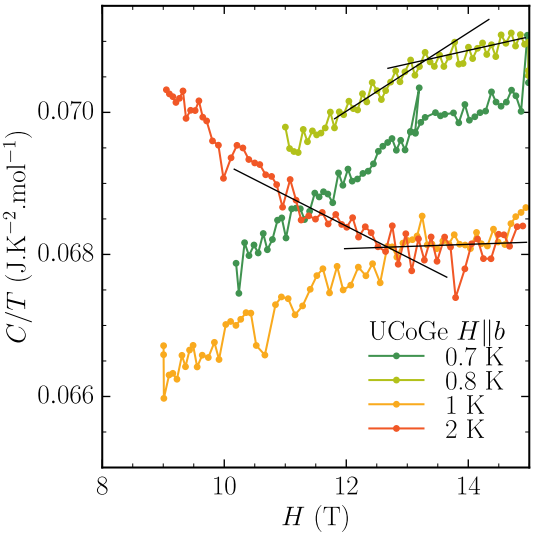


**Fig. 5.8:** *Field sweeps in the normal phase between 9 and 15 T for different temperatures. Black lines show how the kink temperature is determined.*

The ferromagnetic transition occurs at $T_C = 2.77$ K. Figure 5.5 shows the measurements for H‖**c** and Figure 5.6 shows for H‖**a**. When field is applied along the easy magnetisation **c** axis, $T_C$ slightly increases and the transition rapidly collapses for very low fields ($< 0.25$ T) as expected for the easy magnetisation axis. Along the

hard **a** axis, the anomaly is still seen at 15 T with a large broadening and decreasing of the jump, but $T_C$ remains the same.

For **b** axis, the behaviour of the Curie anomaly is more complex. $T_C$ decreases when field is above 4 T and the width drastically increases (more than for H||**a**) reaching 2.1 K at 10 T (see Figure 5.7). Above 10 T the transition is lost. However, in the field sweeps performed between 0.7 K and 2 K (in the normal phase), a change of slope is visible. It is shown in Figure 5.8 for several temperatures. If we consider this kink as $T_C$, the final phase diagram for H||**b** is shown in Figure 5.9.

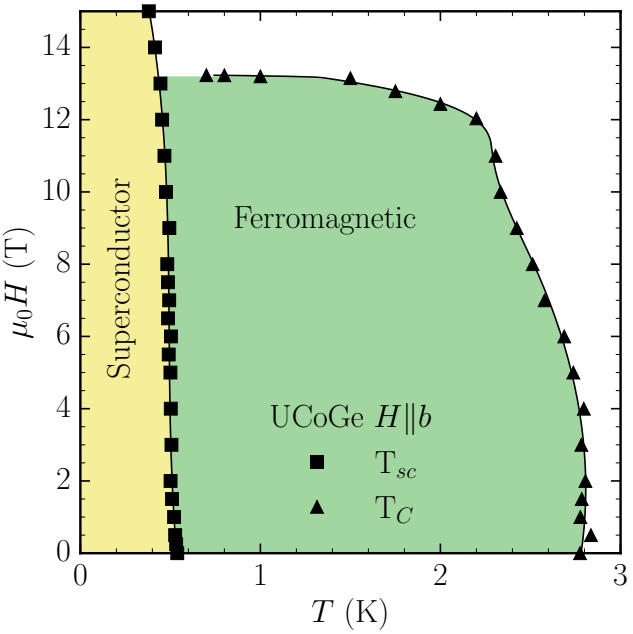


**Fig. 5.9:** *Phase diagram for H||**b** of UCoGe, obtained from specific heat measurements. Points for $T_C$ above 10 T are determined from the field sweeps.*

This phase diagram is in agreement with the previous phase diagram established by transport measurements [11] and shown in Figure 5.10. The difference is: in our measurements $T_C$ joins $H_{c2}$ at around 12.5 T with an horizontal line, while in transport measurements the $T_C$ line seems to join $H_{c2}$ at around 15 T with a constant increase. However, the Curie anomaly was very difficult to follow at high field in these transport measurements, and it is also unclear if the change of slope of C/T in the field sweeps is really marking $T_C$.

Anyway, these results show that the Curie anomaly has an influence on C/T down to $T_{sc}$. Thus, a determination of $\gamma(H)$, by assuming that C/T just above $T_{sc}$ is roughly equal to $\gamma$, and link it to $\lambda(H)$ as done in the previous study ref [140], may be questionable because of the field behaviour of the Curie anomaly.

Recent NMR measurements have shown a maximum of $1/T_1$ and $1/T_2$ terms around 12.5 T [56]. It is attributed to a ferromagnetic criticality arising from the longitudinal fluctuations along the **c** axis, the ones inducing superconductivity. Moreover they found $T_C$ determined from $1/T_1T$ peak has the same behaviour as

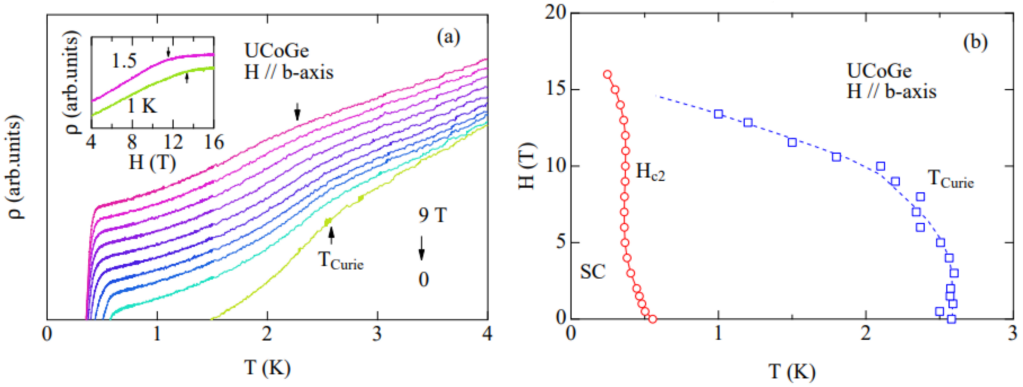


**Fig. 5.10:** *(a) Resistivity measurements for H‖**b**, where the $T_C$ is seen as broad anomaly. (b) The corresponding phase diagram. All from ref [11].*

in resistivity measurements which are similar except near 12.5 T where we see a drastic suppression of $T_C$ in our specific heat measurements.

It is worth to note that the anisotropy of the ferromagnetic fluctuations has an impact on our measurements. Due to the Co contribution, a second exponential appears in the heat pulses in field and at low temperatures below ~ 200 mK (see section 2.2.1). The second exponential is more pronounced for field along the **c** axis than the other two axes (see Figure 5.12). Indeed, the ferromagnetic fluctuations are suppressed for H‖**c**, thus the coupling of the nuclear spin with the electrons is reduced, so the relaxation time of the second exponential is increased.

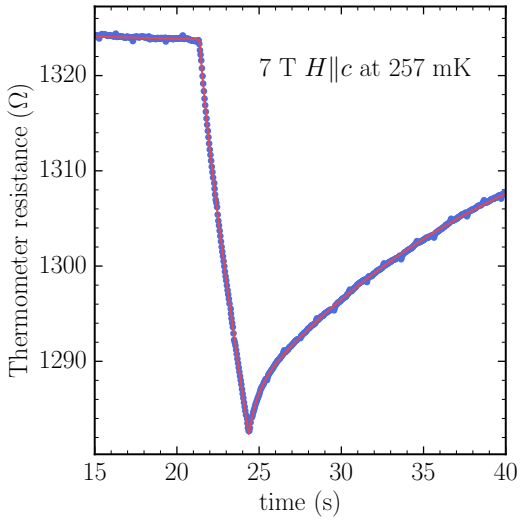


**Fig. 5.11:** *Thermometer resistance during pulse sequence done at 257 mK for 7 T H‖**c**. The red line corresponds to the fit of the pulse.*

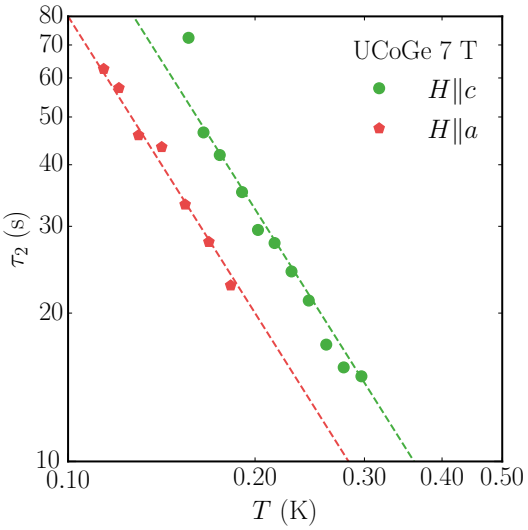


**Fig. 5.12:** *Relaxation rate $\tau_2$ of the second exponential decay of the pulse at 7 T H‖**c** and **a**. For H‖**b** no second exponential is observed down to 200 mK, the lowest temperature we could achieve for H‖**b**. Dashed lines represent $1/T^2$ laws.*

## 5.3 SUPERCONDUCTING PHASE

The superconducting transition, despite its large width, can be followed in field, up to 15 T for H||**b**. Along the **c** and **a** axes it becomes harder to follow the transition because it shifts to lower temperatures, and for the **a** axis the nuclear specific heat contribution becomes large enough to make it very difficult to distinguish the superconducting anomaly.

The evolution in field of the transition jump will be discussed in the next section.

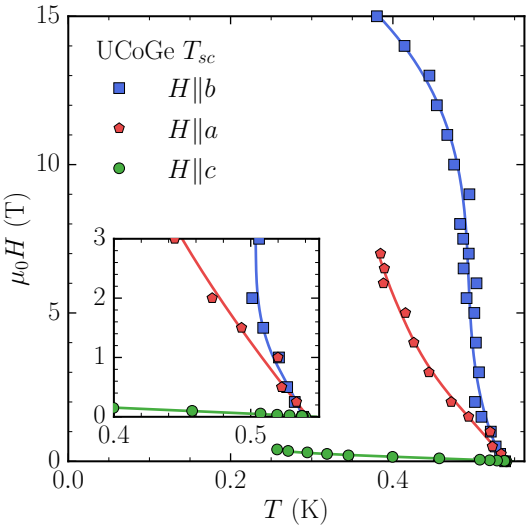


**Fig. 5.13:** *Phase diagram of UCoGe by specific heat measurements. Lines are guides to the eyes. Inset: enlargement for fields below 3 T.*

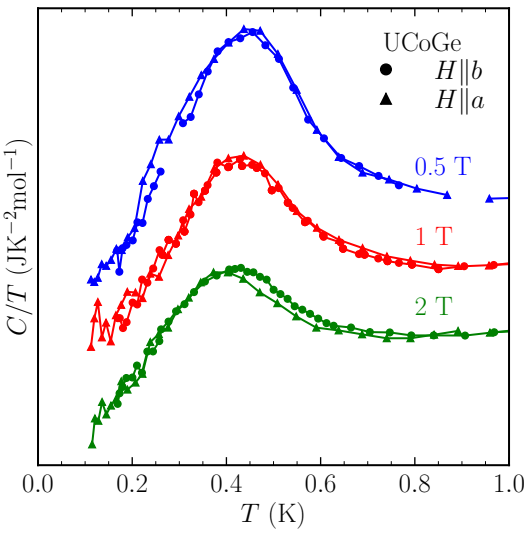


**Fig. 5.14:** *specific heat superconducting transitions for H||**a** and H||**b** at 0.5, 1 and 2 T. Curves have been shift for clarity.*

The phase diagram is shown in Figure 5.13. We recover the large anisotropy already found in other studies between the **a**,**b** axes and the **c** axis [11]. $H^{\mathbf{a}}_{c2}$ and $H^{\mathbf{b}}_{c2}$ have the same slopes at $T_{sc}$ and are identical below 1 T(inset Figure 5.13). This is also seen with a direct comparison of the specific heat transitions: they are superposed below 1 T. The comparison is shown in Figure 5.14. Thus near $T_{sc}$: $H^{\mathbf{a}}_{c2} = H^{\mathbf{b}}_{c2}$. The slope at $T_{sc}$ for the **a** and **b** axes is of $-53 \pm 4$ T/K, while along the **c** axis it is 50 times lower: $-1 \pm 0.1$ T/K.

The slope at $T_{sc}$ for H||**c** is determined with the points above 15 mT, because below this field, $H^{\mathbf{c}}_{c2}$ is vertical due to magnetic domains, as shown in Figure 5.15 (see explanation after in section 5.3.1).

The anisotropy of $H_{c2}$ is strong and similar to that of a quasi 2D material. However, UCoGe is 3D. Such an anisotropy of $H_{c2}$, as explained in the introduction, comes from the sharp suppression of the superconducting coupling when field is applied H||**c** (see section 1.2.1).

Away from the region near $T_{sc}$, $H^{\mathbf{b}}_{c2}$ is almost vertical up to 10 T. The S-shape found in some transport measurements [11] is not recovered, which is in agree-

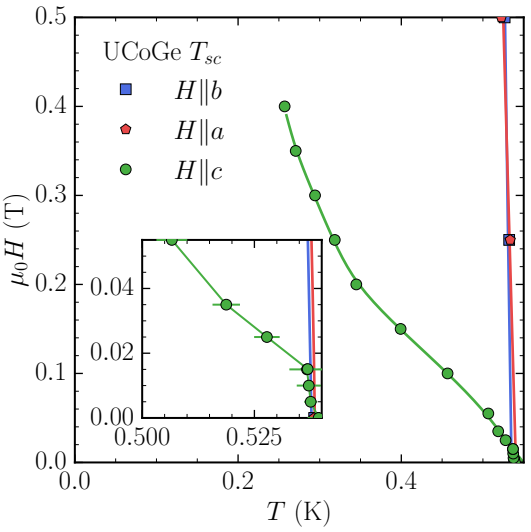


**Fig. 5.15:** *Enlargement of the phase diagram on $H^c_{c2}$. Inset: enlargement of the fields below 50 mT.*

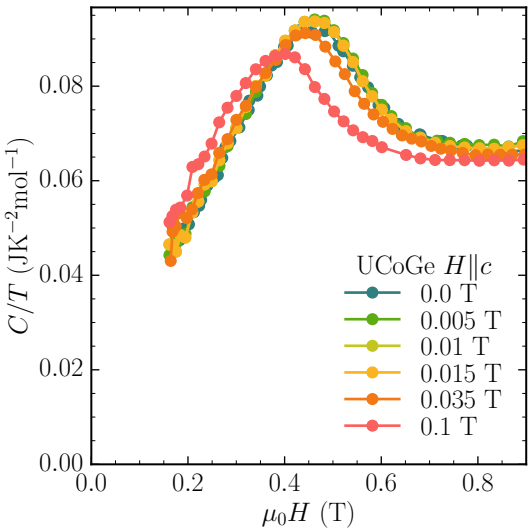


**Fig. 5.16:** *Superconducting transitions at very low fields for H‖**c**.*

ment with previous specific heat study [102] and thermal expansion measurement. But, the near vertical $H^b_{c2}$ and the positive upturn above 1 T does confirm the field reinforcement of $H^b_{c2}$. The inset of Figure 5.13 emphasises the completely unusual deviation from linearity with positive curvature close to $T_{sc}$.

For H‖**a** we could not follow the superconducting transition above 7 T, due to experimental limitation, but its upward curvature is similar to that obtain in resistivity measurements [11].

$H^c_{c2}$ is shown in Figure 5.13. It also exhibits a positive curvature as expected from different measurements [8, 140].

### 5.3.1 H‖*c very low fields behaviour*

Figure 5.16 shows the superconducting transitions at different very low fields for H‖**c**. Below 15 mT the transition does not evolve, the $T_{sc}$ remains identical. It results in a vertical $H^c_{c2}$, within the error bars, below 15 mT as shown in inset of Figure 5.15. This behaviour has been seen in URhGe with transport measurements, and is attributed to the internal field: see Figure 5.17 from ref [43]. It was expected that UCoGe should show the same behaviour. It had never been clearly observed due to the smaller spontaneous magnetisation compared to URhGe. Resistivity measurements can also be influenced by superconducting filaments near $T_{sc}$ inducing a tail to $H_{c2}$, thus a vertical $H_{c2}$ could not be detected.

To understand the mechanism, when a field is applied, the domain walls are moved so that the field inside the sample is equal to zero. When H reaches the

value where the magnetisation is saturated ($M_s$), only one single domain remains. If $u_\uparrow$ is the proportion of $\uparrow$ oriented domains, then:

$$M = (u_\uparrow - (1 - u_\uparrow))M_s = (2u \uparrow -1)M_s \tag{5.1}$$

The field in the crystal $\mathbf{H}_{sample}$ is equal to $\mathbf{H} + \mathbf{H}_d$, where the demagnetisation field $\mathbf{H}_d = -\mathbf{NM}$ (N the demagnetising factor). The total energy of these magnetic domains is:

$$E_{tot} = E + E_d + E_H \tag{5.2}$$

$$E_{tot} = E_0 + (-\frac{\mu_0}{2}\mathbf{H}_d\mathbf{M}) + (-\mu_0\mathbf{MH}) \tag{5.3}$$

$$E_{tot} = E_0 + \frac{\mu_0}{2}N(2u_\uparrow - 1)^2M_s^2 - \mu_0\mathbf{MH} \tag{5.4}$$

The equilibrium of the system for each value of H is reached when:

$$\frac{\partial E_{tot}}{\partial u_\uparrow} = 0 \tag{5.5}$$

$$(2u_\uparrow - 1)NM_s = H \tag{5.6}$$

We can conclude with eq 5.6 and 5.1 that the applied field $\mathbf{H}$ is equal to $\mathbf{NM}$. And as a consequence, $\mathbf{H}_{sample} = \mathbf{H} + \mathbf{H}_d$ is equal to 0. When $H < NM_s$, $H_{sample} = 0$. While when $H > NM_s$, $H_{sample} = H - NM_s$. Thus, below $M_s$ the field seen by the electrons is constant and not equal to the applied field. Concretely the electrons experience a magnetic induction B as:

$$B = B_{loc} + \mu_0 H_{sample} \tag{5.7}$$

$$B = B_{loc} + \mu_0(H + H_d) \tag{5.8}$$

Where $B_{loc}$ is the local induction equal to $\mu_0\alpha M_s$ (Clausius Mossotti): as ferromagnetism is probably itinerant in UCoGe, the field perceives by the charge carriers is the internal field minus the one created by the charge carriers themselves; for a dipolar field, it is opposed and proportional to the magnetisation, hence $B = B_{sample} - (-\alpha\mu_0 M_s) = \alpha\mu_0 M_s$.

So when $H < NM_s$, $B = \mu_0\alpha M_s$; and when $H > NM_s$, $B = \mu_0(\alpha M_s - NM_s + H)$.

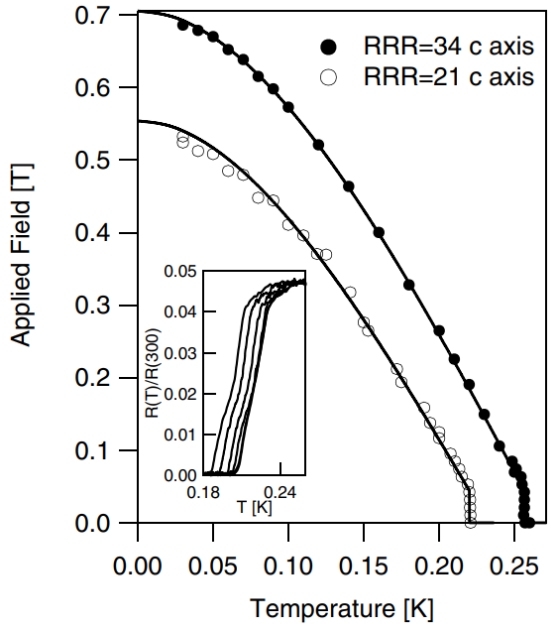


**Fig. 5.17:** $H_{c2}$ *of URhGe determined by resistivity measurements for field along the easy magnetisation axis. Note the verticality below* 50 *mT. From ref [43].*

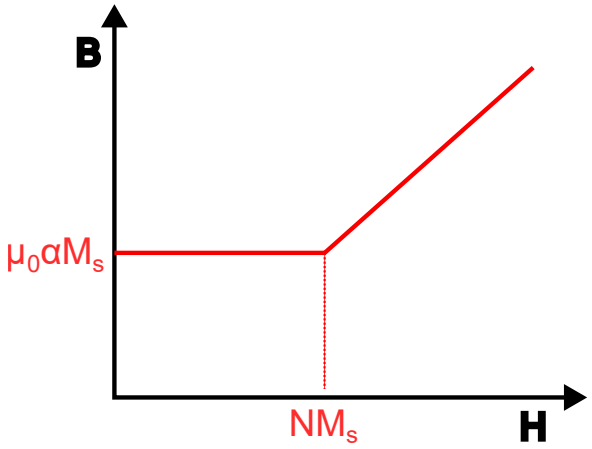


**Fig. 5.18:** *Magnetic induction B seen by the electrons as a function of applied field H, in a ferromagnetic superconductor.*

The behaviour of B is summarised in the schema Figure 5.18. From zero field the electrons see a constant field until H overpasses $NM_s$. This is why $H_{c2}$ is vertical at very low fields in URhGe and in UCoGe.

In the case of UCoGe, previous magnetisation measurements determined that $M_s$ is reached for a field around 15 mT [107], which is the same order as the field where $H_{c2}$ is vertical in our specific heat measurements (Figure 5.15).

For $H \| \mathbf{b}$ and $H \| \mathbf{a}$ this effect might not be present. Indeed, for these axes, $\mathbf{M}_s \cdot \mathbf{H} = 0$, because $\mathbf{M}_s$ is along the **c** axis.

### 5.3.2 *Determination of* $\lambda(H)$

From the $H_{c2}$ established by our specific heat measurements we can determine the field dependence of the strong-coupling constant $\lambda(H)$. To do this, we used the same model and procedure as previously for $UTe_2$.

For UCoGe, as emphasized by the relatively small ratio $\frac{\Delta C}{\gamma T_{sc}}$, the weak-coupling regime is assumed. The value of $\lambda(H = 0)$ is set to 0.58 as in the previous study [140].

The second assumption is that the normal phase is isotropic: we assumes that the average Fermi velocities $\bar{v}_F^{i,bare}$ are equal along each axis $i$. Therefore, the $H_{c2}$ anisotropy arises only from the difference in the field dependences of $\lambda$. This assumed isotropy is supported by quantum oscillations measurements detecting small spherical Fermi pocket [13].

The slopes at $T_{sc}$ of $H_{c2}^{\mathbf{a}}$ and $H_{c2}^{\mathbf{b}}$, that are identical below 1 T, are used to determined $\bar{v}_F^{bare}$.

As explained just before, for $H\|\mathbf{c}$, $H_{c2}^{\mathbf{c}}$ is vertical below 15 mT ($= NM_s$) due to the magnetic domain. When the field is below 15 mT, the magnetic induction is constant, so $\lambda$ too. Therefore, to determine $\lambda(H\|\mathbf{c})$, $H_{c2}^{\mathbf{c}}$ has been shift down by 15 mT.

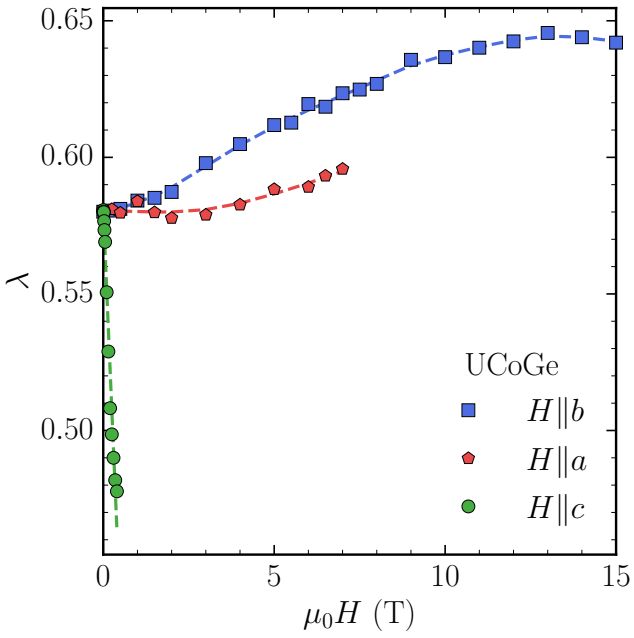


**Fig. 5.19:** $\lambda(H)$ *determined from* $H_{c2}$ *established by our specific heat measurements. Dashed lines are guide to the eyes.*

Figure 5.19 shows the field dependence of $\lambda$ for the three axes. As expected, for $H\|\mathbf{c}$, $\lambda$ is strongly suppressed and $\frac{d\lambda}{dH}\big|_{H=0} < 0$ .

For $H\|\mathbf{a}$ and $H\|\mathbf{b}$, $\lambda$ is roughly constant below 1 T, and then increases relatively slightly compared with $H\|\mathbf{c}$.

For H‖**b**, λ(H) seems to exhibit a maximum near 12.5 T, the field range where the Curie temperature vanishes. Measurement at higher fields would be necessary to confirm this maximum.

### 5.3.3 *Width of the transitions H‖**b***

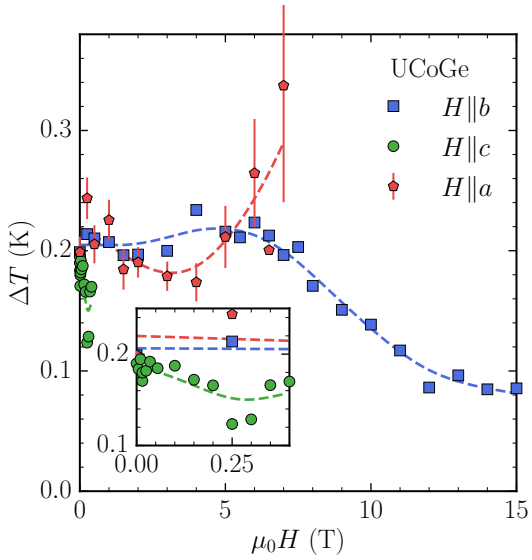


**Fig. 5.20:** *Superconducting transitions widths* ΔT *as function of field along the three axes. Dashed lines are guide to the eyes. Inset: enlargement of the low-field region.*

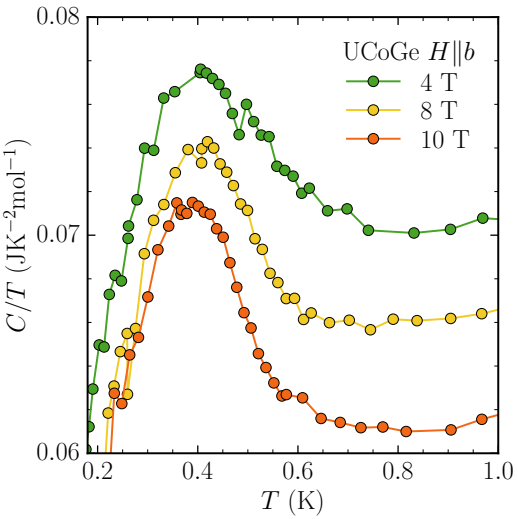


**Fig. 5.21:** *Superconducting transitions* H‖***b*** *at several fields where it becomes na. The curves are shifted between each other for clarity.*

The transitions widths as function of field are shown in Figure 5.20. Due to the broad transitions and the large hyperfine contribution, the dispersions of the widths are higher than for $UTe_2$, especially H‖**a** above 5 T. Nevertheless, we can discuss the overall trends.

For H‖**a** the transition width is decreasing slightly, and ends up increasing above 5 T even if the error bars becomes large.

For H‖**c**, the width seems roughly constant taking into account the dispersion. The two points at 250 mT and 300 mT are certainly wrong considering their smaller values compared to the other points.

For H‖**b**, it is clear that the width decreases above 5 T (the transition becomes sharper). It is visible on the raw data. Figure 5.21 compares the transitions at several fields for H‖**b**, highlighting their narrowing. This effect is already known from resistivity measurements and also thermal conduction measurements [139]. More recently ac susceptibility measurements have also detected this reduction of the width [56].

This narrowing of the transition might be related to a change in the mixed state [139]. In UCoGe above 8 T, the $H_{c2}$ determined by resistivity (R = 0) have been shown to be lower than the one determined by thermal conduction measurements

(see Figure 5.22 from [139]). A possible origin is a strong decrease of the vortex pinning, inducing a large reversible region below $T_{sc}$ where R remains finite due to the flux flow despite the bulk superconductivity.

This kind of behaviour is also observed in the HF phase of $UTe_2$ [116]. In both cases, it is rather unexpected, the only known example where this happens being 2D superconductors like high-$T_{sc}$ cuprates or organic superconductors.

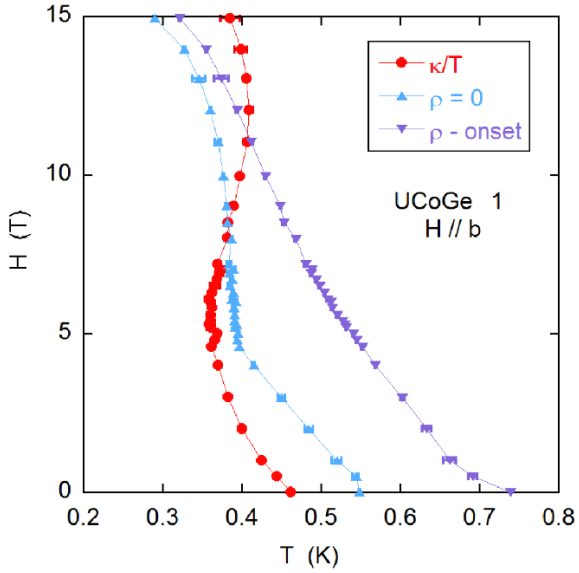


**Fig. 5.22:** *Phase diagram H‖**b** from ref [139]. It shows $H_{c2}$ determined with thermal conductivity measurements, and with resistivity measurements according to two criterion which highlight the transition width dependence in field.*

It will be interesting to also measure the resistive transition on the same sample and compare the $H_{c2}$ obtained from specific heat and resistivity measurements.

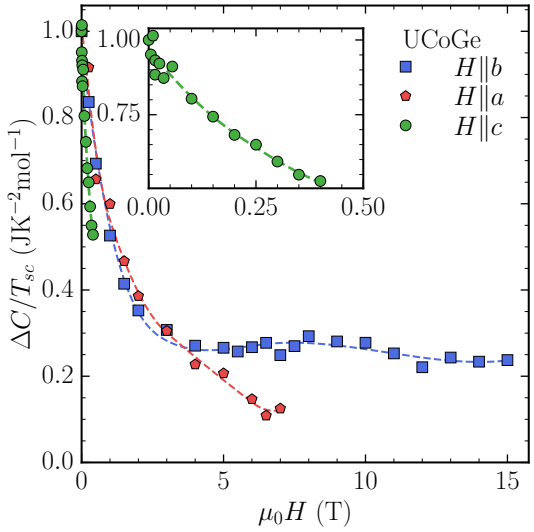


**Fig. 5.23:** *Transition jump* $\Delta C/T_{SC}$ *at* $T_{sc}$ *as a function of field* H. *Dashed lines are guide to the eyes. Inset: enlargement for field below* 500 *mT.*

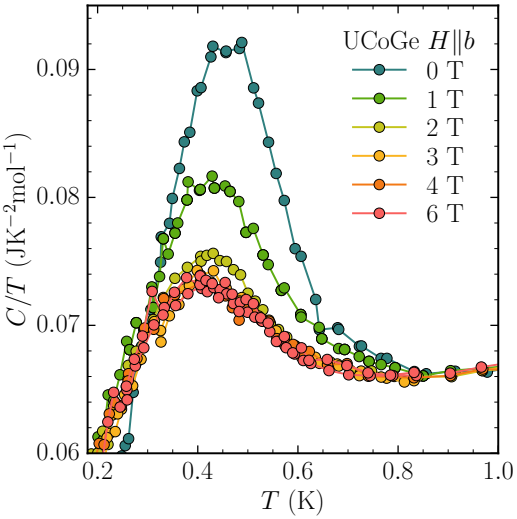


**Fig. 5.24:** *Superconducting transitions* H$\|$***b*** *at different fields below* 6 *T.*

## 5.4 SUPERCONDUCTING TRANSITION JUMP

The transition jumps at $T_{sc}$ as function of field are shown in Figure 5.23. As expected the jump decreases with field, but for H$\|$**b** and H$\|$**a** the decrease is particularly fast which can be considered as an anomalous behaviour. The most remarkable effect is for H$\|$**b**. Figure 5.24 shows the superconducting transition H$\|$**b** for different fields. The jump collapses by 70% above 3 T and then remains roughly constant up to 15 T. This collapse happens at fields ($H < 3$ T) where the Curie temperature $T_C$ does not change, so we can exclude a possible influence of the ferromagnetic transition on the superconducting one in this field range.

This behaviour is similar to that of $UTe_2$ for H$\|$**b** at high field (Figure 3.26). In $UTe_2$, near 15 T the LF transition jump has a sudden decrease and then remains roughly constant up to 20 T. The superconducting transition jump in $CeRh_2As_2$ also has sudden change of behaviour at fields close to its multicritical point (Figure 3.28).

In UCoGe, such a change of behaviour at 3 T could also be the signature of a superconducting phase change. The **d**-vector is expected to be perpendicular to **c** axis at zero field, but when field is applied H$\|$**b**, the **d**-vector could rotate in the (**a**,**b**) plane, so as to be perpendicular to the **b** axis in order to reduce the Zeeman effect (suppressing the paramagnetic limitation). Figure 5.25 shows the phase diagram H$\|$**b**. The dashed line in the phase diagram represents the field at which the **d**-vector could be perpendicular to the applied field when its rotation is complete. However, the rotation of the **d**-vector can be expected to begin at very low fields.

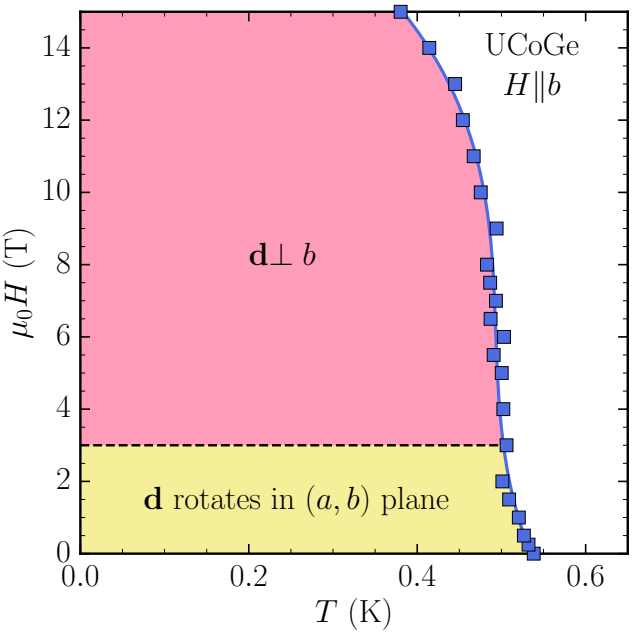


**Fig. 5.25:** *Phase diagram* H‖***b*** *with the hypothetical two superconducting phases. The dashed line corresponds to* 3 *T, when transition jump becomes constant.*

Field sweeps were performed between 0 T and 4 T at 300 mK, the lowest temperature we could achieve to measure properly. No anomaly has been detected. However, it does not mean there no transition in this region. More precise measurements as well as magnetostriction or ultrasound measurements should be performed at these fields to check if a transition is visible are not. Indeed, from the Ehrenfest relations, if the transition line is horizontal, no anomaly is expected in the specific heat.

The same mechanism could be expected for H‖**a**, a rotation of the **d**-vector in order to be perpendicular to the **a** axis. The strong decrease of the jump might be the sign of such a rotation. However, we could not follow the superconducting transition above 7 T, so we cannot say if the transition jump will end up being constant like for H‖**b**.

### *Jump versus* $T_{SC}$

When plotted against $T_{sc}/T_{sc}(H = 0)$, the transitions jumps normalised by the value at zero field have an unusual behaviour for the three axes, and show a strong anisotropy. Figure 5.26 compares the transitions jumps normalised against $T_{sc}/T_{sc}(H = 0)$ in UCoGe and $UTe_2$ for H‖**b**. The curves of UCoGe are clearly shifted compared to $UTe_2$ H‖**b**, toward lower $T_{sc}/T_{sc}(H = 0)$ for H‖**c** and higher $T_{sc}/T_{sc}(H = 0)$ for H‖**b** and **a**. We could conclude this anisotropy is a consequence of the critical field anisotropy. However, even if the anisotropy is much less pronounced in $UTe_2$, we do not recover such an anisotropy of the jump against

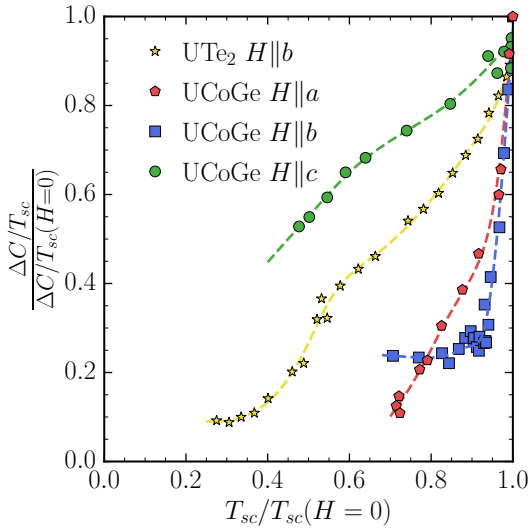


**Fig. 5.26:** *Specific heat jumps normalised by the value at* $H = 0$ *as a function of* $T_{sc}$ *normalised at* $H = 0$.

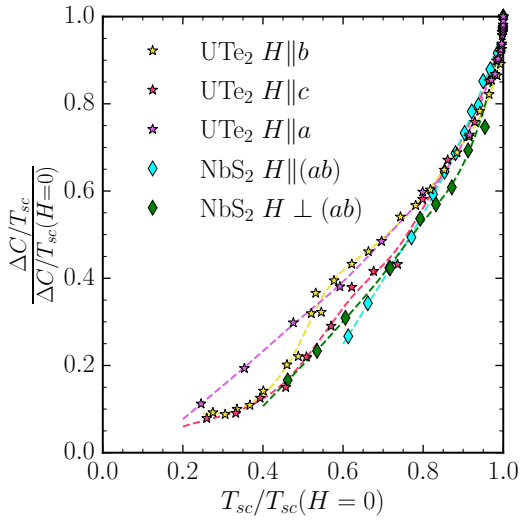


**Fig. 5.27:** *Specific heat normalised by the value at* $H = 0$ *as a function of* $T_{sc}$ *normalised at* $H = 0$ *for UTe$_2$ and NbS$_2$ from ref [66].*

$T_{sc}/T_{sc}(H = 0)$ (see Figure 5.27). In Figure 5.27, the transition jumps of $NbS_2$ from ref [66] are also shown. And again no anisotropy is found.

In fact, the anisotropy of the transition jumps in UCoGe can be explained by a variation of the coupling. To remember, in a weak coupling regime, $\lambda$ is related to $T_{sc}$ at zero field by:

$$T_{sc} \sim \Omega \exp\left(-\frac{1}{\lambda - \mu^*}\right) \tag{5.9}$$

For $H\|\mathbf{c}$, the strong-coupling constant $\lambda$ decreases with field. Thus, the $T_{sc}$ at zero field corresponding to a $\lambda$ at a given field is lower than the $T_{sc}$ measured at zero field.

Figure 5.28 shows $H_{c2}$ calculated for different values of $\lambda$, with the same model used for $UTe_2$ (section 4.2.1), and emphasize the change of $T_{sc}(H = 0)$ depending of $\lambda$. So, when we compare the jumps normalised at 0 T to $T_{sc}/T_{sc}(H = 0)$, this ratio is too low because $T_{sc}(H = 0)$ should be the one for $\lambda(H)$, so lower than the one measured. This explains that the curve for $H\|\mathbf{c}$ in Figure 5.26 points to a jump of C/T remaining anomalously high for low value of $T_{sc}/T_{sc}(H = 0)$. The same demonstration can be done on axes **a** and **b**, with an increasing $\lambda$ explaining the shift to higher $T_{sc}/T_{sc}(H = 0)$.

However, for these two axes, the sharp drop of the jump seen for field below 3 T can also influence the anisotropy seen in Figure 5.26.

However, in $UTe_2$ the coupling also varies with field, and no such anisotropy is seen. The difference is: $UTe_2$ is in a strong-coupling regime, so the jumps are enhanced when the strong-coupling constant increases. And when $\lambda$ decreases the

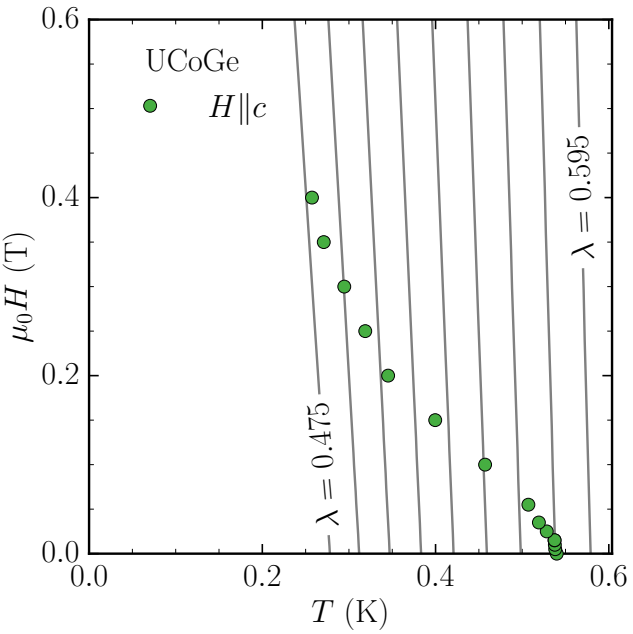


**Fig. 5.28:** *Critical fields calculated for different* $\lambda$ *for* $H \| \mathbf{c}$ *are depicted as grey lines (increment of* 0.015 *for* $\lambda$*). The same model as* $UTe_2$ *is used for the calculations. The experimental* $H_{c2}$ *established by specific heat measurements is shown by green circles.*

jumps too. So both effects, the decreases of $T_{sc}$ $(H = 0)$ and the decrease of the jump with $\lambda$, compensate each other.

In the case of UCoGe, it is most likely that the coupling is weak, so the effect of the strong-coupling constant on the jump magnitudes is negligible. That is why we can see such an anisotropy. This is an indirect support that UCoGe is in a weak coupling regime .

To go a step further in the analysis, with the $H_{c2}$ calculated to extract $\lambda(H)$ for $H \| \mathbf{c}$, we can determine the $T_{sc}$ at zero field for each $\lambda$: $T_{sc}^{H}(H = 0)$. Then the specific heat jumps normalised at zero field are plotted against $\frac{T_{sc}}{T_{sc}^{H}(H=0)}$. The result are shown in Figure 5.29.

The anisotropy between the **c** axis and the two other axes vanishes. It confirms that this anisotropy was induced by the field dependence of the coupling strength as explained above.

However, we do not recover an unusual behaviour like $UTe_2$. For $H \| \mathbf{b}$ and $H \| \mathbf{a}$ it can be understood by the strong decrease in field of the specific jump below 3 T, which might be due to a rotation of the **d**-vector.

For $H \| \mathbf{c}$, it might comes from the assumption that the Fermi velocity is isotropic. If this assumption is wrong, and the average Fermi velocity along the **c** axis is lower, therefore the initial slope at $T_{sc}$ would be smaller for $H \| \mathbf{c}$ and the decrease of $\lambda$ would be less strong. Hence, the decrease of $T_{sc}^{H}(H = 0)$ would also be lower.

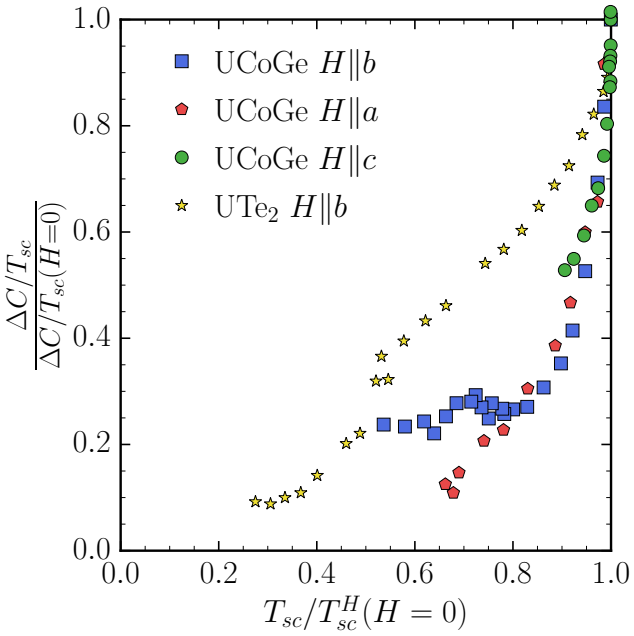


**Fig. 5.29:** *Specific heat jumps normalised by the value at* $H = 0$ *as a function of* $T_{sc}$ *normalised by* $T_{sc}^{H}(H = 0)$ *determined from the fit of* $H_{c2}^{c}$.

## 5.5 CONCLUSION ON UCoGe

One of the main goals for studying again UCoGe was to have a new look at the phase diagram for $H\|\mathbf{b}$ after what have been done on $UTe_2$.

In UCoGe the reinforcement of $H_{c2}^{b}$ happens without a trace on the specific heat anomaly. The shapes remain the same: the width progressively narrows probably due to a change of pinning in the mixed state, and the specific heat jumps remain constant after a strong initial decrease below 3 T.

The strong contrast between these two systems, UCoGe and $UTe_2$, is most likely due to the fact that the same pairing mechanism is controlling the pairing over the whole field range in UCoGe.

This is strongly supported by the recent NMR results [56] which show that at the field induced quantum critical point (12.5 T), $1/T_1T$ and $1/T_2T$ are enhanced, but only due to the same Ising fluctuations along the easy **c** axis (see Figure 5.30).

Beside a possible transition at very low field due to a rotation of the **d**-vector, there is probably no transition between different superconducting phases to expect in UCoGe.

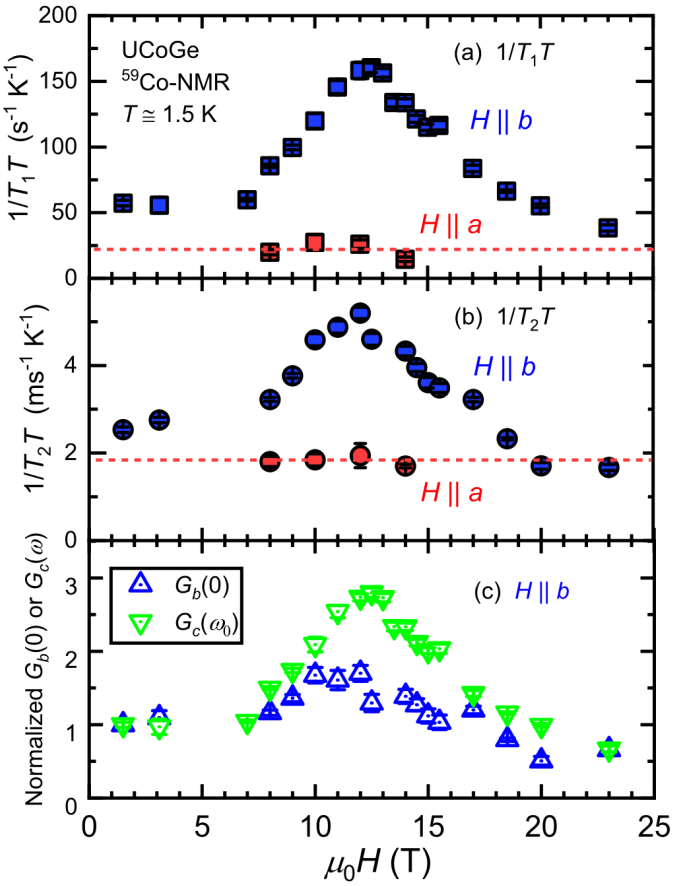


**Fig. 5.30:** *Field dependence of* $1/T_1T$ *(a) and* $1/T_2T$ *(b) measured for* $H \| \boldsymbol{a}$ *and* $H \| \boldsymbol{b}$.
$1/T_1T$ *is equal to* $G_\perp(\omega_0)$. *In UCoGe, the susceptibility along the* ***c*** *axis is much larger than along the* ***a*** *axis, thus* $1/T_1T$ *is equal to* $G_c(\omega_0)$ *when field is applied along the* ***b*** *axis.* $1/T_2T$ *is equal to* $\alpha G_\perp(\omega_0) + G_\parallel(0)$, *so it is equal to* $\alpha G_c(\omega_0) + G_b(0)$ *when field is applied along the* ***b*** *axis.*
*These functions* $G_x(\omega)$ *are the spectral density of the fluctuating hyperfine field* $h_x$, *which is the field generated at the nucleus by its surrounding electrons and magnetic dipoles, and are defined as:* $G_x(\omega) = \int_{-\infty}^{\infty} \langle h_x(t) h_x(0) \rangle \exp(i\omega t)$.
*(c) The field dependence of the spectral densities* $G_b(0)$ *and* $G_c(\omega_0)$ *derived from* $1/T_1T$ *and* $1/T_2T$ *for* $H \| \boldsymbol{b}$.
*From ref [56].*

# 6

# GLOBAL CONCLUSION

$UTe_2$ quickly drew a lot of attention due to its unique properties and especially its strong magnetic field resistance. Due to the similarities with the ferromagnetic superconductors UCoGe and URhGe, the possibility of spin-triplet superconductivity induced by ferromagnetic fluctuations was quickly proposed.

In this work, $UTe_2$ and UCoGe have been investigated by the use of specific heat measurements at low temperatures and high fields (up to 36 T for $UTe_2$). The first complete thermodynamic phase diagrams have been established for the two compounds.

We can conclude that $UTe_2$ and UCoGe share two main features: a superconducting pairing mechanism influenced by magnetic field, and possibly a pairing induced by ferromagnetic fluctuations, at least in the low-field phase for $UTe_2$.

Specific heat measurements on $UTe_2$ could show the presence of two phases when the field is applied along the hard magnetisation axis (**b** axis), one at low field below 15 T and the second emerging above 15 T up to the metamagnetic transition at $H_m = 34.7$ T. Furthermore, this two phases have different pairing mechanisms . This change of mechanism is revealed by the drastic change in the shape of the specific heat transition of $H_{c2}^{\mathbf{b}}$. The high-field phase has a superconducting transition that is ten times broader than the transition in the low-field phase.

At low fields, the superconducting phase could be induced by ferromagnetic fluctuations. This is confirmed by the strong curvature of the critical field along the easy magnetisation (**a** axis), which reveals a suppression of the pairing strength. This result is reminiscent of studies on ferromagnetic superconducting compounds, especially UCoGe.

At high fields, the second phase detected above 15 T could be a spin-singlet phase induced by antiferromagnetic fluctuations that are enhanced on approaching $H_m$.

The competition between ferromagnetic and antiferromagnetic fluctuations has already been suggested in several theoretical studies and has been advanced to explain the phase diagram under pressure. This phase diagram under pressure is linked to the one obtained for $H\|\mathbf{b}$, so it is not unreasonable to imagine that the same competition is influenced by the magnetic field.

Without going too far, it can be concluded that the low-field and high-field phases have different mechanisms, regardless of their actual nature. This makes $UTe_2$ a unique case among superconductors where competing mechanisms influenced by the magnetic field at ambient pressure. This could make it an ideal

compound for theoretical models to better understand the conditions for the emergence of spin triplet superconductivity.

UCoGe, on the other hand, shows no change in the pairing mechanism. Our specific heat measurements confirm the very strong anisotropy of $H_{c2}$ due to the influence of the magnetic field on the ferromagnetic fluctuations that are at the origin of the superconductivity.

$H_{c2}$ for $H \| \mathbf{b}$ appears even more "vertical" in this higher quality sample than in the previous thermal transport measurements. However, $H_{c2}$ remains "smooth" and does not show any sign of an additional phase transition that would explain the field reinforcement for $H \| \mathbf{b}$.

However, the collapse of the specific heat jump for $H \| \mathbf{b}$ and $H \| \mathbf{a}$ at very low fields could be the sign of a rotation of the **d** vector. Such a change of symmetry is expected to minimise the Zeeman effect and to explain the absence of paramagnetic limitation along the **b** and **a** axis. Therefore, a transition in the superconducting state would be expected, requiring further experiments to detected it and theoretical studies to evaluate if such a rotation of the **d**-vector could explain our observation.

# 7

# RÉSUMÉS EN FRANÇAIS

## 7.1 CHAPITRE: INTRODUCTION ET QUELQUES BASES SUR LA SUPRACONDUCTIVITÉ

L'avancée majeure de ces 40 dernières années dans le domaine de la supraconductivité a été la découverte de plusieurs familles de supraconducteurs non-conventionnels : les fermions lourds, les composés organiques, les cuprates à haute $T_{sc}$ et les pnictides et les hydrides, par ordre chronologique. Tous sont contrôlés par des mécanismes d'appariement dominés par des interactions purement électroniques au lieu de l'interaction électron-phonon classique (BCS), sauf pour dans le cas des hydrides. Ces nouveaux mécanismes d'appariement conduisent également à de nouveaux états supraconducteurs, avec différents états de spin possibles (spin-singlet ou spin-triplet). La nature de ces mécanismes d'appariement est aujourd'hui un sujet d'étude crucial pour une compréhension plus globale de la supraconductivité.

En 2018, la supraconductivité a été détectée pour la première fois dans le composé $UTe_2$ entre 1.4 K et 2 K. Rapidement, ce composé a attiré beaucoup d'attention en raison de ses propriétés uniques et de la possibilité d'être spin-triplet, un état d'appariement rare mais très recherché. La propriété la plus remarquable est de loin sa forte résilience au champ magnétique. La supraconductivité est détectée jusqu'à 60 T pour certaines directions de champ dans le cristal. Et pour des champs magnétiques appliqués le long de l'axe de difficile aimantation, la supraconductivité est renforcée au dessus de 15 T jusqu'à une transition métamagnétique aux alentours de 35 T.

Cependant, avant les mesures présentées dans ce manuscrit, peu de mesures thermodynamiques ont été effectuées sur $UTe_2$, et aucune preuve de supraconductivité dans le bulk n'a été fournie.

C'est une des raisons qui a motivé ces mesures de chaleur spécifique. L'autre motivation était d'avoir un angle d'attaque différent pour essayer d'élucider l'origine du mécanisme d'appariement et la symétrie de la supraconductivité sous champ. Actuellement, le mécanisme et la symétrie de l'appariement sont encore en débat avec de nombreuses mesures différentes prétendant à des scénarios opposés, et peu d'études théoriques reposant sur des calculs microscopiques.

Cette thèse se concentre principalement sur l'étude d'$UTe_2$ et de son champ critique, mais pour présenter ce composé et ses propriétés uniques, le meilleur point d'entrée sont les supraconducteurs ferromagnétiques et plus particulièrement UCoGe, qui est supraconducteur à 550 mK et ferromagnétique à 2.5 K. Ces

deux composés partagent des similitudes, notamment en ce qui concerne leurs champs critiques et le possible mécanisme d'appariement d'$UTe_2$.

Dans ce chapitre, tout d'abord, quelques bases de physiques sur la supraconductivité sont données, notamment sur les mécanismes à l'origine du champ critique $H_{c2}$, et sur la symétrie de l'appariement avec une introduction au vecteur **d** (le paramètre d'ordre des supraconducteurs spin-triplet).

Puis le composé UCoGe est introduit avec un focus sur son mécanisme d'appariement et son influence sur les $H_{c2}$. Dans ce composé la supraconductivité est induite par les fluctuations ferromagnétiques (fluctuations longitudinales selon l'axe de facile aimantation). Des mesures de RMN ont montré qu'un petite composante de champ selon l'axe de facile aimantation (axe **c**) engendre une suppression rapide des fluctuations, donc une diminution du couplage supraconducteur. Cela explique l'énorme anisotropie de $H_{c2}$ entre l'axe **c** et les deux autres axes, ainsi que la grande sensibilité à l'alignement dans le champ des échantillons.

Pour finir $UTe_2$ est introduit. Tout d'abord ses propriétés dans l'état normal, notamment la transition métamagnétique apparaissant à $H_m = 34$ T. Il s'agit d'un saut d'aimantation, aussi détecté dans des mesures de résistivité et des mesures de chaleur spécifique en champs pulsés. Puis sa phase supraconductrice est présentée ainsi que les différentes symétries possibles, ainsi que l'état actuel des recherches sur ce point. Un focus est fait sur l'axe **b** de difficile aimantation qui montre un renforcement de $H_{c2}$ au dessus de 15 T jusqu'à $H_m$.

## 7.2 CHAPITRE: CHALEUR SPÉCIFIQUE

Dans ce chapitre sont présentés quelque bases théoriques sur la chaleur spécifique. Notamment son comportement dans l'état normal dû aux phonons et à la contribution des électrons. L'effet de la supraconductivité est aussi présenté ainsi que la contribution du spin nucléaire à basse température.

Il existe une multitude de technique pour mesurer la chaleur spécifique. Pour les mesures présentées seulement deux ont été utilisées. La première est appelée technique "quasi-adiabatique". Le principe est d'appliquer de petits pulses de chaleur sur l'échantillon qui est connecté au frigo par un lien thermique. La réponse en température de l'échantillon durant l'entièreté de la séquence de pulse est utilisée pour extraire la chaleur spécifique.

Le montage pour cette technique est aussi présenté notamment pour expliquer comment la rigidité est obtenue afin d'éviter que le couple entre l'aimantation et le champ magnétique ne désaligne l'échantillon durant les mesures.

La deuxième technique est la calorimétrie ac reposant sur une oscillation imposée de la puissance de chauffage. La phase et l'amplitude de l'oscillation de la température de l'échantillon mesurée permet de déterminer la chaleur spécifique. L'avantage de cette technique est d'avoir des mesures quasi continu et de pouvoir effectuer facilement et rapidement des rampes en champ où en température. Cette technique a été utilisée pour les mesures à haut champ ($> 15$ T).

## 7.3 CHAPITRE: RÉSULTATS EXPÉRIMENTAUX SUR UTE$_2$

Ce chapitre présente les résultats des mesures effectuées sur $UTe_2$.

Le résultat principal est la détection d'une seconde phase supraconductrice au dessus de 15 T $H\|\mathbf{b}$. Elle se caractérise par l'émergence d'une seconde transition supraconductrice très large en température (350 mK). Cette seconde transition est suivie jusqu'à la transition métamagnétique à 34.75 T, où la supraconductivité est brusquement supprimée. Le champ critique $H_{c2}$ déterminé par cette transition montre un courbure positive comme dans les mesures de transport précédentes, validant l'hypothèse d'un renforcement de la supraconductivité par le champ. Cette phase sera appelée HF (High-Field).

La première transition supraconductrice quand à elle très raide (20 mK à 0 T), est suivie de 0 T jusqu'à 18.5 T $H\|\mathbf{b}$. Le $H_{c2}$ déterminé par cette transition s'extrapole jusqu'à 20 T. Cette phase sera appelée par LF (Low-Field).

La grande différence de largeur entre les deux transitions des deux phases supraconductrices pointe un changement de mécanisme d'appariement entre les deux phases.

Il existe plusieurs exemples dans le monde des supraconducteurs d'un changement de symétrie de l'état supraconducteur induit par le champ magnétique. Cependant un changement de mécanisme induit par le champ magnétique à pression ambiante comme observé dans $UTe_2$ est un cas unique dans le monde des supraconducteur.

En plus des résultats $H\|\mathbf{b}$, les mesures selon les autres axes sont aussi présentées. Un autre résultat important est la confirmation d'une très forte courbure du champ critique $H\|\mathbf{a}$. cette courbure pourrait être le signe d'une suppression du couplage supraconducteur selon cet axe et valider l'hypothèse des fluctuations ferromagnétiques à l'origine de la supraconduction.

Pour finir, les rampes en champ effectuées jusqu'à 36 T mettent en évidence une chute de la chaleur spécifique à la transition métamagnétique. Ces résultats sont mis en comparaison avec des mesures d'aimantation et de chaleur spécifique en champs pulsés d'études antérieures.

## 7.4 CHAPITRE: ANALYSE DES RÉSULTATS SUR UTE$_2$

Dans ce chapitre l'analyse des résultats est présentée et discutée.

Les $H_{c2}$ obtenues sont analysés à l'aide d'un modèle de champ critique établie pour les supraconducteurs propres *s*-wave. Les champs critiques dans la phase LF montrent tous un comportement anormal. Pour les décrire correctement il est nécessaire de faire varier la constante du couplage supraconducteur $\lambda$ avec le champ. Il en résulte que $\lambda$ diminue pour $H\|\mathbf{a}$, et augmente selon les deux autres axes. Cela serait cohérent avec l'hypothèse que la supraconductivité dans la phase LF est induite par des fluctuations ferromagnétiques, à l'image du supraconducteur ferromagnétique UCoGe.

Pour le $H_{c2}$ $H\|\mathbf{b}$ de la phase HF, sans surprise $\lambda$ augmente avec le champ comme sa courbure positive pouvait le laisser deviner. L'analyse est poussée un peu plus loin en calculant la transition supraconductrice HF en prenant une dispersion de $T_{sc}$ venant d'une dispersion de $\lambda$ à un champ donné, elle même provoquée par une dispersion de $H_m$ à la transition métamagnétique. Avec ce modèle la moitié de la largeur de la transition supraconductrice peut être expliquée. Cependant cela ne fonctionne uniquement pour un couplage spin-singlet, le cas spin-triplet échouant complètement. De plus dans le même cadre, la dépendance angulaire de la transition HF peut être expliquée en prenant en compte une possible mosaïcité du cristal de 3° et la dépendance angulaire de $H_m$.

De manière étonnante nos résultats démontreraient que la phase LF serait spin-triplet induite par des fluctuations ferromagnétiques, et que la phase HF quand elle serait spin-singlet. De plus cette phase HF serait liée à $H_m$, ce qui n'est pas étonnant en considérant le nombre de grandeurs qui semblent reliées à $H_m$ dans $UTe_2$ (aimantation, coefficient A...).

Ce scénario n'est pas impossible et serait à relier à ce qui est vue sous pression. En effet, sous pression une seconde phase supraconductrice apparait et des mesures non publiées à ce jour ont montré que la phase HF et cette deuxième phase supraconductrice sous pression sont identiques.

Des calculs microscopique ont montré que cette seconde phase sous pression serait spin-singlet et induite par des fluctuations antiferromagnétiques. Ces dernières ont d'ailleurs été détectées par des mesures de neutrons à pression ambiante et champ nulle.

Donc des fluctuations ferromagnétiques et antiferromagnétiques pourraient être en compétition, à bas champ les fluctuations ferromagnétiques seraient favorisées induisant une phase supraconductrices spin-triplet (LF). Puis lorsqu'un champ magnétique est appliqué, les fluctuations antiferromagnétiques prendraient le pas et induiraient une phase supraconductrice spin-singlet (HF).

Cependant si ce scénario est correct, il est attendue que la transition entre la phase LF et HF soit du premier ordre. Des mesures en dilution jusqu'à 120 mK ont donc été effectuées à très haut champ (jusqu'à 36 T). Malheureusement aucune hystéresis n'a été détectée, ce qui est possible si la transition est faiblement du premier ordre.

## 7.5 CHAPITRE: MESURES SUR UCoGe

Dans ce chapitre les résultats obtenues sur UCoGe sont présentés, sachant que les mesures sont toujours en cours ainsi que l'analyse au moment de la rédaction.

Les mesures sur UCoGe ont été plus difficile que pour $UTe_2$, car étaient plus sensibles aux puissances parasites. De plus une énorme contribution nucléaire due au Co a dû être retirée.

La transition ferromagnétique est observée et correspond à une anomalie à 2.77 K de largeur 853 mK. Elle est suivie en champ jusqu'à 15 T $H\|\mathbf{a}$. La hauteur du

saut a diminué mais $T_C$ reste identique comme attendue pour l'axe de difficile aimantation. Pour $H\|\mathbf{c}$ l'anomie s'effondre dès les petits champs comme attendue pour l'axe de facile aimantation. Son comportement lorsque $H\|\mathbf{b}$ n'est pas triviale. Sa largeur augmente et son saut diminue mais $T_C$ reste globalement identique. Cependant au alentour de 10 T, $T_C$ diminue fortement pour finir par rejoindre $H_{c2}^{\mathbf{b}}$ à 12 T. Dans cette même gamme de champs, une remonté de C/T à basse température apparait. Tout cela peut être mis en regard avec des mesures de RMN montrant un pique des fluctuations ferromagnétiques vers 12 T. Les fluctuations ferromagnétiques seraient renforcées par le champ tandis que $T_{sc}$ est supprimée.

Pour ce qui est du champ critique, on retrouve la même très forte anisotropie que les études précédentes. Les pentes à $T_{sc}$ sont identiques selon l'axe **a** et **b**, et elles sont 50 fois plus élevées que la pente à $T_{sc}$ selon l'axe **c**. Cela est la conséquence directe de la suppression du couplage dès que le champ est appliqué selon l'axe **c**.

Lorsque $H\|\mathbf{b}$, deux autres effets sur la transition supraconductrice sont intéressants. Premièrement, au dessus de 7 T la transition devient plus raide. Cela a déjà été observé dans des mesures de résistivité, conduction thermique et de susceptibilité magnétique.

Le deuxième effet est la rapide diminution du saut de la transition en dessous de 3 T. Puis jusqu'à 15 T la hauteur du saut reste constante. Cela rappelle les dépendances anormales obtenues dans $UTe_2$, ou $CeRh_2As_2$ lorsque la symétrie de l'appariement change. Dans UCoGe ce pourrait être le signe d'une rotation du vecteur **d** dans le plan (**a**,**b**) afin d'être perpendiculaire à **b** pour diminuer l'effet Zeeman. La même rotation est attendue selon l'axe **a**, cependant la transition n'a pu être suivie à plus haut champ que 7 T, et seulement un forte diminution anormale du saut est détectée sur toute la gamme de champ.

Les sauts normalisés à champ nulle tracés en fonction de la $T_{sc}$ normalisée par la valeur à champ nulle montrent une très forte anisotropie entre l'axe **c** et les axes **a** et **b**. De plus le comportement est différent de celui des autres supraconducteurs (s-wave, $UTe_2$, $MgB_2$...). Cela s'explique par l'effet de la variation du couplage supraconducteur dans le cadre d'un couplage faible.

Cela apporte une preuve supplémentaire d'un couplage faible, supprimé pour des champs selon l'axe de facile aimantation et renforcé selon les deux autres axes.

## 7.6 CONCLUSION

$UTe_2$ a rapidement attiré l'attention en raison de ses propriétés uniques et surtout de sa forte résistance aux champs magnétiques. En raison des similitudes avec les supraconducteurs ferromagnétiques UCoGe et URhGe, la possibilité d'une supraconductivité de spin-triplet induite par des fluctuations ferromagnétiques a rapidement été proposée.

Dans ce travail, $UTe_2$ et UCoGe ont été étudiés en utilisant des mesures de chaleur spécifique à basse température et à des champs élevés (jusqu'à 36 T pour

$UTe_2$). Les premiers diagrammes de phase thermodynamiques complets ont été établis pour ces deux composés.

Nous pouvons conclure que $UTe_2$ et UCoGe partagent deux caractéristiques principales: un mécanisme d'appariement supraconducteur influencé par le champ magnétique, et peut-être un appariement induit par des fluctuations ferromagnétiques, au moins dans la phase à faible champ pour $UTe_2$. Les mesures de chaleur spécifique sur $UTe_2$ ont pu montrer la présence de deux phases lorsque le champ est appliqué le long de l'axe de difficile aimantation (axe b), l'une à faible champ en dessous de 15 T et la seconde émergeant au-dessus de 15 T jusqu'à la transition métamagnétique à $H_m = 34,7$ T. De plus, ces deux phases ont des mécanismes d'appariement différents. Ce changement de mécanisme est révélé par le changement drastique de la forme de la transition de chaleur spécifique de $H_{c2}^{\mathbf{b}}$. La transition supraconductrice de la phase haut champ est dix fois plus large que celle de la phase bas champ.

À bas champ, la phase supraconductrice pourrait être induite par des fluctuations ferromagnétiques. Cela est confirmé par la forte courbure du champ critique le long de l'axe de facile aimantation (axe a), qui révèle une suppression de la force d'appariement. Ce résultat rappelle les études sur les composés supraconducteurs ferromagnétiques, notamment UCoGe. À haut champ, la deuxième phase détectée au-dessus de 15 T pourrait être une phase spin-singlet induite par des fluctuations antiferromagnétiques qui seraient renforcées à l'approche de $H_m$. Cette compétition entre les fluctuations ferromagnétiques et antiferromagnétiques a déjà été suggérée dans plusieurs études théoriques et dans la littérature pour expliquer le diagramme de phases sous pression. Ce diagramme de phases sous pression est lié à celui obtenu pour $H\|\mathbf{b}$, il n'est donc pas déraisonnable d'imaginer que la même compétition est influencée par le champ magnétique.

Sans aller trop loin, on peut conclure que les phases à bas champ et à haut champ ont des mécanismes différents, quelle que soit leur réelle nature. Cela fait d'$UTe_2$ un cas unique parmi les supraconducteurs où des mécanismes concurrents seraient influencés par le champ magnétique à pression ambiante. Cela pourrait en faire un composé idéal pour les modèles théoriques visant à mieux comprendre les conditions d'émergence de la supraconductivité triplet de spin.

UCoGe, en revanche, ne présente aucun changement dans le mécanisme d'appariement. Nos mesures de chaleur spécifique confirment la très forte anisotropie de $H_{c2}$ due à l'influence du champ magnétique sur les fluctuations ferromagnétiques à l'origine de la supraconductivité.

$H_{c2}$ pour $H\|\mathbf{b}$ apparaît encore plus "vertical" dans cet échantillon de meilleure qualité que dans les mesures de transport thermique précédentes. Cependant, $H_{c2}$ reste "lisse" et ne montre aucun signe d'une transition de phase supplémentaire qui expliquerait le renforcement du champ pour $H\|\mathbf{b}$.

Cependant, l'effondrement du saut de chaleur spécifique pour $H\|\mathbf{b}$ et $H\|\mathbf{a}$ à des champs faibles pourrait être le signe d'une rotation du vecteur $\mathbf{d}$. Un tel changement de symétrie devrait minimiser l'effet Zeeman et expliquer l'absence de limitation paramagnétique le long des axes **b** et **a**. Par conséquent, Il faut donc

s'attendre à une transition dans l'état supraconducteur, ce qui nécessite des études théoriques pour évaluer si une telle rotation du vecteur **d** peut expliquer notre observation de l'effondrement du saut de chaleur spécifique.

# APPENDIX

## A.1 SPECIFIC HEAT MEASUREMENTS ON $UTe_2$ SAMPLE #2

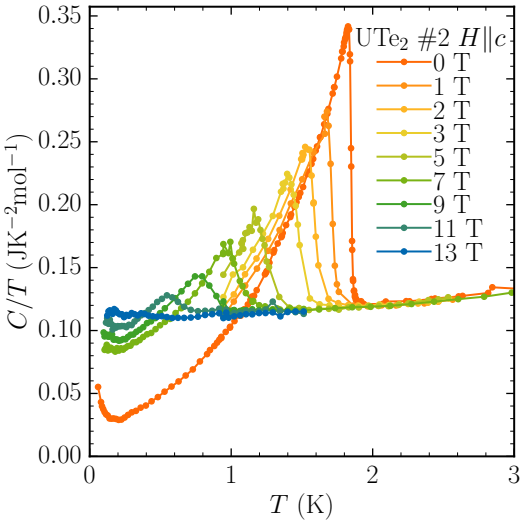


**Fig. A.1:** *Specific heat superconducting transition for* H||***c*** *on* $UTe_2$ *sample* #2.

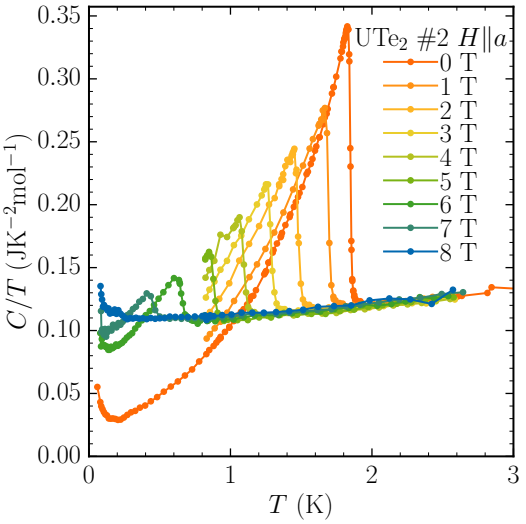


**Fig. A.2:** *Specific heat superconducting transition for* H||***a*** *on* $UTe_2$ *sample* #2

## A.2 SPECIFIC HEAT MEASUREMENTS ON $UTe_2$ SAMPLE #3

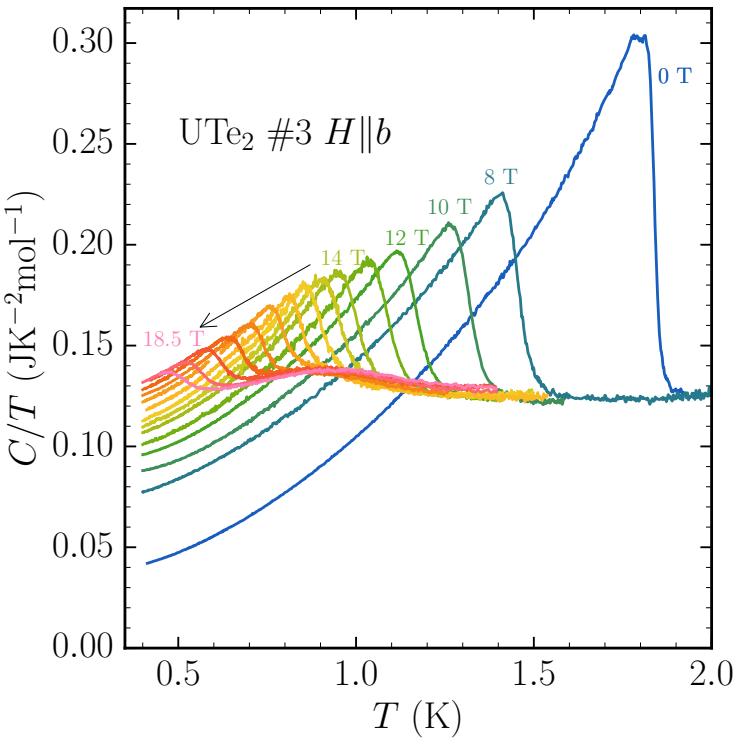


**Fig. A.3:** *Specific heat superconducting transitions (LF and HF) for* H||***b*** *on* $UTe_2$ *sample* #3 *measured by ac calorimetry.*

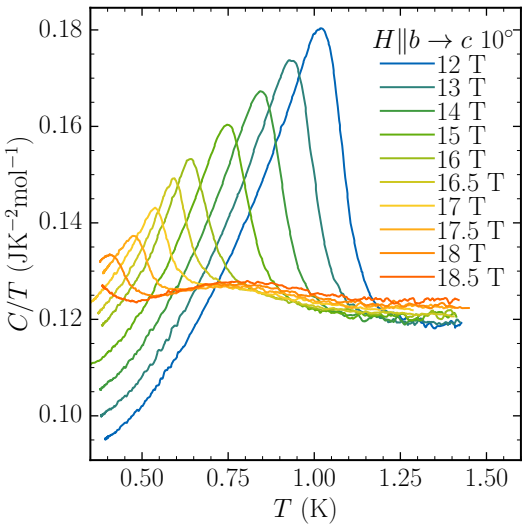


**Fig. A.4:** *Specific heat superconducting transitions (LF and HF) for* H *applied* 10° *away from* ***b*** *axis toward* ***c*** *axis, on* $UTe_2$ *sample* #3 *measured by ac calorimetry.*

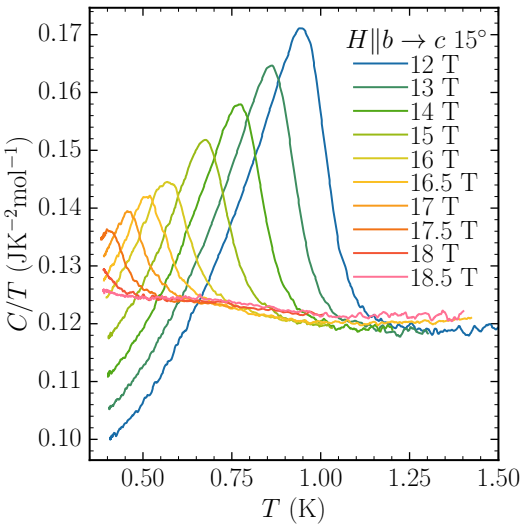


**Fig. A.5:** *Specific heat superconducting transitions (LF and HF) for* H *applied* 10° *away from* ***b*** *axis toward* ***c*** *axis, on* $UTe_2$ *sample* #3 *measured by ac calorimetry.*

## A.3 SPECIFIC HEAT MEASUREMENTS ON $GdLiF_4$

$GdLiF_4$ is long time known magnetic compound from the family of (Rare Earth)$LiF_4$. Despite an extensively used for adiabatic refrigeration, its basic magnetic properties are still largely unknown. No magnetic ordering has been observed down to 300 mK. Recent magnetisation measurements have detected magnetic transitions at 230 mK and 150 mK.

To confirm these transitions we did perform specific heat measurements down to 35 mK. The quasi adiabatic technique was used with the same setup as for $UTe_2$. Figure A.6 shows the temperature dependence of C/T at zero field. And Figure A.7 is an enlargement of the temperatures close to the anomalies.We can see three main anomalies at 200 mK, 140 mK and 90 mK.

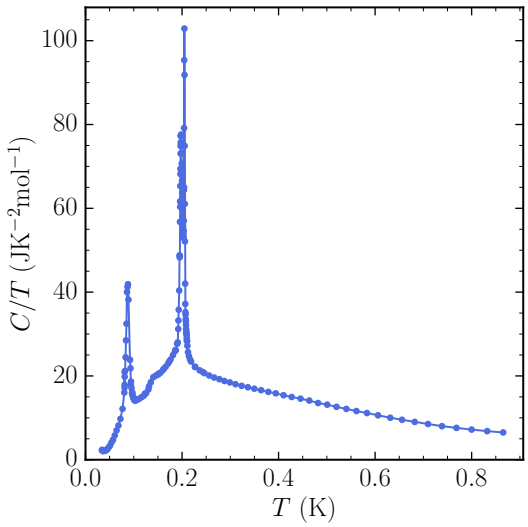


**Fig. A.6:** *Temperature dependence of the specific heat at zero field of* $GdLiF_4$.

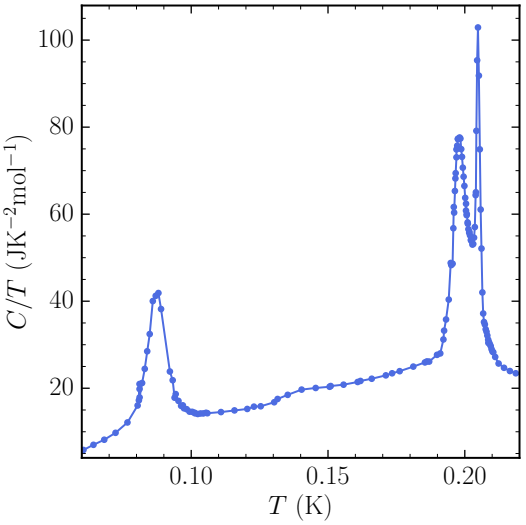


**Fig. A.7:** *Enlargement of the temperature dependence of the specific heat at zero field of* $GdLiF_4$*, near the three transitions.*

The transition at 200 mK is split into two peaks because of crystal symmetry and is believed to be an antiferromagnetic transition. What interests us is: it is a typical first order transition. The specific heat, especially for the first peak at 205 mK, almost diverge. Thus, when approaching this first peak, the heat pulses were strongly flattened because of the drastic increase of the specific heat. The $\delta T$ of the heat pulses had to be reduced to few per mile of the temperature, so the pulses did not crossed the transition.

If we had increased the temperature slowly by heating the sample continuously, when crossing this transition the temperature would have remained constant for a short time. However, it would have been impossible to distinguish whether this constant temperature came from the latent heat of the first order transition or from the divergence of the specific heat. Therefore, this method to characterise the order of the transition is useless in practise.

# BIBLIOGRAPHY


[1] A. Abragam. *The Principles of Nuclear Magnetism*. Clarendon Press, 1961. 666 pp. ISBN: 978-0-19-852014-6.

[2] S. Adenwalla et al. "Phase diagram of $UPt_3$ from ultrasonic velocity measurements." In: *Phys. Rev. Lett.* 65.18 (Oct. 29, 1990), pp. 2298–2301.

[3] T. Akazawa et al. "Pressure-Induced Superconductivity in Ferromagnetic UIr without Inversion Symmetry." In: *J. Phys.: Condens. Matter* 16.4 (Jan. 2004), p. L29. ISSN: 0953-8984.

[4] K. An et al. "Sign Reversal of Field-Angle Resolved Heat Capacity Oscillations in a Heavy Fermion Superconductor $CeCoIn_5$ and $d_{x^2-y^2}$ Pairing Symmetry." In: *Phys. Rev. Lett.* 104.3 (Jan. 22, 2010), p. 037002.

[5] P. W. Anderson. "Theory of Dirty Superconductors." In: *Journal of Physics and Chemistry of Solids* 11.1 (Sept. 1, 1959), pp. 26–30. ISSN: 0022-3697.

[6] D. Aoki et al. "Unconventional Superconductivity in UTe2." In: *J. Phys.: Condens. Matter* 34.24 (Apr. 2022), p. 243002. ISSN: 0953-8984.

[7] Dai Aoki and Jacques Flouquet. "Superconductivity and Ferromagnetic Quantum Criticality in Uranium Compounds." In: *J. Phys. Soc. Jpn.* 83.6 (June 15, 2014), p. 061011. ISSN: 0031-9015.

[8] Dai Aoki, Kenji Ishida, and Jacques Flouquet. "Review of U-Based Ferromagnetic Superconductors: Comparison between UGe2, URhGe, and UCoGe." In: *J. Phys. Soc. Jpn.* 88.2 (Feb. 15, 2019), p. 022001. ISSN: 0031-9015.

[9] Dai Aoki, William Knafo, and Ilya Sheikin. "Heavy fermions in a high magnetic field." In: *Comptes Rendus Physique*. Physics in High Magnetic Fields / Physique en champ magnétique intense 14.1 (Jan. 1, 2013), pp. 53–77. ISSN: 1631-0705.

[10] Dai Aoki et al. "Coexistence of Superconductivity and Ferromagnetism in URhGe." In: *Nature* 413.6856 (6856 Oct. 2001), pp. 613–616. ISSN: 1476-4687.

[11] Dai Aoki et al. "Extremely Large and Anisotropic Upper Critical Field and the Ferromagnetic Instability in UCoGe." In: *J. Phys. Soc. Jpn.* 78.11 (Nov. 15, 2009), p. 113709. ISSN: 0031-9015.

[12] Dai Aoki et al. "Ferromagnetic Quantum Critical Endpoint in UCoAl." In: *J. Phys. Soc. Jpn.* 80.9 (Sept. 15, 2011), p. 094711. ISSN: 0031-9015.

[13] Dai Aoki et al. "First Observation of Quantum Oscillations in the Ferromagnetic Superconductor UCoGe." In: *J. Phys. Soc. Jpn.* 80.1 (Jan. 15, 2011), p. 013705. ISSN: 0031-9015.

[14] Dai Aoki et al. "First Observation of the de Haas–van Alphen Effect and Fermi Surfaces in the Unconventional Superconductor UTe2." In: *J. Phys. Soc. Jpn.* 91.8 (Aug. 15, 2022), p. 083704. ISSN: 0031-9015.

[15] Dai Aoki et al. "Superconductivity Reinforced by Magnetic Field and the Magnetic Instability in Uranium Ferromagnets." In: *J. Phys. Soc. Jpn.* 80 (Suppl.A Jan. 2, 2011), SA008. ISSN: 0031-9015.

[16] Dai Aoki et al. "Unconventional Superconductivity in Heavy Fermion UTe2." In: *J. Phys. Soc. Jpn.* 88.4 (Apr. 15, 2019), p. 043702. ISSN: 0031-9015.

[17] Seokjin Bae et al. "Anomalous Normal Fluid Response in a Chiral Superconductor UTe2." In: *Nat Commun* 12.1 (1 May 11, 2021), p. 2644. ISSN: 2041-1723.

[18] L. Balicas et al. "Superconductivity in an Organic Insulator at Very High Magnetic Fields." In: *Phys. Rev. Lett.* 87.6 (July 19, 2001), p. 067002.

[19] J. Bardeen, L. N. Cooper, and J. R. Schrieffer. "Theory of Superconductivity." In: *Phys. Rev.* 108.5 (Dec. 1, 1957), pp. 1175–1204.

[20] D. Braithwaite et al. "Multiple Superconducting Phases in a Nearly Ferromagnetic System." In: *Commun Phys* 2.1 (1 Nov. 22, 2019), pp. 1–6. ISSN: 2399-3650.

[21] M. Brando et al. "Metallic Quantum Ferromagnets." In: *Rev. Mod. Phys.* 88.2 (May 31, 2016), p. 025006.

[22] L. N. Bulaevskii, O. V. Dolgov, and M. O. Ptitsyn. "Properties of Strong-Coupled Superconductors." In: *Phys. Rev. B* 38.16 (Dec. 1, 1988), pp. 11290–11295.

[23] Luke Pritchard Cairns et al. "Composition dependence of the superconducting properties of UTe2." In: *J. Phys.: Condens. Matter* 32.41 (July 2020), p. 415602. ISSN: 0953-8984.

[24] Gesina C. Carter. *Metallic Shifts in NMR : A Review of the Theory and Comprehensive Critical Data Compilation of Metallic Materials*. 1977.

[25] A. M. Clogston. "Upper Limit for the Critical Field in Hard Superconductors." In: *Phys. Rev. Lett.* 9.6 (Sept. 15, 1962), pp. 266–267.

[26] Leon N. Cooper. "Bound Electron Pairs in a Degenerate Fermi Gas." In: *Phys. Rev.* 104.4 (Nov. 15, 1956), pp. 1189–1190.

[27] Kazuhiko Deguchi et al. "Absence of Meissner State and Robust Ferromagnetism in the Superconducting State of UCoGe: Possible Evidence of Spontaneous Vortex State." In: *J. Phys. Soc. Jpn.* 79.8 (Aug. 15, 2010), p. 083708. ISSN: 0031-9015.

[28] Chunruo Duan et al. "Incommensurate Spin Fluctuations in the Spin-Triplet Superconductor Candidate $UTe_2$." In: *Phys. Rev. Lett.* 125.23 (Dec. 1, 2020), p. 237003.

[29] Chunruo Duan et al. "Resonance from Antiferromagnetic Spin Fluctuations for Superconductivity in UTe2." In: *Nature* 600.7890 (7890 Dec. 2021), pp. 636–640. ISSN: 1476-4687.

[30] A. G. Eaton et al. *Quasi-2D Fermi surface in the anomalous superconductor $UTe_2$*. Feb. 9, 2023. arXiv: 2302.04758 [cond-mat]. URL: http://arxiv.org/abs/2302.04758. preprint.

[31] G. M. Eliashberg. "Interactions between Electrons and Lattice Vibrations in a Superconductor." In: *Sov. Phys. JETP* 11.3 (1960), pp. 696–702.

[32] Yun Suk Eo et al. "c-axis transport in $UTe_2$: Evidence of three-dimensional conductivity component." In: *Phys. Rev. B* 106.6 (Aug. 24, 2022), p. L060505.

[33] W. A. Fertig et al. "Destruction of Superconductivity at the Onset of Long-Range Magnetic Order in the Compound $ErRh_4B_4$." In: *Phys. Rev. Lett.* 38.17 (Apr. 25, 1977), pp. 987–990.

[34] Ø. Fischer. "Chevrel phases: Superconducting and normal state properties." In: *Appl. Phys.* 16.1 (May 1, 1978), pp. 1–28. ISSN: 1432-0630.

[35] Hiroki Fujibayashi et al. "Superconducting Order Parameter in UTe2 Determined by Knight Shift Measurement." In: *J. Phys. Soc. Jpn.* 91.4 (Apr. 15, 2022), p. 043705. ISSN: 0031-9015.

[36] Shin-ichi Fujimori et al. "Electronic Structure of Heavy Fermion Uranium Compounds Studied by Core-Level Photoelectron Spectroscopy." In: *J. Phys. Soc. Jpn.* 81.1 (Jan. 15, 2012), p. 014703. ISSN: 0031-9015.

[37] Shin-ichi Fujimori et al. "Electronic Structure of UTe2 Studied by Photoelectron Spectroscopy." In: *J. Phys. Soc. Jpn.* 88.10 (Oct. 15, 2019), p. 103701. ISSN: 0031-9015.

[38] Peter Fulde and Richard A. Ferrell. "Superconductivity in a Strong Spin-Exchange Field." In: *Phys. Rev.* 135 (3A Aug. 3, 1964), A550–A563.

[39] W. J. Gannon et al. "Spin susceptibility of the topological superconductor $UPt_3$ from polarized neutron diffraction." In: *Phys. Rev. B* 96.4 (July 10, 2017), p. 041111.

[40] P. G. De Gennes. *Superconductivity Of Metals And Alloys*. Boca Raton: CRC Press, May 23, 2019. 292 pp. ISBN: 978-0-429-49703-2.

[41] Leonard W. Gruenberg and Leon Gunther. "Fulde-Ferrell Effect in Type-II Superconductors." In: *Phys. Rev. Lett.* 16.22 (May 30, 1966), pp. 996–998.

[42] F. Guillou et al. "Non-Hysteretic First-Order Phase Transition with Large Latent Heat and Giant Low-Field Magnetocaloric Effect." In: *Nat Commun* 9.1 (1 July 26, 2018), p. 2925. ISSN: 2041-1723.

[43] F. Hardy and A. D. Huxley. "p-Wave Superconductivity in the Ferromagnetic Superconductor URhGe." In: *Phys. Rev. Lett.* 94.24 (June 24, 2005), p. 247006.

[44] K. Hasselbach et al. "Superconducting Phase Diagram of UPt3 Studied by Thermal Expansion and Specific Heat." In: *J Low Temp Phys* 81.5 (Dec. 1, 1990), pp. 299–315. ISSN: 1573-7357.

[45] K. Hattori and H. Tsunetsugu. "p-wave superconductivity near a transverse saturation field." In: *Phys. Rev. B* 87.6 (Feb. 5, 2013), p. 064501.

[46] T. Hattori et al. "Superconductivity Induced by Longitudinal Ferromagnetic Fluctuations in UCoGe." In: *Phys. Rev. Lett.* 108.6 (Feb. 6, 2012), p. 066403.

[47] Taisuke Hattori et al. "Spin-Triplet Superconductivity Induced by Longitudinal Ferromagnetic Fluctuations in UCoGe Probed by $^{59}$Co NMR Measurement." In: *J. Phys. Soc. Jpn.* 83.6 (June 15, 2014), p. 061012. ISSN: 0031-9015.

[48] I. M. Hayes et al. "Multicomponent Superconducting Order Parameter in UTe2." In: *Science* 373.6556 (Aug. 13, 2021), pp. 797–801.

[49] N. T. Huy et al. "Superconductivity on the Border of Weak Itinerant Ferromagnetism in UCoGe." In: *Phys. Rev. Lett.* 99.6 (Aug. 10, 2007), p. 067006.

[50] Y. Ihara et al. "Anisotropic Magnetic Fluctuations in the Ferromagnetic Superconductor UCoGe Studied by Direction-Dependent $^{59}$Co NMR Measurements." In: *Phys. Rev. Lett.* 105.20 (Nov. 10, 2010), p. 206403.

[51] Shugo Ikeda et al. "Single Crystal Growth and Magnetic Properties of UTe2." In: *J. Phys. Soc. Jpn.* 75 (Suppl Jan. 2006), pp. 116–118. ISSN: 0031-9015.

[52] K. Ikushima et al. "First-order phase transition in $UO_2$ : $^{235}$U and $^{17}$O NMR study." In: *Phys. Rev. B* 63.10 (Feb. 9, 2001), p. 104404.

[53] Kenji Ikushima et al. "Observation of $^{235}$U NMR in the Antiferromagnetic State of $UO_2$." In: *J. Phys. Soc. Jpn.* 67.1 (Jan. 15, 1998), pp. 65–66. ISSN: 0031-9015.

[54] S. Imajo et al. "Thermodynamic evidence for the formation of a Fulde-Ferrell-Larkin-Ovchinnikov phase in the organic superconductor $\lambda-(BETS)_2GaCl_4$." In: *Phys. Rev. B* 103.22 (June 1, 2021), p. L220501.

[55] Shusaku Imajo et al. "Thermodynamic Investigation of Metamagnetism in Pulsed High Magnetic Fields on Heavy Fermion Superconductor UTe2." In: *J. Phys. Soc. Jpn.* 88.8 (Aug. 15, 2019), p. 083705. ISSN: 0031-9015.

[56] K. Ishida et al. "Pairing Interaction in Superconducting UCoGe Tunable by Magnetic Field." In: *Phys. Rev. B* 104.14 (Oct. 18, 2021), p. 144505.

[57] K. Ishihara et al. *Anisotropic Enhancement of Lower Critical Field in Ultraclean Crystals of Spin-Triplet Superconductor UTe2*. Jan. 11, 2023. arXiv: 2301.04801 [cond-mat]. URL: http://arxiv.org/abs/2301.04801. preprint.

[58] K. Ishihara et al. *Chiral Superconductivity in UTe2 Probed by Anisotropic Low-Energy Excitations*. Jan. 26, 2022. arXiv: 2105.13721 [cond-mat]. URL: http://arxiv.org/abs/2105.13721. preprint.

[59] Jun Ishizuka and Youichi Yanase. "Periodic Anderson model for magnetism and superconductivity in $UTe_2$." In: *Phys. Rev. B* 103.9 (Mar. 5, 2021), p. 094504.

[60] Jun Ishizuka et al. "Insulator-Metal Transition and Topological Superconductivity in $UTe_2$ from a First-Principles Calculation." In: *Phys. Rev. Lett.* 123.21 (Nov. 19, 2019), p. 217001.

[61] V. Jaccarino and M. Peter. "Ultra-High-Field Superconductivity." In: *Phys. Rev. Lett.* 9.7 (Oct. 1, 1962), pp. 290–292.

[62] Lin Jiao et al. "Chiral Superconductivity in Heavy-Fermion Metal UTe2." In: *Nature* 579.7800 (7800 Mar. 2020), pp. 523–527. ISSN: 1476-4687.

[63] Robert Joynt and Louis Taillefer. "The superconducting phases of $UPt_3$." In: *Rev. Mod. Phys.* 74.1 (Mar. 11, 2002), pp. 235–294.

[64] S. Kasahara et al. "Evidence for an Fulde-Ferrell-Larkin-Ovchinnikov State with Segmented Vortices in the BCS-BEC-Crossover Superconductor FeSe." In: *Phys. Rev. Lett.* 124.10 (Mar. 10, 2020), p. 107001.

[65] Harukazu Kato et al. "Direct Observation of $^{235}$U NMR in an Itinerant 5f Electron System, $USb_2$." In: *J. Phys. Soc. Jpn.* 73.8 (Aug. 15, 2004), pp. 2085–2088. ISSN: 0031-9015.

[66] J. Kačmarčík et al. "Specific heat measurements of a superconducting $NbS_2$ single crystal in an external magnetic field: Energy gap structure." In: *Phys. Rev. B* 82.1 (July 14, 2010), p. 014518.

[67] S. Khim et al. "Field-Induced Transition within the Superconducting State of CeRh2As2." In: *Science* 373.6558 (Aug. 27, 2021), pp. 1012–1016.

[68] S. Khmelevskyi, L. V. Pourovskii, and E. A. Tereshina-Chitrova. *Structure of the Normal State and Origin of Schottky Anomaly in the Correlated Heavy Fermion Superconductor UTe2*. Sept. 15, 2022. arXiv: 2209.07314 [cond-mat]. URL: http://arxiv.org/abs/2209.07314. preprint.

[69] K. Kinjo et al. *Magnetic Field-Induced Transition with Spin Rotation in the Superconducting Phase of UTe2*. June 7, 2022. arXiv: 2206.02444 [cond-mat]. URL: http://arxiv.org/abs/2206.02444. preprint.

[70] Shunichiro Kittaka et al. "Orientation of Point Nodes and Nonunitary Triplet Pairing Tuned by the Easy-Axis Magnetization in UTe2." In: *Phys. Rev. Research* 2.3 (July 13, 2020), p. 032014.

[71] W. Knafo et al. "Comparison of Two Superconducting Phases Induced by a Magnetic Field in UTe2." In: *Commun Phys* 4.1 (1 Mar. 1, 2021), pp. 1–9. ISSN: 2399-3650.

[72] W. Knafo et al. "High-Field Moment Polarization in the Ferromagnetic Superconductor UCoGe." In: *Phys. Rev. B* 86.18 (Nov. 12, 2012), p. 184416.

[73] W. Knafo et al. "Low-Dimensional Antiferromagnetic Fluctuations in the Heavy-Fermion Paramagnetic Ladder Compound UTe2." In: *Phys. Rev. B* 104.10 (Sept. 14, 2021), p. L100409.

[74] William Knafo et al. "Magnetic-Field-Induced Phenomena in the Paramagnetic Superconductor UTe2." In: *J. Phys. Soc. Jpn.* 88.6 (June 15, 2019), p. 063705. ISSN: 0031-9015.

[75] Georg Knebel et al. "Anisotropy of the Upper Critical Field in the Heavy-Fermion Superconductor UTe2 under Pressure." In: *J. Phys. Soc. Jpn.* 89.5 (May 15, 2020), p. 053707. ISSN: 0031-9015.

[76] Georg Knebel et al. "Field-Reentrant Superconductivity Close to a Metamagnetic Transition in the Heavy-Fermion Superconductor UTe2." In: *J. Phys. Soc. Jpn.* 88.6 (June 15, 2019), p. 063707. ISSN: 0031-9015.

[77] Andreas Kreisel, Yundi Quan, and P. J. Hirschfeld. "Spin-Triplet Superconductivity Driven by Finite-Momentum Spin Fluctuations." In: *Phys. Rev. B* 105.10 (Mar. 14, 2022), p. 104507.

[78] A. G. Lebed and O. Sepper. "Quantum Limit in a Magnetic Field for Triplet Superconductivity in a Quasi-One-Dimensional Conductor." In: *Phys. Rev. B* 90.2 (July 11, 2014), p. 024510.

[79] Andrei G. Lebed. "Restoration of Superconductivity in High Magnetic Fields in UTe2." In: *Mod. Phys. Lett. B* 34.32 (Nov. 20, 2020), p. 2030007. ISSN: 0217-9849.

[80] A. J. Leggett. "Implications of the $^3$He Phase Diagram below 3 mK." In: *Progress of Theoretical Physics* 51.4 (Apr. 1, 1974), pp. 1275–1277. ISSN: 0033-068X.

[81] Anthony J. Leggett. "A theoretical description of the new phases of liquid $^3$He." In: *Rev. Mod. Phys.* 47.2 (Apr. 1, 1975), pp. 331–414.

[82] R. Lortz et al. "Calorimetric Evidence for a Fulde-Ferrell-Larkin-Ovchinnikov Superconducting State in the Layered Organic Superconductor $\kappa-(BEDT-TTF)_2Cu(NCS)$ In: *Phys. Rev. Lett.* 99.18 (Oct. 30, 2007), p. 187002.

[83] V. Lupei. "The hyperfine interaction of trivalent uranium and the nuclear magnetic moment of 235U." In: *J. Phys. C: Solid State Phys.* 16.34 (Dec. 1983), p. 6627. ISSN: 0022-3719.

[84] K. Maki and E. Puchkaryov. "Impurity Effects in P-Wave Superconductors." In: *EPL* 50.4 (May 15, 2000), p. 533. ISSN: 0295-5075.

[85] Masahiro Manago, Kenji Ishida, and Dai Aoki. "Single ferromagnetic fluctuations in UCoGe revealed by $^{73}$Ge- and $^{59}$Co-NMR studies." In: *Phys. Rev. B* 97.7 (Feb. 14, 2018), p. 075130.

[86] F. Marsiglio and J. P. Carbotte. "Strong-Coupling Corrections to Bardeen-Cooper-Schrieffer Ratios." In: *Phys. Rev. B* 33.9 (May 1, 1986), pp. 6141–6146.

[87] N. D. Mathur et al. "Magnetically Mediated Superconductivity in Heavy Fermion Compounds." In: *Nature* 394.6688 (6688 July 1998), pp. 39–43. ISSN: 1476-4687.

[88] W. L. McMillan. "Transition Temperature of Strong-Coupled Superconductors." In: *Phys. Rev.* 167.2 (Mar. 10, 1968), pp. 331–344.

[89] Tristin Metz et al. "Point-node gap structure of the spin-triplet superconductor $UTe_2$." In: *Phys. Rev. B* 100.22 (Dec. 19, 2019), p. 220504.

[90] H. W. Meul et al. "Observation of Magnetic-Field-Induced Superconductivity." In: *Phys. Rev. Lett.* 53.5 (July 30, 1984), pp. 497–500.

[91] Lin Miao et al. "Low Energy Band Structure and Symmetries of $UTe_2$ from Angle-Resolved Photoemission Spectroscopy." In: *Phys. Rev. Lett.* 124.7 (Feb. 19, 2020), p. 076401.

[92] A. B. Migdal. "Interaction between Electrons and Lattice Vibrations in a Normal Metal." In: *Sov. Phys. JETP* 7.6 (1958), pp. 996–1001.

[93] V. P. Mineev. "Reentrant Superconductivity in UTe2." In: *Jetp Lett.* 111.12 (June 1, 2020), pp. 715–719. ISSN: 1090-6487.

[94] V. P. Mineev. "Superconducting States in Ferromagnetic Metals." In: *Phys. Rev. B* 66.13 (Oct. 4, 2002), p. 134504.

[95] V. P. Mineev. "Superconductivity in Uranium Ferromagnets." In: *Phys.-Usp.* 60.2 (May 1, 2017), p. 121. ISSN: 1063-7869.

[96] V. P. Mineev and T. Champel. "Theory of superconductivity in ferromagnetic superconductors with triplet pairing." In: *Phys. Rev. B* 69.14 (Apr. 27, 2004), p. 144521.

[97] Vladimir P. Mineev. "Low Temperature Specific Heat and Thermal Conductivity in Superconducting UTe2." In: *J. Phys. Soc. Jpn.* 91.7 (July 15, 2022), p. 074601. ISSN: 0031-9015.

[98] T. M. Mishonov, S. I. Klenov, and E. S. Penev. "Temperature Dependence of Specific Heat and Penetration Depth of Anisotropic-Gap Bardeen-Cooper-Schrieffer Superconductors for a Factorizable Pairing Potential." In: *Phys. Rev. B* 71.2 (Jan. 27, 2005), p. 024520.

[99] Atsushi Miyake et al. "Enhancement and Discontinuity of Effective Mass through the First-Order Metamagnetic Transition in UTe2." In: *J. Phys. Soc. Jpn.* 90.10 (Oct. 15, 2021), p. 103702. ISSN: 0031-9015.

[100] Atsushi Miyake et al. "Metamagnetic Transition in Heavy Fermion Superconductor UTe2." In: *J. Phys. Soc. Jpn.* 88.6 (June 15, 2019), p. 063706. ISSN: 0031-9015.

[101] Genki Nakamine et al. "Superconducting Properties of Heavy Fermion UTe2 Revealed by 125Te-Nuclear Magnetic Resonance." In: *J. Phys. Soc. Jpn.* 88.11 (Nov. 15, 2019), p. 113703. ISSN: 0031-9015.

[102] Shota Nakamura et al. "Anisotropic Field Response of Specific Heat for a Ferromagnetic Superconductor UCoGe in Magnetic Fields." In: *Phys. Rev. B* 106.3 (July 28, 2022), p. 035152.

[103] A. M. Nikitin et al. "Superconducting and Ferromagnetic Phase Diagram of UCoGe Probed by Thermal Expansion." In: *Phys. Rev. B* 95.11 (Mar. 28, 2017), p. 115151.

[104] Q. Niu et al. "Fermi-Surface Instability in the Heavy-Fermion Superconductor $UTe_2$." In: *Phys. Rev. Lett.* 124.8 (Feb. 26, 2020), p. 086601.

[105] Tetsuya Ohta et al. "Ferromagnetic Quantum Critical Fluctuations and Anomalous Coexistence of Ferromagnetism and Superconductivity in UCoGe Revealed by Co-NMR and NQR Studies." In: *J. Phys. Soc. Jpn.* 77.2 (2008), pp. 023707–023707.

[106] C. Paulsen et al. "Anomalous anisotropy of the lower critical field and Meissner effect in $UTe_2$." In: *Phys. Rev. B* 103.18 (May 5, 2021), p. L180501.

[107] C. Paulsen et al. "Observation of the Meissner-Ochsenfeld Effect and the Absence of the Meissner State in UCoGe." In: *Phys. Rev. Lett.* 109.23 (Dec. 3, 2012), p. 237001.

[108] C. Pfleiderer and A. D. Huxley. "Pressure Dependence of the Magnetization in the Ferromagnetic Superconductor $UGe_2$." In: *Phys. Rev. Lett.* 89.14 (Sept. 16, 2002), p. 147005.

[109] *Phonons and the Debye Specific Heat*. URL: http://hyperphysics.phy-astr.gsu.edu/hbase/Solids/phonon.html.

[110] A. Pogrebna et al. "Coexistence of Ferromagnetism and Superconductivity in Iron Based Pnictides: A Time Resolved Magnetooptical Study." In: *Sci Rep* 5.1 (1 Jan. 13, 2015), p. 7754. ISSN: 2045-2322.

[111] Sheng Ran et al. "Expansion of the High Field-Boosted Superconductivity in UTe2 under Pressure." In: *npj Quantum Mater.* 6.1 (1 Sept. 6, 2021), pp. 1–5. ISSN: 2397-4648.

[112] Sheng Ran et al. "Extreme Magnetic Field-Boosted Superconductivity." In: *Nat. Phys.* 15.12 (12 Dec. 2019), pp. 1250–1254. ISSN: 1745-2481.

[113] Sheng Ran et al. "Nearly Ferromagnetic Spin-Triplet Superconductivity." In: *Science* 365.6454 (Aug. 16, 2019), pp. 684–687.

[114] Stéphane Raymond et al. "Feedback of Superconductivity on the Magnetic Excitation Spectrum of UTe2." In: *J. Phys. Soc. Jpn.* 90.11 (Nov. 15, 2021), p. 113706. ISSN: 0031-9015.

[115] Priscila F. S. Rosa et al. "Single Thermodynamic Transition at 2 K in Superconducting UTe2 Single Crystals." In: *Commun Mater* 3.1 (1 May 23, 2022), pp. 1–6. ISSN: 2662-4443.

[116] A. Rosuel et al. "Field-Induced Tuning of the Pairing State in a Superconductor." In: *Phys. Rev. X* 13.1 (Feb. 22, 2023), p. 011022.

[117] S. L. Ruby et al. "Nuclear Gamma-Ray Resonance Study of Hyperfine Interactions in $^{238}U$." In: *Phys. Rev.* 184.2 (Aug. 10, 1969), pp. 374–380.

[118] H. Rudigier, H. R. Ott, and O. Vogt. "Low-temperature specific heat of uranium monopnictides and monochalcogenides." In: *Phys. Rev. B* 32.7 (Oct. 1, 1985), pp. 4584–4591.

[119] H. Sakai et al. *Field Induced Multiple Superconducting Phases in UTe2 along Hard Magnetic Axis*. Dec. 19, 2022. arXiv: 2210.05909 [cond-mat]. URL: http://arxiv.org/abs/2210.05909. preprint.

[120] H. Sakai et al. "Single crystal growth of superconducting $UTe_2$ by molten salt flux method." In: *Phys. Rev. Mater.* 6.7 (July 29, 2022), p. 073401.

[121] K. V. Samokhin and V. P. Mineev. "Gap Structure in Noncentrosymmetric Superconductors." In: *Phys. Rev. B* 77.10 (Mar. 18, 2008), p. 104520.

[122] S. S. Saxena et al. "Superconductivity on the Border of Itinerant-Electron Ferromagnetism in UGe2." In: *Nature* 406.6796 (6796 Aug. 2000), pp. 587–592. ISSN: 1476-4687.

[123] Rico Schönemann et al. *Thermodynamic evidence for high-field bulk superconductivity in $UTe_2$*. Version 1. June 13, 2022. arXiv: 2206.06508 [cond-mat]. URL: http://arxiv.org/abs/2206.06508. preprint.

[124] Konstantin Semeniuk et al. *Superconductivity versus quadrupole density wave in $CeRh_2As_2$*. Jan. 22, 2023. arXiv: 2301.09151 [cond-mat]. URL: http://arxiv.org/abs/2301.09151. preprint.

[125] Alexander B. Shick, Shin-ichi Fujimori, and Warren E. Pickett. "$UTe_2$: A nearly insulating half-filled $j = \frac{5}{2}$ $5f^3$ heavy-fermion metal." In: *Phys. Rev. B* 103.12 (Mar. 16, 2021), p. 125136.

[126] Tatsuya Shishidou et al. "Topological band and superconductivity in $UTe_2$." In: *Phys. Rev. B* 103.10 (Mar. 5, 2021), p. 104504.

[127] C. Stock et al. "Anisotropic Critical Magnetic Fluctuations in the Ferromagnetic Superconductor UCoGe." In: *Phys. Rev. Lett.* 107.18 (Oct. 27, 2011), p. 187202.

[128] Shyam Sundar et al. "Coexistence of Ferromagnetic Fluctuations and Superconductivity in the Actinide Superconductor ${\mathrm{UTe}}_{2}$." In: *Phys. Rev. B* 100.14 (Oct. 23, 2019), p. 140502.

[129] Shyam Sundar et al. "Ubiquitous Spin Freezing in the Superconducting State of UTe2." In: *Commun Phys* 6.1 (1 Feb. 1, 2023), pp. 1–11. ISSN: 2399-3650.

[130] M. Tachiki et al. "Superconducting bloch-wall in ferromagnetic superconductors." In: *Solid State Communications* 32.8 (Nov. 1, 1979), pp. 599–602. ISSN: 0038-1098.

[131] V. Taufour et al. "Tricritical Point and Wing Structure in the Itinerant Ferromagnet $UGe_2$." In: *Phys. Rev. Lett.* 105.21 (Nov. 15, 2010), p. 217201.

[132] M. Taupin et al. "Superconducting Gap of UCoGe Probed by Thermal Transport." In: *Phys. Rev. B* 90.18 (Nov. 14, 2014), p. 180501.

[133] T. Thebault et al. "Anisotropic signatures of electronic correlations in the electrical resistivity of $UTe_2$." In: *Phys. Rev. B* 106.14 (Oct. 7, 2022), p. 144406.

[134] F. Thomas et al. "Strong Coupling Effects on the Upper Critical Field of the Heavy-Fermion Superconductor UBe13." In: *J Low Temp Phys* 102.1 (Jan. 1, 1996), pp. 117–132. ISSN: 1573-7357.

[135] S. M. Thomas et al. "Spatially inhomogeneous superconductivity in $UTe_2$." In: *Phys. Rev. B* 104.22 (Dec. 3, 2021), p. 224501.

[136] Yo Tokunaga et al. "125Te-NMR Study on a Single Crystal of Heavy Fermion Superconductor UTe2." In: *J. Phys. Soc. Jpn.* 88.7 (July 15, 2019), p. 073701. ISSN: 0031-9015.

[137] G. E VOLOVIK. "Superconductivity with Lines of GAP Nodes: Density of States in the Vortex." In: *JETP lett* 58.6 (1993), pp. 469–473. ISSN: 0021-3640.

[138] Kristin Willa et al. "Thermodynamic Signatures of Short-Range Magnetic Correlations in UTe2." In: *Phys. Rev. B* 104.20 (Nov. 8, 2021), p. 205107.

[139] Beilun Wu, Dai Aoki, and Jean-Pascal Brison. "Vortex liquid phase in the p-wave ferromagnetic superconductor UCoGe." In: *Phys. Rev. B* 98.2 (July 26, 2018), p. 024517.

[140] Beilun Wu et al. "Pairing Mechanism in the Ferromagnetic Superconductor UCoGe." In: *Nat Commun* 8.1 (1 Feb. 23, 2017), p. 14480. ISSN: 2041-1723.

[141] Yuanji Xu, Yutao Sheng, and Yi-feng Yang. "Quasi-Two-Dimensional Fermi Surfaces and Unitary Spin-Triplet Pairing in the Heavy Fermion Superconductor $UTe_2$." In: *Phys. Rev. Lett.* 123.21 (Nov. 19, 2019), p. 217002.

[142] S. K. Yip, T. Li, and P. Kumar. "Thermodynamic considerations and the phase diagram of superconducting $UPt_3$." In: *Phys. Rev. B* 43.4 (Feb. 1, 1991), pp. 2742–2747.

[143] Josephine J. Yu et al. *Theory of the low- and high-field superconducting phases of $UTe_2$*. Mar. 3, 2023. arXiv: 2303.02152 [cond-mat]. URL: http://arxiv.org/abs/2303.02152. preprint.

[144] Yue Yu and S. Raghu. "Quenched randomness, thermal fluctuations, and reentrant superconductivity: Application to $UTe_2$." In: *Phys. Rev. B* 105.17 (May 4, 2022), p. 174506.